**UNIVERSITY OF SOUTHAMPTON**

FACULTY OF ENGINEERING AND THE ENVIRONMENT

Institute of Sound and Vibration Research

# Prediction and analysis of broadband interaction noise using synthetic turbulence

by

**Thomas Hainaut**

Thesis for the degree of Doctor of Philosophy

November 2017

UNIVERSITY OF SOUTHAMPTON

ABSTRACT

FACULTY OF ENGINEERING AND THE ENVIRONMENT
Institute of Sound and Vibration Research

Doctor of Philosophy

# PREDICTION AND ANALYSIS OF BROADBAND INTERACTION NOISE USING SYNTHETIC TURBULENCE

by Thomas Hainaut

Broadband interaction noise is a major source of noise in turbofan engines and will become more dominant with the increase of the bypass ratio. Generated by the interaction of turbulent fan wakes with outlet guide vanes, it can be numerically predicted by restricting the configuration to the stator only and introducing turbulent fan wakes with stochastic methods. In this work, a new method to inject turbulence using multiple sources of vorticity is proposed. It can generate either one-component or two-component frozen turbulence while being easy to implement and has no influence on the parallelization of an already existing solver. This method is successfully applied to an isolated 2D aerofoil and compared to experiments. In complex 2D geometries, the distortion of turbulence upstream of an aerofoil plays an important role in interaction noise, yet little is known regarding the mechanisms involved. Thus, the second part of this work focuses on turbulence distortion near the leading edge. To provide more physical insights in these mechanisms, a numerical vorticity approach in the frequency domain is developed. It allows the decomposition of the vorticity field into the incoming vorticity which is distorted close to the leading edge, and the bound vortices at the solid surfaces and wakes which represents the vorticity response of the aerofoil to respect a non-penetration condition at its boundaries. The size of the stagnation region at the leading edge is found to be a key factor in understanding turbulence distortion. Indeed, the larger this region, the more skewed the incoming vorticity field is. It results in attenuated transverse velocities retrieved from this vorticity field as well as reduced velocity perturbations from the bound vortices, which decreases the incoming turbulence levels, and therefore leads to noise reductions. However, at low wavenumbers, as the wavelength is large with respect to the stagnation region, no turbulence alteration is observed. To maximize the effect on the distortion of turbulence, the geometric changes need to be located as close as possible to the leading edge, as it will have more influence on the size of the stagnation region. Indeed, in this work, the geometry after the maximum thickness is found to have no effect on turbulence distortion.

# Contents

# List of Figures

# List of Tables

# Declaration of Authorship

I, Thomas HAINAUT, declare that the thesis entitled *Prediction and analysis of broadband interaction noise using synthetic turbulence* and the work presented in the thesis are both my own, and have been generated by me as the result of my own original research. I confirm that:

- this work was done wholly or mainly while in candidature for a research degree at this University;
- where any part of this thesis has previously been submitted for a degree or any other qualification at this University or any other institution, this has been clearly stated;
- where I have consulted the published work of others, this is always clearly attributed;
- where I have quoted from the work of others, the source is always given. With the exception of such quotations, this thesis is entirely my own work;
- I have acknowledged all main sources of help;
- where the thesis is based on work done by myself jointly with others, I have made clear exactly what was done by others and what I have contributed myself;
- parts of this work have been published as: [5, 6, 7]

Signed:.....

Date:.....

# Acknowledgements

This work was funded by Innovate UK, HARMONY Programme (GA n101367).

Acknowledged in the completion of this work are Rolls-Royce Plc for the financial and technical support given, DLR for providing the CAA solver PIANO and the use of the IRIDIS High Performance Computing Facility, and associated support services at the University of Southampton.

I would like to thank first my supervisors Gwénael Gabard and Phil Joseph for their support, advice and being more than just supervisors.

On many levels, this has been a very culturally enriching experience, where I had the chance of meeting people from 39 countries (probably more). Special thank to the people in my office and nearby offices, my neighboors, the Erasmus community, Jesters, etc.

I wanted to state at least the most important ones, but I am sure I will forget some people, so I will make a rather unusual acknowledgment by stating only the initial of their first name, along with the number of person associated (I'll replace the 0's by 1's just in case :P). But special thanks to (you know who you are)

A×4, B×2, C×3, D×1, E×2, F×2, G×3, H×2, I×1, J×7, K×3, L×2, M×4, N×1, O×2, P×1, Q×1, R×1, S×5, T×2, U×1, V×1, W×1, X×1, Y×1, Z×1.

# Nomenclature and Conventions

## Greek letters

| | |
|---|---|
| $\alpha$ | Angle of attack of the profile |
| $\Delta f$ | Frequency resolution |
| $\Delta t$ | Time-step |
| $\Delta \mathbf{x}$ | Spacing of the mesh |
| $\gamma$ | Ratio of specific heats |
| $\gamma_i$ | Bound vortices on the aerofoil surface |
| $\gamma_i^{(w)}$ | Bound vortices in the aerofoil wake |
| $\Gamma$ | Gamma function |
| $\Gamma_i$ | Point vortex |
| $\lambda$ | Integral length scale |
| $\omega$ | Angular frequency |
| $\rho$ | Total density |
| $\rho_\infty$ | Static density |
| $\rho_0$ | Mean flow density |
| $\rho'$ | Density perturbation |
| $\varphi$ | Phase |
| $\phi_{ij}$ | Wave number spectrum of the fluctuating velocity |
| $\Phi_{ij}$ | Wave number spectrum integrated over one $k$ |
| $\psi$ | Stream function |
| $\mathbf{\Psi}$ | Velocity potential |
| $\xi$ | Distance to the leading edge |
| $\boldsymbol{\xi}_n$ | Stochastic vector |
| $\boldsymbol{\zeta}_n$ | Stochastic vector |

## Roman letters

| | |
|---|---|
| $a_0$ | Local speed of sound |
| $a_\infty$ | Static speed of sound |

| | |
|---|---|
| $a_x^{(i,.)}$ | Coefficient in the vortex panel method |
| $A$ | Amplitude of the source of vorticity |
| $A_g$ | Amplitude of the incoming gust |
| $A_{i,j}$ | Geometrical influence coefficient from the aerofoil panels |
| $A_{i,j}^{(w)}$ | Geometrical influence coefficient from the wake panels |
| $b$ | Half-radius of the source of vorticity |
| $b_i$ | Coefficient in the vortex panel method |
| $c$ | Chord of the geometry |
| $C$ | Circulation around a geometry |
| $c_i$ | Coefficient in the vortex panel method |
| $d^{(l)}$ | Length of $l$-th panel |
| $\mathbf{e}$ | Axis of rotation |
| $E$ | Energy spectrum of the turbulence |
| $E_0$ | Total energy |
| $f_s$ | Sampling frequency |
| $\mathbf{g}$ | Spatial distribution of the source of vorticity |
| $\mathcal{G}$ | Green function |
| $G$ | Kernel filter in RPM |
| $J_i$ | Bessel function of $i^{\text{th}}$-order |
| i | Imaginary unit that satisfies $\mathrm{i}^2 = -1$ |
| $I$ | Index indicating the nose radius |
| $\mathbf{k}$ | Wave number |
| $m$ | Index indicating the chordwise location of the maximum thickness |
| $M$ | Mach number |
| $p$ | Total pressure |
| $p_\infty$ | Static pressure |
| $p_0$ | Mean flow pressure |
| $p'$ | Pressure perturbation |
| $P$ | Probability function |
| $q$ | Heat flux |
| $R_{\text{LE}}$ | Nose radius |
| $s$ | Temporal signal of the source of vorticity |
| $S$ | Spectral Density of the temporal signal of the source of vorticity |
| $S_{pp}$ | Analytical power spectral density |
| St | Strouhal number |
| $\boldsymbol{\mathcal{S}}_v$ | Source of vorticity |
| $S_{\text{u2}}$ | Density spectrum of the transverse velocity |
| $t$ | Index indicating the maximum thickness |
| $T_I$ | Turbulence intensity |
| $T(\mathbf{X})$ | Drift function |
| $\mathcal{U}$ | Spatial white noise |

| | |
|---|---|
| $\mathbf{u}$ | Total velocity |
| $\mathbf{u}_0$ | Mean flow velocity |
| $\mathbf{u}_c$ | Convection velocity |
| $\mathbf{u}'$ | Velocity perturbation |
| $\overline{u_w^2}$ | Mean square velocity for the wake turbulence |
| $\mathbf{x}$ | Coordinates in space |
| $\mathbf{X}$ | Coordinates in space of a particle on a streamline |
| $\mathbf{x}_c$ | Coordinates of the centre of the source |
| $\mathbf{y}$ | Coordinates of the observer in space |

## Symbols

| | |
|---|---|
| $\nabla$ | Del operator |
| $\delta$ | Dirac function |
| $.*$ | Non-dimensionalized variable |
| $\langle . \rangle$ | Ensemble average |
| $\bar{.}$ | Complex conjugate |
| $\|.\|$ | Norm |
| $.^t$ | Transpose of a vector |
| $\hat{.}$ | Fourier-transform of function . |
| $\bar{\bar{.}}$ | Tensor |

## Acronyms

| | |
|---|---|
| ACARE | Advisory Council for Aeronautics Research in Europe |
| AoA | Angle of attack |
| APE | Acoustic Perturbation Equations |
| ASD | Artificial Selective Damping |
| BEM | Boundary Element Method |
| CAA | Computational Aero-Acoustics |
| CFD | Computational Fluid Dynamics |
| CFL | Courant-Friedrichs-Lewy number |
| DDES | Delayed Detached-Eddy Simulation |
| DLR | Deutsches Zentrum fur Luft- und Raumfahrt e.V. / German Aerospace Center |
| DNS | Direct Numerical Simulations |
| DRP | Dispersion-Relation-Preserving finite-difference scheme |
| FWH | Ffowcs-Williams Hawking |
| fRPM | fast Random-Particle-Mesh |
| IATA | International Air Transport Association |

| | |
|---|---|
| ICAO | International Civil Aviation Organization |
| IDDES | Improved Delayed Detached Eddy Simulation |
| ISVR | Institute of Sound and Vibration Research |
| LDDRK | Low-dissipation, low-dispersion Runge-Kutta |
| LBM | Lattice-Boltzmann Methods |
| LEE | Linearised Euler Equations |
| LES | Large Eddy Simulations |
| MPI | Message Passing Interface |
| OASPL | Overall Sound Pressure Level |
| OGVs | Outlet Guide Vanes |
| PDE | Partial Differential Equations |
| PIANO | Perturbation Investigation of Aerodynamic NOise |
| PSD | Power Spectral Density |
| PWL | Sound Power Level |
| RANS | Reynolds Averaged Navier-Stokes |
| RDT | Rapid Distortion Theory |
| RMS | Root Mean Square |
| RPM | Random-Particle-Mesh |
| SEM | Synthetic Eddy Methods |
| SPL | Sound Pressure Level |

# Chapter 1

# Introduction

## 1.1 Background

The air traffic constantly increased since the first commercial flight over 100 years ago. This increase is however not about to slow down as the air traffic was up 6.3% in 2016 according to the International Air Transport Association (IATA)[1] and could carry as many as 16 billions passengers by 2050 (as opposed to 2.4 billions in 2010)[2]. This increase has become a major issue regarding the people living next to an airport because additional noise is not any more tolerated by the population and therefore by the authorities. To overcome the problem, the noise regulations fixed by the International Civil Aviation Organization (ICAO) has become over the years more and more demanding. In FlightPath 2050[3], the Advisory Council for Aeronautics Research in Europe (ACARE) defined that the perceived noise emission of flying aircraft should decrease by 65 % by 2050, relative to year-2000 aircraft.

With more demanding noise regulations, substantial resources are spent by aircraft manufacturers to design quieter airliners. The noise sources from airplanes are noises induced by the flow on the airframe and noises generated by the jet engines. The first one is mainly due to high-lift devices, landing gears and cavities. On the other hand, jet engine noises can be decomposed into jet noise, combustion noise and fan noise. A few decades ago, jet noise was the dominant source, hence the majority of the previous research were focused on it. Nevertheless, nowadays, all the noise sources equally contribute to the perceived noise as jet noise has been drastically reduced mainly due to the increase of the bypass-ratio. However, this increase in the engine diameter has a limit as engines are getting closer to the ground and to the wings, and the velocity at the tip of the blades becomes supersonic. The Figure 1.1 compares the relative power levels of noise sources in modern aircraft at take-off and approach.

[1] http://atwonline.com/airline-traffic/iata-air-passenger-traffic-rebounded-2h-2016-63-overall
[2] Vision 2050, IATA, Singapore, 12 February 2011
[3] Flightpath 2050 Europe's Vision for Aviation, Report of the High Level Group on Aviation Research

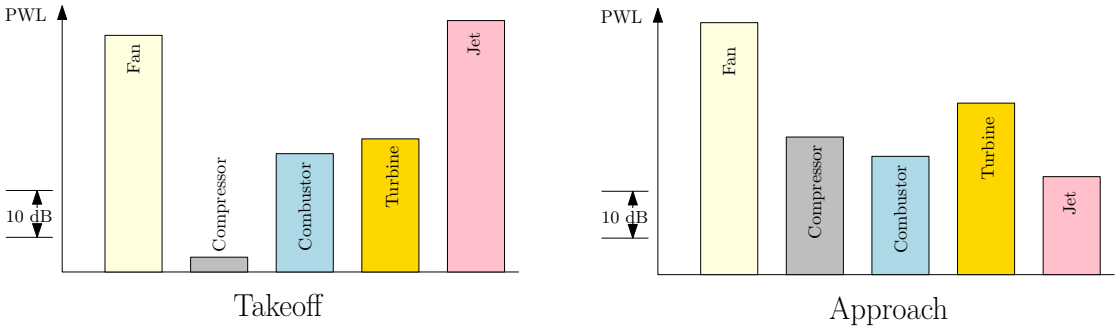


Figure 1.1: Relative power levels of noise sources in modern aircraft engines at take-off and approach. Data taken from Astley *et al.* [1].

Fan noise, dominant at reduced thrust level [8], is a combination of tonal and broadband noise. It can be decomposed into the rotor and guide vanes self noises, the rotor-boundary layer interaction noise and the rotor-wake guide vanes interaction noise. The fan noise is however complex to reduce as the combination of the fan and the guides vanes are responsible for the majority of the total thrust, so noise reductions has to come without sacrificing performance.

## 1.2 Fan interaction noise

The numerical study of broadband noise generated by a turbulent flow is demanding in computational resources due to the presence of a large variety of scales, from the small turbulent scales to the large acoustic length scales. In the context of predicting broadband noise generated by the interaction of the turbulent wakes of the fan blades and the outlet guide vanes, a Direct Numerical Simulations (DNS) approach consists in considering the complete rotor-stator stage or an angular sector including one or more blade/vane channels. However, correctly modelling the turbulent wakes of the rotors require to solve the full governing equations, coupled with a fine mesh, thus the computational cost associated is prohibitive. To limit the cost, Large Eddy Simulations (LES) could be used as the small scales are not simulated but approximated through a sub-grid scale model. Nevertheless it does not allow regular simulations in an industrial context.

To further reduce the computational cost, hybrid simulations can be used. They are composed of two different solvers; the first one is dedicated to the calculation of the acoustic source regions. Using equivalent sources of this first simulation, the second solver predicts the acoustic field, propagating the equivalent sources to the far field. To correctly calculate the acoustic sources, a good representation of the turbulence is required, implying a large variety of length-scale to be resolved, thus this alternative remains computationally intensive.

An alternative methodology, used in this work, consists in restricting the configuration to the stator only, and introducing a synthetic turbulence in the computational domain. This allows a drastic reduction in the size of the computational domain and, as the problem is limited to the study of the interaction of the injected turbulence with the stator, the generation and propagation of the noise can be obtained without solving the full governing equations. Indeed, the steady and unsteady simulations are separated. The steady part is simulated using RANS while a model able to compute acoustic sources and propagate them is used for the unsteady part. Finally, as the configuration is restricted to the stator only, rotor wakes need to be synthesized and injected in the unsteady computation. The quality of sound predictions mainly depends on the turbulence wake used as input. This synthetic velocity field is generated using stochastic methods which try to reproduce specific time and space correlations. This could be achieved by the use of stochastic methods, as introduced in 1970 by Kraichnan [9] where the fluctuating turbulent field is decomposed as a sum of Fourier modes. Nevertheless, this summation can become computationally expensive as the number of modes increases. A second solution is the decomposition of the turbulence in a sum of eddies, either by filtering a white noise to reproduce imposed spatial and temporal correlations of the incoming turbulence, as proposed by Ewert *et al.* [10] in the Random-Particle-Mesh (RPM) or by Dieste & Gabard [11, 12], or by directly calibrating the eddies to match the desired features of the turbulence as introduced by Jarrin *et al.* [13, 14, 15] in Synthetic Eddy Methods (SEM).

## 1.3 Aims and contributions of this thesis

The general aim of this project is to assess and develop stochastic methods for computational aeroacoustic purposes to better understand interaction noise of realistic isolated 2D profiles.

The stochastic method used in this work is based on the decomposition of the turbulence in a sum of eddies. In this group of methods, the synthetic turbulent field could be generated by either filtering a white noise to reproduce imposed spatial and temporal correlations of the incoming turbulence, or by directly calibrating the eddies to match the desired features of the turbulence. Both techniques generate synthetic turbulent flows and require as inputs some statistical properties of the turbulent flow. These properties can be either modelled using empirical laws, measured experimentally or estimated from RANS simulations.

The synthesized field is then injected in a computational domain. While it is usually performed through an inlet boundary or by using a patch, its implementation in a solver can be cumbersome. In this work, in contrast with these methods of injection, the

turbulence is injected through multiple sources of vorticity, which is arguably easier to implement.

Aside from the ease of implementation , the developed method has the advantage of being able to independently control the turbulent spectrum in the two directions, thus it could be used to synthesize isotropic turbulent fields as well as anisotropic turbulent fields. This last characteristic was previously mainly achieved using additional steps applied to already synthesized isotropic fields. Nevertheless, these steps are time-consuming as they often rely on filtering and scaling operations.

In this work, the developed method to inject synthetic turbulence using multiple sources of vorticity is combined with the LEE, which models the propagation of small amplitude perturbations on a mean flow. It is numerically solved in the time-domain, finite-difference solver called Perturbation Investigation of Aerodynamic NOise (PIANO), developed by Deutsches Zentrum fur Luft- und Raumfahrt e.V. / German Aerospace Center (DLR).

The model combined with the developed method is firstly verified in free-field and then on flat plate interaction noise. Afterwards, it is then applied on the interaction of turbulent gusts with a more realistic configuration. This last configuration is a cambered aerofoil and is validated against experiments.

Recent studies suggest that the distortion of the incoming turbulence by the mean flow close to the leading edge plays an important role in the radiated noise. Analytical methods are restricted by the assumptions made on the geometries and the flow solution, and experimental studies are limited by technical difficulties to collect data. Therefore, numerical simulations seem to be an adequate solution as it is possible to record any variable at any location in the computational domain in the same simulation and at every time-step if necessary.

To better understand turbulence distortion, in combination with the CAA solver PIANO, a second numerical method is developed. Based on a vorticity approach in the frequency domain, it allows the decomposition of the vorticity field into the incoming vorticity which is distorted close to the leading edge, and the bound vortices at the solid surfaces and wakes which represents the vorticity response of the aerofoil to respect a non-penetration condition at its boundaries. Finally, a parametric study altering turbulence, mean flow and geometrical factors reveal some physical insights in turbulence distortion mechanisms.

## 1.4 Structure of the thesis

Chapter 2 of this work is a literature review of the existing methods to numerically predict interaction noise, from simple geometries to complete rotor-stator configurations.

It also provides a description of the existing methods to generate synthetic turbulence using stochastic methods.

Chapter 3 describes a physical model to study interaction noise and its numerical implementation in the solver PIANO. Then, using a harmonic gust interacting with a flat plate case, the feasibility of injecting perturbations using a source of vorticity is assessed.

Chapter 4 details the development and validation of a new method to inject either one- or two-component frozen synthetic turbulence in a computational domain using localized sources of vorticity. The method is then validated for both a free field case and a flat plate interaction noise case.

Chapter 5 focuses on the interaction noise from turbulent gusts with a cambered aerofoil and is validated against experiments. Then, a parametric study is performed by looking at the effect of the angle of attack and integral length scale of the turbulence on the radiated noise.

Chapter 6 focuses on the turbulence distortion by the mean flow in the vicinity of the leading edge. Indeed, this distortion is believed to play an important role in the interaction noise, yet very little is known about it. A first analysis is performed using the LEE model. Then, to gain more physical insights, a vorticity based numerical approach is developed.

In Chapter 7, a parametric study altering turbulence, mean flow and geometrical factors is performed using both the LEE model and vorticity approach.

Finally, Chapter 8 discusses the main conclusions and future work.

# Chapter 2

# Review of methods to predict broadband fan noise

Interaction noise is the main source of broadband noise and has become over the years more and more important with the increase of the bypass ratio and the reduction of the other noise sources. This first chapter focuses on presenting interaction noise and how to predict it using numerical methods. After introducing interaction noise, the main numerical methods used in this context are described. Then, the previous numerical applications are reviewed, from interaction noise with isolated profiles to ducted profile cascades.

## 2.1 Interaction noise

On modern high-bypass ratio jet engines, fan noise has become a major noise source. Fan noise is however complex to reduce as the combination of the fan and the guides vanes are responsible for the majority of the total thrust, so noise reductions has to come without sacrificing the performances. Fan noise can be decomposed into the rotor and guide vanes self noises, the rotor-boundary layer interaction noise and the rotor-wake guide vanes interaction noise. Those four noise sources produce a tonal noise directly related to the rotational speed of the fan and the number of blades, and a broadband noise. Some tones called cut-off frequency, are not propagating far as they are attenuated quickly. The others, called cut-on frequencies, travel over a large distance and are considered as the main nuisance. To reduce tonal noise, one can change the number of blades and the rotational speed to generate cut-off modes or shift the produced frequencies to others considered less disturbing. Absorbing material can also be applied within the inside of the body, which explicitly target desired frequencies. However these techniques are not efficient when applied to broadband noise. Broadband noise is linked to the incoherent

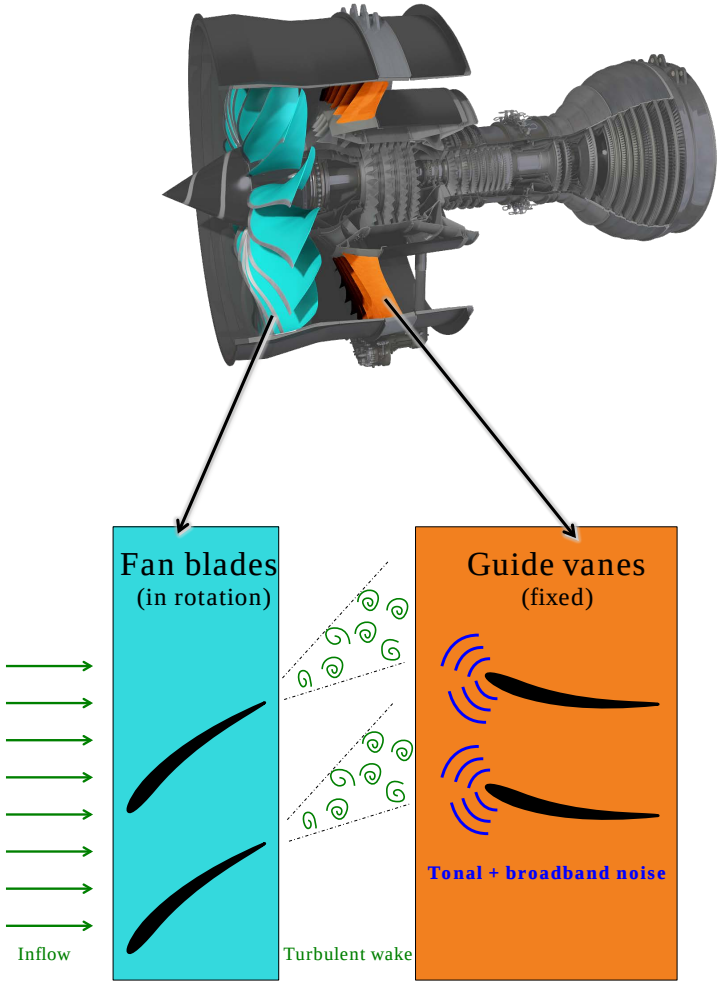


Figure 2.1: Simplified sketch of the interaction of the turbulent wakes of the fan with the guide vanes.

part of the flow. The main broadband noise source comes from the interaction of the turbulent wakes of the fan with the guide vanes, as depicted in Figure 2.1.

## 2.2 Numerical methods to predict broadband fan noise

The main disadvantages of analytical methods are the lack of adaptability and the simplified hypothesis made in terms of geometry and flow field configurations. To remedy these difficulties, numerical methods appear to be a good candidate. However, even nowadays, with the considerably increased computational power available, these numerical simulations remain a challenge to accurately simulate complex cases.

These methods can be separated in multiple families. The most accurate methods, called Direct Numerical Simulations (DNS) consist in directly solving the governing equations such as the Navier-Stokes equations, but it is too expensive for the current computational resources available. Indeed, the variety of length scale in a flow, from the small turbulence structures to the large acoustic wavelengths, implies using high-order methods along with fine grids within large computational domains. Those requirements limit DNS to low Reynolds numbers.

Large Eddy Simulations (LES) are an alternative solution to DNS. In those simulations, all the scales are resolved except for the small scales which are approximated through a sub-grid scale model. As a result, LES are greatly accelerated compare to DNS, but it still does not allow regular simulations in an industrial context.

For commercial purposes, hybrid simulations are often used. They are composed of two different solvers; the first one is dedicated to the calculation of the acoustic source regions. Using equivalent sources of this first simulation, the second solver predicts the acoustic field, propagating the equivalent sources to the far-field. However, for proper noise predictions, a necessary condition in the first simulation is an accurate turbulence generation and propagation which could be performed using DNS or LES methods. Hence, this approach remain demanding in computational resources.

More recently, Lattice-Boltzmann Methods (LBM), which are methods based on a mesoscopic view of the flow using Boltzmann equation, showed promising results in simulating aeroacoustic problems [16]. The Boltzmann equation describes the evolution of the flow particles in space as a function of time, and has the advantage of being easily implemented in a parallel solver. If the gas is dense enough, the particles are going to collide with each other. This collision term is difficult to model but is however important as it determines how the collision energy is distributed between the particles. The Bhatnagar–Gross–Krook operator [17] is often use as the collision term, for instance in the code *LaBS* or in the code *PowerFLOW*. To speed-up the simulations, as for LES, small scales are often approximated through a sub-grid scale model.

To study broadband noise, it seems necessary to solve full governing equations such as the Navier-Stokes equations to capture the main characteristics of the turbulent structures. An alternative can however be used, consisting of separately studying the behaviour of perturbations on a given mean flow. Hence, the steady and unsteady part are separated. The steady part, i.e. mean flow, can be calculated using a Reynolds Averaged Navier-Stokes (RANS). Then, the statistical data provided by the RANS can be used to create the unsteady field with stochastic methods. Instead of synthesizing the turbulence, the unsteady part can also originate from previous unsteady numerical simulations like LES, or from experimental measurements. The governing equations of perturbations need to be able to compute acoustic sources and propagate them. Moreover, linear interaction models between vorticity and sound generation are generally considered sufficient in

the study of interaction noise. These assumptions make the Linearised Euler Equations (LEE) a satisfactory candidate to study interaction noise. This alternative is less computationally demanding than DNS or LES, which allows simulations with higher Reynolds numbers. Moreover, the use of linear models for the acoustic generation and propagation imply that only the turbulence used as an input is present in the simulation. In the context of fan wake turbulence interacting with guide vanes, it means no guide vane self noise can be generated. Furthermore, this modular approach gives the possibility to independently alter the mean flow, the geometry or the turbulence characteristics to study its impact. The quality of sound predictions mainly depends on the turbulence used as input. This synthetic velocity field is generated using stochastic methods which try to reproduce the time and space correlations of a prescribed spectrum. These methods can be separated into two different main methods that are explained in the next section (2.3).

## 2.3 Stochastic methods

All stochastic methods can be separated into two different principles. The first is based on the decomposition of the fluctuating turbulent field as a sum of Fourier modes. The second, based on the principle that a turbulence can be decomposed in a sum of eddies [18], is generated either by filtering a white noise to reproduce imposed spatial and temporal correlations of the incoming turbulence, or by directly calibrating the eddies to match the desired features of the turbulence. These approaches are relatively recent due to the constant increase in computational power.

Depending on the application, a choice has to be made on the required properties the synthetic velocity field has to feature. Some of these properties are a specific energy spectrum, spatial correlations, temporal correlations, convection by the mean flow, inhomogeneity, anisotropy and sweeping effects. The more properties are featured, the more realistic the turbulence is but also the more computationally expensive the simulation is.

The first part of this section is a description of the original ideas of these methods, followed by some extensions of these methods by adding more properties to the turbulent flow.

### 2.3.1 Original ideas

#### 2.3.1.1 Decomposition in Fourier modes

In order to study the diffusion of particles by a turbulent velocity field, Kraichnan [9] synthesized the turbulent velocity field using a stochastic process. To generate an isotropic, incompressible and stationary synthetic turbulent field, he made the assumption that the velocity field can be expressed by a discrete sum of Fourier modes:

$$\mathbf{u}'(\mathbf{x},t) = \sum_{n=1}^{N} \left[\mathbf{a}_n \cos(\mathbf{k}_n \cdot \mathbf{x} + \omega_n t) + \mathbf{b}_n \sin(\mathbf{k}_n \cdot \mathbf{x} + \omega_n t)\right], \tag{2.1}$$

where $N$ is the number of modes, $\omega_n$ is the angular frequency of each mode that follows a Gaussian distribution of an arbitrary chosen standard deviation, and $\mathbf{k}_n$ is the wave number vector that is randomly chosen on a sphere with a radius $||\mathbf{k}_n||$. The amplitudes $\mathbf{a}_n$ and $\mathbf{b}_n$ are linked to the desired kinetic energy of the velocity flow. Moreover, the turbulent kinetic energy spectrum is discretized using a statistically isotropic distribution, hence, if $N \to \infty$, the desired spectrum is realized.

For the perturbations to ensure the incompressibility condition, the amplitude vectors $\mathbf{a}_n$ and $\mathbf{b}_n$ are chosen orthogonal to $\mathbf{k}_n$ ($\mathbf{a}_n \cdot \mathbf{k}_n = 0$ and $\mathbf{b}_n \cdot \mathbf{k}_n = 0$). This is performed by Kraichnan [9] by defining $\mathbf{a}_n = \boldsymbol{\zeta}_n \times \mathbf{k}_n$ and $\mathbf{b}_n = \boldsymbol{\xi}_n \times \mathbf{k}_n$ with $\boldsymbol{\zeta}_n$ and $\boldsymbol{\xi}_n$ random vectors. A graphic representation of the wavenumber $\mathbf{k}_n$ and the random vectors $\boldsymbol{\zeta}_n$ and $\boldsymbol{\xi}_n$ in the spherical coordinates $(k_n, \phi_n, \theta_n)$ is depicted in figure 2.2. The random vectors $\boldsymbol{\zeta}_n$ and $\boldsymbol{\xi}_n$ are chosen in the plane normal to $\mathbf{k}$. Thus they are only defined by the angle $\phi'_n$. It follows that the probability function for each angle

$$\mathrm{P}(\phi_n) = \mathrm{P}(\phi'_n) = \frac{1}{2\pi} \qquad \text{with } 0 \leq \phi_n, \phi'_n \leq 2\pi\ , \tag{2.2}$$

$$\mathrm{P}(\theta_n) = \frac{1}{2\pi}\sin(\theta_n) \qquad \text{with } 0 \leq \theta_n \leq \pi\ . \tag{2.3}$$

To remove the time-dependence of the generated turbulent field, Fung *et al.* [19, 20] added some temporal modes for each spatial mode:

$$\mathbf{u}'(\mathbf{x},t) = \sum_{n=1}^{N}\sum_{p=1}^{P_\omega} \left[(\mathbf{a}_{np} \times \hat{\mathbf{k}}_n)\cos(\mathbf{k}_n \cdot \mathbf{x} + \omega_{np} t) + (\mathbf{b}_{np} \times \hat{\mathbf{k}}_n)\sin(\mathbf{k}_n \cdot \mathbf{x} + \omega_{np} t)\right]\ , \tag{2.4}$$

with $\hat{\mathbf{k}}_{mn} = \mathbf{k}_{mn}/|\mathbf{k}_{mn}|$. $P_w$ is the number of angular frequencies associated with a mode $k_n$, and $N$ is the number of spatial mode $k_n$. To get a non time-dependent turbulent velocity field, Fung *et al.* [19, 20] found that only a few temporal modes for each spatial mode is satisfactory.

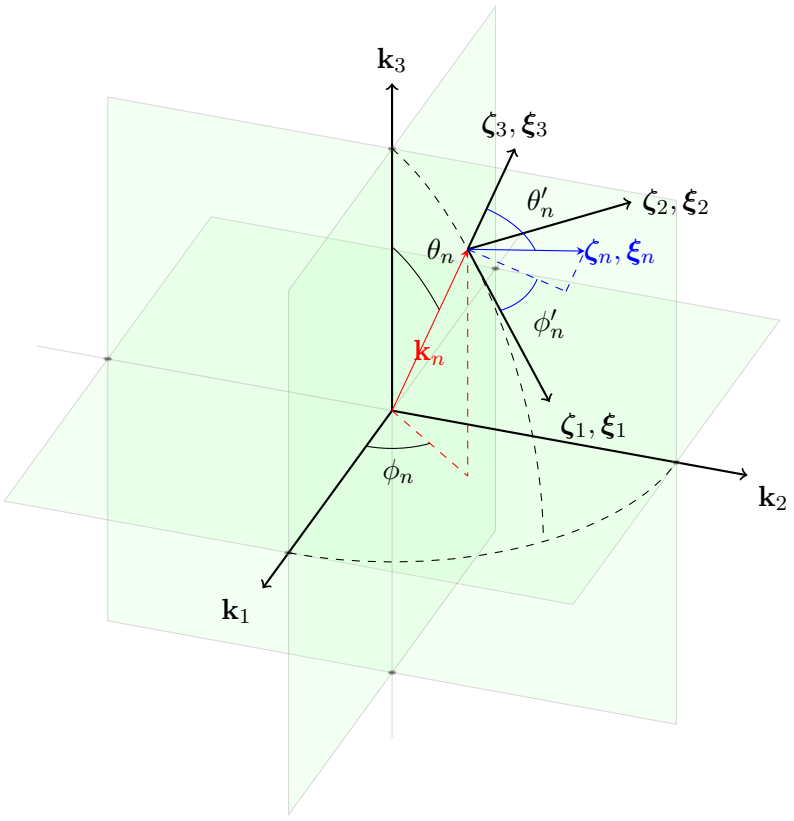


Figure 2.2: Decomposition in Fourier modes: Definition of the wavenumber $\mathbf{k}_n$ and the random vectors $\boldsymbol{\zeta}_n$ and $\boldsymbol{\xi}_n$.

#### 2.3.1.2 Discretized distribution of vortices

The Fourier modes decomposition method can be expensive as the number of considered modes increases. To address this issue, a second group of method based on the decomposition of the turbulence in a sum of eddies can be used. It could be generated by either filtering a white noise to reproduce imposed spatial and temporal correlations of the incoming turbulence, or by directly calibrating the eddies to match the desired features of the turbulence.

**White-noise filtering methods**

The first method, called Random-Particle-Mesh (RPM) or fast Random-Particle-Mesh (fRPM) depending on the numerical implementation, has been proposed by Ewert [21, 10]. It relies on the filtering of a white noise in order to reproduce spatial and temporal correlations of the turbulent field.

In these methods, the streamlines of the mean flow are discretized, and particles carrying the stream function of the fluctuating turbulence field are introduced at each node.

For each time step, the particles are convected along the streamlines, then temporal decorrelations and spatial filtering are applied. This filtering relies on the calculation of the stream function $\psi$, using a kernel filter $G$.

$$\psi_i(\mathbf{x},t) = \int_{\Re^3} G(|\mathbf{x}-\mathbf{x}'|)\mathcal{U}_i(\mathbf{x}',t)\mathrm{d}\mathbf{x}', \tag{2.5}$$

with $i = 1,2,3$, $\mathcal{U}_i$ being a spatial white noise (independent for each direction) with a zero-mean value. The turbulent velocity field is then derived from this stream function

$$\mathbf{u}' = \nabla \times \boldsymbol{\psi}, \tag{2.6}$$

In this method, the form of the filter $G$ is given by a Gaussian distribution :

$$G(|\mathbf{x}-\mathbf{x}'|) = A\exp\left(-\frac{\pi|\mathbf{x}-\mathbf{x}'|^2}{2\lambda^2}\right), \tag{2.7}$$

with $A$ and $\lambda$ respectively the kinetic energy and the integral length of turbulence. The use of Gaussian filters is mainly due to the fact that is simplify drastically the calculations.

The original RPM method [10] considers only a Gaussian spatial correlation function (or, by extension a Gaussian energy spectrum), as the kernel filter is expressed as (2.7) for the stream function $\psi_i$. To overcome this limitation, Siefert and Ewert [22] extended the method to be able to deal with non-Gaussian spectrum. This is possible by summing $N$ stochastic fields with a Gaussian spectrum

$$\psi_i^{(n)}(\mathbf{x},t) = \int_{\Re^3} G^{(n)}(|\mathbf{x}-\mathbf{x}'|)\mathcal{U}_i^{(n)}(\mathbf{x}',t)\mathrm{d}\mathbf{x}', \tag{2.8}$$

$$\psi_i(\mathbf{x},t) = \sum_{n=0}^{N-1} \psi_i^{(n)}(\mathbf{x},t), \tag{2.9}$$

where the kernels filters $G^{(n)}$ are chosen accordingly to the desired spectrum.

This summing of Gaussian filters to reproduce non-Gaussian energy spectrum is time-consuming. Instead, Dieste and Gabard [23, 12] proposed to directly use non-Gaussian filters, derived from the energy spectrum $E(k)$

$$G(|\mathbf{x}-\mathbf{x}'|) = \frac{1}{\sqrt{\pi}}\int_0^\infty \left(\frac{E(k)}{k}\right)^{\frac{1}{2}} \mathrm{J}_0(k|\mathbf{x}-\mathbf{x}'|)\mathrm{d}k \ , \tag{2.10}$$

or from the desired correlation tensor of the flow $R_{ij}$

$$G(|\mathbf{x}-\mathbf{x}'|) = \frac{1}{\sqrt{2\pi}}\int_0^\infty \mathcal{F}\left\{\frac{R_{ij}}{2}\right\}^{\frac{1}{2}} \mathrm{J}_0(k|\mathbf{x}-\mathbf{x}'|)\mathrm{d}k \ , \tag{2.11}$$

where $\mathcal{F}\{(.)\}$ is the Fourier transform of (.), and $J_0$ is the Bessel function of the zero$^{th}$ order.

They applied this method to Liepmann and von Karman energy spectra, however, as the filters are not separable unlike Gaussian filter, it involves the calculation of hyper-geometric functions which can be very costly. To address this issue, they interpolated the filters instead of using the exact equations.

After discretization, independent of the filter used, this process comes down to a sum of point vortices in the computational domain.

**Cloud of point vortices**

This second method directly calibrates the eddies to match the desired features of the turbulence as proposed by Jarrin *et al.* [13, 14, 15]. This method, called Synthetic Eddy Methods (SEM), injects the eddies through an inlet boundary, using Taylor's hypothesis (frozen turbulence). The fluctuating velocity $\mathbf{u}'$ is defined as a sum of $N$ eddies injected inside the domain

$$u_i'(\mathbf{x}) = \frac{1}{\sqrt{N}} \sum_{n=1}^{N} a_{ij} \epsilon_j^n f_\lambda \left( \frac{\mathbf{x} - \mathbf{x}^n}{\lambda^n} \right), \tag{2.12}$$

where $\mathbf{x}^n$ the spatial location of the centre of the $n$th eddy, $\lambda^n$ the turbulent length scale and $f_\lambda$ the velocity distribution of the eddies. The random numbers $\epsilon_j^n$ which have a zero average and $\langle \epsilon_j^n \epsilon_j^n \rangle = 1$, give the size and amplitude of vortex $n$. Finally, $a_{ij}$ is the Cholesky decomposition of the Reynolds stress tensor [24]

$$\begin{pmatrix} \sqrt{R_{11}} & 0 & 0 \\ R_{21}/a_{11} & \sqrt{R_{22} - a_{21}^2} & 0 \\ R_{31}/a_{11} & (R_{32} - a_{21}a_{31})/a_{22} & \sqrt{R_{33} - a_{31}^2 - a_{32}^2} \end{pmatrix}. \tag{2.13}$$

However, the generated velocity field does not respect the incompressibility condition. This has been addressed by Poletto *et al.* [25, 26]. They transformed the above velocity field into a vorticity field and then took the curl of this vorticity field. The vorticity $\omega'$ and the velocity fields are related together by the following equation

$$\nabla \times \boldsymbol{\omega}' = \nabla(\nabla \cdot \mathbf{u}') - \nabla^2 \mathbf{u}'. \tag{2.14}$$

The divergence-free condition impose that the first term on the right-hand side of the Equation (2.14) vanishes. It gives a Poisson equation that has been solved using the Biot-Savart kernel to give

$$\mathbf{u}'(\mathbf{x}) = \frac{1}{\sqrt{N}} \sum_{n=1}^{N} \frac{q_\sigma(\mathbf{r}^n)}{|\mathbf{r}^n|^3} \mathbf{r}^n \times \boldsymbol{\alpha}^n \ , \tag{2.15}$$

where $\mathbf{r}^n = \frac{\mathbf{x}-\mathbf{x}^n}{\lambda^n}$ , $q_\sigma\left(\mathbf{r}^n\right)$ is the velocity distribution of the eddies and $\alpha_i^n$ are random number with zero average and $\langle \alpha_i^n \alpha_i^n \rangle = 1$ that gives the size and amplitude of vortex $n$.

Instead of constructing the divergence-free synthetic turbulence using vorticity fields, Sescu *et al.* [27] used the vector velocity potential. Indeed, taking the curl of the vector velocity potential gives a velocity field that automatically satisfies the incompressibility condition. They described the vector velocity potential $\mathbf{\Psi}$ as the superposition of $N$ eddies defined by their associated vector velocity potential $\psi_n$

$$\mathbf{\Psi}(\mathbf{x}, t) = \sqrt{\frac{A_{\text{inflow}}}{N}} \sum_{n=1}^{N} \epsilon_n \boldsymbol{\psi}_n \left( \frac{\mathbf{x} - \mathbf{x}_n^0}{\lambda_b}, \frac{t - t_n^0}{\tau_b} \right), \tag{2.16}$$

where $\mathbf{x}_n^0$ is the spatial position of the centre of the $n$th eddy and $t_n^0$ is the "location" in time of the $n$th eddy. $\lambda_b$ and $\tau_b$ are respectively the turbulent length and time scales, $A_{\text{inflow}}$ is the area of the inflow boundary.

### 2.3.2 Convection by the mean flow

In the Fourier decomposition method, Bailly *et al.* [28] took the convection of the turbulent structures by the mean flow into account, directly in the expression of the velocity field by adding the convective term $\mathbf{u}_c t$. Thus, the turbulent velocity field becomes

$$\mathbf{u}'(\mathbf{x}, t) = 2 \sum_{n=1}^{N} a_n \cos(\mathbf{k}_n \cdot (\mathbf{x} - t\mathbf{u}_c) + \phi_n + \omega_n t) \boldsymbol{\sigma}_n \ , \tag{2.17}$$

where $\mathbf{u}_c$ is the convection velocity, and $a_n$, $\omega_n$ and $\boldsymbol{\sigma}_n$ are respectively the amplitude, the angular frequency and the direction of the $n$th mode. The randomly phase $\phi_n$, independently drawn between 0 and $2\pi$ for each mode, was introduced by Drummond *et al.* [29] to ensure the homogeneity of the velocity field. However, Bailly *et al.* [28] claimed that $\mathbf{k}_n$ and $\omega_n$ should not be independent for aerodynamic noise generation. Indeed, contrary to Kraichnan [9] where $\mathbf{k}_n$ and $\omega_n$ are independent, Bailly *et al.* [28] took $\omega_n$ to follow a Gaussian probability function directly linked to the value of $\mathbf{k}_n$. Moreover, the Equation (2.17) proposed by Bailly *et al.* [28] is highly correlated in time due to its composition of only cosine and sine functions, which often overestimates the acoustic field radiated by the source terms [30].

In the RPM, the convection by the mean flow is included in the original idea of RPM proposed by Ewert *et al.* [10, 21] by convecting the random field along the streamlines using a transport equation

$$\frac{D_0}{Dt} \mathcal{U}_i = 0 \qquad \text{with } \frac{D_0}{Dt} = \frac{\partial}{\partial t} + \mathbf{u}_c \nabla \ , \tag{2.18}$$

where $\mathbf{u_c}$ is the convection velocity.

In the SEM, as the vortices are injected through a boundary directly inside the computational domain, the convection by the mean flow is naturally ruled by the governing equations.

### 2.3.3 Specific temporal coherence

In the Fourier modes decomposition method, Bechara *et al.* [31] were the first to introduce the temporal evolution of the turbulent field. At each time step, the turbulent velocity field is randomly generated and then a numerical filter is applied to add a chosen temporal coherence. Moreover, the turbulent kinetic energy spectrum is not discretized with a statistically isotropic distribution as Kraichnan [9], but uses a logarithmic distribution which provides a better discretization of the power in the lower wavenumber range, and as most of the energy is contains in the lower wavenumber range, it provides more realistic energy spectrum.

To include the convection of the turbulence by the mean flow but to overcome the high time-correlation proposed by Bailly *et al.* [28] in the Equation (2.17), Billson *et al.* [30] proposed to include a time filter directly as the velocity field is generated and not after as Bechara *et al.* [31]. The velocity field at the iteration (it) reads

$$\mathbf{u}'^{(\mathrm{it})}(\mathbf{x}) = a\mathbf{u}'^{(\mathrm{it}-1)}(\mathbf{x}) + b\boldsymbol{\zeta}'^{(\mathrm{it})}(\mathbf{x}) \ , \tag{2.19}$$

where $a = \exp(-\Delta t/\tau)$, $b = f_A\sqrt{(1-a)/2}$ and $\tau$ is the temporal characteristic of the simulation that corresponds to the time needed for the autocorrelation function to decrease to $\exp(-1)$. $\boldsymbol{\zeta}'^{(\mathrm{it})}(\mathbf{x})$ is a white noise signal, generated at each iteration (it), with a zero-mean value. In this expression, the amplitude factor $f_A$ enables the control of the kinetic energy of the synthesized turbulence. The convection effect is included in the term $\mathbf{u}'^{(\mathrm{it}-1)}(\mathbf{x})$ which is calculated at each iteration through an advection function

$$\frac{D_0}{Dt}\mathbf{u}^{(\mathrm{it}-1)}(\mathbf{x}) = 0 \qquad \text{with} \qquad \frac{D_0}{Dt} = \frac{\partial}{\partial t} + \mathbf{u}_c\nabla \ , \tag{2.20}$$

$\mathbf{u}_c$ being the convection velocity. This method has however an issue to calculate the time-derivatives because $\mathbf{u}_n(\mathbf{x})$ fluctuates rapidly and thus leads to some difficulties to compute the derivatives. A solution to this problem has been given by Billson *et al.* [32]. They included the white noise component of the previous time $\boldsymbol{\zeta}'^{(\mathrm{it}-1)}(\mathbf{x})$ in the Equation (2.19), which gives

$$\mathbf{u}'^{(\mathrm{it})}(\mathbf{x}) = a\mathbf{u}'^{(\mathrm{it}-1)}(\mathbf{x}) + b[\boldsymbol{\zeta}'^{(\mathrm{it})}(\mathbf{x}) + \boldsymbol{\zeta}'^{(\mathrm{it}-1)}(\mathbf{x})] \ . \tag{2.21}$$

One clear inconvenience of this method is the requirement to store the value of the previous white noise signal $\boldsymbol{\zeta}'^{(\mathrm{it}-1)}(\mathbf{x})$ at each point of the grid, which can be an issue in large simulations like in three-dimensions.

In order to include the time-correlation effect in the RPM, Ewert *et al.* [33] used a Langevin equation instead of a transport equation to convect the particles

$$\frac{D_0}{Dt}\mathcal{U}_i = -\alpha\mathcal{U}_i + \beta\zeta_i, \tag{2.22}$$

where $\zeta_i$ is a white noise which respects those conditions :

$$\langle\zeta_i\rangle = 0, \qquad \text{and} \qquad \langle\zeta_i(x_1,t_1)\zeta_j(x_2,t_2)\rangle = \delta(r)\delta(t)\delta_{ij}, \tag{2.23}$$

where $\langle(.)\rangle$ corresponds to the mean value of $(.)$.

To obtain a temporal correlation function defined as a decreasing exponential $\exp(-t/\tau)$ with $\tau$ the Lagrangian integral time scale, it follows $\alpha = 1/\tau$. Assuming a stationary process, $\langle\mathcal{U}_i(t)^2\rangle$ must remain constant hence $\langle\mathcal{U}_i(t)^2\rangle = \langle\mathcal{U}_{(0)i}^2\rangle$. Using a Gaussian distribution with a zero-mean value and a standard deviation of 1 for the white noise $\mathcal{U}_i$, we obtain $\beta = \sqrt{2\alpha\langle\mathcal{U}_{(0)i}^2\rangle} = \sqrt{2\alpha}$. The Langevin Equation (2.22) becomes

$$\frac{D_0}{Dt}\mathcal{U}_i = \frac{1}{\tau}\mathcal{U}_i + \sqrt{\frac{2}{\tau}}\zeta_i. \tag{2.24}$$

However, the use of a single Langevin Equation (2.24) presents some issues because $\zeta_i$ can fluctuates quickly, rendering the partial derivative $\partial u_i/\partial t$ difficult to calculate which can lead to unwanted noise. To resolve this problem, Siefert and Ewert [22] and then Dieste and Gabard [23] used a 2$^{\text{nd}}$ order Langevin model. The general form of the Langevin equation is

$$\frac{D_0}{Dt}\mathcal{U}_i = -\alpha\mathcal{U}_i + W, \tag{2.25}$$

where $W$ is the source term. In order to obtain a smoother signal for $\mathcal{U}_i$, the source term is not a white noise but is a solution of a second Langevin equation

$$\frac{D_0}{Dt}W = -\alpha' W + \beta'\zeta_i, \tag{2.26}$$

where $\zeta_i$ is a white noise with the properties (2.23). Finally the 2$^{\text{nd}}$ order Langevin model is written

$$\begin{cases} \frac{D_0}{Dt}\mathcal{U}_i = -\frac{1}{\tau}\mathcal{U}_i + W, \\ \frac{D_0}{Dt}W = -\gamma W + \sqrt{2\gamma\langle W_0^2\rangle}\zeta, \end{cases} \tag{2.27}$$

where $\gamma = (1/\tau_d - 1/\tau)$ with $\tau_d$ an additional temporal scale such that $\tau_d \ll \tau$ (see [34]). The initial condition imposes an initial source term $W_0$ defined as $W_0 = (1/\tau)\mathcal{U}_{(0)i} + \sqrt{\gamma/\tau}\xi$ where $\xi$ is a random Gaussian variable with a zero-mean value and a standard variation of 1.

In the SEM, as the particles can no longer be controlled after being injected, the turbulence is frozen, hence, no temporal coherence can be imposed.

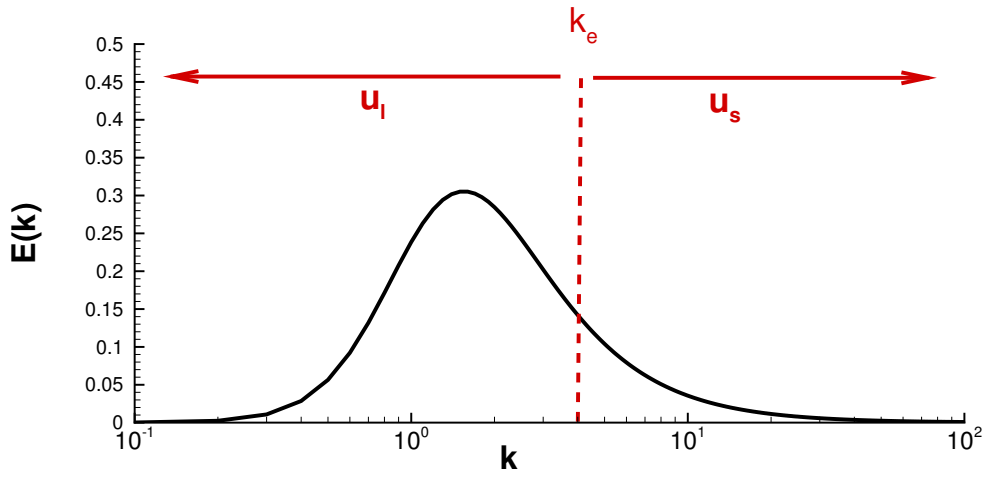


Figure 2.3: Sweeping: Splitting of the von Karman energy spectrum (where $E(k)$ is proportional to $k^4$ as $k \to 0$ and $E(k)$ is proportional to $k^{\frac{-5}{3}}$ as $k \to \infty$) at a wavenumber $k_e$ into large $(.)_l$ and small $(.)_s$ scales.

### 2.3.4 Sweeping

The sweeping phenomenon corresponds to the convection of the small eddies by the large eddies.

To include the sweeping phenomenon in the Fourier modes decomposition method, Fung *et al.* [19, 20] split the turbulent kinetic energy spectrum into large and small scales and write the turbulent field as

$$\mathbf{u}'(\mathbf{x},t) = \mathbf{u}'_l(\mathbf{x},t) + \mathbf{u}'_s(\mathbf{x},t) \ , \tag{2.28}$$

where $\mathbf{u}'_l(\mathbf{x},t)$ corresponds to the large scales and $\mathbf{u}'_s(\mathbf{x},t)$ to the small scales. The figure 2.3 shows the splitting of the turbulent kinetic energy spectrum $E(k)$ at the wavenumber $k_c$.

The turbulent velocity field of the large scales $\mathbf{u'}_l(\mathbf{x},t)$ is generated using Equation (2.4) but, to model the time-dependence in a simple way, only a single frequency mode $P_w = 1$ for each wavenumber mode is considered (thus we obtain the same equation as Kraichnan [9], Equation (2.1)). On the other side, the small eddies are generated using a modified version of Equation (2.4) to include the convection effect by the large scales

$$\frac{\partial \mathbf{u}'_s}{\partial t} = \underbrace{-\mathbf{u}'_l.\nabla\mathbf{u}'_s}_{\text{advection}} - \underbrace{[(\mathbf{u}'_s.\nabla)\mathbf{u}'_l + (\mathbf{u}'_l.\nabla)\mathbf{u}'_s + 1/\rho\nabla p'}_{\text{decorrelation}} . \tag{2.29}$$

The fluctuating pressure field $p'$ is however difficult to calculate, so Fung *et al.* [20] decided to neglect the decorrelation term containing the pressure field. Considering

that the velocity field $\mathbf{u}'_s$ is written

$$\mathbf{u}'_s(\mathbf{x},t) = \sum_{n=N_c}^{N} \left[ (\mathbf{a}_n \times \hat{\mathbf{k}}_n) \cos(\mathbf{k}_n \cdot \mathbf{X} - \omega_n t) + (\mathbf{b}_n \times \hat{\mathbf{k}}_n) \sin(\mathbf{k}_n \cdot \mathbf{X} - \omega_n t) \right], \quad (2.30)$$

where the amplitude of each mode is chosen using the von Karman energy spectrum, $N_c$ is the mode where the energy spectrum is split into the small and large scales (i.e. $k = k_c$) and $\mathbf{X}$ is the trajectory of a point convected by the large eddies

$$\mathbf{X} = \mathbf{x}(t) - \int_0^t \mathbf{u}'_l(\mathbf{x}_l(t'), t')\mathrm{d}t' \ . \quad (2.31)$$

However the divergence-free condition is not respected any more as the term $(\mathbf{a}_n \times \hat{\mathbf{k}}_n).\nabla(\mathbf{k}_n \cdot \mathbf{X})$ is not equal to zero. Indeed, as the small scales are convected by the large scales, the motion of the small scales is not uniform in space. To solve this issue, the wavenumber $\mathbf{k}_n$ should be time-dependant [20]. Nonetheless, without this time-dependence on the wavenumber, Fung *et al.* [19, 20] found that the error on the divergence-free condition is not greater than 10%.

Lafitte *et al.* [35, 36, 37] introduced an hybrid model that includes the convection of the turbulent flow field by the mean flow as well as the sweeping phenomenon using Fung *et al.* [20] idea to separate the spectrum into large and small scales; the small scales being convected by the large ones. The generation of the turbulent velocity field uses the method introduced by Bailly *et al.* [28] for the large eddies and an hybrid method between Fung *et al.* [20] and Billson *et al.* [30] for the small eddies. Lafitte *et al.* wrote for the large eddies the following sum of Fourier modes

$$\mathbf{u}'_l(\mathbf{x},t) = 2 \sum_{n=0}^{N_c-1} \mathrm{A}_n \cos(\mathbf{k}_n(\mathbf{x} - \mathbf{u}_c t) + \omega_n t + \varphi_n)\boldsymbol{\sigma}_n \ , \quad (2.32)$$

with amplitude $\mathrm{A}_n = \sqrt{E(k_n)\Delta k_n}$ built to conserve locally the turbulent kinetic energy imposed to the large scale structures. $N_c$ is the mode where the energy spectrum is split and the other variables being chosen as Bailly *et al.* [28] in the Equation (2.17). For the small scales, Lafitte *et al.* [35, 36, 37] wrote the following temporal filter which is a combination of an advected term to include the sweeping effect, and a random term that contributes to the decorrelation

$$\mathbf{u}'_s(\mathbf{x},t) = \underbrace{a(\mathbf{x})\mathbf{v}'(\mathbf{x},t)}_{\text{advection}} + \underbrace{b(\mathbf{x})\boldsymbol{\zeta}(\mathbf{x},t)}_{\text{decorrelation}} \ , \quad (2.33)$$

where $a(\mathbf{x}) = \mathrm{e}^{-\frac{\Delta t}{\tau}}$ corresponds to the exponential temporal decorrelation, $b(\mathbf{x}) = \sqrt{1 - a(\mathbf{x})^2}$ is built to preserve the kinetic energy, $\mathbf{v}'$ is the solution of the following

advection equation at the previous iteration in time (noted it − 1)

$$\frac{\partial \mathbf{u}_s^{'(\mathrm{it}-1)}}{\partial t} + (\mathbf{u}_0 + \mathbf{u}_l^{'(\mathrm{it}-1)}) \cdot \nabla \mathbf{u}_s^{'(\mathrm{it}-1)} = \mathbf{0} \ , \tag{2.34}$$

and the locally white noise $\boldsymbol{\zeta}(\mathbf{x}, t)$ is defined as a sum of Fourier modes

$$\boldsymbol{\zeta}(\mathbf{x}, t) = 2 \sum_{n=N_c+1}^{N} A_n \cos(\mathbf{k}_n \cdot \mathbf{x} + \varphi_n) \boldsymbol{\sigma}_n \ , \tag{2.35}$$

where the $A_n$, $N_c$, $\mathbf{k}_n$, $\varphi_n$ and $\boldsymbol{\sigma}_n$ are defined as in the Equation (2.32). The complete synthesized turbulent velocity field being obtained by the same decomposition as Fung *et al.* [20], namely $\mathbf{u}'(\mathbf{x}, t) = \mathbf{u}'_l(\mathbf{x}, t) + \mathbf{u}'_s(\mathbf{x}, t)$.

The sweeping phenomenon have not been investigated in RPM. In SEM, the sweeping phenomenon can not be implemented as, after injecting the eddies through the boundary, the particles can no longer be controlled.

### 2.3.5 Inhomogeneous turbulence

In the Fourier modes decomposition method, the inhomogeneity is difficult to implement, as argued by Omais *et al.* [38]. Indeed, the spatial correlation tensor $R_{ijn}$ in the directions $\mathbf{x}_i$ and $\mathbf{x}_j$ of a single node $n$, of an inhomogeneous flow can be written

$$R_{ijn}(\mathbf{r}) = \frac{F}{T} \left\{ 1 - \left[ \frac{\omega_n(\mathbf{x}) + \mathbf{k}_n \cdot \mathbf{u}_c(\mathbf{x})}{\omega_n(\mathbf{x} + \mathbf{r}) + \mathbf{k}_n \cdot \mathbf{u}_c(\mathbf{x} + \mathbf{r})} \right]^2 \right\}^{-1} \tag{2.36}$$

where $F$ is a finite non-zero quantity and $T$ is the time over which the averaging is performed. This spatial correlation tensor tends to zero as $T$ tends to infinity, which is not physical.

In the RPM, Dieste *et al.* [39, 23] proposed to generate inhomogeneous turbulence through the addition of a scaling factor $K^{\frac{1}{2}}$ in the filter, $G = K^{\frac{1}{2}} \tilde{G}$. This could be numerically implemented in three different ways

$$u'_i(\mathbf{x}, t) = \varepsilon_{ij} \sum_{n=1}^{N} K^{\frac{1}{2}}(\mathbf{x}_n, t) \frac{\partial}{\partial x_j} \tilde{G}(|\mathbf{x} - \mathbf{x}'|) \mathcal{U}_n(t) \ , \tag{2.37}$$

$$u'_i(\mathbf{x}, t) = \varepsilon_{ij} \sum_{n=1}^{N} \frac{\partial}{\partial x_j} \left[ K^{\frac{1}{2}}(\mathbf{x}_n, t) \tilde{G}(|\mathbf{x} - \mathbf{x}'|) \right] \mathcal{U}_n(t) \ , \tag{2.38}$$

$$u'_i(\mathbf{x}, t) = \varepsilon_{ij} K^{\frac{1}{2}}(\mathbf{x}_n, t) \sum_{n=1}^{N} \frac{\partial}{\partial x_j} \tilde{G}(|\mathbf{x} - \mathbf{x}'|) \mathcal{U}_n(t) \ . \tag{2.39}$$

Dieste *et al.* [39, 23] found that the three different implementations give similar results. Yet, the third model (Equation (2.39)) is computationally less expensive.

In the SEM, no development has been done regarding inhomogeneous turbulence.

### 2.3.6 Extension to anisotropic turbulence

All the previous methods are generating isotropic turbulence (i.e. same properties in all the spatial directions). In order to generate synthetic anisotropic turbulence, Maxey [40] proposed a technique based on filtering and scaling operations applied to a previously generated isotropic velocity field. However, these additional operations are time-consuming. Smirnov *et al.* [41] elaborated a fast and efficient strategy based on scaling and coordinates transformation operations. Smirnov *et al.* [41] started with the hypothesis that the anisotropic Reynolds stress tensor $\mathbf{R}$ is symmetric, thus it can be diagonalized through the relation

$$\mathbf{R}^* = \mathbf{A}^{\mathrm{t}}\mathbf{R}\mathbf{A} \ , \tag{2.40}$$

where $\mathbf{R}^*$ is the diagonalized anisotropic Reynolds stress tensor and $\mathbf{A}$ is an orthogonal transformation tensor that contains the degree of anisotropy of the turbulence, $(.)^{\mathrm{t}}$ being the transpose of the matrix $(.)$.

Using a previously generated isotropic turbulent velocity field $\mathbf{u}$, the anisotropic turbulent velocity field $\mathbf{v}$ is obtained from the transformation

$$\mathbf{v} = \mathbf{A}\mathbf{R}^*\mathbf{u}. \tag{2.41}$$

This process has the advantage of being independent of the method used to generate the isotropic velocity field. It has been designed to generate anisotropic turbulence with desired Reynolds stresses, integral length and time scales from any isotropic turbulent velocity field. However, this method fails to satisfy the incompressibility condition for high degree of anisotropy.

Using a Fourier mode approach, to conserve the divergence-free condition regardless of the anisotropy, Yu *et al.* [42] performed anisotropic transformation on a vector potential field. The divergence-free anisotropic turbulent field is then obtained by taking its curl.

In RPM, instead of applying the transformation at the end of the process on the generated isotropic field, it is possible to apply a scaling matrix directly on the white noise before filtering it [43], or after the filtering step, when transforming the stream functions into the velocity field [44]. However, this first approach introduces some errors in the reconstruction of the local variances, and the second one only approximates the

incompressibility condition. As the numerical implementation of RPM is a sum of Gaussian eddies, Gea-Aguilera *et al.* [45] modified the shape of these eddies by considering anisotropic Gaussian eddies, i.e. different streamwise and transverse length scales.

In SEM, Poletto *et al.* [26] modified the inclination of the eddies to control the anisotropy in the turbulent field, which still respects the incompressibility condition.

## 2.4 Numerical applications for interaction noise

The use of numerical methods progressively took into account more and more realistic cases, following the increase of computational resources available. This section reviews the previous studies that have been done regarding the interaction noise. This section is organised as follow. First, a single aerofoil interacting with an harmonic perturbation is considered, using methods in the frequency domain and then in the temporal domain. Thereafter, the interaction of a single aerofoil with a synthetic turbulent perturbation generated using previously reviewed stochastic methods is treated. Afterwards, broadband perturbations interacting with cascades of aerofoils are studied. Finally, the interaction noise is studied without the use of artificial turbulence, but directly simulated using Computational Fluid Dynamics (CFD) methods. Those CFD methods were applied to investigate the tone noise and then the broadband interaction noise, on simplified to complete rotor-stator configurations.

The first interaction noise studies focused on a single aerofoil impacted by an harmonic gust. Scott *et al.* [46, 47] developed a method based on the LEE, the input perturbation being divergence-free to ensure that it is not a pressure source. The gust being harmonic and the problem being linear, the solution oscillates at the same frequency as the input gust. Thus the temporal dependence is removed to solve this problem in the frequency domain. The same principle can be applied to factorise the span dependence to only solve the problem in a 2D plane. The developed numerical method is the starting point of the solver *GUST3D* developed by the NASA. The method gives good results for the near-field but faces some difficulties in the far-field. To solve this issue, Atassi *et al.* [48] coupled this method with a Kirchhoff integral method. Scott *et al.* [49] proposed an alternative to this coupling, the domain is split into a near-field domain and a far-field domain and for each region an adapted equation is solved.

In the temporal domain, this problem has been investigated using the Navier-Stokes equations or the non-linearized Euler equations. Lockard *et al.* [50, 51] studied the interaction of a gust at Mach 0.5 with a flat plate and then NACA profiles with different thickness in two-dimensions. Then, Hixon *et al.* [52] and Golubev *et al.* [53, 54], at Mach 0.5, studied the effect of the gust frequency and its amplitude on Joukowsky profiles and found that for gust with a high amplitude, some non-linear effects appear, leading to the generation of harmonics and also to instabilities in the wake of the profile.

To study the broadband noise, as mentioned previously, it is possible to artificially generate a turbulent velocity field which is then used in combination with governing equations. The stochastic methods (described in section 2.3) were first used to generate synthetic turbulence in aeroacoustic problem in 1991 by Karweit *et al.* [55]. To study the behavior of an acoustic wave propagating through a turbulent medium, they used the original idea of Kraichnan [9], but removed the angular frequency considerations, resulting in a turbulence fixed in time. Then, a ray-trace method is used to determine the trajectory of the acoustic waves through this turbulence medium. Afterwards, to include acoustic generation, the following works in aeroacoustics define the turbulent velocity field as a source term, so it could be included into governing equations.

Ewert *et al.* [56, 57] used the RPM to study the slat noise and the trailing edge noise at Mach numbers up to 0.208 in two-dimensions. They used the Computational Aero-Acoustics (CAA) solver *PIANO* which uses high-order finite difference spatial schemes and an low-dissipative and low-dispersive explicit temporal advancement. The synthetic turbulence is only generated on specific zones inside the computational domain such as the interior of the slat cavity. The calculations are realised in two-dimensions but Ewert *et al.* [57] used a correction factor to predict the three-dimensions acoustic field for a three-dimensions wing with a finite span. More recently, at similar Mach numbers, Bauer *et al.* [58] also studied the slat noise using RPM, but using the solver *DISCO* which uses the discontinuous Galerkin method for the spatial discretization. This allow the use of non-structured mesh, which can be useful when meshing complex geometries.

Dieste *et al.* [39, 12], studied the leading edge noise of a two-dimensions flat plate at Mach 0.362 using a similar method as Ewert. They showed that the inclusion of the temporal evolution in the synthesized turbulence has a very limited effect on the acoustic radiation of a flat plate interacting with this turbulent velocity field. This is probably true since the turbulence has a correlation time long regarding to the time needed to convect past the leading edge. This indicates that the generation of a frozen turbulence is sufficient when it comes to study its interaction with a thin aerofoil. Clair *et al.* [59] developed a specific stochastic model to generate a frozen turbulent velocity field for the study of its interaction with an aerofoil. They formulated their stochastic model taking inspiration from Amiet's model [60]. Amiet's model is a semi-analytical model developed to predict the acoustic radiation of a flat plate impinged by a turbulent velocity field. This model only requires the spectrum of the velocity component normal to the plate, thus Clair *et al.* [59] wrote the velocity field as a Fourier modes sum

$$u_2'(\mathbf{x},t) = 2\sum_{n=1}^{N}\sum_{m=-M}^{M}\sqrt{\Phi_{22}(k_x,k_y)\Delta k_x \Delta k_y}\cos(k_{x,n}x + k_{y,n}y - \omega_{nm}t + \varphi_{nm}) \ , \quad (2.42)$$

where $u_2'$ is the normal velocity component with respect to the aerofoil, $N$ and $(2M+1)$ are respectively the number of modes in the $x$ and $y$ directions, $\Phi_{22}(k_x,k_y)$ is the wavenumbers spectrum of the fluctuating velocity $u_2'$, $\Delta k_x$ and $\Delta k_y$ are the wavenumbers

spacing used for the discretization of $k_x$ and $k_y$. $\varphi_{nm}$ is a random phase, independently drawn between 0 and $2\pi$ for each mode, as introduced by Drummond *et al.* [29] to ensure the homogeneity of the synthesized velocity field. The other novelty of this method is the need of the wavenumbers spectrum of the fluctuating velocity instead of the turbulent kinetic energy spectrum to generate turbulence.

Gill *et al.* [61, 62, 63], also using frozen isotropic turbulence synthesized using a sum of Fourier modes, studied the effects of aerofoil geometry on the radiated noise. It has been found that an increased aerofoil thickness causes a reduction in the turbulence interaction noise for high reduced frequencies, however the characteristics of this reduction is highly dependent on the Mach number. An increase in the leading edge radius also seems to cause a reduction in the predicted noise. On the other hand, the angle of attack and the camber of the aerofoil does not seem to have an effect.

To study interaction noise, Gea-Aguilera *et al.* [64] synthesized frozen turbulence using a method based on RPM. However, only the direction of rotation of all eddies are undetermined, which in theory introduces less randomness in the turbulent field. Nevertheless, they claim it gives faster satisfactory acoustic predictions on two-dimensional cases compared to original RPM or sum of Fourier modes methods.

Due to a large computational cost required for full 3D simulations, very few studies have yet been performed. Kim and Haeri [65] developed a method based on SEM to synthesize frozen 3D turbulence in combination with span wise periodic boundary conditions. The method introduces new constraint parameters to have a better control over the generated turbulence, however, to properly select these parameters, a complex optimization process is required. This method is successfully applied to study interaction noise on a flat plate with wavy leading edge.

The interaction noise on linear cascades have first been investigated using harmonic perturbations. In the frequency domain, Hall *et al.* [66] studied the tone noise of a two-dimensions blade cascade configuration, using the previously described method based on the linearised Euler equations developed by Scott *et al.* [46, 47]. In the temporal domain, Nallasamy *et al.* [67] then Hixon *et al.* [68] applied non-linearised Euler equations to study two-dimensions unducted rotor-stator interaction noise at Mach 0.5. A periodic mean flow and periodic boundary conditions in the azimuthal direction are applied.

Atassi *et al.* [69, 70, 71] studied the acoustic response of a ducted annular cascade of loaded aerofoil impinged by an isotropic turbulent velocity at Mach 0.5. They extended Golubev *et al.* [72], Atassi *et al.* [73] and Elhadidi *et al.* [74] frequency method based on Euler equations. Atassi *et al.* [73] showed that the parameters of the mean flow significantly modify the unsteady load on the aerofoil, as well as the generation of the acoustic modes in the duct. Atassi *et al.* [75] also studied the acoustic response of a ducted annular cascade in anisotropic turbulence compared to isotropic turbulence.

They found that a significant reduction in the scattered acoustic power from low to high frequency is observed in anisotropic turbulence compared to isotropic turbulence.

To study linear cascade, Wohlbrandt *et al.* [76] extended the RPM method to periodic turbulent flows by having either a periodic background flow or periodic turbulence statistics. The synthetic turbulence is generated only in one vane to study the scattering of the acoustic field by the other blades. The preliminary results of this study, using only Gaussian turbulent spectra, seem to indicate that the variation of the turbulent kinetic energy amplitude across the blade passage alone, as well as its period of fluctuation, has a little impact on the radiated noise spectra. On the other hand, variations of the mean flow, and especially the wake velocity deficit, seem to have a major effect on the level of the radiated acoustic field.

The increase in computational resources made possible unsteady CFD simulations of a complete rotor in rotation and stator configuration. In these new methods, the incident turbulence does not have to be artificially generated but can be simulated. The first studies focused on the tone noise using hybrid methods that separate the aerodynamic and the aeroacoustic calculations. The unsteady aerodynamic calculation is first done to obtain the interaction of the wake of the rotor with the stator. The data from this first simulation are then used in aeroacoustic methods to study the acoustic propagation. Rumsey *et al.* [77] and Biedron *et al.* [78] used an unsteady RANS approach to obtain the acoustic field in an upstream section of a three-dimensions ducted fan at Mach 0.25. These acoustic data are thereafter decomposed in modes to be used as an input in an acoustic method that solves the wave equation. This method is however too computationally expensive to get far-field results, so a Kirchhoff integral method is applied using the near-field results.

To study broadband noise in CFD, more precise numerical methods are needed. However these methods are computationally demanding so it not conceivable to use them to propagate acoustic. Instead, these methods are used to estimate the unsteady load on the aerofoils and are then coupled to an acoustic analogy. To do a broadband calculation, Olausson *et al.* [79] used an hybrid RANS/LES method. A RANS on the rotor allow the authors to feed the inlet of the LES on the stator with the mean rotor wake. To limit the computational requirements but to allow some non-periodic, turbulent behaviour in the flow, the stator configuration is limited to a portion of three vanes passages with time lagged periodic boundary condition in the azimuthal direction (also known as chorochronic periodicity or the “shape correction method”) [80, 81]. A stochastic isotropic fluctuation is also added to the inlet profile to trigger the turbulence in the mean rotor wake. A Ffowcs Williams-Hawkings method is then used to calculate the far-field noise. They found that a small modification of the number of blades on the stator only have an effect on the low frequency broadband noise.

Greschner *et al.* [82] used a Improved Delayed Detached Eddy Simulation (IDDES) approach [83] which extends the LES region of the Delayed Detached-Eddy Simulation (DDES) approach [84] to the turbulent boundary layer. They applied this IDDES approach on a two-and-a-half-dimensions rotor-stator configuration, that is to say only a radial slice is meshed with periodic boundary conditions in the span direction. Moreover, to keep a reasonable number of grid points, the geometry has been simplified to a 1-1 rotor-stator set-up with periodic boundary conditions in the azimuthal direction. Despite those geometric considerations to limit the computational resources, the inlet Mach number in this simulation is only 0.038. They found that the IDDES approach did not lose important information regarding sound source mechanisms compared to LES approach which is more expensive.

Carolus *et al.* [85] and then Reese *et al.* [86] simulated a complete ducted rotor impinged by a turbulent inflow at low inlet Mach number. In order not to model the incident turbulence, a grid is placed upstream of the rotor which acts as a turbulence generator. Owing to the cost of such LES, the grid is not much refined and only large aerodynamic structures are resolved. The radiated acoustic power associated with the unsteady blade forces is then obtained using a two-dimensions acoustic model for duct propagation.

Mann *et al.* [87] simulated a complete rotor-stator configuration with an inlet Mach number of 0.15 using LBM, including the duct and ensuring the acoustic propagation in the far-field (three duct diameters upstream and downstream the rotor-stator). Despite the 168 million cubic elements, the used resolution can not propagate the far-field acoustic to a frequency higher than 2500 Hz. Up to this cut-off frequency, the numerical results showed good agreement for the far-field acoustic compared with experiments [88, 89]. The duct modes have also been captured correctly.

## 2.5 Conclusion

The aim of this project is to study interaction noise, generated from the interaction of the turbulent wakes of the fan blades with the guide vanes. Its study using full unsteady simulations such as LES are however very computationally expensive. The chosen alternative is to separate the steady and unsteady parts of the fluid. The steady part, or mean flow, is calculated first, using for instance steady Euler or RANS models. For the unsteady part, using statistical data provided by RANS or experiments, stochastic methods can be used to create the fluctuating fields. Then, using the steady flow as an input, the evolution of these unsteady fields can be simulated. One main advantage of this method is the possibility to alter each parameters in the simulations, independently, and investigate its impact on interaction noise predictions.

Among the stochastic methods available, a distribution of points vortices is preferred as it requires less resources than Fourier modes decomposition when a large number

of frequencies is synthesized. The quality of noise predictions partly depends on the properties of the synthesized turbulence. The ideal solution would be to include all the properties into the fluctuating field, but it would remain heavy in computational resources. Nevertheless, some properties of the turbulent field have a negligeable effect on the radiated noise, hence, by not including these properties, the computational cost can be reduced. The energy spectrum, spatial correlations and convection by the mean flow are among the requiered properties to include for interaction noise. On the other hand, Dieste *et al.* [39, 12] found that a specific temporal evolution in the synthesized turbulence has a very limited effect on the acoustic radiation and suggests that only frozen turbulence is necessary to get accurate noise predictions.

For interaction noise, a linear inviscid interaction model between vorticity and sound is generally sufficient, as long as the amplitude of the fluctuating part with respect to the mean flow is small [59]. This approach has the advantage of only generating leading edge noise as, for instance, no additional turbulence can be generated within a linear model, therefore no self noise can be generated, simplifying the post processing analysis. Moreover, interaction noise is a broadband phenomena, hence a model in the time domain is chosen. Finally, regarding the turbulence injection, in order to limit the computational cost, discretized vortices injected directly in the domain are preferred over injection through inlet boundaries as turbulence can be injected anywhere in the domain, thus limiting the size of the mesh. However, the existing methods of perturbation injection inside a computational domain usually requires the use of windowing functions and can be cumbersome to implement in an already existing solver. In this work, to simplify the implementation of such approach while having little to no influence on the parallelization of a already existing CAA solver, a new method of injection which uses sources of vorticity is investigated. Chapter 3 focuses on a single harmonic source of vorticity while Chapter 4 extends it to multiple sources used to generate turbulence.

# Chapter 3

# Flat plate interaction noise

In this work, vorticity sources are used in the CAA simulations to generate velocity perturbations. This chapter aims to investigate this method in the context of interaction noise by considering a harmonic gust impacting a zero-incidence flat plate. These single frequency cases allow specific interaction effects such as non-compactness of the acoustic response of the plate when the frequency of the incoming gust increases. This configuration has been extensively studied in the literature, for instance it has been investigated semi-analytically by Amiet in 1975 [60]. Moreover, a flat plate has two singularities (located at the leading edge and the trailing edge), which can be difficult to numerically simulate. These elements make this test-case a good benchmark to both evaluate the suitability of gust injection via vorticity sources and understand the behaviour and performances of the CAA solver.

The first part of this chapter provides details about the model, its numerical implementation in the CAA solver and the use of vorticity sources to generate harmonic velocity perturbations. Then, this method is applied on the flat plate application, by considering a zero-thickness plate impinged by harmonic perturbations at three different frequencies. This first simulation showed some high frequency oscillations on the Root Mean Square (RMS) pressure at the leading and trailing edges of the plate. These high-frequency oscillations are not physical, but are due to the combination of the geometric singularities and the numerical method used. The evolution of those high-frequency oscillations are then studied through the effect of the discretization and the effect of thickness. It leads to three different simulations, two using zero-thickness flat plates but with different grid refinements, and a third one using a thin profile, similar to a flat plate.

## 3.1 Model

The model used here solves the LEE, which describes the propagation of small amplitude perturbations on a mean flow. To obtain these equations, one can start from the Navier-Stokes equations which are non linear Partial Differential Equations (PDE) describing the dynamic of continuous fluids. In 3D, using Cartesian coordinates, it is composed of one equation for the mass conservation, three equations for the momentum conservation, and one for the energy conservation. In 2D, the momentum conservation only contains two equations, one for each velocity component. These equations are written below with an external force $\boldsymbol{\mathcal{S}}_v$ on the right-hand side of the momentum equation $\boldsymbol{\mathcal{S}}_v$ which represents a source of vorticity. In this work, the source term $\boldsymbol{\mathcal{S}}_v$ is used to inject velocity perturbations.

$$\begin{cases} \dfrac{\partial \rho}{\partial t} + \nabla \cdot (\rho \mathbf{u}) = 0 \ , & \text{(Conservation of mass)} \quad (3.1a) \\ \dfrac{\partial \rho \mathbf{u}}{\partial t} + \nabla \cdot (\rho \mathbf{u} \otimes \mathbf{u} + \bar{\bar{\boldsymbol{\Sigma}}}) = \boldsymbol{\mathcal{S}}_v \ , & \text{(Conservation of momentum)} \quad (3.1b) \\ \dfrac{\partial \rho E_0}{\partial t} + \nabla \cdot (\rho \mathbf{u} E_0 + \bar{\bar{\boldsymbol{\Sigma}}} \odot \mathbf{u} + \mathbf{q}) = 0 \ , & \text{(Conservation of energy)} \quad (3.1c) \end{cases}$$

where $\bar{\bar{\boldsymbol{\Sigma}}}$ is the stress tensor of the fluid ($\bar{\bar{\boldsymbol{\Sigma}}} = p\bar{\bar{\mathbf{I}}} - \bar{\bar{\boldsymbol{\tau}}}$ with $\bar{\bar{\mathbf{I}}}$ the identity tensor and $\bar{\bar{\boldsymbol{\tau}}}$ the viscous stress tensor), $E_0$ is the total energy, $q$ is the heat flux, $\otimes$ denotes the tensor product and $\odot$ denotes the tensor contraction.

We assume that the flow can be decomposed into two parts, the base flow and the perturbations. The base flow (denoted with $_0$) is assumed to be steady, with an arbitrary amplitude, and includes viscosity and heat transfers. The perturbations (denoted with $'$) are supposed to be unsteady, with a small amplitude in comparison with the base flow, and are isentropic (no viscosity and no heat transfer). Following these assumptions, one can then write the governing equations of the perturbations, often called the Euler equations. As the perturbations are small with regards to the mean flow, the noise generation and propagation is supposed to be linear. Using a Taylor decomposition, the Euler equations are linearised to give the LEE, written here in a non-conservative form

$$\begin{cases} \dfrac{\partial \rho'}{\partial t} + \mathbf{u}_0 \cdot \nabla \rho' + \mathbf{u}' \cdot \nabla \rho_0 + \rho_0 \nabla \cdot \mathbf{u}' + \rho' \nabla \cdot \mathbf{u}_0 = 0 \ , & (3.2a) \\ \dfrac{\partial \mathbf{u}'}{\partial t} + (\mathbf{u}_0 \cdot \nabla)\mathbf{u}' + (\mathbf{u}' \cdot \nabla)\mathbf{u}_0 + \dfrac{\nabla p'}{\rho_0} - \dfrac{\nabla p_0 \rho'}{\rho_0^2} = \boldsymbol{\mathcal{S}}_v \ , & (3.2b) \\ \dfrac{\partial p'}{\partial t} + \mathbf{u}_0 \cdot \nabla p' + \mathbf{u}' \cdot \nabla p' + \gamma p_0 \nabla \cdot \mathbf{u}' + \gamma p' \nabla \cdot \mathbf{u}_0 = 0 \ , & (3.2c) \end{cases}$$

where $\rho$, $p$, $\mathbf{u}$ and $\gamma$ denote the density, pressure, velocity and specific heat ratio, respectively. The LEE can be used as governing equations to study leading edge noise

generation and acoustic wave propagation since they are able to support vortical, entropy and acoustic modes [90].

In sheared mean flows, where the entropy, the vorticity and the acoustic waves are not decoupled, the LEE may lead to physical growing hydrodynamic instabilities. To tackle this problem, the Acoustic Perturbation Equations (APE) can be used, which are derived [10] by the decomposition of the flow into acoustic and non-acoustic quantities based on a filtering of the non-linear and viscous terms of the Navier-Stokes equations in Fourier/Laplace space. The APE can be expressed for the pressure and velocity perturbations ($p'$, $\mathbf{u}'$)

$$\begin{cases} \dfrac{\partial p'}{\partial t} + a_0^2 \nabla \cdot \left( \rho_0 \mathbf{u} + \mathbf{u}_0 \dfrac{p'}{c_0^2} \right) = 0 \ , & \text{(3.3a)} \\ \dfrac{\partial \mathbf{u}'}{\partial t} + \nabla(\mathbf{u}_0 \cdot \mathbf{u}) + \nabla \left( \dfrac{p'}{\rho_0} \right) = \boldsymbol{\mathcal{S}}_v \ , & \text{(3.3b)} \end{cases}$$

where $a_0 = \sqrt{\gamma p_0 / \rho_0}$ is the local speed of sound and $\boldsymbol{\mathcal{S}}_v$ is the vorticity source.

## 3.2 Numerical implementation

The LEE are numerically implemented in the CAA finite-difference solver Perturbation Investigation of Aerodynamic NOise (PIANO) developed by the Deutsches Zentrum fur Luft- und Raumfahrt e.V. / German Aerospace Center (DLR). This code is designed to simulate aeroacoustic noise generation and acoustic wave propagation in non-uniform flows. Based on structured, curvilinear multi-block grids, the solver mostly written in Fortran relies on the Message Passing Interface (MPI) library for the parallelization.

To ensure aeroacoustic noise generation and acoustic wave propagation, low-dispersive and low-dissipative numerical methods are implemented in PIANO. The spatial derivatives are numerically computed using the Dispersion-Relation-Preserving finite-difference scheme (DRP) finite difference scheme with a 7-point stencil proposed by Tam & Webb [91]. This scheme provides a $4^{\text{th}}$-order accuracy (instead of a $6^{\text{th}}$-order accuracy on a traditional 7-point stencil scheme) but minimizes the numerical dispersion introduced by the discretization, as plotted in Figure 3.1a against standard central difference (CDS) schemes. For instance, the first derivative of the quantity $f$ in the $x$ direction are written

$$\left. \frac{\partial f}{\partial x} \right|_i = \frac{1}{\Delta x} \sum_{l=M}^{N} a_l f_{i+l} \ , \tag{3.4}$$

where $\Delta x$ is the grid spacing and $a_l$ are the coefficients of the stencil. The stencil is symmetric for most of the points, however, near the outside boundaries of the computational domain, only a asymmetric stencil can be applied. Hence, away from the boundaries, the

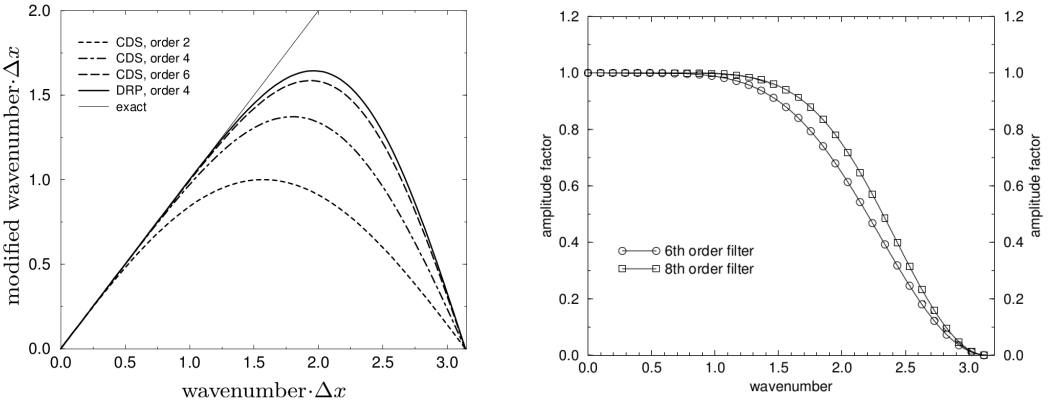


(a) (b)

Figure 3.1: (a) Dispersion error in the spectral domain of DRP vs CDS approaches and (b) spectral characteristics of a $6^{\text{th}}$- and $8^{\text{th}}$-order filter.

stencil reads $(M, N) = (-3, +3)$. The stencil then reads $(M, N) = (-2, +4)$, $(M, N) = (-1, +5)$ and $(M, N) = (0, +6)$ as the point gets closer to a boundary. For instance, the $a_l$ coefficients of the symmetric stencil $(M, N) = (-3, +3)$ are $a_{-3} = a_3 \approx 0.0201$, $a_{-2} = a_2 \approx -0.1667$, $a_{-1} = a_1 \approx 0.7709$ and $a_0 = 0$. On solid objects, the symmetric stencil is used in combination with slip boundary conditions. In this solver, it is performed by extending the mesh with ghost cells (also called mirror points), then $\partial p/\partial \mathbf{n} = 0$ and $\mathbf{u} \cdot \mathbf{n} = 0$ are imposed at the surface, while keeping tangential velocities unchanged.

The time discretization is computed using the Low-dissipation, low-dispersion Runge-Kutta (LDDRK) algorithm proposed by Hu *et al.* [92]. The LDDRK algorithm uses two alternating steps in the optimization stage (4-stage Runge-Kutta and 6-stage Runge-Kutta) which aims at reducing the dispersion errors while maintaining a high order of accuracy.

With this numerical approach, spurious short numerical waves can appear, especially at mesh-size-change interfaces. To have a high-quality solution, a $8^{\text{th}}$-order selective filter [93, 94] is performed in each grid-index direction ($i, j$, and $k$), at each time step. The spectral characteristics of such filter against a $6^{\text{th}}$-order version is plotted in Figure 3.1b. For instance, the filtering operation $(.)^F$ on a variable $\phi_{i,j,k}$ in the $i$-index direction, using a $8^{\text{th}}$-order filter reads

$$\phi^F_{i,j,k} = \phi_{i,j,k} - \sum_{l=-4}^{4} f_l \phi_{i+l,j,k} \ , \tag{3.5}$$

with $f_l$ the coefficients of the filters. To ensure that the filtering operation does not introduce dispersion error [95], the coefficients are such that $f_l = f_{-l}$.

In this work, using the DRP scheme for the spatial derivative, the LDDRK for the numerical integration, along with the $8^{\text{th}}$-order selective filter described above, in order to stay on the conservative side, a minimum of 10 points per wavelength has been used.

## 3.3 Source of vorticity

A source vorticity, denoted $\boldsymbol{\mathcal{S}}_v(\mathbf{x},t)$ in Equation (3.2b), is assumed to be decomposed in $\boldsymbol{\mathcal{S}}_v(\mathbf{x},t) = \mathbf{g}(\mathbf{x})s(t)$, where $\mathbf{g}(\mathbf{x})$ is the spatial distribution of the source, and $s(t)$ its modulation with time. To ensure a harmonic perturbation, the temporal signal of the source reads $s(t) = \cos(\omega t)$. However, as the perturbations are frozen once injected, there is a direct relation between the angular frequency of the pulsation and the streamwise wavenumber, such that $\omega = k_x u_0$, with $u_0$ the mean flow in the streamwise direction. The source term can then be expressed

$$\boldsymbol{\mathcal{S}}_v(\mathbf{x},t) = \mathbf{g}(\mathbf{x})\cos(k_x u_0 t) \ . \tag{3.6}$$

It is important that a source of vorticity does not create pressure/density perturbations when injected. Indeed, in the case of aeroacoustic simulations, it would make the acoustic analysis very difficult. In this work, it is performed by injecting an incompressible velocity field, which directly follows from Equation (3.2a) that the injected velocity is divergence-free. To respect this condition, the source term is constructed by taking the curl of a velocity vector potential $\boldsymbol{\Psi}(\mathbf{x},t)$. The considered velocity vector potential is a Gaussian distribution and is defined as

$$\boldsymbol{\Psi}(\mathbf{x},t) = Ab\sqrt{\frac{\exp(1)}{\ln(4)}}\exp\left[-\ln(2)\frac{|\mathbf{x}-\mathbf{x}_c|^2}{b^2}\right]s(t)\mathbf{e}_\Psi, \tag{3.7}$$

where $b$ is the half-radius of the Gaussian, $A$ the amplitude, $\mathbf{x}_c$ the coordinates of the centre of the Gaussian and $\mathbf{e}_\Psi$ the axis of rotation.

The associated vorticity $\boldsymbol{\omega}$ is then

$$\boldsymbol{\omega}(\mathbf{x},t) = \nabla \times (\nabla \times \boldsymbol{\Psi}(\mathbf{x},t)) \ . \tag{3.8}$$

## 3.4 Problem definition

To assess the validity of injecting velocity perturbations through vorticity sources for interaction noise, a two-dimensional plate with zero thickness, no camber and no incidence is chosen.

These single frequency cases allow specific interaction effects such as non-compactness of the acoustic response of the plate when the frequency of the incoming gust increase. Four gust frequencies have been considered so the different interaction effects can be observed.

The non-dimensionalization of the problem is realised using the chord of the flat plate $c = 1$ m, the density at infinity $\rho_\infty = 1.2$ kg.m$^{-3}$, and the speed of sound at infinity

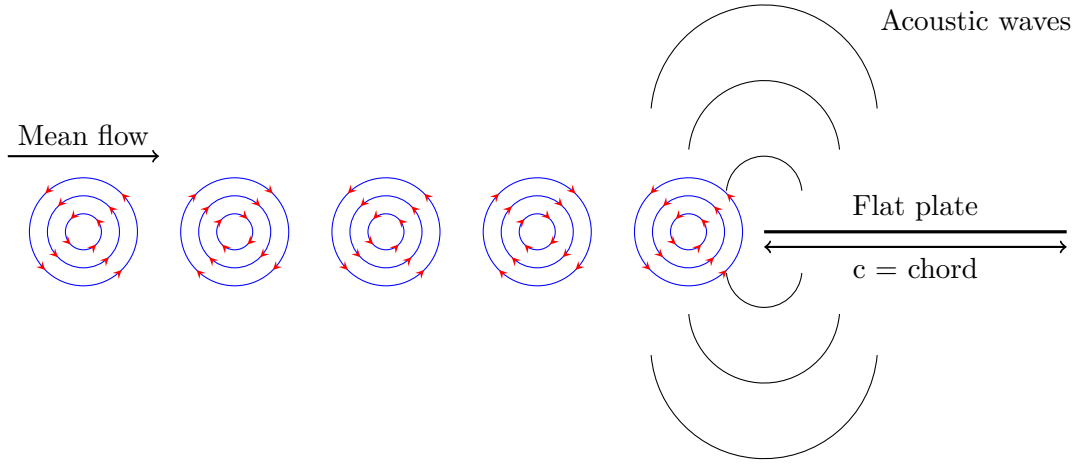


Figure 3.2: Sketch of the flat plate setup where the vortices are convected by the mean flow and interact with the flat plate.

$a_\infty = 340$ m.s$^{-1}$. It follows the non-dimensional pressure $p^* = \frac{(a^*)^2\rho^*}{\gamma} = \frac{1}{\gamma}$ with $\gamma = 1.4$. The mean flow velocity is uniform, parallel to the $x$-axis and its associated Mach number is $M = 0.5$.

The harmonic gusts are generated through a vorticity source. For each frequency, the parameters of the spatial distribution in Equation (3.7) remain constant, with an amplitude $A$ given by $A/(a_\infty c) = 0.01$ and an half-radius of the Gaussian $b$ given by $b/c = 0.2$. Those parameters give the gusts a small velocity amplitude (less than 2% of the speed of sound), which guarantees that no non-linear effect appears [53, 54, 52]. The situation is depicted in Figure 3.2.

A similar case using the PIANO solver has already been investigated by Wohlbrandt *et al.* [96] but the harmonic gusts were generated using two different methods. The first method uses a sponge zone at the upstream boundary to generate the gusts. The second method uses a windowing function along with fRPM, method briefly presented in Chapter 2.

## 3.5 Flat plate with zero thickness

### 3.5.1 Computational setup

The simulation domain extends to 10 chords in all directions. The flat plate is located on the $x$-axis, from $x = -0.5c$ to $x = 0.5c$. The gusts are injected upstream of the flat plate, using a single vortex centred at $[-2c, 0]$. The structured mesh, generated using the software ANSYS ICEM, is refined at the leading and trailing edge of the flat plate to a minimum grid element $\Delta x_{min}$ of $0.005c$ (1/200 of the chord). Moreover, the grid expansion is limited to 1.05, which has been successfully used for similar cases [59, 96].

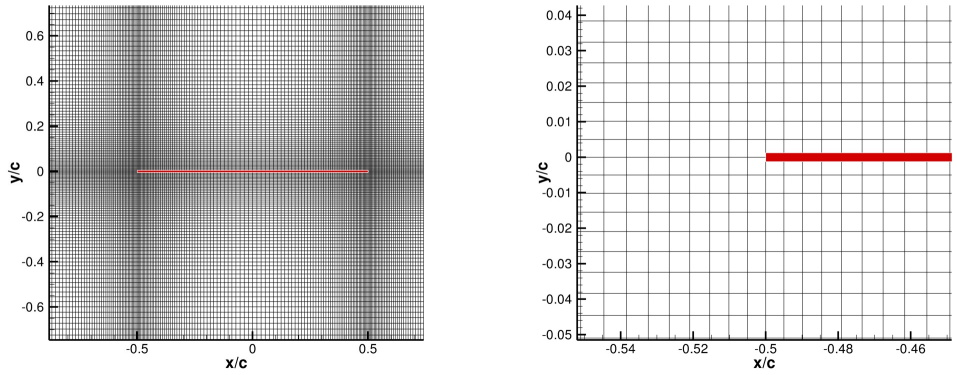


(a) Structured mesh

(b) Zoom of the mesh at the leading edge

Figure 3.3: Structured grid with a refinement of 1/200% of the chord at the singularities. The red line (—) denotes the location of the plate.

The grid is designed to support both the acoustic and hydrodynamic wavelength to a distance of 6 chords in all directions. Outside this region, the mesh gradually increases (with a grid expansion limited to 1.05) to slowly damp hydrodynamic structures before reaching the outflow boundary. Asymptotic conditions [91] are set on the boundaries of the domain, with the centre of the acoustic source defined, as required by these conditions, at the leading edge of the flat plate. A zoom of the mesh is represented in Figure 3.3, where the red line depicts the location of the flat plate. The time step $\Delta t$ is set to $(a_\infty/c)\Delta t = 2.93.10^{-3}$, which gives a maximum Courant-Friedrichs-Lewy number (CFL) [97] number of 0.9 near the leading edge, a minimum CFL number of 0.02 near the boundaries, and a mean CFL in the simulation of 0.2. The CFL number is a necessary condition, but may not be sufficient for the convergence of finite-difference approximations and is calculated CFL $= (u_{0i}+u_{ai})\Delta t/\Delta x$, where $u_{0i}$ and $u_{ai}$ respectively denote the mean flow velocity and acoustic velocity in the $i$-th space direction. The no-thickness flat plate is modelled using a slip-wall boundary condition in between two adjacent blocks.

To allow the parallelization of the simulation, the PIANO solver requires the computational domain to be split in blocks. However, some precautions should be observed regarding this decomposition [96]. Indeed, at the leading edge, a pressure jump between the top and bottom is required to generate the source of noise. However, if the leading edge is at the intersection of more than two blocks, its value in PIANO is unpredictable, as detailed by Wohlbrandt *et al.* [96]. The Figure 3.4a depicts the situation with four blocks intersecting at the leading edge. To remove the ambiguity, the leading edge is positioned at the intersection of 2 blocks, using the topology depicted in Figure 3.4b, which has been successfully used by Wohlbrandt *et al.* [96].

At the trailing edge, there should not be any pressure jump to satisfy the Kutta condition. Several methods have been assessed, such as applying a window filter to the

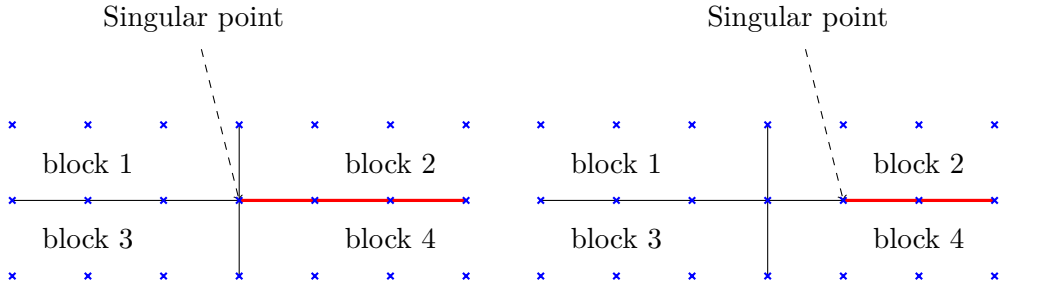


(a) Singular point at the intersection of 4 blocks

(b) Singular point at the intersection of 2 blocks

Figure 3.4: Blocks organisation regarding the singularity at the leading edge. The blue crosses denote the point of the mesh and the red line (—) denotes the localisation of the flat plate.

perturbations along the plate [39, 23] which damps the wall velocities as they move towards the trailing edge, to finally reach zero at the singularity. Another method, used by Sandberg and Sandham [98], consists in calculating the first two points downstream the trailing edge using a central difference scheme, using the averaged between the top and bottom surface for the two grid points directly upstream the trailing edge. Similarly, Wohlbrandt *et al.* [96] averaged the trailing edge pressure value using the surrounding points, but did not use a central scheme. As this last method was proven successful using the solver PIANO [96], it is used in this work. The final decomposition gives 16 blocks, which allows the parallelization of the simulation on 16 or less CPU core(s).

### 3.5.2 Results

To compare the numerical solution, the semi-analytical method proposed by Amiet [60], which is in very close agreement with experiments [99], is used as a reference. However, as it is for three-dimension configuration, the method is modified to propagate acoustic in a 2D field, using a 2D convected Green function in free-field (Appendix B). The Amiet model [60] predicts a pressure jump on the surface of the plate, with a maximum going to infinity at the leading edge and a Kutta condition at the trailing edge. In the Amiet model [60], the unsteady loading on the plate is split into two contributions, the leading edge scattering half-plane problem, and the back scattering trailing edge problem.

To observe the specific interaction effects such as non-compactness of the acoustic response of the plate when the wavenumber of the incoming gust increases, using the source of vorticity detailed in Section 3.3, three harmonic cases, with a streamwise wavenumbers $k_x$ given by $k_x c = 4, 8,$ and 12, are simulated. The wavenumber $k_x$ being related for frozen turbulence by $k_x = \omega/u_0$ with $\omega$ the angular frequency and $u_0$ the convective velocity of the gust.

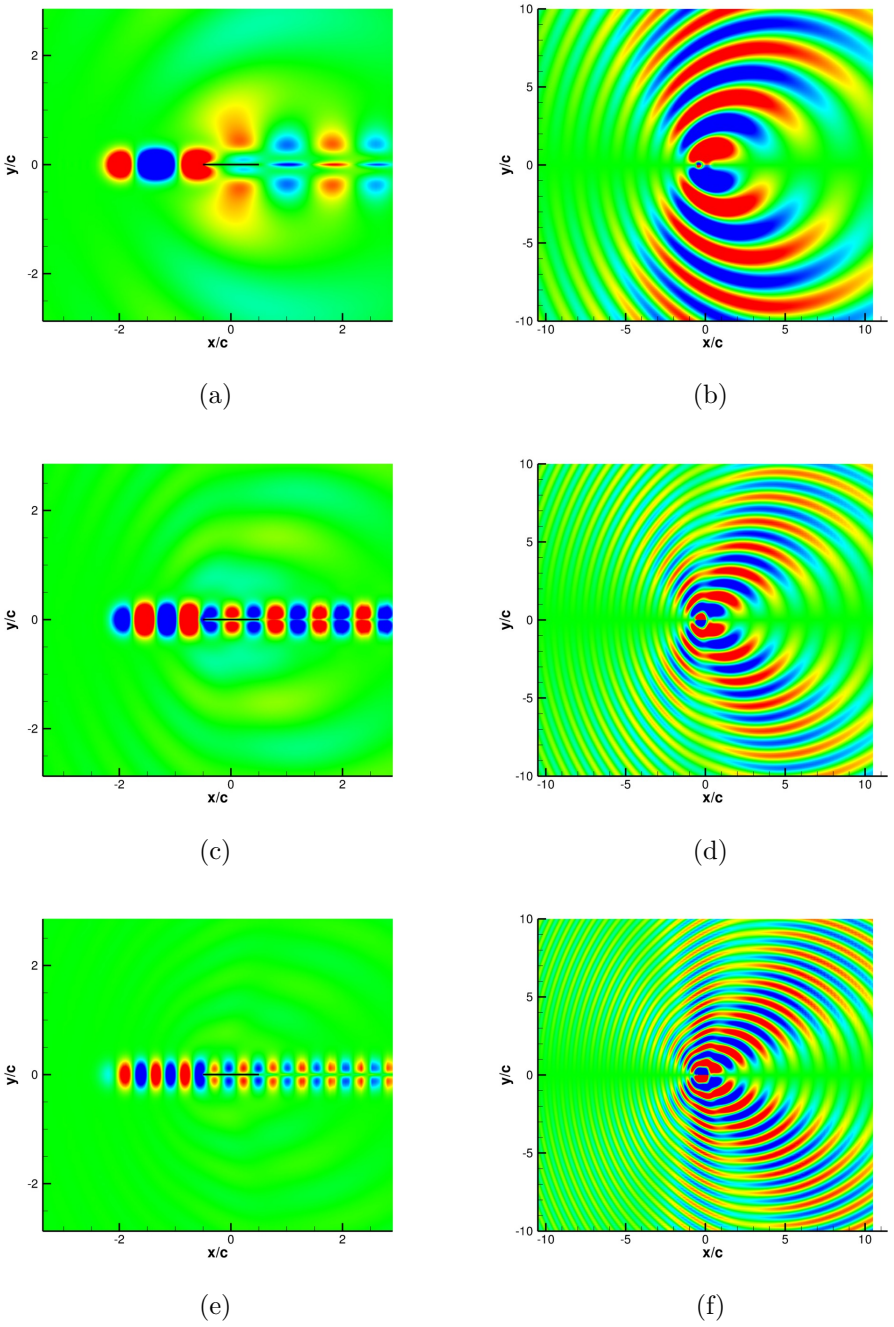


Figure 3.5: (a)(c)(d) Instantaneous $y$-velocity field $u_2/a_\infty$ (levels between $\pm 2.10^{-4}$) and (b)(d)(e) instantaneous pressure field $p/(\rho_0 a_\infty^2)$ (levels between $\pm 1.5.10^{-4}$) for a harmonic gust at (a)(b) $k_x c = 4$, (c)(d) $k_x c = 8$, (e)(f) $k_x c = 12$ with the mesh refined down to 1/200 of the chord at the leading and trailing edge.

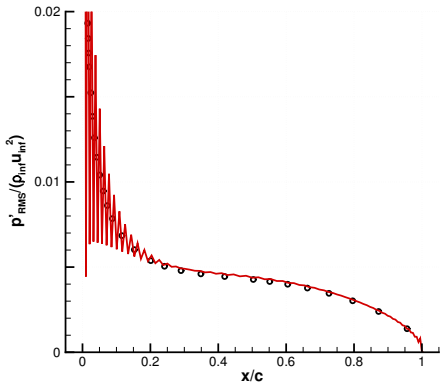


(a) $k_x c = 4$

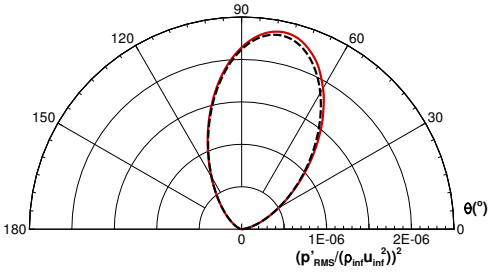


(b) $k_x c = 4$

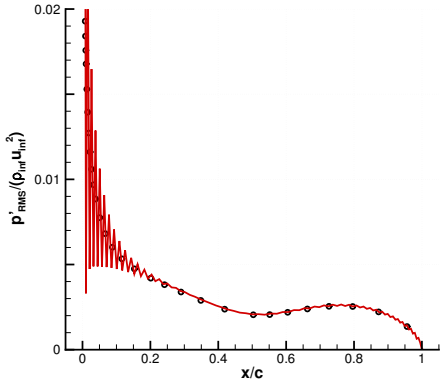


(c) $k_x c = 8$

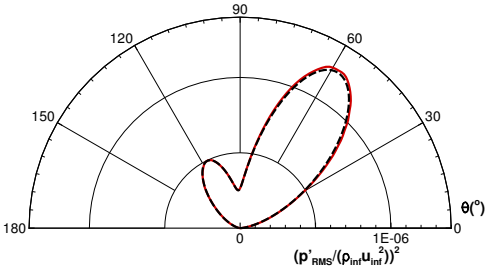


(d) $k_x c = 8$

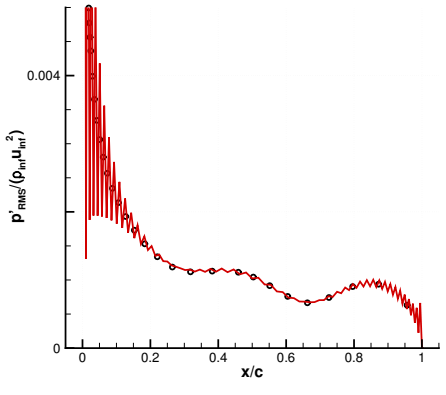


(e) $k_x c = 12$

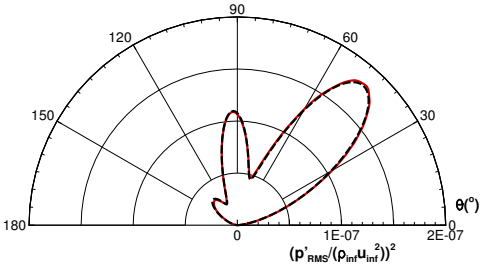


(f) $k_x c = 12$

Figure 3.6: No thickness plate with $\Delta x_{\min}/c = 0.005$ - (a) (c) (e) RMS pressure along the flat plate and (b) (d) (f) directivity of the acoustic field at $R = 4c$ around the flat plate: (——) numerical results and (——) Amiet model.

The instantaneous velocity and pressure fields are plotted for the different wavenumbers considered, namely $k_x c = 4, 8$ and 12, in the Figure 3.5. In all three cases, the radiated pressure is symmetric, as expected for a no-thickness flat plate impinged by a no-incidence gust. Moreover, the acoustic waves do not seem to be altered by the boundaries when leaving the domain.

For a wavenumber $k_x$ given by $k_x c = 4$, the RMS pressure $p'_{\mathrm{RMS}}$ along the flat plate plotted in Figure 3.6a and non-dimensionalised using $p'_{\mathrm{RMS}}/(\rho_0 U_0^2)$, reveals some high-amplitude, high-frequency oscillations from the leading edge to about 20% of the chord, as well as at the trailing edge, but with smaller amplitudes. These spurious oscillations are induced by the numerical method and their associated wave length is directly related to the mesh, with about one full oscillation every two mesh cells. Nevertheless, the rest of the RMS pressure along the plate compares well with the Amiet model [60], including at the trailing edge where the pressure goes to zero, which fulfils the Kutta condition. The distance between the spurious oscillations is very small with respect to the acoustic wavelength $\lambda_a$, therefore the leading edge region is acoustically compact and can then be considered as a point dipole, thus these spurious oscillations are not visible in the far-field directivity in Figure 3.6b. Moreover, the chord of the plate $c$ is also small with respect to the acoustic wavelength $\lambda_a$, (i.e. $c/\lambda_a \approx 0.2$), therefore the flat plate region is also acoustically compact, and can then be considered as a point dipole, which is confirmed by the directivity plotted in Figure 3.6b. The directivity is computed from the RMS fluctuating pressure $p'_{\mathrm{RMS}}$ on a circle centred on the middle of the plate (i.e. at $(0, 0)$) with a radius of four chords. As the radiated acoustic pressure field is symmetric, the directivity is only plotted on half the circle (from 0° to 180°). The results are non-dimensionalized via $\left(p'_{\mathrm{RMS}}/(\rho_\infty u_\infty^2)\right)^2$ and are plotted on a linear scale. With respect to the Amiet model [60], the directivity is in good agreement.

For an incoming harmonic gust at a wavenumber of $k_x c = 8$, the RMS pressure along the flat plate plotted in Figure 3.6c still present high-amplitude, high-frequency oscillations at the leading edge, going to about 20% of the chord, but it remains acoustically compact, therefore these oscillations are not visible in the far-field directivity, plotted in Figure 3.6d. The Kutta condition is still respected and the predicted values are in good agreement with the Amiet model [60]. The instantaneous pressure field (Figure 3.5d) depicts the apparition of non-compactness effects. Indeed, in this case, the chord of the plate $c$ is not considered small with respect to the acoustic wavelength $\lambda_a$, (i.e. $c/\lambda_a \approx 0.4$), therefore the flat plate is not acoustically compact. This is confirmed by the directivity plotted in Figure 3.6d.

At a wavenumber of $k_x c = 12$, with respect to the lower wavenumber cases, the spurious oscillations on the RMS pressure (plotted in Figure 3.6e) are more pronounced, yet it compares well with the predicted values given by the Amiet model [60] and the Kutta condition is satisfied. As the wavenumber is increased, the acoustic wavelength of the perturbations decreases, therefore the non-compactness effects between the leading and

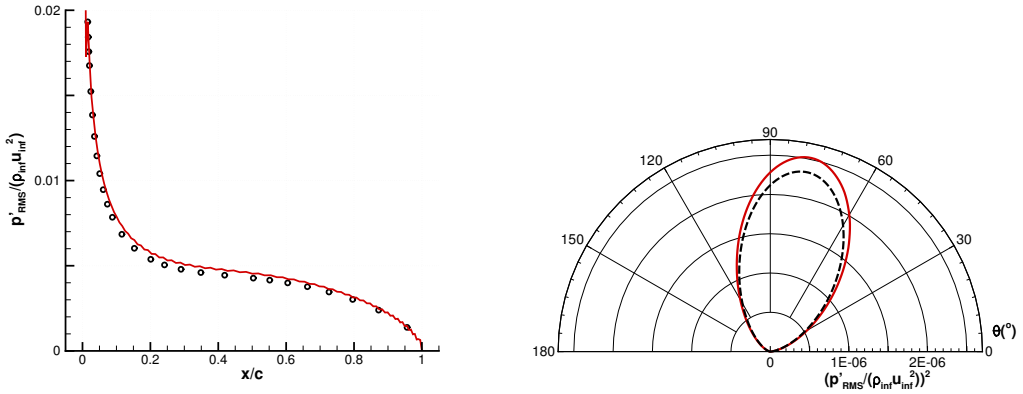


(a) (b)

Figure 3.7: No thickness plate with $\Delta x_{\min}/c = 0.005$, $k_x c = 4$, and a Local ASD at the leading edge - (a) RMS pressure along the flat plate and (b) directivity of the acoustic field at $R = 4c$ around the flat plate: (——) numerical results and (——) Amiet model.

trailing edge region are more important, with for instance the apparition of a third lobe on the directivity plot (Figure 3.6f).

To reduce the spurious oscillations at the singularities, one attempt consisted in adding a local Artificial Selective Damping (ASD) at the leading edge. This ASD [95, 100] relies on a damping term added to the finite difference scheme, based on the Fourier transform to damp the high-frequency oscillations without affecting the low-frequency perturbations. As plotted in Figure 3.7a, this solution succefully removes the majority of the spurious oscillations on the RMS pressure at the leading edge, but surprisingly overestimates the pressure along the plate. Therefore, the far-field acoustic in Figure 3.7b is also overestimated compared to the Amiet model [60]. As this approach is not satisfactory, another strategy is investigated to remove the spurious oscillations, such as the discretization of the grid.

## 3.6 Effect of the discretization

To reduce the oscillations at the singularities, a grid resolution five-time finer at the leading and trailing edges is used, which gives a minimum grid element of $\Delta x_{\min}/c = 0.001$. The time step $\Delta t$ is set to $c/a_\infty \Delta t = 4.9.10^{-4}$, which gives a maximum CFL [97] number of 0.9 near the leading edge, a minimum CFL [97] number of 0.005 near the boundaries of the computational domain, and a mean CFL in the simulation of 0.04. All the other parameters are identical to the previous case considered.

As expected, the directivity and RMS pressure along the plate, plotted in Figure 3.8, still compares well with the analytical model of Amiet [60]. Regarding the spurious

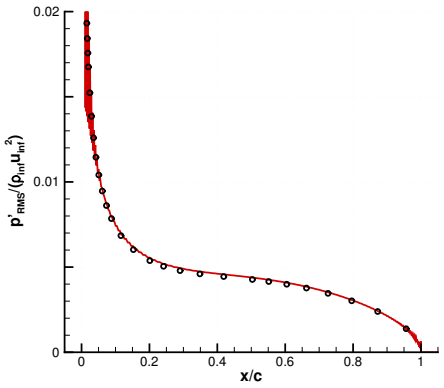


(a) $k_x c = 4$

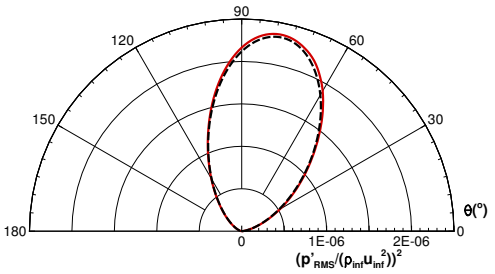


(b) $k_x c = 4$

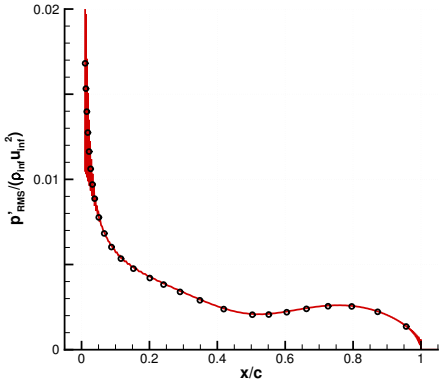


(c) $k_x c = 8$

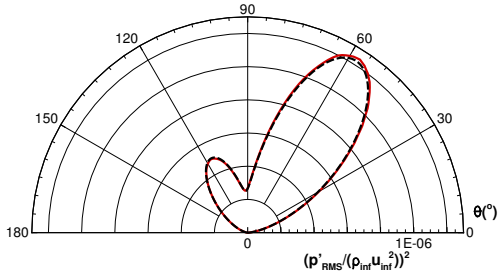


(d) $k_x c = 8$

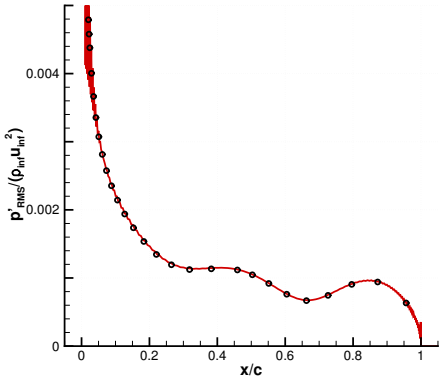


(e) $k_x c = 12$

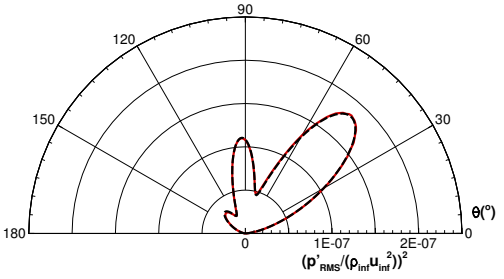


(f) $k_x c = 12$

Figure 3.8: No thickness plate with $\Delta x_{\min} c = 0.001$ - (a) (c) (e) RMS pressure along the flat plate and (b) (d) (f) directivity of the acoustic field at $R = 4c$ around the flat plate: (——) numerical results and (——) Amiet model

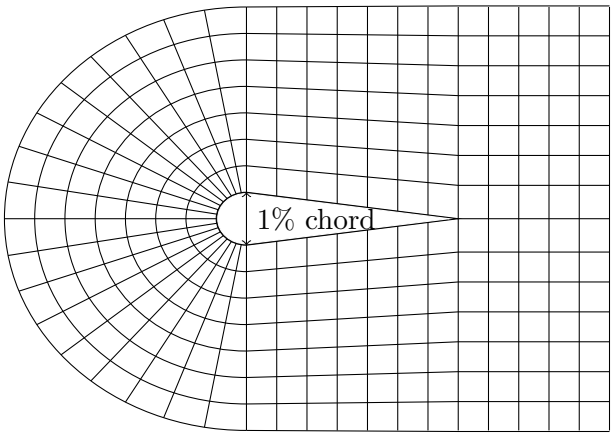


(a) Sketch of the C-mesh structure.

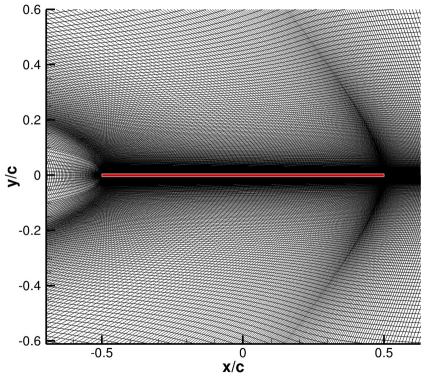


(b) Structured mesh

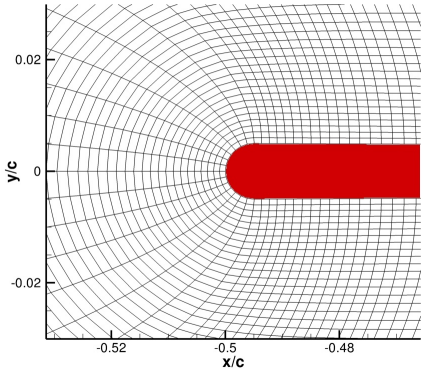


(c) Zoom of the mesh at the leading edge

Figure 3.9: Sketch of the profile and mesh where the leading edge singularity is replaced by a cylinder shape nose. The red line (—) denotes the position of the profile.

oscillations at the singularities, their amplitude is greatly reduced and their extent is now constraint within the first 5% of the chord. Moreover, as these oscillations are grid-related, their wavelength is five times smaller than previously.

This improvement is however still not satisfactory as some high-amplitude, high-wavenumber oscillations still remain close to the leading edge. To maintain a similar cost of the simulation, the mesh is not refined anymore but a different geometry is investigated.

## 3.7 Effect of the geometry

Singularities are difficult to numerically simulate, therefore, a different geometry without a singularity at the leading edge is considered. However, in order to compare the results with the Amiet model [60], the thickness should be small [61]. In this configuration, the flat plate is approximated by half a circle for the leading edge, and a triangle for the rest of the geometry. Therefore, the singularity at the trailing edge is still present, but

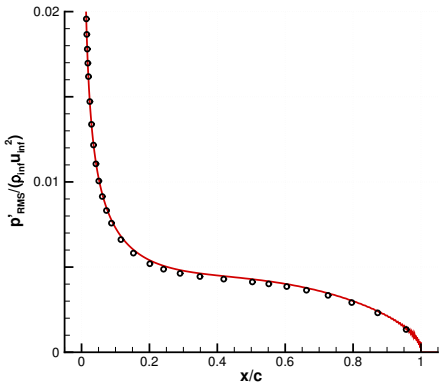


(a) $k_x c = 4$

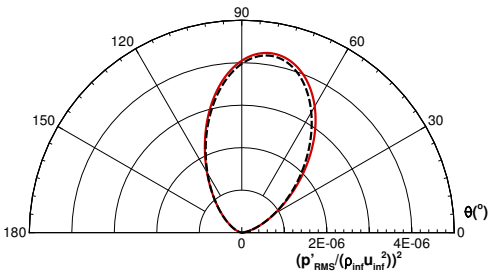


(b) $k_x c = 4$

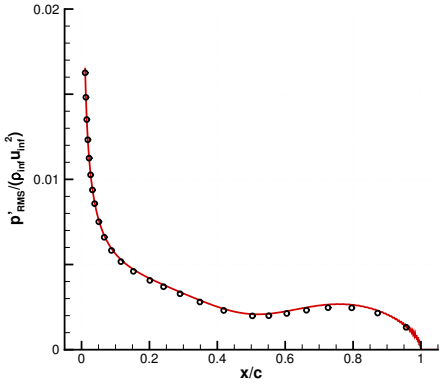


(c) $k_x c = 8$

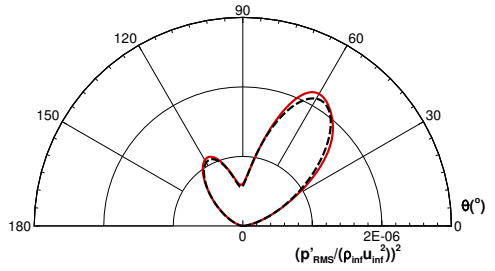


(d) $k_x c = 8$

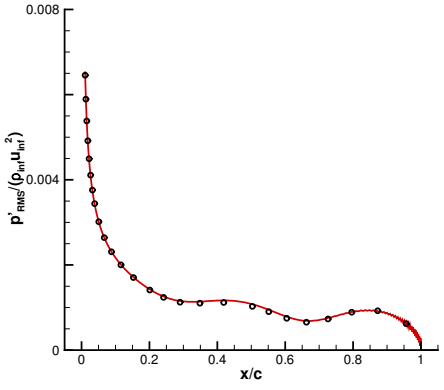


(e) $k_x c = 12$

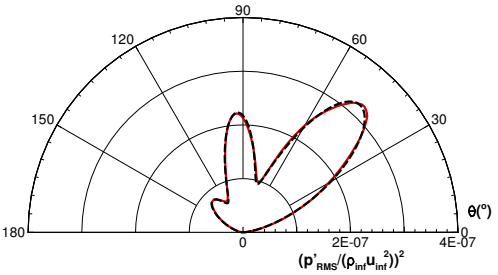


(f) $k_x c = 12$

Figure 3.10: 1% thickness plate with $\Delta x_{\min} c = 0.001$ - (a) (c) (e) RMS pressure along the flat plate and (b) (d) (f) directivity of the acoustic field at $R = 2c$ around the flat plate: (——) numerical results and (——) Amiet model

the spurious oscillations in the two previous cases were negligible. To approximate a flat plate, the thickness of the geometry is set to 1% of the chord. This thin geometry induces a high curvature at the leading edge, hence a small grid size is required to correctly mesh the geometry. At the singularities, the same element size as the previous simulation is retained ($\Delta x_{\min} c = 0.001$). Unlike for the previous meshes, for ease of generation, the grid is generated analytically and is organised in a C-mesh as shown in Figure 3.9a. The outward normal lines to the geometry are defined using a cubic Hermite spline formulation[1]. The grid expansion is kept to 1.05, expect for some cells upstream the profile, close to the leading edge, due to the high curvature of the profile. The mesh generated is visible in Figure 3.9b. The time step of the simulations is set to $c/a_\infty \Delta t = 5.10^{-4}$ which gives a maximum CFL of 0.9 near the leading edge.

As expected, the blunt leading edge removes the oscillations on the RMS pressure for the three harmonic gust cases simulated (Figures 3.10a, 3.10c and 3.10e). Moreover, the non-compliance to a grid expansion of 1.05 for a few cells upstream of the profile does not seem to affect the results. Indeed, the RMS pressure compares well with the Amiet model [60]. Similarly, the directivities (Figures 3.10b, 3.10d and 3.10f) compare well with the analytical model. Notice that, due to the C-mesh structure, the mesh was not designed to support the acoustic wavelengths further than two chords away from the plate. Therefore, the directivities are taken in a circle with a radius of two chords.

## 3.8 Conclusion

In this chapter, the generation and injection of fluctuating velocities through vorticity sources for interaction noise is investigated on a two-dimensional plate interaction noise. The plate has no camber and no incidence and is impinged by an harmonic gust, using the LEE model implemented in the CAA solver PIANO. A specific meshing strategy has to be applied at the leading and trailing edges to respectively prevent undetermined values and the Kutta condition. A first simulation considering a no-thickness flat plate shows at the singularities some high-frequency spurious oscillations. A refined grid does not entirely solve the problem as these unwanted oscillations remain, but with a reduced amplitude and extent. To tackle this issue, a second simulation with a finer grid is performed, nevertheless, the spurious oscillations are still present. Finally, to limit the computational cost of such simulation, instead of using an even finer mesh, a different geometry is investigated. In spite of the no-thickness flat plate, a thin geometry is used which successfully removes the spurious oscillations at the singularities. These results indicate that the injection of velocity gusts through vorticity sources can be used to

[1] The equation of a cubic Hermite spline in a unit interval [0,1] is defined as $p(t) = (2t^3 - 3t^2 + 1)p_0 + (t^3 - 2t^2 + t)m_0 + (-2t^3 + 3t^2)p_1 + (t^3 - t^2)m_1$ where $p_0$, $p_1$ are respectively the starting and ending point of the spline and $m_0$, $m_1$ there associated tangent.

study interaction noise. In the next Chapter, the relation between sources of vorticity and turbulence spectra is investigated.

# Chapter 4

# Synthetic turbulence injected through vorticity sources

Synthetic turbulence can be injected inside a computation domain using either an inlet boundary or a patch, as explained in Chapter 2. However, an efficient parallel implementation of these method in a solver can cumbersome. This chapter introduces a new method to inject artificial turbulence which is easy and parallelize in an already existing solver. It relies on localized sources of vorticity modulated in time to reproduce desired turbulence characteristics. The developed method allows the generation of one- or two-component, anisotropic or isotropic, frozen synthetic turbulence. This method can also be extended to three-component turbulence, but the mathematical development has yet to be carried out.

The first part of this chapter details the mathematical development of the method. Starting from the analysis of a single source of vorticity used to generate perturbations, the synthesis of one-component and two-component turbulence is detailed using a continuous distribution of sources in the transverse direction of the mean flow. The implementation of a continuous distribution of sources is difficult in a finite difference code, thus the impact of discrete sources is assessed. A minimal distance between each source is required and the amplitude of each source needs to be adjusted to respect prescribed turbulent spectra. The construction of the time signals modulating the sources and the implementation of the method in the solver is then discussed. Using this process, the synthesized turbulence is naturally anisotropic. The degree of anisotropy is controlled by the parameters of the sources. The technique is validated in free-field with a uniform mean flow. Finally, the method is applied on a flat plate interaction case. It is the extension of the flat plate interaction noise problem detailed in the last Chapter, from harmonic to turbulent gusts.

## 4.1 Single source of vorticity

In this section, we focuses on the relation between a single source of vorticity in a uniform mean flow along the $x$-axis, and the generated perturbations convected downstream. Away from any other source, it follows $\rho' = 0$, $p' = 0$ and $\nabla \cdot \mathbf{u}' = 0$. Following those assumptions, one can simplify the LEE to obtain a transport equation

$$\left(\frac{\partial}{\partial t} + u_0 \frac{\partial}{\partial x}\right) \mathbf{u}' = \boldsymbol{\mathcal{S}}_v(\mathbf{x}, t) \ , \tag{4.1}$$

where the vorticity source term $\boldsymbol{\mathcal{S}}_v(\mathbf{x}, t)$ can be decomposed in a spatial distribution $\mathbf{g}(\mathbf{x})$ and a temporal signal $s(t)$ so that $\boldsymbol{\mathcal{S}}_v(\mathbf{x}, t) = \mathbf{g}(\mathbf{x})s(t)$.

We consider the problem as two-dimensional in the $xy$-plane, the velocity field is then expressed as $\mathbf{u}'(x, y, t)$. The Fourier transform on the spatial variable $x$ and the temporal variable $t$ gives

$$\hat{\mathbf{u}}'(k_x, y, \omega) = \frac{1}{4\pi^2} \iint_{\Re^2} \mathbf{u}'(x, y, t) \mathrm{e}^{-\mathrm{i}\omega t + \mathrm{i}k_x x} \mathrm{d}x\mathrm{d}t \ . \tag{4.2}$$

The Fourier transform of the transport Equation (4.1) gives

$$\hat{\mathbf{u}}' = \frac{\hat{\mathbf{g}}(k_x, y)\hat{s}(\omega)}{\mathrm{i}(\omega - k_x u_0)} \ . \tag{4.3}$$

This can formally be written in the physical space through an inverse Fourier transform

$$\mathbf{u}'(x, y, t) = \iint_{\Re^2} \frac{\hat{\mathbf{g}}(k_x, y)\hat{s}(\omega)}{\mathrm{i}(\omega - k_x u_0)} \mathrm{e}^{\mathrm{i}\omega t - \mathrm{i}k_x x} \mathrm{d}\omega\mathrm{d}k_x \ , \tag{4.4}$$

where we assume that $\hat{\mathbf{g}}$ and $\hat{s}$ are regular and decay sufficiently rapidly at infinity for the integrals to be well defined. If we perform the integral with respect to $\omega$ and use the Cauchy theorem (residue theorem) as there is a real pole for $\omega = k_x u_0$, we have

$$\mathbf{u}'(x, y, t) = \pi \int_{\Re} \hat{\mathbf{g}}(k_x, y)\hat{s}(k_x u_0) \mathrm{e}^{-\mathrm{i}k_x(x - u_0 t)} \mathrm{d}k_x \ , \tag{4.5}$$

which tells us that each wavenumber $k_x$ travels at a velocity $u_0$ and has an amplitude given by $\pi\hat{\mathbf{g}}(k, y)\hat{s}(k_x u_0)$.

To understand the link between Equation (4.5) and a velocity spectrum, we can start by calculating $\langle \hat{s}(\omega_1)\overline{\hat{s}(\omega_2)} \rangle$ using Fourier transforms

$$\langle \hat{s}(\omega_1)\overline{\hat{s}(\omega_2)} \rangle = \frac{1}{4\pi^2} \iint_{\Re^2} \langle s(t_1)s(t_2) \rangle \mathrm{e}^{-\mathrm{i}\omega_1 t_1} \mathrm{e}^{+\mathrm{i}\omega_2 t_2} \mathrm{d}t_1\mathrm{d}t_2 \ . \tag{4.6}$$

If we write $t_1 = t$ and $t_2 = t_1 + \tau = t + \tau$, and assume that $s(t)$ is a stationary random signal, it follows that $\langle s(t)s(t + \tau) \rangle$ is independent of time $t$, so we can calculate the

integral with respect to time

$$\langle \hat{s}(\omega_1)\overline{\hat{s}(\omega_2)}\rangle = \frac{1}{4\pi^2}\int_{\Re}\langle s(t)s(t+\tau)\rangle \mathrm{e}^{-\mathrm{i}\omega_2\tau}\mathrm{d}\tau \underbrace{\int_{\Re}\mathrm{e}^{-\mathrm{i}(\omega_1-\omega_2)t}\mathrm{d}t}_{=2\pi\delta(\omega_1-\omega_2)} , \tag{4.7}$$

$$= \delta(\omega_1-\omega_2)S(\omega_1) , \tag{4.8}$$

where $S$ is the spectral density of the time signal $s$.

We define the velocity spectra of the fluctuating velocity

$$\phi_{ij}(\mathbf{k}) = \frac{1}{(2\pi)^2}\iint_{\Re^2}\langle u_i'(\mathbf{x},t)u_j'(\mathbf{x}+\mathbf{r},t)\rangle \mathrm{e}^{\mathrm{i}\mathbf{k}\cdot\mathbf{r}}\mathrm{d}\mathbf{r} \quad \text{and} \quad \Phi_{ij}(k_x) = \int \phi(k_x,k_y)\mathrm{d}k_y , \tag{4.9}$$

which gives

$$\Phi_{ij}(k_x) = \frac{1}{2\pi}\int_{\Re}\langle u_i'(x,y,t)u_j'(x+r,y,t)\rangle \mathrm{e}^{\mathrm{i}k_x r}\mathrm{d}r , \tag{4.10}$$

or

$$\int_{\Re}\Phi_{ij}(k_x)\mathrm{e}^{-\mathrm{i}kr}\mathrm{d}k_x = \langle u_i'(x,y,t)u_j'(x+r,y,t)\rangle . \tag{4.11}$$

In Equation (4.11), the spatial correlation can be expressed as

$$\langle u_i'(x,y,t)u_j'(x+r,y,t)\rangle = \pi^2\iint_{\Re^2}\hat{g}_i(k_{x_1},y)\overline{\hat{g}_j(k_{x_2},y)}\langle \hat{s}_i(k_{x_1}u_0)\overline{\hat{s}_j(k_{x_2}u_0)}\rangle \mathrm{e}^{-\mathrm{i}k_{x_1}(x-u_0t)}\mathrm{e}^{-\mathrm{i}k_{x_2}(x-u_0t+r)}\mathrm{d}k_{x_1}\mathrm{d}k_{x_2} , \tag{4.12}$$

using Equation (4.8), it yields

$$\langle u_i'(x,y,t)u_j'(x+r,y,t)\rangle = \frac{\pi^2}{|u_0|}\int_{\Re}\hat{g}_i(k_x,y)\overline{\hat{g}_j(k_x,y)}S(k_xu_0)\mathrm{e}^{-\mathrm{i}k_xr}\mathrm{d}k_x . \tag{4.13}$$

Comparing with the definition of $\Phi_{ij}(k_x)$, Equation (4.11), we can see that

$$\Phi_{ij}(k_x) = \frac{\pi^2}{|u_0|}\hat{g}_i(k_x,y)\overline{\hat{g}_j(k_x,y)}S(k_xu_0) . \tag{4.14}$$

The spatial Fourier transform of the spatial component will affect the frequency spectrum of the velocity fluctuations convected downstream of the source. Hence the frequency spectrum of the time component $s(t)$ injected through the local source has to be chosen to ensure that the desired spectrum is obtained for the turbulence convected downstream of the source. The frozen turbulence hypothesis implies $k_x = \omega/u_0$, thus the spectral density $S(\omega)$ of the time signal $s(t)$ is

$$S(\omega) = \frac{|u_0|}{\pi^2}\frac{\Phi_{22}(\omega/u_0)}{|\hat{g}_2(\omega/u_0,y_c)|^2} , \tag{4.15}$$

where $\Phi_{22}(\omega/u_0)$ is the desired wavenumber spectrum of the fluctuating velocity component normal to the chord, $|(.)|$ is the norm $(.)$, and $\hat{g}_2(k_x = \omega/u_0, y_c)$ is the Fourier transform of the spatial component of the source $\mathbf{g}(\mathbf{x})$, on the streamwise direction at the center of the source (i.e. $y = y_c$).

## 4.2 One-component turbulence

By considering a single source of vorticity, the desired velocity spectrum $\Phi_{22}(\omega/u_0)$ is only respected at the centre $y_c$ of the source. Away from the centre, the amplitude of the injected perturbations varies with the Fourier transform of the spatial distribution $\hat{\mathbf{g}}$. To construct a one-component turbulence with the same properties over a transverse extent, a spatial distribution constant in the vertical direction over the desired extent can be used. This can be easily achieved by considering a continuous distribution of sources of vorticity, modulated by the same realization of the temporal signal $s(t)$, with their centre $y_c$ located on a line orthogonal to the mean flow.

The perturbation velocity $\mathbf{u}'$ given in Equation (4.5) is modified to consider a continuous distribution of sources

$$\mathbf{u}'(x, y, t) = \int_{\Re} \pi \int_{\Re} \hat{\mathbf{g}}(k_x, y - y_c)\hat{s}(k_x u_0)\mathrm{e}^{-\mathrm{i}k_x(x-u_0 t)}\mathrm{d}k_x\mathrm{d}y_c \ , \tag{4.16}$$

where $y_c$ represents the centre of a source.

It follows Equation (4.15) to become

$$S(\omega) = \frac{|u_0|}{\pi^2} \frac{\Phi_{22}(\omega/u_0)}{\int_{\Re} |\hat{g}_2(\omega/u_0, y_c)|^2 \mathrm{d}y_c} \ . \tag{4.17}$$

## 4.3 Two-component turbulence

To synthesize a two-component frozen turbulence, similar to the one-component method described in Section 4.2, a continuous distribution of sources in the transverse direction with regards to the mean flow can be imposed, with the main difference of the sources being uncorrelated. Indeed, in the one-component method, each time signal $s(t)$ are the same realisation of $S(\omega)$, whereas for the two-component turbulence, each time signal $s(t)$ is a different realisation of $S(\omega)$. Moreover, as explained later in this section, the spatial distribution $\mathbf{g}$ of the sources fully determine the velocity spectrum $\Phi_{11}(k_y)$. Hence, to control $\Phi_{11}(k_y)$, a number $N_l$ of continuous distributions of sources are stacked, each having a different spatial distribution $\mathbf{g}(x, y, \lambda_l)$, where $\lambda_l$ represents a characteristic length of the source.

The perturbation velocity $\mathbf{u}'$ given in Equation (4.5) can be modified to consider the $N_l$ continuous distributions of sources, to write

$$\mathbf{u}'(x,y,t) = \sum_{l}^{N_l} \int_{\Re} \pi \int_{\Re} \hat{\mathbf{g}}(k_x, y-y_c, \lambda_l)\hat{s}_l(k_x u_0, y_c)\mathrm{e}^{-\mathrm{i}k_x(x-u_0 t)}\mathrm{d}k_x\mathrm{d}y_c \ , \tag{4.18}$$

where $y_c$ represents the centre of a source. The spatial correlation can be expressed as

$$\begin{aligned}\langle u_i'(x,y,t)u_j'(x+r_x,y+r_y,t)\rangle = \pi^2 \sum_{l_1}^{N_l}\sum_{l_2}^{N_l} \iiiint_{\Re^4} \hat{g}_i(k_{x_1}, y-y_{c_1}, \lambda_{l_1})\overline{\hat{g}_j(k_{x_2}, y+r_y-y_{c_2}, \lambda_{l_2})} \\ \langle \hat{s}_{l_1}(k_{x_1}u_0, y_{c_1})\overline{\hat{s}_{l_2}(k_{x_2}u_0, y_{c_2})}\rangle \mathrm{e}^{-\mathrm{i}k_{x_1}(x-u_0t)}\mathrm{e}^{+\mathrm{i}k_{x_2}(x+r_x-u_0t)}\mathrm{d}k_{x_1}\mathrm{d}y_{c_1}\mathrm{d}k_{x_2}\mathrm{d}y_{c_2} \ .\end{aligned} \tag{4.19}$$

The sources are uncorrelated, hence using inverse Fourier transforms, it follows

$$\begin{aligned}\langle \hat{s}_{l_1}(k_{x_1}u_0, y_{c_1})\overline{\hat{s}_{l_2}(k_{x_2}u_0, y_{c_2})}\rangle = \frac{\delta(y_{c_1}-y_{c_2})\delta(l_1-l_2)}{4\pi^2} \iint_{\Re^2} \langle s_{l_1}(t_1, y_{c_1})s_{l_1}(t_2, y_{c_1})\rangle \\ \mathrm{e}^{-\mathrm{i}k_{x_1}u_0t_1}\mathrm{e}^{+\mathrm{i}k_{x_2}u_0t_2}\mathrm{d}t_1\mathrm{d}t_2 \ .\end{aligned} \tag{4.20}$$

If we write $t_1 = t$ and $t_2 = t_1 + \tau = t + \tau$, and assume that $s_{l_1}(t, y_{c_1})$ is a stationary random signal, it follows that $\langle s_{l_1}(t, y_{c_1})s_{l_1}(t+\tau, y_{c_1})\rangle$ is independent of $t$, so we can calculate the integral with respect to time

$$\begin{aligned}\langle \hat{s}_{l_1}(k_{x_1}u_0, y_{c_1})\overline{\hat{s}_{l_1}(k_{x_2}u_0, y_{c_2})}\rangle = \delta(y_{c_1}-y_{c_2})\delta(l_1-l_2)\frac{1}{4\pi^2}\int_{\Re}\langle s_{l_1}(t, y_{c_1})s_{l_1}(t+\tau, y_{c_1})\rangle \\ \mathrm{e}^{-\mathrm{i}k_{x_1}u_0\tau}\mathrm{d}\tau \underbrace{\int_{\Re}\mathrm{e}^{-\mathrm{i}(k_{x_1}-k_{x_2})u_0t}\mathrm{d}t}_{=\frac{2\pi}{|u_0|}\delta(k_{x_1}-k_{x_2})} \ ,\end{aligned} \tag{4.21}$$

$$= \frac{1}{|u_0|}\delta(k_{x_1}-k_{x_2})\delta(y_{c_1}-y_{c_2})\delta(l_1-l_2)S_l(k_{x_1}u_0) \ . \tag{4.22}$$

The function $\hat{g}_j$ is assumed to be separable, consequently $\hat{g}_j(k_x, y, \lambda_l) = \hat{g}_{jx}(k_x, \lambda_l)g_{jy}(y, \lambda_l)$ where $g_{jy}$ is real and $\hat{g}_{jx}$ is complex valued, leading to the spatial correlation

$$\begin{aligned}\langle u_i'(x,y,t)u_j'(x+r_x,y+r_y,t)\rangle = \frac{\pi^2}{|u_0|}\sum_{l}^{N_l}\int_{\Re}\hat{g}_{ix}(k_x,\lambda_l)\overline{\hat{g}_{jx}(k_x,\lambda_l)}S_l(k_xu_0)\mathrm{e}^{-\mathrm{i}k_xr_x}\mathrm{d}k_x \\ \int_{\Re} g_{iy}(y-y_c,\lambda_l)g_{jy}(y-y_c+r_y,\lambda_l)\mathrm{d}y_c\end{aligned} \tag{4.23}$$

By definition, the fluctuating velocity spectrum is

$$\phi_{ij}(\mathbf{k}) = \frac{1}{(2\pi)^2}\iint_{\Re^2}\langle u_i'(\mathbf{x},t)u_j'(\mathbf{x}+\mathbf{r},t)\rangle \mathrm{e}^{\mathrm{i}\mathbf{k}.\mathbf{r}}\mathrm{d}\mathbf{r} \ . \tag{4.24}$$

Hence, injecting Equation (4.23) in the definition of the fluctuating velocity wavenumber (Equation (4.24)), it writes for the $k_x$ part

$$\phi_{ij}(k_x,k_y) = ... \iint_{\Re} \hat{g}_{ix}(k_x,\lambda_l)\overline{\hat{g}_{jx}(k_x,\lambda_l)}S_l(k_x u_0)\mathrm{e}^{-\mathrm{i}k_x r_x}\mathrm{d}k_x \mathrm{e}^{\mathrm{i}k_x r_x}\mathrm{d}r_x \tag{4.25}$$

$$= ... \; 2\pi \hat{g}_{ix}(k_x,\lambda_l)\overline{\hat{g}_{jx}(k_x,\lambda_l)}S_l(k_x u_0) \tag{4.26}$$

and for the $k_y$ part, using the change of variable $Y = y - y_c + r_y$

$$\phi_{ij}(k_x,k_y) = ... \iint_{\Re} g_{iy}(y-y_c,\lambda_l)g_{jy}(y-y_c+r_y,\lambda_l)\mathrm{d}y_c \mathrm{e}^{\mathrm{i}k_y r_y}\mathrm{d}r_y \tag{4.27}$$

$$= ... \int_{\Re} g_{iy}(y-y_c,\lambda_l)\left(\int_{\Re} g_{jy}(Y,\lambda_l)\mathrm{e}^{\mathrm{i}k_y Y}\mathrm{e}^{-\mathrm{i}k_y(y-y_c)}\mathrm{d}Y\right)\mathrm{d}y_c \tag{4.28}$$

$$= ... \; 4\pi^2 \hat{g}_{jy}(k_y,\lambda_l)\overline{\hat{g}_{iy}(k_y,\lambda_l)} \tag{4.29}$$

which leads to fluctuating velocity wavenumber to be

$$\phi_{ij}(k_x,k_y) = \frac{2\pi^3}{|u_0|}\sum_{l}^{N_l} \hat{g}_{ix}(k_x,\lambda_l)\overline{\hat{g}_{jx}(k_x,\lambda_l)}\hat{g}_{jy}(k_y,\lambda_l)\overline{\hat{g}_{iy}(k_y,\lambda_l)}S_l(k_x u_0) \tag{4.30}$$

By definition, we have $\Phi_{22}(k_x) = \int_{\Re}\phi_{22}(k_x,k_y)\mathrm{d}k_y$ and $\Phi_{11}(k_y) = \int_{\Re}\phi_{11}(k_x,k_y)\mathrm{d}k_x$ which give:

$$\Phi_{11}(k_y) = \frac{2\pi^3}{|u_0|}\sum_{l}^{N_l}|\hat{g}_{1y}(k_y,\lambda_l)|^2\int_{\Re} S_l(k_x u_0)|\hat{g}_{1x}(k_x,\lambda_l)|^2\mathrm{d}k_x \ , \tag{4.31}$$

$$\Phi_{22}(k_x) = \frac{2\pi^3}{|u_0|}\sum_{l}^{N_l}|\hat{g}_{2x}(k_x,\lambda_l)|^2 S_l(k_x u_0)\int_{\Re}|\hat{g}_{2y}(k_y,\lambda_l)|^2\mathrm{d}k_y \ . \tag{4.32}$$

To better understand equations (4.31) and (4.32), we define

$$\mathbb{K}_l^{(11)}(\lambda_l,S_l) = \int_{\Re} S_l(k_x u_0)|\hat{g}_{1x}(k_x,\lambda_l)|^2\mathrm{d}k_x, \tag{4.33}$$

$$\mathbb{F}_l^{(11)}(k_y,\lambda_l) = |\hat{g}_{1y}(k_y,\lambda_l)|^2, \tag{4.34}$$

$$\mathbb{K}_l^{(22)}(\lambda_l) = \int_{\Re}|\hat{g}_{2y}(k_y,\lambda_l)|^2\mathrm{d}k_y, \tag{4.35}$$

$$\mathbb{F}_l^{(22)}(k_x,\lambda_l,S_l) = |\hat{g}_{2x}(k_x,\lambda_l)|^2 S_l(k_x u_0), \tag{4.36}$$

such that equations (4.31) and (4.32) can be written

$$\Phi_{11}(k_y) = \frac{2\pi^3}{|u_0|}\sum_{l}^{N_l} \underbrace{\mathbb{K}_l^{(11)}(\lambda_l,S_l)}_{\text{Independent of } k_y} \underbrace{\mathbb{F}_l^{(11)}(k_y,\lambda_l)}_{\text{Dependent of } k_y}, \tag{4.37}$$

$$\Phi_{22}(k_x) = \frac{2\pi^3}{|u_0|}\sum_{l}^{N_l} \underbrace{\mathbb{K}_l^{(22)}(\lambda_l)}_{\text{Independent of } k_x} \underbrace{\mathbb{F}_l^{(22)}(k_x,\lambda_l,S_l)}_{\text{Dependent of } k_x} \ . \tag{4.38}$$

The functions $\mathbb{K}^{(11)}$ and $\mathbb{K}^{(22)}$ in Equations (4.37) and (4.38) are respectively independent of $k_y$ and $k_x$, hence they can be seen as coefficients which modulate in amplitude the contribution of each group $l$ of sources to the velocity spectra. On the other hand, the functions $\mathbb{F}^{(11)}$ and $\mathbb{F}^{(22)}$, which depend of $k_y$ and $k_x$, give the shape of the contribution of each group $l$ of sources to the velocity spectra. Therefore the shapes of the spectra $\Phi_{11}(k_y)$ and $\Phi_{22}(k_x)$ are not automatically similar, leading to anisotropic turbulence.

Nevertheless, in order to choose the input parameters of the sources to control the spectra $\Phi_{11}(k_y)$ and $\Phi_{22}(k_x)$, from Equations (4.37) and (4.38), there are not enough constraints to fully determine the functions $S_l$. While this means that for prescribed velocity spectra, not one but multiple sets of the parameters $S_l$ and $\lambda_l$ can be used, it also makes their determination cumbersome.

In this work, to simplify the determination of the $S_l$ and $\lambda_l$, additional constraints on the functions $S_l$ are imposed. As only the integration of the $S_l$ are necessary in Equation (4.31) (i.e. velocity spectrum $\Phi_{11}(k_y)$), it is preferred to impose additional conditions on Equation (4.32) (i.e. velocity spectrum $\Phi_{22}(k_x)$).

### 4.3.1 Determination of the $\lambda_l$ and $S_l$: First approach

A first approach is to assume that each group $l$ of sources contributes to the whole spectrum $\Phi_{22}(k_x)$ in term of wavenumber range, but only at a reduced amplitude ratio $a_l$ ($a_l \leq 1$). Hence to achieve the desired $\Phi_{22}(k_x)$, the sum of $a_l$ should be equal to one. A sketch of this approach is depicted on Figure 4.1a. The spectral density of the sources can be expressed as

$$S_l(k_x u_0) = a_l \frac{|u_0|}{2\pi^3} \frac{\Phi_{22}(k_x)}{|\hat{g}_{2x}(k_x,\lambda_l)|^2 \int_{\Re} |\hat{g}_{2y}(k_y,\lambda_l)|^2 \mathrm{d}k_y} \ , \qquad \text{with} \quad \sum_l^{N_l} a_l = 1 \ . \tag{4.39}$$

It directly follows the wavenumber velocity spectrum $\Phi_{11}(k_y)$ to write

$$\Phi_{11}(k_y) = \sum_l^{N_l} a_l \frac{|\hat{g}_{1y}(k_y,\lambda_l)|^2}{\int_{\Re} |\hat{g}_{2y}(k_y,\lambda_l)|^2 \mathrm{d}k_y} \int_{\Re} \Phi_{22}(k_x) \frac{|\hat{g}_{1x}(k_x,\lambda_l)|^2}{|\hat{g}_{2x}(k_x,\lambda_l)|^2} \mathrm{d}k_x \ . \tag{4.40}$$

In this approach, from Equation (4.39), the determination of the functions $S_l$ are reduced to the determination of a single amplitude parameter $a_l$ per group $l$. Hence, to realize specific velocity spectra $\Phi_{11}(k_y)$ and $\Phi_{22}(k_x)$, the problem is reduced to determining the $\lambda_l$ and $a_l$, which corresponds to $2N_l$ unknown variables ($N_l$ being the number of groups of sources $l$).

Nevertheless, this first approach faces problems when the wavenumber range of $k_x$ in $\Phi_{22}(k_x)$ becomes too large, as discussed later in Section 4.8.

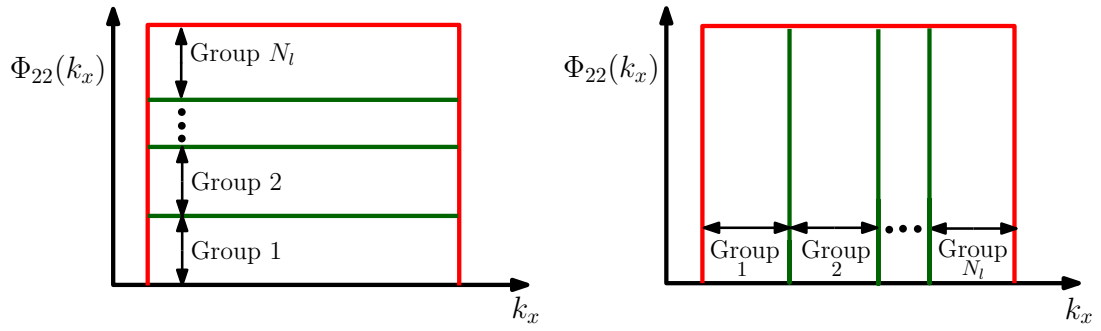


(a) First approach. (b) Second approach.

Figure 4.1: Two approaches used to simplify the determination of the $S_l$ and $\lambda_l$ of each group $l$ of sources to achieve desired velocity spectra $\Phi_{11}(k_y)$ and $\Phi_{22}(k_x)$.

### 4.3.2 Determination of the $\lambda_l$ and $S_l$: Second approach

As the first approach faces problems when the wavenumber range of $\Phi_{22}(k_x)$ is large, as discussed later in Section 4.8, a second approach which limits this range is considered. It assumes that each group of sources contributes to the full $\Phi_{22}(k_x)$, but on a limited wavenumber extent $k_x$, written for each group $[\Phi_{22}(k_x)]_l$. Hence to respect the desired $\Phi_{22}(k_x)$, the combination of the set of sources has to cover the whole wavenumber range of $\Phi_{22}(k_x)$. The situation is depicted on Figure 4.1b. In this case, the spectral density of the time signals is

$$S_l(k_x u_0) = \frac{|u_0|}{2\pi^3} \frac{[\Phi_{22}(k_x)]_l}{|\hat{g}_{2x}(k_x,\lambda_l)|^2 \int_{\Re} |\hat{g}_{2y}(k_y,\lambda_l)|^2 \mathrm{d}k_y} \ . \tag{4.41}$$

It directly follows the wavenumber velocity spectrum $\Phi_{11}(k_y)$

$$\Phi_{11}(k_y) = \sum_{l}^{N_l} \frac{|\hat{g}_{1y}(k_y,\lambda_l)|^2}{\int_{\Re} |\hat{g}_{2y}(k_y,\lambda_l)|^2 \mathrm{d}k_y} \int_{\Re} [\Phi_{22}(k_x)]_l \frac{|\hat{g}_{1x}(k_x,\lambda_l)|^2}{|\hat{g}_{2x}(k_x,\lambda_l)|^2} \mathrm{d}k_x \ . \tag{4.42}$$

In this approach, from Equation (4.41), the determination of the functions $S_l$ are reduced to the determination of the wavenumber $k_x$ extent of each group $l$. Hence, to realize specific velocity spectra $\Phi_{11}(k_y)$ and $\Phi_{22}(k_x)$, it comes down to determine the $\lambda_l$ and the wavenumber $k_x$ extent $[.]_l$, which corresponds to $3N_l$ unknown variables.

With respect to the first approach Section 4.3.1, this second approach requires to determine $3N_l$ unknown variables instead of $2N_l$ to realise specific velocity spectra $\Phi_{11}(k_y)$ and $\Phi_{22}(k_x)$, which naturally complexifies the process, but on the other hand, it does not face a problem when the wavenumber range of $\Phi_{22}(k_x)$ is large, as explained later in Section 4.8.

To determine the parameters using either the first and second approach, a least square method has been implemented. However, as the convergence of the implemented method

was not optimal, the dermination was mostly done manually.

## 4.4 Spatial distribution g(x)

A source of vorticity $\mathbf{S}_v$ can be defined as the curl of a velocity vector potential $\mathbf{\Psi}(\mathbf{x}, t)$ which automatically ensures a divergence-free flow. The mathematical developments for generating two-component turbulence in Section 4.3 assume that the spatial distribution has separable spatial variables. This condition can be fulfiled by assuming a velocity potential $\mathbf{\Psi}(\mathbf{x}, t)$ following a Gaussian distribution, as used in this work

$$\mathbf{\Psi}(\mathbf{x}, t) = Ab\sqrt{\frac{e}{2\ln 2}}\exp\left[-\ln(2)\frac{|\mathbf{x}-\mathbf{x}_c|^2}{b^2}\right]s(t)\mathbf{e}_\Psi, \tag{4.43}$$

where $b$ is the half-radius of the Gaussian, $A$ the amplitude, $\mathbf{x}_c = (x_c, y_c)$ the coordinates of the centre of the Gaussian, $s(t)$ the temporal signal and $\mathbf{e}_\Psi$ the axis of rotation. The length scale $\lambda$ of each source is assumed to be related with the half-radius $b$ by $\lambda = b/\sqrt{4\ln 2}$.

The source term is separated into the spatial distribution $\mathbf{g}(\mathbf{x})$ and the time signal $s(t)$, to read $\boldsymbol{\mathcal{S}}_v(\mathbf{x}, t) = \mathbf{g}(\mathbf{x})s(t)$, hence the spatial distribution $\mathbf{g}(\mathbf{x})$ writes

$$\mathbf{g}(\mathbf{x}) = \nabla \times \left(Ab\sqrt{\frac{e}{\ln(4)}}\exp\left[-\ln(2)\frac{|\mathbf{x}-\mathbf{x}_c|^2}{b^2}\right]\mathbf{e}_z\right) . \tag{4.44}$$

**One-component turbulence:** The proposed method for the generation of a one-component turbulence, described in Section 4.2, shows that the velocity fluctuations convected downstream of the sources are modulated by the spatial Fourier transform of the spatial component $\hat{g}_2(k_x, y)$. Thus, using the Fourier transform on the streamwise direction (i.e. on $x$-axis as the mean flow flow is uniform and parallel to the $x$-axis), we get (details of the calculation in Appendix A)

$$|\hat{g}_2(k_x, y - y_c)| = \frac{A\sqrt{e}}{\sqrt{\pi}}\left(\frac{b}{\sqrt{2\ln 2}}\right)^2 k_x \exp\left(-\frac{\ln 2}{b^2}y_c^2\right)\exp\left(-\frac{b^2}{4\ln 2}k_x^2\right), \tag{4.45}$$

which directly follows the spectral density $S(\omega)$ of the signal $s(t)$, given in Equation (4.17), to become

$$S(k_x u_0) = \frac{|u_0|}{A^2 e\pi^{3/2}}\left(\frac{\sqrt{2\ln 2}}{b}\right)^5 \frac{\Phi_{22}(k_x)}{k_x^2}\exp\left(\frac{b^2}{2\ln 2}k_x^2\right). \tag{4.46}$$

The filtering effect of the sources on the generated perturbations is minimal at $k_x = \sqrt{2\ln 2}/b$, and gets stronger as the wavenumber lowers or increases, as plotted on Figure 4.2, which shows the shape of $|\hat{g}_2(k_x, y)|$ for $b = 1$, $A = 1$ and $y = y_c$.

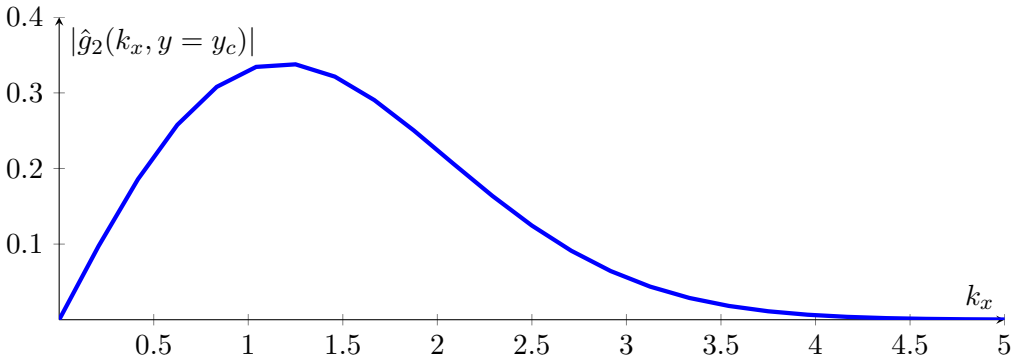


Figure 4.2: $|\hat{g}_2(k_x, y = y_c)|$ plotted for $b = 1$ and $A = 1$.

**Two-component turbulence:** As for the one-component turbulence method, the wavenumber spectrum of the velocity fluctuations convected downstream of the sources is modulated by the spatial Fourier transform of the sources, but in this case in both the streamwise and normal directions of the mean flow, as detailed in Section 4.3. The spatial Fourier transform of the sources is (details of the calculation in Appendix A)

$$\left|\begin{pmatrix}\hat{g_1}(\mathbf{k})\\ \hat{g_2}(\mathbf{k})\end{pmatrix}\right| = \frac{A\sqrt{e}}{\pi\sqrt{2}}\left(\frac{b}{\sqrt{2\ln 2}}\right)^3\begin{pmatrix}k_y\\ k_x\end{pmatrix}\exp\left(-\frac{b^2}{4\ln 2}|\mathbf{k}|^2\right). \tag{4.47}$$

Using the first approach described in Section 4.3.1, such that each set of source contributes to the whole spectrum $\Phi_{22}(k_x)$ in term of wavenumber range, but only at a reduced amplitude ratio $a_l$, Equation (4.39) becomes

$$S_l(k_x u_0) = a_l \frac{|u_0|}{A^2 e \pi^{3/2}}\left(\frac{\sqrt{2\ln 2}}{b_l}\right)^5 \frac{\Phi_{22}(k_x)}{k_x^2}\exp\left(\frac{b_l^2}{2\ln 2}k_x^2\right), \qquad \text{with} \quad \sum_l^{N_l} a_l = 1\ , \tag{4.48}$$

and Equation (4.40)

$$\Phi_{11}(k_y) = \int_{\Re}\frac{\Phi_{22}(k_x)}{k_x^2}\mathrm{d}k_x \sum_l^{N_l} a_l \frac{b_l}{\sqrt{\pi\ln 2}}k_y^2\exp\left(\frac{-b_l^2}{2\ln 2}k_y^2\right). \tag{4.49}$$

## 4.5 Discrete distribution of vortices

In a finite difference code, using a continuous distribution of sources requires a large amount of computational resources, thus the impact of a restricted number of sources is discussed in this section. In this work, each continuous distribution of sources discretized in a finite number of sources with the same spatial distribution is denoted as a group of sources.

The continuous distributions of sources are discretized by superposing $N_s$ evenly spaced Gaussian distributions over a chosen spatial extent in the normal-direction. By doing so, the resulting energy is modified when setting a restricted number of vorticity

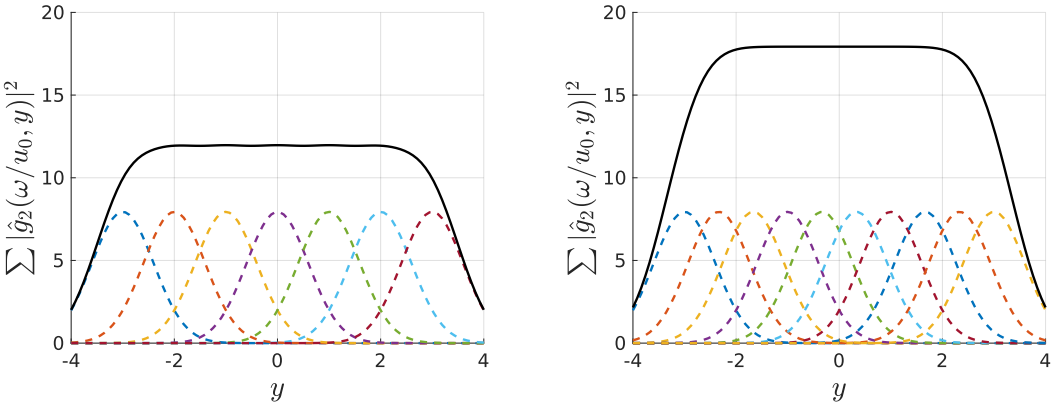


(a) 7 sources (b) 10 sources

Figure 4.3: Amplitude of $\sum |\hat{g}_2(\omega/u_0, y)|^2$ at an angular frequency $\omega_0$ as a function of the y-direction (——) for (a) 7 and (b) 10 sources evenly spaced in the y-direction between $-3 \leq y \leq 3$. The dashed lines in represent the contribution of each individual vorticity source.

sources compared to a continuous distribution as plotted in Figure 4.3. To retain the same amount of energy, the amplitude parameter $A$ in equations (4.17) and (4.39) for respectively the one- and two-component turbulence are corrected.

**One-component turbulence :** The amplitude parameter $A$ in equations (4.17) becomes

$$A = \sqrt{\frac{b_l}{\sqrt{2\ln 2}}\sqrt{\pi}\left[2\sum_{j=0}^{\infty}\exp\left(-\frac{\ln 2}{b^2}(jd)^2\right) - 1\right]^{-1}}, \tag{4.50}$$

where $d$ is the distance (in the transverse direction relative to the mean flow) between each source.

If the distance $d$ between the sources is too large, the amplitude of $\hat{g}_2(k_x, y)$ will vary a lot, thus the turbulent energy will vary as a function of the transverse direction $y$. The amplitude of these variations can be calculated using

$$\text{Variation (in \%)} = 100\left(\frac{\sum_{j=-\infty}^{\infty}\exp\left(-\frac{\ln 2}{b^2}(jd)^2\right)}{\sum_{j=-\infty}^{\infty}\exp\left(-\frac{\ln 2}{b^2}\left(\frac{d}{2} - jd\right)^2\right)} - 1\right). \tag{4.51}$$

To limit these variations to less than 1%, the distance $d$ between each source should be smaller than $1.5b$.

**Two-component turbulence :** The amplitude parameter $A$ in equations (4.39) becomes

$$A_l = \sqrt{\frac{b_l}{\sqrt{2\ln 2}}\sqrt{\pi}\left[2\sum_{j=0}^{\infty}\exp\left(-\frac{2\ln 2}{b_l^2}(jd_l)^2\right) - 1\right]^{-1}}, \tag{4.52}$$

where $d_l$ is the distance (in the transverse direction relative to the mean flow) between each source of the same set $l$.

To ensure the proper realisation of the prescribed turbulence spectra, using a trial and error process, that the distance $d_l$ between the center of each source should be smaller than $0.9b_l$.

## 4.6 Construction of the temporal signal $s(t)$

For the one- and two-component turbulence, the method relies on the generation of a time signal $s(t)$ which respects the given spectral density $S(\omega)$. In this work, an inverse Fourier transform based method [101] is used. It reconstructs a discrete time signal $s_n = s(t_n)$ which achieves the spectral density $S(\omega)$ through

$$s_n = \frac{1}{N}\sum_{m=0}^{N-1} \hat{s}_m \mathrm{e}^{2\pi \mathrm{i} mn/N}, \qquad \text{with } \hat{s}_m = \sqrt{2\pi N^2 \Delta f S(\omega_m)}\mathrm{e}^{+\mathrm{i}\phi(\omega_m)} \ , \tag{4.53}$$

where the power spectral density $S$ directly calibrates the magnitude of the Fourier coefficients $\hat{s}_m$. The phase $\phi$, associated with each discrete frequency $\omega_m$, is randomly generated between 0 and $2\pi$ using a uniform probability distribution, with the additional constraint that $\phi(-\omega_m) = -\phi(\omega_m)$ to obtain a real-valued signal. Other techniques could also be used, such as the generation of non-Gaussian signals using non-linear transformations [102], or the Fourier-wavelet method [103].

The resulting discrete temporal signal $s_n = s(t_n)$ is then used to form the vorticity source $\boldsymbol{\mathcal{S}}_v(\mathbf{x}, t_n) = \mathbf{g}(\mathbf{x})s(t_n)$.

## 4.7 Implementation

In this work, each source of vorticity is defined as $\boldsymbol{\mathcal{S}}_v(\mathbf{x}, t) = \mathbf{g}(\mathbf{x})s(t)$, where the functions $\mathbf{g}$ and $s$ are handled separately. For ease of implementation, it is chosen to compute the functions $s$ beforehand the CAA simulation. The computation of these time signals $s(t)$ is quick as only an inverse Fourier transform is needed, as explained in Section 4.6 (Equation 4.53). For instance, the signals $s(t)$ of 100 sources, with a von Karman wavenumber velocity spectrum, considering $2^{18}$ time-step, take less than two minutes to be generated on a single core. Once computed, the values of $s$ are stored in a file where each line corresponds to a time-step of the upcoming CAA simulation, allowing for a sequential read during the simulation.

Then, in the initialisation process of the CAA simulation, the functions $g$ are computed and stored in the RAM memory. As a result, to inject the prescribed turbulence in the

CAA simulation, at each time-step, the functions $s$, which are read from the previously created file, are multiplied by the functions $g$ and then added to the right hand side of the governing equations. The cost of such operation can be approximated to a multiplication plus an addition for each source of vorticity. Moreover, away from the center of each source, the amplitude of the function $g$, defined in Section 4.4, becomes negligible. Hence, to reduce the computational cost, the multiplication and addition operations can be truncated in space.

For $N_s$ sources of vorticity, the right-hand side of the governing equations are written

$$\text{RHS of the governing equations } = \sum_{i}^{N_s} \mathbf{g}_i(\mathbf{x}) s_i(t) \ , \tag{4.54}$$

where $\mathbf{g}_i$ and $s_i$ denote respectively the spatial distribution and time signal of the $i$th source. However, for the one-component turbulence, proposed in Section 4.2, each source of vorticity has the same realisation of the spectral density $S(\omega)$, i.e. the time signals $s_i(t)$ are identical and can be reduced to a single time signal $s(t)$. Therefore, Equation (4.54) becomes

$$\text{RHS of the governing equations } = \underbrace{\left( \sum_{i}^{N_s} \mathbf{g}_i(\mathbf{x}) \right)}_{\mathbf{g}_{\text{equiv}}(\mathbf{x})} s(t) \ . \tag{4.55}$$

Hence, the generation of one-component turbulence can be reduced to the computation of a single source of vorticity with a spatial distribution $\mathbf{g}_{\text{equiv}}(\mathbf{x}) = \sum_i^{N_s} \mathbf{g}_i(\mathbf{x})$, which speeds up the simulations compared to multiple-source cases.

## 4.8 Computational limitation on the wavenumber range

To generate prescribed perturbations in the transverse direction of the mean flow, the amplitude of the time signal $s(t)$ directly depends on the half-radius $b$ of the source, via the term

$$\frac{1}{k_x^2} \exp\left( \frac{b^2 k_x^2}{2 \ln 2} \right) \ , \tag{4.56}$$

in both equations (4.46) and (4.48), respectively for the one- and two-component turbulence.

For a fixed half-radius $b$, the minimum of Equation (4.56) is for $k_x = \sqrt{2 \ln 2}/b$. Away from this specific streamwise wavenumber, this term increases to tend to infinity when the streamwise wavenumber $k_x$ is either quasi-zero or tends to infinity, as plotted in Figure 4.4. As a result, depending on the prescribed perturbations, the time signal $s(t)$ can reach very large values.

While this is theoretically not a problem, it is limiting computationally. Indeed, in a computer, a variable is limited in its range of possible values, depending on its data type

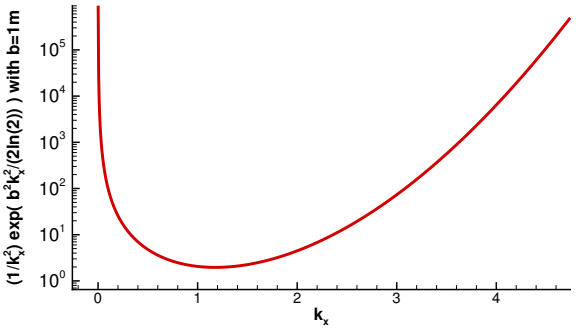


Figure 4.4: Evolution of $\exp\left(b^2k_x^2/(2\ln 2)\right)/k_x^2$ as a function of $k_x$, with $b = 1$ m.

and the number of bits used to represent it. Hence, if the term in Equation (4.56) and by extension the time signal $s(t)$ is very large, the variable in the CAA solver which stores the $s(t)$ might not be able to properly represent it, resulting in unpredictable values.

To tackle this problem, one solution, already presented in Section 4.3.2, consists in splitting the streamwise wavenumber range of $\Phi_{22}(k_x)$ into $N_l$ groups, as plotted in Figure 4.1b. Each group being independent of each other, they can then have a different half-radius $b_l$, depending on the range of $k_x$ to generate.

## 4.9 Verification of the method

To verify the proposed method, two free-field simulations in an uniform mean flow are considered. The first one focuses on the generation of a one-component turbulence, and the second on a two-component turbulence.

The CAA solver PIANO uses non-dimensionalized variables. Hence, the computation is non-dimensionalized using the static density $\rho_\infty = 1$ kg.m$^{-3}$, the static speed of sound $a_\infty = 340$ m.s$^{-1}$ and an arbitrary length $L_{\text{ref}} = 1$ m. The considered computational domain extends between $0 \leq x \leq 7$ and $-5 \leq y \leq 5$ and is discretized with a uniform spacing $L_{\text{ref}}\Delta x = L_{\text{ref}}\Delta y = 0.02$. The mean flow velocity is uniform, oriented in the $x$-direction, with a Mach number $M = 0.5$. The time step $\Delta t$ is set to $(a_\infty/L_{\text{ref}})\Delta t = 0.012$, which gives a CFL number of 0.9, and the simulation is run over $2^{19}$ iterations. Such a large number of iterations is used for validation purposes, to average the wavenumber spectrum on multiple segments by performing a periodogram. An asymptotic outflow boundary condition [91] is used on the downstream boundary, and asymptotic radiation boundary conditions [91] on the others. To prevent spurious oscillations to develop in the domain, a 8$^{\text{th}}$-order explicit filter is applied at every time step.

The generated turbulence $\Phi_{22}(k_x)$ modelled by a von Karman spectrum, using a turbulent integral length scale $\lambda = 0.1L_{\text{ref}}$ and a turbulence intensity $T_I = \sqrt{\overline{u_2'}^2/u_\infty^2} = 2.5\%$,

| One-component turbulence | $A/(a_\infty L_{\text{ref}})$ | $b/L_{\text{ref}}$ | $N_s$ |
|---|---|---|---|
| Group 1 | 0.27822 | 0.25 | 30 |

| Two-component turbulence | $A/(a_\infty L_{\text{ref}})$ | $b/L_{\text{ref}}$ | $N_s$ | $a_l$ |
|---|---|---|---|---|
| Group 1 | 0.49154 | 0.25 | 30 | 0.4103 |
| Group 2 | 0.41334 | 0.18 | 42 | 0.3590 |
| Group 3 | 0.29410 | 0.09 | 82 | 0.2308 |

Table 4.1: Parameters of the sources of vorticity for the one- and two-component turbulence verification cases.

can be expressed by:

$$\Phi_{22}(k_x) = \frac{\overline{v'^2}\lambda}{6\pi} \frac{3 + 8\tilde{k}_x^2}{\left[1 + \tilde{k}_x^2\right]^{11/6}} \quad ; \quad \tilde{k}_x = \frac{k_x}{k_e} \quad ; \quad k_e = \frac{\sqrt{\pi}}{\lambda} \frac{\Gamma(5/6)}{\Gamma(1/3)} , \tag{4.57}$$

where $\Gamma(.)$ is the gamma function. The discretization of the spectrum is realized between $k_{x_{\min}} L_{\text{ref}} = 2$ to $k_{x_{\max}} L_{\text{ref}} = 20$.

Regarding the verification of the one-component turbulence, all the sources have the same spatial distribution $g$, i.e. the same half-radius $b$ (see Table 4.1). On the other hand, for the two-component turbulence, three groups of spatial distribution are used to achieve a similar spectrum between $\Phi_{11}(k_y)$ and $\Phi_{22}(k_x)$ from a wavenumber $kL_{\text{ref}} = 7$ to 17. The vorticity sources are evenly spaced on a line, normal to the mean flow, at $x/L_{\text{ref}} = 1.5$ from $y/L_{\text{ref}} = -3.5$ to 3.5 and 300 velocity sensors located at $x = 6.5$ from $y/L_{\text{ref}} = -3$ to 3 record the velocity fluctuations as the gusts convect. The parameters used in both cases are listed in the Table 4.1.

One realization for each different source of the time signal $s(t)$ for the two-component turbulence, generated using a method based on the Fourier transform (section 4.6), is plotted in Figure 4.5. It clearly shows the density spectrum $S$ affected by the spatial Fourier transform of the spatial component. The filtering effect is especially visible on the source with $b/L_{\text{ref}} = 0.25$, where the density spectrum highly compensates for high-wavenumber perturbations, such that one realization of the temporal signal $s(t)$ for this source has dominant high-wavenumber components, with a large amplitude.

The instantaneous $y$-velocity fluctuations for the two simulations are plotted in Figure 4.6. It shows the turbulence generated at the vorticity source locations, on the desired $y$-extent and convected downstream by the uniform mean flow. Moreover, the solution does not seem to be contaminated by reflections on the downstream boundary.

To check the turbulence properties inside the computational domain, the instantaneous velocity perturbations are recorded. The velocity spectrum $\Phi_{11}(k_y)$ is computed from the two-point correlation $R_{ij}$ using the unsteady values of the sensors. However, while it can also be used to obtain $\Phi_{22}(k_x)$, a property of frozen turbulence is used instead. Indeed,

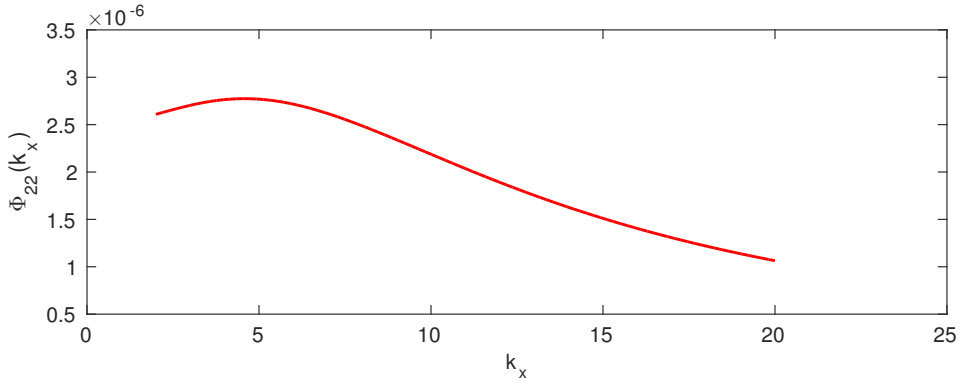


(a) Desired wavenumber spectrum of the fluctuating velocity $\Phi_{22}(k_x)$

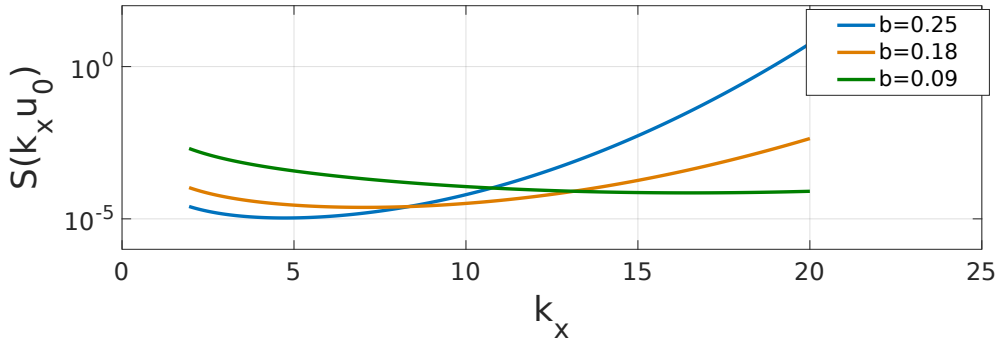


(b) Corresponding spectral density of the temporal signal $S(k_x u_0)$

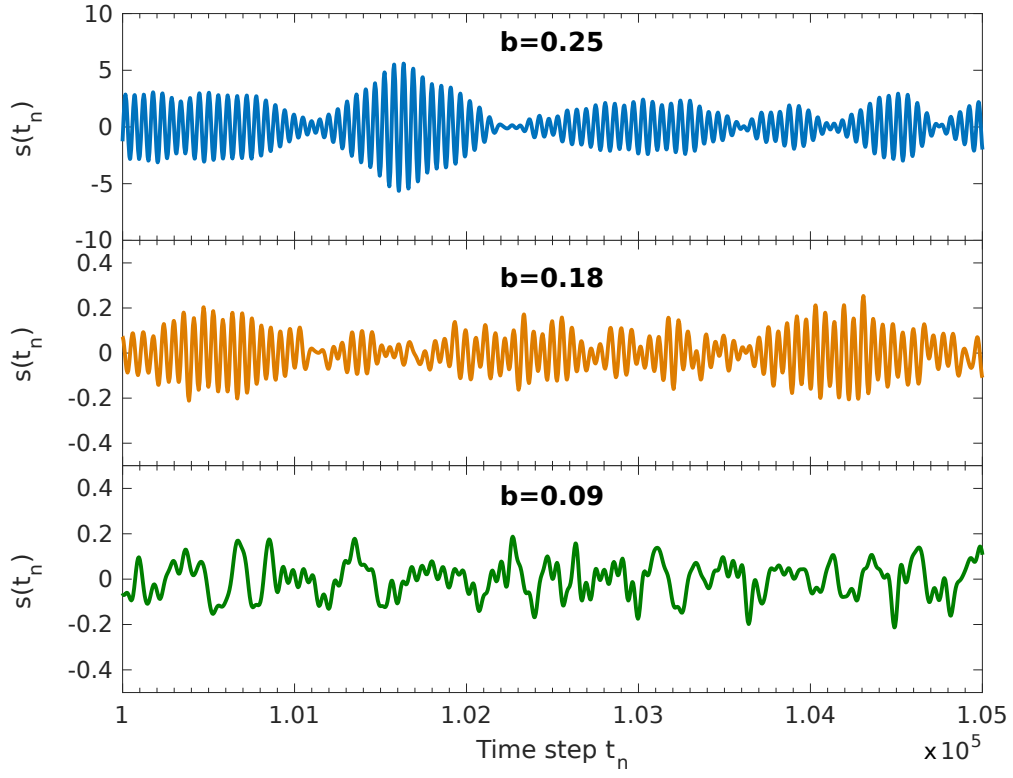


(c) One realization of $s(t_n)$ for a source with a half-radius $b = 0.25$, $b = 0.18$ and $b = 0.09$.

Figure 4.5: Generation of the temporal signals $s(t_n)$ for the vorticity sources.

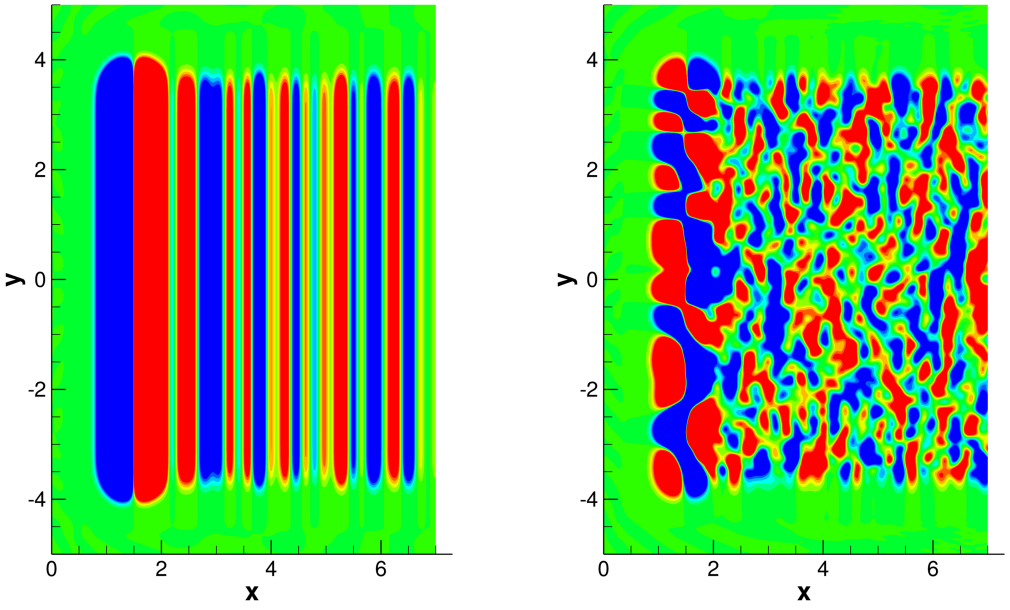


(a) (b)

Figure 4.6: Instantaneous transverse velocity fluctuations for the one- (a) and two-component (b) verification simulations, plotted between $u_2^{'*} \pm 0.01$.

the spectral density of each sensor, labelled $S_{\text{sensor}}(\omega)$, is directly linked to $\Phi_{22}(k_x)$ by

$$S_{\text{sensor}}(\omega = ku_0) = \frac{\Phi_{22}(k_x)}{u_0}, \tag{4.58}$$

which simplifies the calculation. The spectral density is calculated using a periodogram, arbitrary chosen with 80 segments and an overlap of 50%. The velocity spectrum $\Phi_{11}(k_y)$ and $\Phi_{22}(k_x)$ derived from the two simulations are plotted in Figure 4.7. It shows a good agreement in terms of wavenumber limits and amplitudes between the prescribed and simulated spectra.

## 4.10 Application to flat plate interaction noise

In this section, the developed method to inject synthetic turbulence is applied on flat plate interaction case. This case is identical to the one used to verify the use of vorticity sources for interaction noise, in Chapter 3, with the difference that the gusts are no longer harmonic but broadband. Only the third flat plate configuration is studied in this section, to limit the spurious oscillations located at the singularities. The set-up, described in Section 3.7, consists in a plate with a round leading edge, with a thickness of 1% of the chord $c$ and the grid has a C-mesh structure with a minimum grid element $\Delta x_{min}$ is $0.001c$ (1/1000 of the chord) at the leading edge.

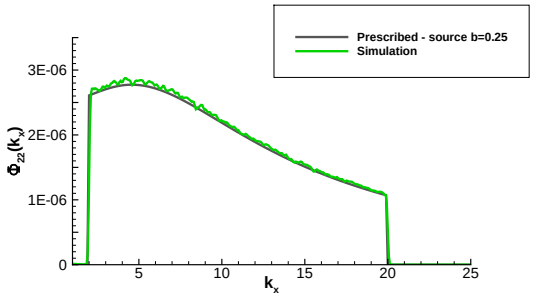


(a) One-component turbulence : $\Phi_{22}(k_x)$

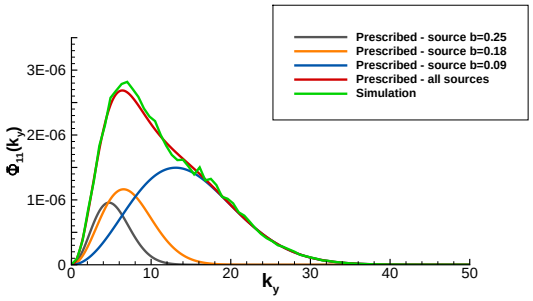


(b) Two-component turbulence : $\Phi_{11}(k_y)$

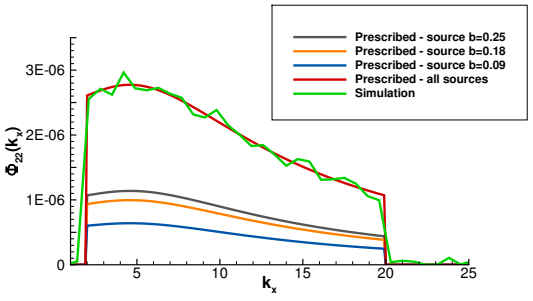


(c) Two-component turbulence : $\Phi_{22}(k_x)$

Figure 4.7: Measured spectra against theoretical turbulent velocity spectra in the computational domain, for the one- (a) and two-component (b)(c) turbulence.

In the Amiet model for a flat plate [60], only the normal component of the velocity perturbations is important. Following this approach, a one-component turbulent gust is generated using the previously described method, and calibrated to respect a von Karman wavenumber spectrum. The parameters of the spectrum are a turbulent intensity $T_I = 4.56\%$ and an integral length scale $\lambda c = 0.18$. The streamwise wavenumber range of the injected spectrum is limited from $k_x c = 4$ to 12. Indeed, high wavenumbers are numerically limited by the mesh to avoid wavenumber aliasing and low wavenumbers require a simulation to be run for a large number of time step in order to properly retrieve the low wavenumber fluctuations.

The Overall Sound Pressure Level (OASPL), which represents the total energy contained in the Sound Pressure Level (SPL) for each angle, is plotted in Figure 4.8a. It shows the directivity of the acoustic field at $R = 2c$ around the flat plate. A good agreement is found for all direction with the Amiet model [60]. The RMS pressure along the flat plate also is in good agreement with the Amiet model [60], shown in Figure 4.8b. Moreover, it does not show spurious fluctuations at the leading edge or trailing edge, which is consistent with the harmonic cases studied in Section 3.7.

As the model is linear and the amplitude of the gusts are small, the contribution of each wavenumber composing the turbulent gust can be retrieved using a Fourier transform. For instance, one can obtain the directivity around the flat plate at different wavenumber, as plotted in Figure 4.9 for three wavenumbers ($k_x c = 4$, 8, and 12). The behaviour is

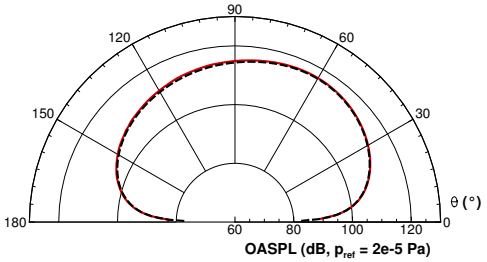


(a) Broadband directivity

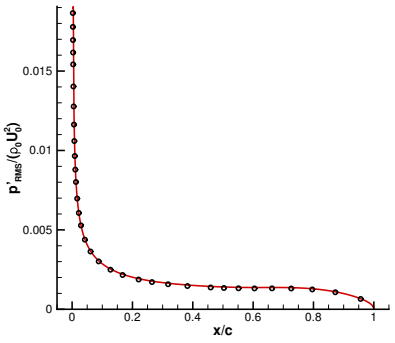


(b) Broadband RMS pressure along the flat plate

Figure 4.8: Broadband directivity of the acoustic field at $R = 2c$ around the flat plate (a) and broadband RMS along the flat plate (b).

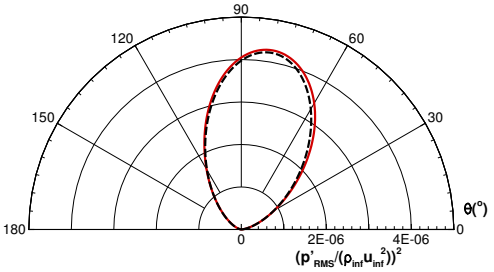


(a) $k_x c = 4$

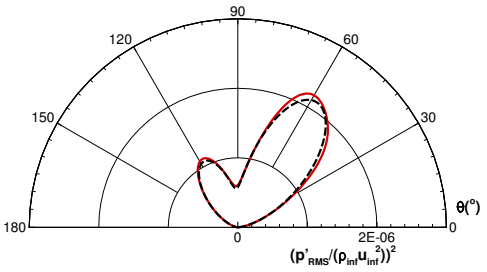


(b) $k_x c = 8$

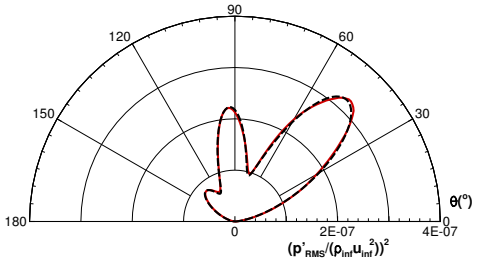


(c) $k_x c = 12$

Figure 4.9: 1% thickness plate with $\Delta x_{\min} c = 0.001$ - (a) (b) (c) directivity of the acoustic field at $R = 2c$ around the flat plate: (—) numerical results and (—) Amiet model

similar to the results observed with a harmonic gust (Chapter 3), which is consistent with the linearity of LEE model.

## 4.11 Conclusion

In this chapter, a new method to inject synthetic turbulence in a computational domain using localized vorticity sources has been developed. The proposed method is very similar to SEM or RPM as it consists of a sum of vortices. Hence, compared to Fourier modes it is less demanding in computational resources when the number of modes considered is large. To inject the velocity perturbations inside the domain, unlike a windowing function or an inlet boundary, the proposed method uses localized vorticity sources which makes it very easy to implement and has no influence on the parallelization of a already existing CAA solver. However, as the perturbations can not be controlled once injected, the generated turbulence is frozen, which can be a problem depending on the application. As described, the proposed method can be used to generate either one-component or two-component turbulence. For the two-component turbulence, it allows to independently control the turbulent spectrum in the two directions, thus it could be used to synthesize isotropic turbulent fields as well as anisotropic turbulent fields. The method is verified in a free-field simulation, where the gusts are naturally convected by the mean flow. Afterwards, the method is applied to flat plate interaction noise and successfully compared to the Amiet model for a flat plate [60]. As expected, the results are consistent with the results found in Chapter 3 where only harmonic gusts were considered.

This method could be extended to three-component turbulence by having multiple sources spaced on a plan, transverse to the mean flow velocity. Mathematically, the derivation is similar to the two-component turbulence (Section 4.3) and shows that the synthesized turbulence is, as for the two-component turbulence, anisotropic. However, to control the properties of the synthesized three-component turbulence, the number of parameters to determine is naturally higher than with the two-component turbulence method proposed in Section 4.3.

The proposed method can also, in theory, be extended to amplitude modulation, for instance to model wake passages. It could be performed by modulating the levels of the time signal $s(t)$ of each source, accordingly to the desired modulation. Moreover, as the spatial distribution of the sources $g$ are not altered, the divergence-free condition would still be respected. Nevertheless, the developments have not been performed.

However, in the presence of a solid boundary near the injection region, for instance to study trailing edge noise as performed by Ewert *et al.* [57] using RPM, this method might not be suitable. Indeed, in this work, the spatial distribution of a source of vorticity $\mathbf{g}(\mathbf{x})$ is defined as the curl of a Gaussian-distributed velocity potential. It implies that the amplitude of $\mathbf{g}(\mathbf{x})$ decays from the center of the source. Nevertheless, if the distance

between a solid surface and the center of a source is small, the amplitude of $\mathbf{g}(\mathbf{x})$ at this surface might not be negligible, hence not respecting the divergence-free condition and potentially generating spurious acoustic sources. To avoid this problem, the half-radius $b$ of the sources can be decreased so that the decay of $\mathbf{g}(\mathbf{x})$ is quicker. However, there are numerical limitations in which values the half-radius $b$ can be, as discussed in Section 4.8. Another approach to avoid this problem could be to use a different velocity potential distribution. However, if the spatial variables $\mathbf{x}$ in $\mathbf{g}(\mathbf{x})$ are not separable any more, some mathematical steps for the two-component turbulence in Section 4.3 are no longer valid.

# Chapter 5

# Aerofoil interaction noise

For interaction noise, the effects of aerofoil geometry can not be neglected at high wavenumbers [61, 63], therefore a flat plate is not a valid assumption for a realistic 2D outlet guide vanes. In this work, the numerical method presented in Chapter 4 is assessed on the Fundamental test Case 1 (FC1) from the Fan Stage Broadband Noise Benchmark Programme [104]. It focuses on the noise generated by a turbulent velocity field impinging an isolated NACA 65(12)-10 aerofoil with a chord of $c = 0.15$ m with an incoming free stream velocity of $u_\infty = 60$ m.s$^{-1}$. To validate the noise predictions obtained with this numerical method, experiments were performed in the anechoic wind tunnel facility within the ISVR [99].

The multiple stages in this numerical approach serve as the structure of the first sections of this Chapter. The first step consists in calculating the averaged flow around the aerofoil. For aerofoils, a uniform mean flow does not represent the reality, hence, a more representative mean flow is required to obtain more accurate noise prediction. Indeed, the importance of the mean flow is investigated in this Chapter using three different mean flows: a uniform, an inviscid and a viscous mean flow. Inviscid mean flows take into account the geometry but as the flow is not viscous, it unrealistically slips on objects and therefore no boundary layer is present. Viscous flow simulations are a close approximation of the real mean flow, but the presence of large velocity gradients in the boundary layers can lead to numerical instabilities which can be difficult to tackle.

The synthetic turbulence is the second step in this numerical approach. The characteristics of the incoming turbulence are extracted from experiments performed at the ISVR and follow a von Karman spectrum with a turbulence intensity of 1.7% and an integral length scale of 8 mm. As mentioned in Chapter 3, the Amiet model for a flat plate in a uniform mean flow [60] shows that only the normal component of the fluctuating velocity contributes to interaction noise. To assess the validity of this hypothesis for aerofoils, simulations with either one- or two-component turbulence are carried out.

Once the mean flow and incoming turbulence are set, they are used as an input for the CAA simulation. The implications of these inputs on the setup are discussed. To limit the computational resources, an acoustic analogy is used to propagate the noise to the far-field, which allows the CAA domain to be restricted to the source region only.

To compare the noise predictions with experiments, as the mean flow assumptions do not include the jet to limit numerical instabilities, the shear layer effect on the acoustic radiation is corrected. Moreover, as the simulation is in 2D, the acoustic radiation is also corrected to take into account the propagation in the third direction.

## 5.1 Noise predictions using 2D simulations

### 5.1.1 Mean flow

The mean flow provides information on the convection of the perturbations and, as seen later in this Chapter, it is essential to give accurate noise predictions using the LEE model.

In experiments, the presence of the jet of the wind tunnel has been shown to have an influence on the loading of the aerofoil [105, 106]. To validate the mean flow setup with experiments, a first case with the jet is simulated. However the presence of a jet imply the presence of shear layers and then significant velocity gradients which can be a source of linear instabilities in the LEE. Then a second calculation without the jet is performed. In this free flow case, there is no deflection of the flow as in the jet configuration, thus the $15^o$ angle of attack is corrected to $4.21^o$, as calculated by Gruber [3]. These two calculations are performed by solving the RANS equations, thus, the boundary layer developing on the surface of the aerofoil will induce strong velocity gradients. When interpolated (performed with a linear method to the 1st order) on the CAA mesh (see section 5.1.3) where the cell size in the vicinity of the aerofoil is large compared to the RANS mesh, these gradients can introduce instabilities leading to the divergence of the computation. To tackle this issue, the third configuration considered is similar to the second one (free stream), but steady Euler's equations are solved instead of RANS. Since the flow is allowed to slip on the aerofoil surface with Euler's equations, the velocity gradients in this region are expected to be less important. The meshes are designed to ensure a cell size at the wall such that the dimensionless wall distance[1] $y^+ \leq 1$. The cells are stretched with an expansion ratio less than 15% and the grids extend up to 30 chords in the normal and downstream directions. For the free stream cases, the upstream extent is also 30 chords, whereas it is only one chord for the configuration including the jet due to the presence of the nozzle (note also that the nozzle has a 0.15 $m$ height).

[1] $y^+$ defined as $y^+ \equiv (y\, u_*)/\nu$ with $y$ the distance to the nearest wall, $u_*$ the friction velocity at the nearest wall and $\nu$ the local kinetic viscosity.

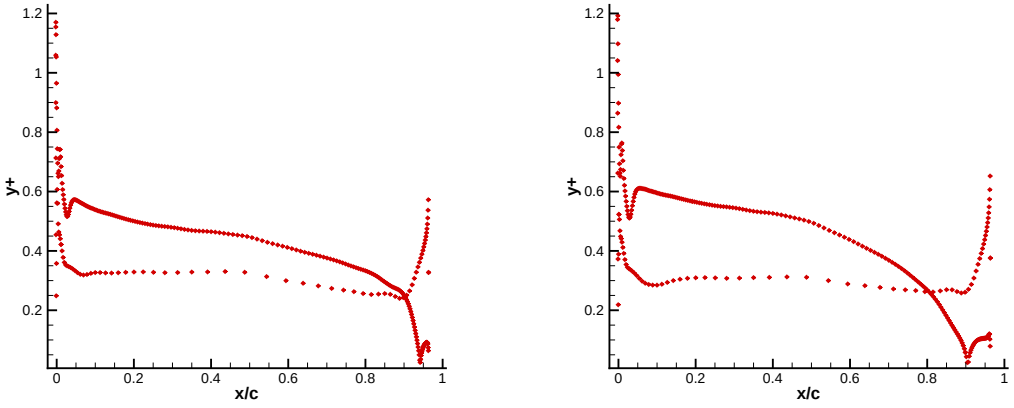


(a) Jet configuration

(b) Freestream configuration

Figure 5.1: Evolution of the normal cell size at the aerofoil surface in wall units ($y^+$) (a) in the jet configuration and (b) in free stream configurations.

The meshes contain about $1.3.10^5$ points for the jet configuration and $7.5.10^4$ points for the free stream configurations. The parameters of the different meshes are summarized in Table 5.1. The turbulence model used for the calculations is a SST $k-\omega$ model [107].

All the mean flow simulations have been done performed using the commercial software ANSYS Fluent[2], using the pressure-based solver, with a second-order spatial discretization.

| Configuration | Eq. solved | $\alpha$ | $x$-extent | $y$-extent | Grid points |
|---|---|---|---|---|---|
| Jet | RANS | $15^o$ | $-c \leq x \leq 30c$ | $-30c \leq x \leq 30c$ | 131 576 |
| Free stream 1 | RANS | $4.21^o$ | $-30c \leq x \leq 30c$ | $-30c \leq x \leq 30c$ | 76 252 |
| Free stream 2 | Euler | $4.21^o$ | $-30c \leq x \leq 30c$ | $-30c \leq x \leq 30c$ | 76 252 |

Table 5.1: Parameters of the different meshes for the 3 configurations considered for the mean flow calculations.

The evolution of the normal cell size in wall units ($y^+$) along the aerofoil surface, plotted in Figure 5.1 for the two configurations where the RANS equations are solved, is shown to have values inferior or close to unity.

The pressure coefficients obtained in the jet configuration are in good agreement (in Figure 5.2) with the experiments conducted by Gruber *et al.*[2, 3], where the nozzle outflow is of height 0.15 m and at a distance of 0.15 m from the leading edge.

The mean velocity in the $x$-direction and pressure fields are shown in Figure 5.3, 5.4 and 5.5, respectively for the RANS with the jet, the RANS in free-field and the Euler in free-field simulations. The confinement effect due to the presence of the jet is clearly visible in Figure 5.3 compared to the free stream configurations. In the Euler computation, the

[2]ANSYS Fluent : www.ansys.com

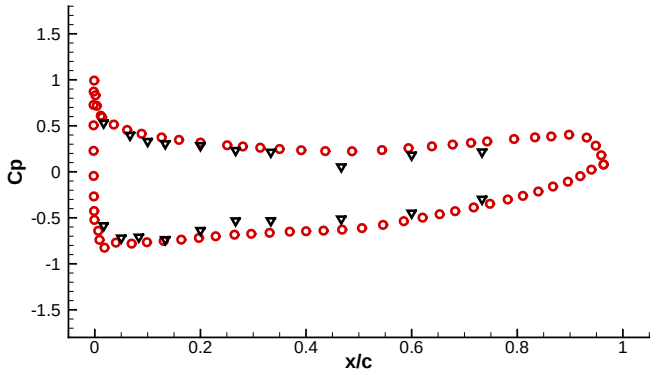


Figure 5.2: Comparison of the pressure coefficient along the aerofoil between the RANS simulation in a jet configuration (○) and the experiments conducted by Gruber *et al.*[2, 3] (▽).

absence of boundary layer is observable, especially on the suction side of the aerofoil, as well as the absence of wake downstream of the aerofoil.

### 5.1.2 Synthetic turbulence

To compare the noise predictions with experiments, similar turbulence characteristics are imposed in the numerical simulations. The incoming turbulence is modelled by a one-wavenumber von Karman spectrum, using the integral length scale and the turbulence intensity extrapolated from experiments conducted by Gruber *et al.*[2, 3], respectively $\lambda = 8\text{mm}$ and $T_I = \sqrt{\overline{v'^2}/u_\infty^2} = 1.7\%$. It can be expressed by

$$\Phi_{22}(k_x) = \frac{\overline{v'^2}\lambda}{6\pi} \frac{3 + 8\tilde{k}_x^2}{\left[1 + \tilde{k}_x^2\right]^{11/6}} \quad ; \quad \tilde{k}_x = \frac{k_x}{k_e} \quad ; \quad k_e = \frac{\sqrt{\pi}}{\lambda} \frac{\Gamma(5/6)}{\Gamma(1/3)} , \tag{5.1}$$

where $\Gamma(.)$ is the gamma function.

To limit the computational requirements, the frequency range of the turbulence injected inside the CAA domain is limited to the non-dimensionalized Strouhal numbers[3] $0.75 \leq \text{St} \leq 25$, which is equivalent for this baseline case to frequencies ranging from 300 Hz to 10 kHz. Indeed, injecting very low frequencies require a CAA simulation to run for a long solution time, while very high frequencies require CAA meshes to be very fine, and by extension a smaller associated time step, increasing both the total number of iterations and the computing time for each time step. Moreover, to also limit the mesh size requirements, the incoming turbulence is only injected on a limited vertical extent, from $y = -0.25c$ and $y = 0.25c$. The turbulence is injected at a distance $x = -2.75c$ upstream the leading edge, where the viscous and inviscid mean flows are uniform.

[3]Strouhal number defined as $\text{St} = (f\,c)/u$ with $f$ the frequency, $c$ the chord of the aerofoil and $u$ the free stream velocity

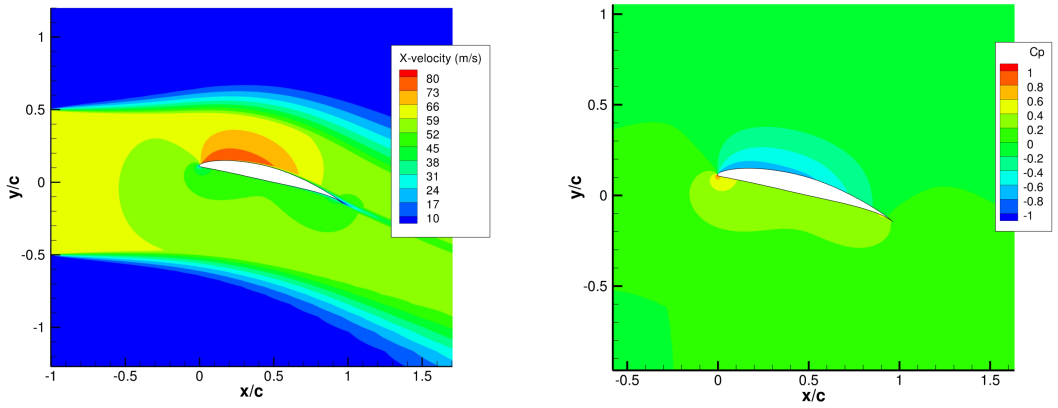


Figure 5.3: RANS solution for the jet configuration. ($a$) Velocity in the $x$-direction and ($b$) pressure coefficient.

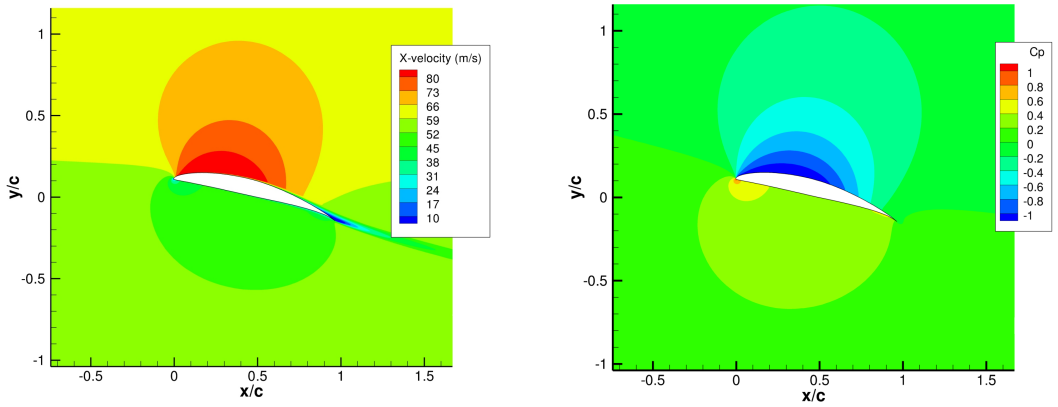


Figure 5.4: RANS solution for the free stream configuration. ($a$) Velocity in the $x$-direction and ($b$) pressure coefficient.

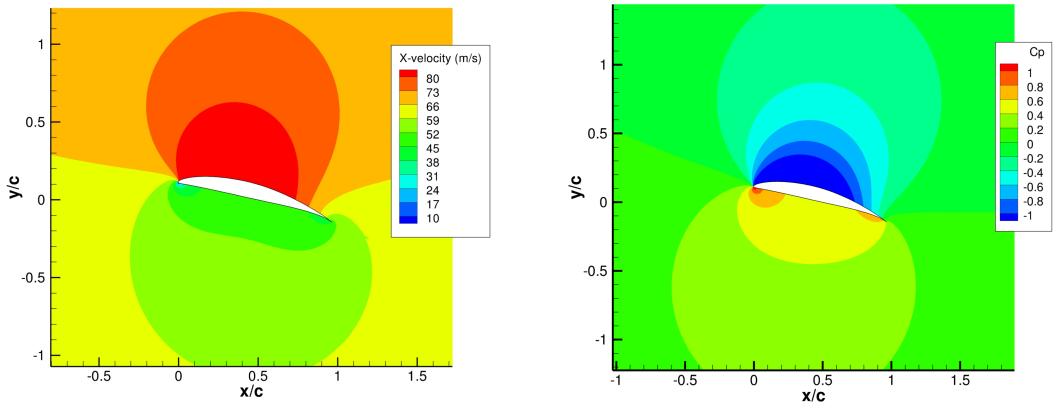


Figure 5.5: Steady Euler solution for the free stream configuration. ($a$) Velocity in the $x$-direction and ($b$) pressure coefficient.

The Amiet model for a flat plate in a uniform mean flow [60] only requires the normal component of the fluctuating velocity to evaluate interaction to the far field. To assess the validity of this hypothesis for aerofoils, simulations with either an incoming one- or two-component turbulence are carried out.

The one-component turbulence is injected using sources of vorticity located upstream of the aerofoil, all modulated by the same time signal $s(t)$, as discussed in Section 4.5. 50 sources are evenly spaced between $y = -0.25c$ and $y = 0.25c$, each source having a half-value radius $b = 0.027c$ and being spaced by a distance $0.01c$. These parameters are chosen to limit the variation in amplitude of $\Phi_{22}(k_x)$ in the transverse direction using Equation (4.51), and to limit the amplitude required in the time signal $s(t)$ to compensate the filtering effect of the sources, as discussed in Section 4.8.

The two-component turbulence is injected using three groups of sources, for the same $y$-extent as the one-component turbulence, between $y = -0.25c$ and $y = 0.25c$. The total of 68 sources are divided up 15 sources with a half-radius $b = 0.214c$, 16 sources with a half-radius $b = 0.043c$ and 37 sources with a half-radius $b = 0.018c$. Similarly, these parameters are chosen to respect the minimal distance required between each source and to limit the amplitudes of the time signals $s_l(t)$, as explained in Sections 4.5 and 4.8.

### 5.1.3 Aeroacoustic simulation

The CAA mesh supports the turbulence convection upstream of the aerofoil, as well as the acoustic waves resulting in the turbulence-aerofoil interaction. The equations are linear, hence the maximum frequency the mesh has to support is given by the highest frequency of the injected turbulence i.e. 10 kHz. The acoustics waves are supported over a distance of two chords away from the aerofoil in every direction while the velocity perturbations are properly discretized only from the injection plane to the trailing edge of the aerofoil. The total extent of the mesh is however larger as it goes up to 4 chords away from the profile, which slowly dissipate the higher frequencies before reaching the boundaries. For the larger wavelengths, asymptotic radiation boundary condition [91] is applied on the upstream, top and bottom boundaries of the computational domain, and asymptotic outflow boundary condition [91] on the outflow boundary. These boundaries conditions are derived from asymptotic solutions of the linearised Euler equations to let acoustic waves leave the domain while minimizing reflections. The outflow boundary condition also allows hydrodynamic structures to exit the domain. The grid stretching ratio has been kept under 3% to avoid the appearance of numerical spurious oscillations due to the use of a high-order finite difference scheme. The mesh contains approximately $6.10^5$ points and has been split to run parallel computations on up to 128 processors. In practice, for this 2D case 32 or less cores would have been sufficient.

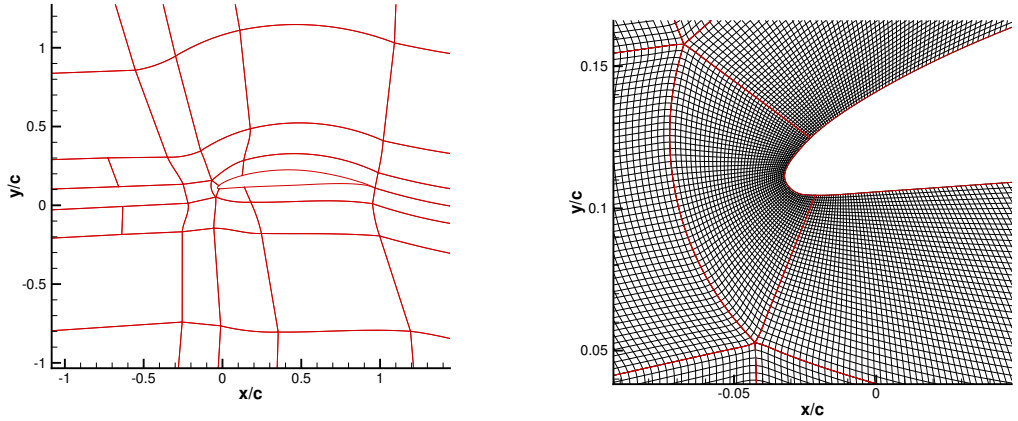


(a) Representation of the mesh splitting into multiple blocks around the aerofoil.

(b) Zoom of the mesh near the leading edge.

Figure 5.6: CAA mesh for the FC1 case. The red lines (—) represent the location of the mesh blocks.

The computation is non-dimensionalized using a reference length $L_{\text{REF}} = 1$ m, the static speed of sound $a_\infty = 340$ m/s and the static density $\rho_\infty = 1.2$ kg/m$^3$. The chord of the aerofoil $c$ is $c = 0.15L_{\text{REF}}$. The non-dimensionalized time step of the simulation is $5.2.10^{-5}$, corresponding to a maximum local CFL number of 0.9 at the leading edge and a mean CFL in the simulation of 0.08.

In the CAA simulation with the viscous mean flow, the boundary layer on the profile leads to high velocity gradients which are potential linear instabilities. Hence, the value of the first four cells of the CAA mesh, starting from the profile, are duplicated in order to reduce the velocity gradient. This technique has already being used [59, 108] with no noticeable effect on the radiated acoustic field. However, with this method, most of the boundary layer is removed as shown in Figure 5.7, therefore, the difference with an inviscid mean flow is small. Nevertheless, some high velocity gradient are still present, for instance at the wake of the aerofoil which can lead to linear instabilities, as shown in Figure 5.8. To address this issue, a local sponge zone is applied in the trailing edge region, so that these hydrodynamic modes are dissipated. The value and shape of this local sponge zone have been determined on a flat plate configuration so that its value can damp the instability without affecting the acoustic response.

To estimate the response of the aerofoil in the farfield while limiting the size of the computational domain, a Ffowcs-Williams Hawking (FWH) analogy in the frequency domain [109, 110] is used. This is an exact rearrangement of the general Navier-Stokes equations with the assumption that the source region is limited within a control surface. It simplifies to a non homogeneous wave equation with equivalent sources located on the control surface that will generate the same acoustic field as if the full Navier-Stokes equations were solved. These equivalent sources are separated into monopole $Q$, dipole

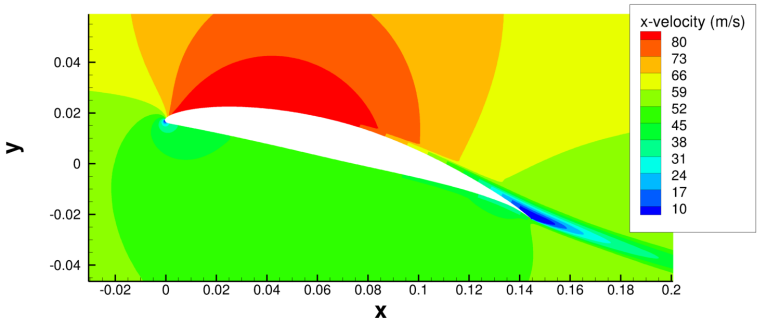


Figure 5.7: $x$-velocity of the viscous mean flow with the boundary layer treatment.

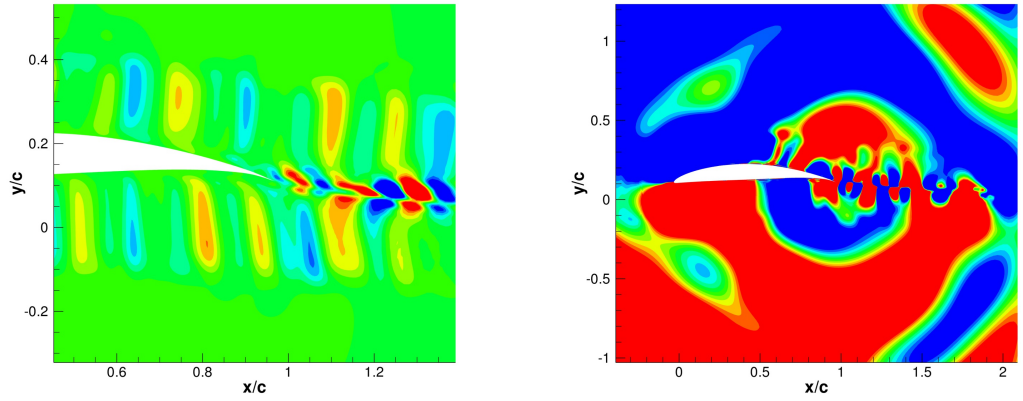


(a) Instantaneous transverse velocity perturbation contour between $\pm 2.7$ m.s$^{-1}$.

(b) Instantaneous pressure perturbation contour between $\pm 1.4$ Pa.

Figure 5.8: Instantaneous transverse velocity and pressure perturbation fields with no specific treatment at the trailing edge.

$F$ and quadrupole $T$ terms. If the control surface contains all the acoustic sources, the quadrupole term can be neglected. Further details on the FWH analogy and its formulation can be found in Appendix B.

It is important to note that vortical structures crossing the extrapolation surface of the FWH analogy can cause spurious acoustic sources [111]. However, in this work, the turbulence is injected between the upstream FWH control surface and the aerofoil, and downstream of the aerofoil, the mesh is designed to damp the hydrodynamic structures. Therefore, only acoustic perturbations cross the FWH control surface.

### 5.1.4 Benchmark case results

The noise predictions considering the three mean flow assumptions, namely uniform, inviscid and viscous, are presented in this section. After the initial transient, the computations are run over $2^{18}$ iterations, taking about 40 minutes with the one-component

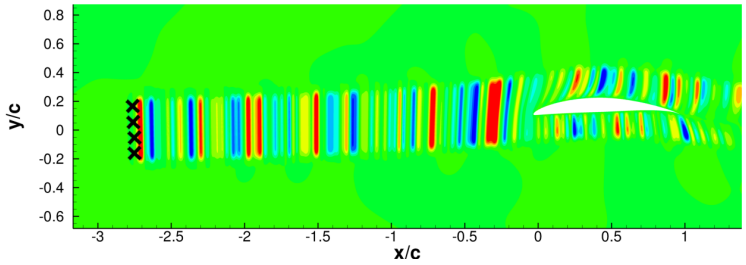


(a) One-component turbulence.

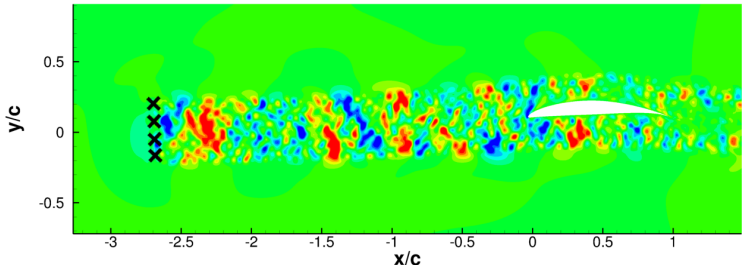


(b) Two-component turbulence.

Figure 5.9: FC1 case: Instantaneous transverse velocity for with (a) one- and (b) two-component turbulence contour between $\pm 1 \mathrm{m.s}^{-1}$. The black crosses denotes the location of turbulence injection.

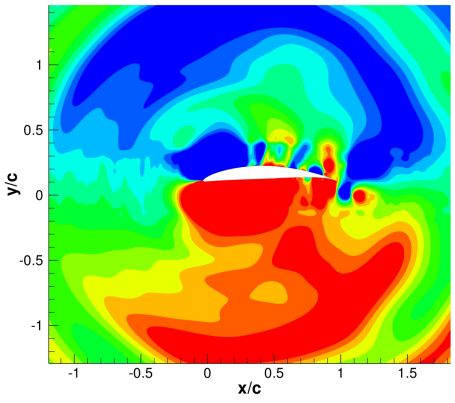


Figure 5.10: FC1 case: Instantaneous pressure perturbation contour between $\pm 4$Pa.

turbulence, and about 1 hour with the two-component turbulence on 128 Intel® Xeon® E5-2670 processor cores. The instantaneous normal velocity fields for a viscous mean flow with one- and two-component turbulence are presented in Figure 5.9. We can observe the turbulent gusts generated upstream of the profile, in between the inlet boundary and the leading edge, with a limited extent in the $y$-direction, and being convected by the mean flow.

The pressure fluctuations, plotted in Figure 5.10, show the expected dipole pattern of the acoustic response of the aerofoil. As mentioned before, using the viscous mean flow

the hydrodynamic modes are scattered by the trailing edge, but the local sponge layer seems to prevent them from radiating.

A set of 720 equally spaced sensors are located on a circle centred on the leading edge, with a radius of 1.7 chords, to record the perturbations and perform the FWH analogy (described in Appendix B). The spectra are averaged over 15 segments using a Hann window and a 50% overlap. For this profile with no angle of attack, the one- and two-component turbulence give the same noise predictions as plotted on Figure 5.11a which shows the SPL at 1.2 m and 90° (above the aerofoil), using a viscous mean flow. This corroborates the assumption made by Gill [61] that a one-component turbulence is satisfactory to predict interaction noise of a profile with no angle of attack.

The numerical predictions using a one-component turbulence with the three mean flow assumptions are compared with the analytical results of the Amiet model which considers a flat plate [60]. Figure 5.11b shows the SPL at 1.2 m and 90° (above the aerofoil), for the three mean flow configurations, and the Amiet model. We can see that the mean flow has little effect on low frequencies, but as the frequency increases, the rate of decay is more pronounced for the inviscid and viscous mean flows. Indeed, for these two configurations, the mean flow close to the leading edge distorts the incoming turbulence. This distortion is more important as the length scale is small. This distortion is investigated in Chapter 6. The noise prediction using a uniform mean flow shows an overestimation at low frequencies, which differs from previous similar simulations [61, 63, 59]. However, no further investigation was performed due to the unrealistic nature of the mean flow. The difference between the inviscid and viscous mean flows is negligible at low frequencies and remain very small at higher frequencies. This is due to the fact that the differences between inviscid and viscous flows are restricted to the boundary layer region, which has a weak influence on the noise generation mechanism [61, 63]. Indeed, interaction noise mainly depends on the region around the leading edge, as shown in Chapter 6. It is also due to the specific treatment performed on the boundary layer of the viscous mean flow, to reduce the high-velocity gradient to prevent linear instabilities, as detailed in Section 5.1.3.

At high frequencies, the upstream directivities (Figure 5.12) computed from the simulations, are tilted compared with the Amiet solution. The angle between the local mean flow velocity and the camber line of the aerofoil can explain this. In section 5.2.1, an investigation is presented regarding the change in angle of attack.

### 5.1.5 Comparison with experiments

The numerical results obtained are compared to the ISVR-rig measurements performed by Paruchuri *et al.* [99], using a profile with a span $L$ of 0.45 m. To compare the numerical results obtained from a 2D simulation with experiments, two elements have

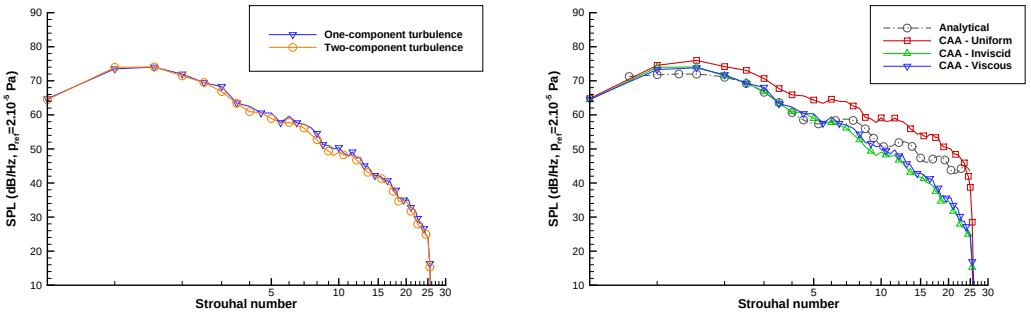


(a) One- and two-component turbulence using a viscous mean flow.

(b) One-component turbulence with different mean flow assumptions.

Figure 5.11: SPL at 90°above the aerofoil, at R=1.2 m.

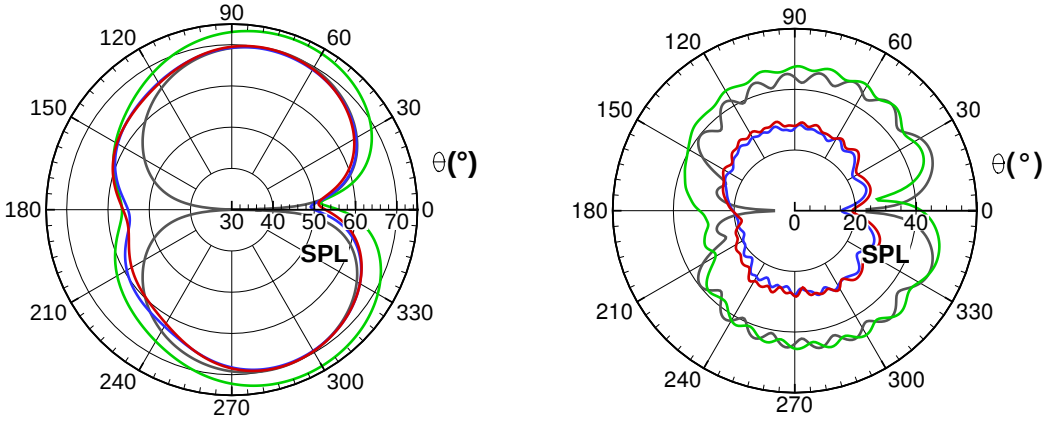


(a) St = 2.5

(b) St = 22.5

Figure 5.12: Directivity at R=1.2m using a uniform (——), inviscid (——) and viscous (——) mean flow assumption, against the Amiet model for a flat plate (——). SPL plotted in dB/Hz, using a reference pressure $p_{\text{ref}} = 2.10^{-5}$ Pa.

to be taken into consideration. Firstly, the acoustic propagation differs in 3D, as the acoustic energy also propagates in the third dimension. Fortunately, if the 3D effects are low (it is the case for an aerofoil with a span large relative to the chord), the pressure fluctuations obtained from a 2D simulation can be duplicated along the span to have a 3D configuration, resulting in correlated sources on the span $L$. Dieste *et al.*[39] then deduced a correction to estimate a 3D far field acoustic pressure $S_{pp}^{3D}$ from a 2D $S_{pp}^{2D}$ result by comparing the 2D and 3D Amiet formulations:

$$S_{pp}^{3D}(x,y,0,\omega) = \frac{k l_y(\omega) L}{\pi\sigma} S_{pp}^{2D}(x,y,\omega) \qquad \text{with } l_y(\omega) = \frac{8\lambda}{3}\left(\frac{\Gamma(1/3)}{\Gamma(5/6)}\right)^2 \frac{\tilde{k}_x^2}{(3+8\tilde{k}_x^2)\sqrt{1+\tilde{k}_x^2}}, \tag{5.2}$$

where $\omega$ is the angular frequency, $k = \omega/c_0$ is the free-field acoustic wavenumber, $k_x = \omega/u_0$ is the hydrodynamic wavenumber in the streamwise direction, and $\sigma = \sqrt{x^2 + (1-M^2)y^2}$. $l_y(\omega)$ is the span-wise correlation length scale.

The second effect to account for in order to compare the numerical free-field results with experiments comes from the setup of the experiments. Indeed, the microphones are located outside the jet flow of the test-rig, thus a shear layer between the aerofoil and the microphones is present. This shear layer affects the radiation direction and the amplitude of the acoustic waves, as shown in Figure 5.13. In the present work, the corrections proposed by Amiet [4] have been used. Assuming that the shear layer has no thickness, that the distance from the source to the observer before and after the correction remain constant ($r_m = r_c$) and that the distance from the source to the shear layer is small compared to distance of the observer ($h \ll r_m$), Amiet writes for the change in angle

$$\Theta_c = \arctan\left(\frac{C}{\beta^2 \cos\Theta_m + M}\right) , \tag{5.3}$$

where $C = (1 - M\cos\Theta_m)^2 - \cos^2\Theta_m$ and $\beta^2 = 1 - M^2$ with $M$ the Mach number. To address the change in amplitude, Amiet writes the correction factor $A_c$

$$A_c = \frac{\sqrt{1 + M^2C^2}}{2}\left[\frac{C}{\sin\Theta_m} + (1 - M\cos\Theta_m)^2\right] . \tag{5.4}$$

These corrections shows that the corrected angle $\Theta_c$ gets more shifted as the Mach number increases, and the amplitude factor $A_c$ gets more significant at angles away from 90°.

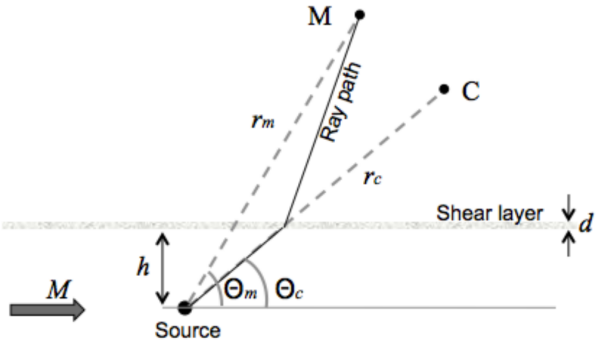


Figure 5.13: Sketch of the refraction of sound by a shear layer [4]

The experimental measurements can only be compared to the simulation within a limited extent of the spectrum where leading-edge noise is dominant. At low frequency, the noise generated by the turbulent grid used to generated desired turbulent flows, as well as the jet noise from the wind tunnel are dominant compared to interaction noise. At the other end of the spectrum, at high frequency, the self noise (or trailing edge noise) becomes dominant. To identify the frequency range where leading edge interaction noise is dominant, two additional experiments are run. The first additional experiment is run without the aerofoil, therefore the jet noise and grid generated noise can be measured. Then, a second experiment is run with the aerofoil, but without any turbulent grid, which gives the aerfoil self noise.

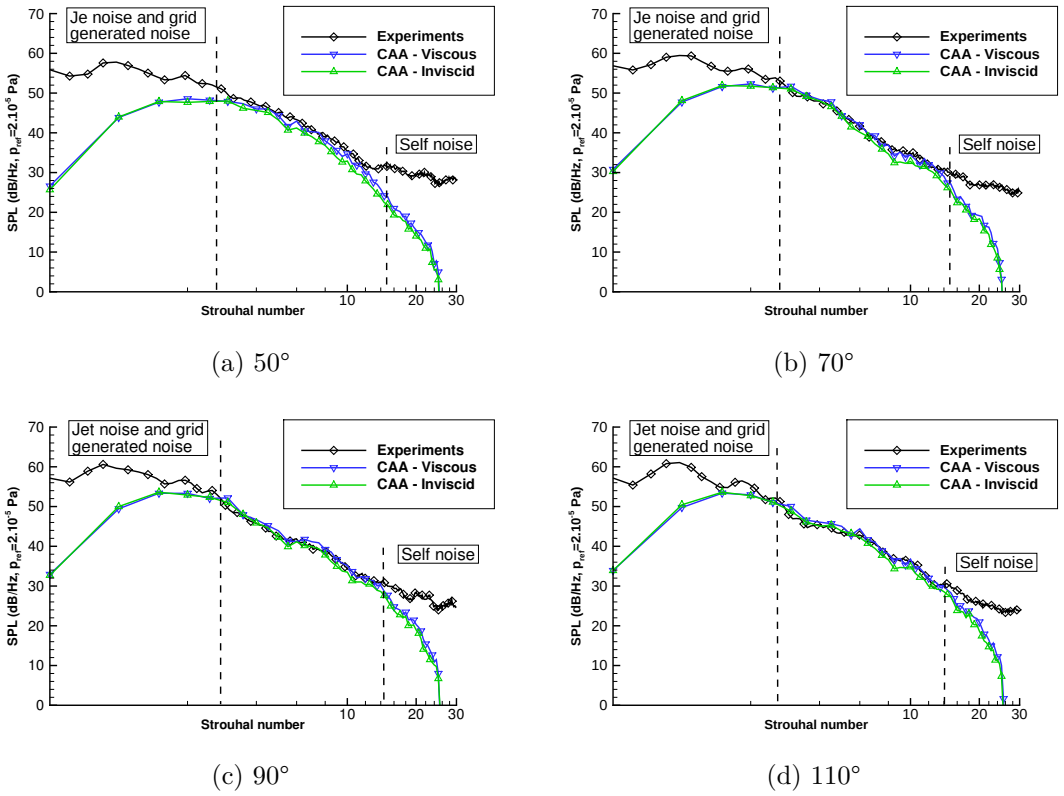


(a) 50° (b) 70°

(c) 90° (d) 110°

Figure 5.14: Comparison of the 2D numerical predictions using the inviscid and viscous mean flow configuration (corrected for the acoustic propagation in 3D and the shear layer refraction effect) with experimental measurements.

The SPL computed from the numerical solutions are compared to the experimental results in Figure 5.14 for four directions, from 50° to 110°. The low and high frequency limits mentioned before, where the leading edge noise is dominant are represented on the graph by the vertical dashed lines. The numerical predictions show very good agreement with experiments. Similar remarks can be made on the directivities plotted in Figure 5.15 for different frequencies. It is important to mention that no data rescaling has been applied.

## 5.2 Parametric study

In this section, the effects of the Angle of attack (AoA) and the integral length scale $\lambda$ are studied.

### 5.2.1 Angle of attack

Simulations have been run for several angles of attack between 0° and 3°, using the same aerofoil and flow conditions as previously. For higher AoA, some numerical instabilities

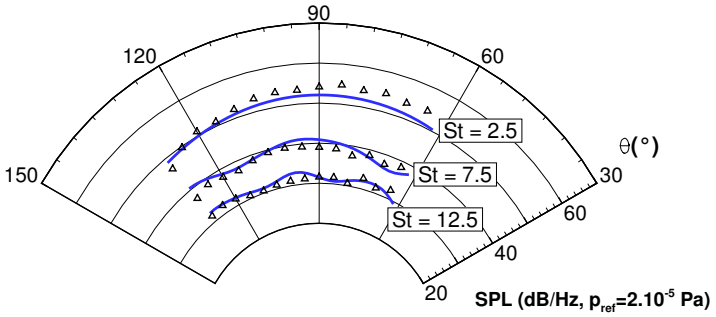


Figure 5.15: Directivity of the 2D numerical predictions using the inviscid mean flow configuration (corrected for the acoustic propagation in 3D and the shear layer refraction effect) (—) with experimental measurements (△).

appeared on the upper surface of the aerofoil with both the viscous and inviscid mean flows.

When the angle of attack is not 0°, discrepancies are visible at high frequencies between the one- and two-component turbulence, as plotted respectively on Figure 5.16a and 5.16b showing the SPL at 90°and $R = 1.2$m using a viscous mean flow. The one-component turbulence depicts a reduction of the noise radiated at high frequencies when the AoA is increased, which is not visible using two-component turbulence. It corroborates the assumption made by Gill [61] that a one-component turbulence is not satisfactory to correctly predict the radiated acoustics of a profile with an AoA. Indeed, he showed that, depending on the angle of attack and the frequency, a peak acoustic response is found at a specific $k_y$ of the turbulent energy spectrum. When there is no angle of attack, the peak response of all wavenumbers is found at $k_y = 0$, which explains why one- and two-component turbulence give similar noise predictions, but as the angle of attack increases, the peak response progressively shifts to higher $k_y$. Moreover, this shift is more important as the frequency increases.

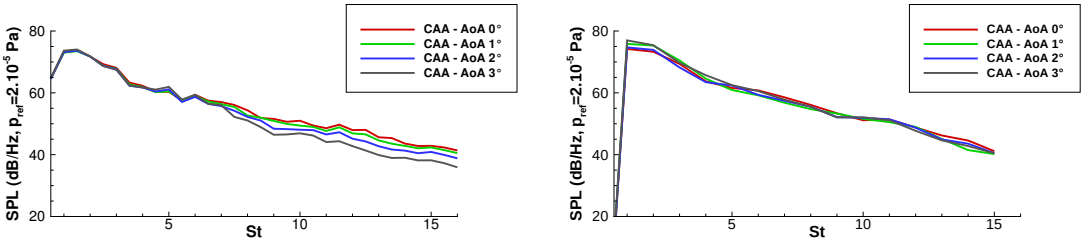


(a) One-component turbulence (b) Two-component turbulence

Figure 5.16: Comparison of the SPL at 90° above the aerofoil, at R=1.2m for profiles at an angle of attack of 0° (—), 1° (—), 2° (—) and 3° (—) using (a) one- and (b) two-component turbulence.

The directivities between the one- and two-component turbulence are similar in shape so only the predictions using one-component turbulence are shown in Figure 5.17. The directivities show very little differences at low frequency at all angles, yet at high frequency,

the upstream minimum is tilted in the clockwise direction as the AoA increases and it reaches $\theta = 0°$ for the aerofoil with 3° AoA for the highest frequency (Figure 5.17b). It could be argued that the steepest AoA considered is close to a zero angle formed between the local mean flow velocity and the camber line of the aerofoil, as previously mentioned in section 5.1.4.

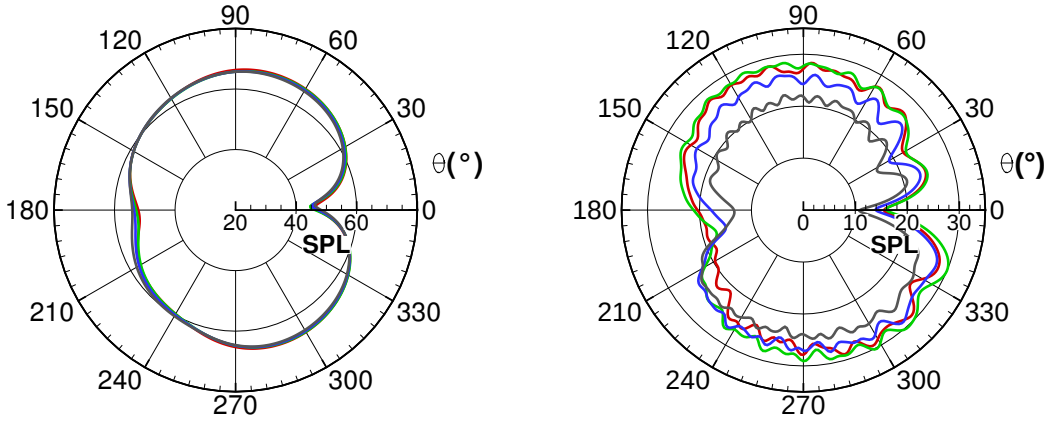


(a) St = 2.5 (b) St = 22.5

Figure 5.17: Directivity at R=1.2m for an AoA of 0°(—), 1°(—), 2°(—) and 3°(—). SPL plotted in dB/Hz, using a reference pressure $p_{\text{ref}} = 2.10^{-5}$ Pa.

### 5.2.2 Integral length scale

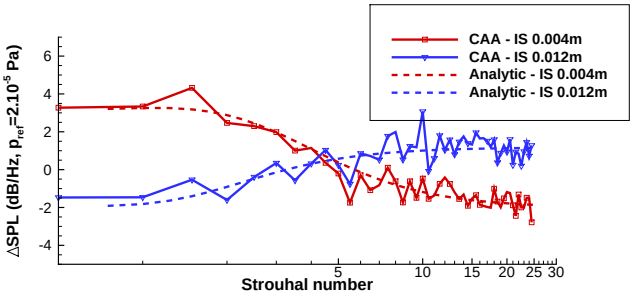


Figure 5.18: Comparison of the ΔSPL for different IS. $\Delta\text{SPL}_{\text{IS}} = \text{SPL}_{\text{IS}_{\text{ref}}} - \text{SPL}_{\text{IS}}$ with $\text{IS}_{\text{ref}} = 8$ mm. The dashed lines are the results for the Amiet model and the continuous lines are for the CAA predictions.

The turbulence is assumed to follow a von Karman energy spectrum, hence it is fully characterized by a turbulent intensity and an integral length scale. The evolution of the spectrum with the turbulent intensity is quadratic, therefore easy to predict, whereas a change of the integral length scale leads to change the distribution of turbulent energy. In this section, the impact of the integral length scale on the noise radiated is assessed using three different values: 0.004 m, 0.008 m and 0.012m. The other parameters remain the same as for the validation case with a viscous mean flow (section 5.1.3).

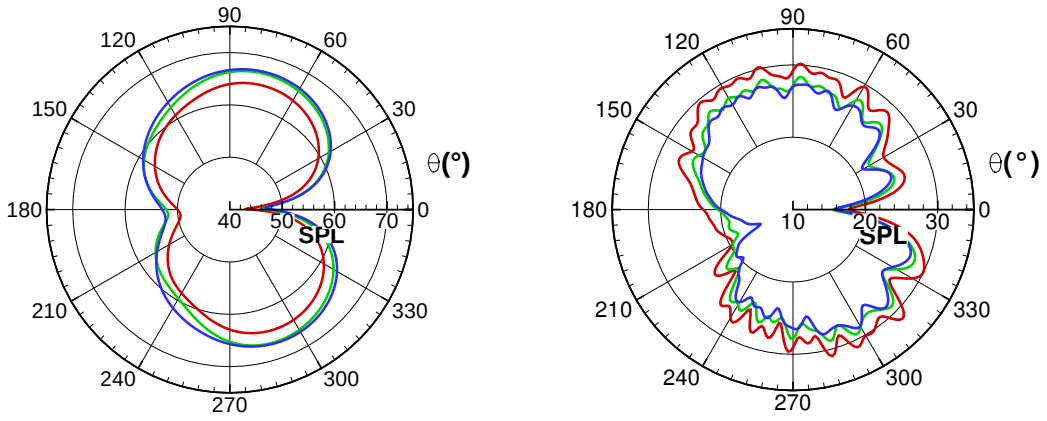


(a) St = 2.5

(b) St = 22.5

Figure 5.19: Directivity at R=1.2 m with IS = 0.004 m (——), IS = 0.008m (——) and IS = 0.012m (——). SPL plotted in dB/Hz, using a reference pressure $p_{\text{ref}} = 2.10^{-5}$ Pa.

Following Amiet's model [60] for a flat plate, the chord-wise integral of the surface loading of a flat plate with a chord $c$ and a span $2d$ is defined as:

$$\mathcal{L}(x, K_x, k_y) = \int_{-c/2}^{c/2} g(x, K_x, k_y) \mathrm{e}^{-i\omega x_0 (M - x/\sigma)/a_\infty \beta^2} \mathrm{d}x_0, \tag{5.5}$$

where $\beta = \sqrt{1 - M^2}$, $\sigma = \sqrt{x^2 + \beta^2(y^2 + z^2)}$ and $g(x, K_x, k_y)$ is the transfer function between turbulent velocity and flat plate pressure jump. The far-field PSD of a flat plate interacting with turbulent gusts can be written as [60]:

$$S_{pp}(x, y, z, \omega) = \left(\frac{\omega z \rho_\infty c}{2 a_\infty \sigma^2}\right)^2 U d\pi \int_{-\infty}^{\infty} \left[\frac{\sin^2(d(k_y + \omega y/a_\infty \sigma))}{(k_y + \omega y/a_\infty \sigma)^2 \pi d}\right] |\mathcal{L}(x, K_x, k_y)|^2 \Phi_{ww}(K_x, k_y) \mathrm{d}k_y. \tag{5.6}$$

In Equation (5.5), the surface loading response function $\mathcal{L}$ of the flat plate is wavenumber-dependent, but is independent in amplitude to the incoming turbulence spectra. Therefore, for a flat plate, changes in the turbulence spectra do not modify the loading function $\mathcal{L}$, hence every changes in the radiated noise spectra are only related to the amplitude of the incoming turbulence at each wavenumber. The comparison (Figure 5.18) of the $\Delta$SPL for different integral scales calculated as $\Delta\text{SPL}_{\text{IS}} = \text{SPL}_{\text{IS}_{\text{ref}}} - \text{SPL}_{\text{IS}}$ with $\text{IS}_{\text{ref}} =$ 8 mm (IS = integral scale), show similar trends between the numerical predictions of the cambered aerofoil and the Amiet model. Moreover, as plotted in Figure 5.19, the pattern of the directivity remain unchanged, suggesting that, as for a flat plate, the loading function of an aerofoil $\mathcal{L}$ is independent of the incoming turbulence and thus, that the changes in the acoustic radiation are only related to the changes in the spectrum of the incoming turbulence.

## 5.3 Conclusion

The new method to inject synthetic turbulence in a computational domain using localized vorticity sources, presented in Chapter 4, is applied to predict the noise resulting from the interaction of an incoming turbulence and an isolated NACA 65(12)10 aerofoil. These computations are part of the Fundamental test Case 1 (FC1) of the Fan Stage Broadband Noise Benchmarking Programme. Using 2D simulations, the noise predictions show a good agreement with ISVR-rig measurements performed by Paruchuri *et al.* [99]. It confirms that, even for realistic isolated cases, the main features of turbulence required for interaction noise are the energy spectrum, the spatial correlations and convection by the mean flow.

Using three mean flow assumptions, uniform, inviscid and viscous, it suggests that the mean flow is crucial for providing accurate noise predictions at high frequencies. Indeed, only inviscid and viscous mean flows showed good agreement with experiments. Nonetheless, it is difficult to assess the effect of the boundary layer in the mean flow on noise predictions, as in this work, a special numerical treatment to reduce the velocity gradient at the aerofoil boundary is applied on the viscous mean flow. Therefore, in this work, the differences between inviscid and viscous flows are limited, yet the good agreement with experiments suggests that the boundary layer region has a relatively weak influence on the noise generation mechanism. A study on the distortion of the turbulence with geometric parameters in Chapters 6 and 7 also suggests interaction noise mainly depends on the region around the leading edge, where the boundary layer is small.

The changes in the radiated noise with the integral length for an aerofoil, display trends that are similar to the one observed for a flat plate, suggesting that the loading of the aerofoil is only modulated with the incoming turbulence and thus, that the changes in the radiated noise are directly related to the changes in the turbulence spectrum. Also, to study a profile at an angle of attack, a one-component turbulent model is not satisfactory, as explained by Gill [61].

# Chapter 6

# Distortion of turbulence

The interaction noise model of a flat plate proposed by Amiet [60] assumes turbulent gusts convected by a uniform mean flow, and is in very close agreement with experiments [99]. To numerically study interaction noise on a flat plate, a uniform mean flow is also a correct assumption, as shown in Chapter 3, Section 3.7. However, for more complex geometries, a uniform mean flow assumption does not seem to be valid. Indeed, in Section 5.1.4 of Chapter 5, the aeroacoustic simulation of an isolated cambered NACA 65(12)-10 aerofoil showed that uniform mean flow assumptions provide poor far field acoustic predictions, especially for high frequencies, while, on the other hand, inviscid mean flow assumptions accurately predicted far-field acoustics across all frequencies. It suggests that the distortion of the incoming turbulence in the vicinity of the leading edge plays an important role in broadband interaction noise of complex profiles.

The distortion of turbulence around the leading edge can be observed by injecting a single vortex in an aeroacoustic simulation. For instance, using the isolated cambered NACA 65(12)-10 aerofoil studied in Section 5.1.4 of Chapter 5, a single vortex injected far upstream of the aerofoil becomes highly distorted in the region near the leading edge, as plotted on Figure 6.1

The importance of the distortion of the incoming turbulence by the mean flow has been seen experimentally [99] and numerically [62] by looking at the impact of the nose radius and thickness on the radiated noise. Recently, Santana *et al.* [112] tried to improve the analytical prediction of the far-field sound generated by a turbulent field interacting with a NACA0012 aerofoil by evaluating the distortion of the turbulence near the leading edge. The evaluation of the up-wash turbulence is done with the Rapid Distortion Theory (RDT) [113] which describes the effect of the mean flow on the turbulence.

Nevertheless, analytical methods developed to estimate interaction noise are restricted by assumptions made on the geometries and flow solution, and experimental studies are limited by technical difficulties to collect data. Therefore, numerical simulations seem

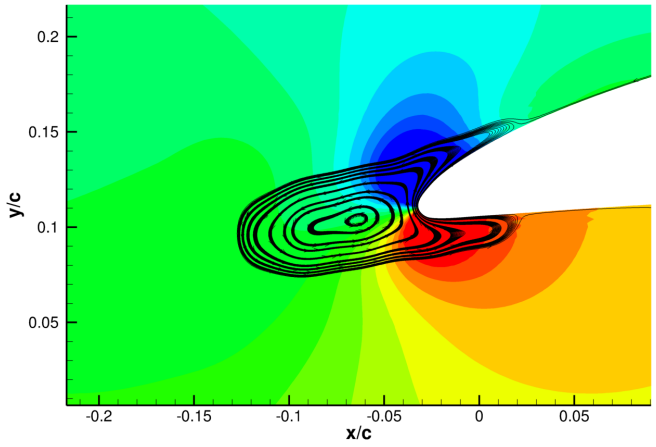


Figure 6.1: Pressure perturbation contour around the leading edge of a single vortex impinging a NACA 65(12)-10 aerofoil. The black lines depict the streamlines of the vortex.

to be an adequate solution as it is possible to record any variable at any location in the computational domain in the same simulation and at every time step if necessary. Previous numerical studies [114, 62] however mainly focused on qualitative observations only such as the size of the stagnation region or the curvature of the streamline at the leading edge. Instead of investigating the distorted turbulence spectra, Glegg *et al.* [115] directly calculated the unsteady loading of an aerofoil in incompressible turbulent flows using panel methods, and Lysak *et al.* [116] predicted the high-frequency response using the vortex lift theory [117].

To simplify the study of turbulence distortion, instead of considering cambered aerofoils with an angle of attack as in Chapter 5, a more simple symmetric NACA0012 aerofoil without an angle of attack is considered in this Chapter. The same numerical implementation of the LEE model as in previous Chapters is used to study the distortion of turbulence by the mean flow on a single streamline which starts upstream of the profile to stop at the stagnation point. From this simulation, it shows that at an upstream threshold distance common to all wavenumbers, the levels of the up wash velocity fluctuations in the transverse direction start to decrease uniformly, independently of the wavenumber. After a second threshold distance, much closer to the leading edge, which is wavenumber dependent (i.e. proportional to the hydrodynamic wavelength), the decay is inverted at low wavenumbers and only slowed at high wavenumbers.

To better understand this distortion and have more physical insights, a vorticity-based boundary element numerical approach is then used. Similar methods have been already used by Grace [118], Glegg *et al.* [115] or Lysak *et al.* [116], but without looking at turbulence distortion by the mean flow. The proposed method shows that turbulence distortion is the result of three terms. The first term describes the contribution of the

incoming vorticty distorted by the mean flow. The second and third terms, represent respectively the induced velocity of the aerofoil and of the wake vortices, which can be viewed as the vorticity response from the aerofoil to the incoming vorticity around it, such that the no-penetration condition is respected. This method is finally verified against the LEE model. Using both the LEE model and the vorticity-based boundary element, a parametric study is then carried out in Chapter 7.

## 6.1 Linearised Euler approach

### 6.1.1 Computational setup

This Chapter focusses on the distortion of the turbulence in the vicinity of the leading edge of a symmetric NACA0012-63 profile, with a chord of $c = 0.1$ m, at no angle of attack and an incoming free stream velocity of $u_\infty = 60$ m.s$^{-1}$. The choice of a modified NACA 4-digit aerofoils is motivated by the possibility to independently control the size of the leading edge radius $R_{\mathrm{LE}}$, the thickness $t$ and the chordwise position of maximum thickness $m$ (in tenths of chord), which will be extensively used in the parametric study in Chapter 7. Usual NACA 4-digit have a fixed maximum thickness located at 30% of the chord, and the leading edge radius is directly proportional to the square of the thickness ($R_{\mathrm{LE}} \propto t^2$). Hence, usual NACA0012 aerofoils are denoted NACA0012-63 using the modified NACA 4-digit aerofoil notation. The symmetric modified NACA 4-digit profiles are written as [119]

$$\text{NACA } 00\underbrace{12}_{t} - \underbrace{6}_{I}\underbrace{3}_{m},$$

where $I$ is the leading edge index which directly relates to the size of the nose radius, and is given by [119]

$$R_{\mathrm{LE}} = \frac{1.1019}{36}\left(\frac{t}{c}\,I\right)^2 , \tag{6.1}$$

As the mean flow defines the streamlines along which the velocity fluctuations are convected, a correct estimation is required. However, in a CAA simulation, the presence of shear layers, boundary layers or significant velocity gradients can be a source of linear instabilities in the LEE. In this Chapter, a steady Euler solver provides the mean flow,hence there is no physical boundary layers on the aerofoil as the flow slips on the surfaces. The CAA computations are more stable while being satisfactory to study broadband interaction noise [61, 5]. Moreover, the computational domain for the mean flow simulation is sufficiently large to limit blockage effects (blockage ratio of 3%).

The CAA mesh, plotted in Figure 6.2, has an extent of $x = -0.5$ to 0.6 m and $y = \pm 0.5$ m and is divided in 64 blocks to allow a parallelization of the computation. It

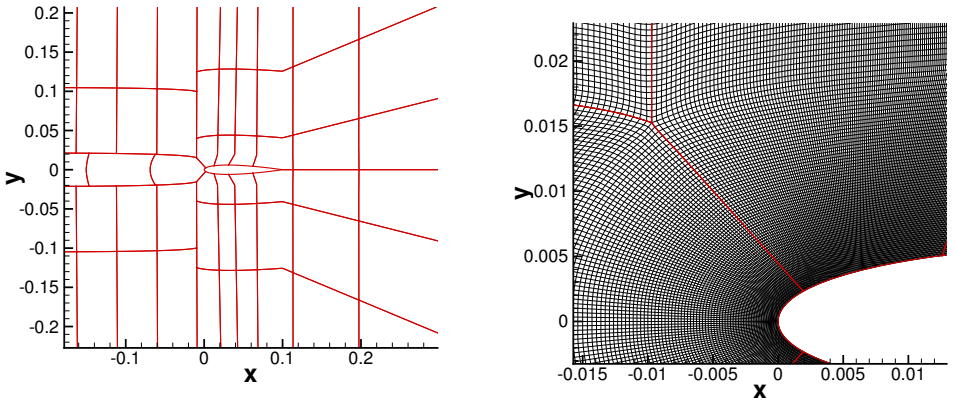


(a) Representation of the mesh splitting into multiple blocks around the aerofoil.

(b) Zoom of the mesh near the leading edge.

Figure 6.2: CAA mesh of the NACA0012-63 case. The red lines (—) represent the location of the mesh blocks.

has been designed to support hydrodynamic and acoustic waves up to 8kHz, considering 12 points per wavelength, for velocities ranging from 60 m/s to 140 m/s. The acoustic waves are resolved everywhere in the domain while the hydrodynamic waves are only well resolved upstream the aerofoil, over a limited $y$-extent, to convect the turbulent gusts. To prevent unwanted reflections at the boundaries, asymptotic radiation boundary conditions [91] are applied on the upstream, top and bottom boundaries of the computational domain, and an asymptotic outflow boundary condition [91].

The turbulence is injected through vorticity sources located upstream of the aerofoil, at a distance $x = -2c$ from the leading edge, where the mean flow is uniform. As discussed in Chapter 4, a row of vorticity sources is modulated in amplitude to generate a prescribed one- or two-component turbulence.

### 6.1.2 Instantaneous and acoustic results

After the transitional period, the computations are run over $2^{18}$ iterations, taking about 1 hours on 64 Intel ® Xeon ® E5-2670 processor cores. The instantaneous normal-velocity perturbations for the one- and two-component turbulence are presented in Figure 6.3. We can observe the turbulent gusts generated upstream of the profile, in between the inlet boundary and the leading edge, with a limited extent in the $y$-direction, and being convected by the mean flow. The pressure fluctuations, plotted in Figure 6.4a, show the expected dipole pattern of the acoustic response of the aerofoil.

Using sensors located on a circle centred on the leading edge, with a radius of four chords, the FWH analogy (described in Appendix B) provides far-field acoustic results. The numerical predictions are compared with the analytical results of the Amiet model

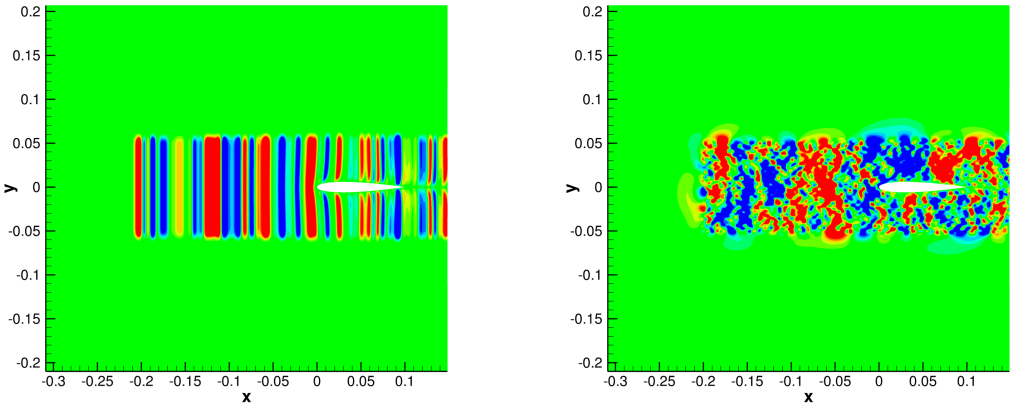


(a) One-component turbulence.

(b) Two-component turbulence.

Figure 6.3: Symmetric NACA0012-63: Instantaneous transverse velocity perturbation contour between ±1 m/s.

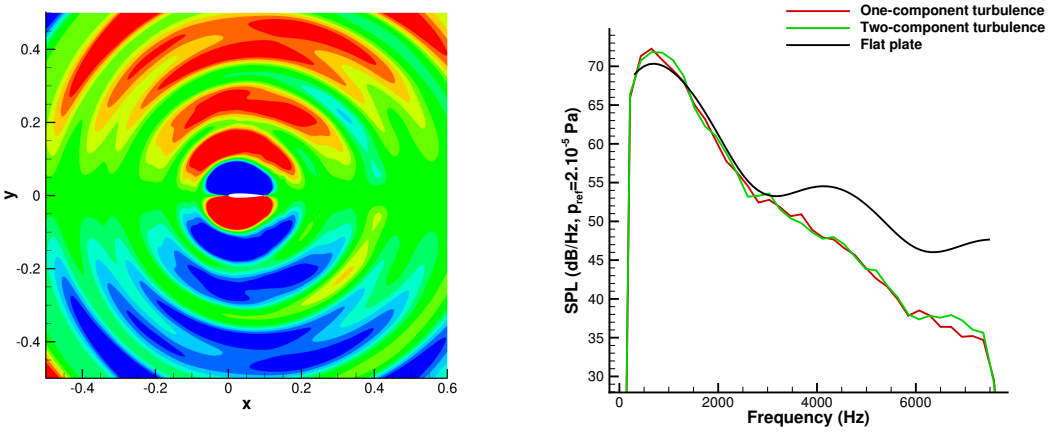


(a) Instantaneous pressure perturbation contour between ±4 Pa. (one-component turbulence).

(b) SPL at 90° and R=1.2 m above the aerofoil.

Figure 6.4: Acoustic response of the symmetric NACA0012-63 with a chord $c = 0.1$ m, at Mach number M=0.176.

which considers a flat plate [60]. Figure 6.4b shows the SPL at 1.2m and 90°(above the aerofoil), along with the Amiet model prediction. The spectra are averaged on 15 segments using a Hann window and an overlap of 50%. The low-frequency part of the acoustic spectrum is similar to a flat plate response, as the wavelength is greater than the chord of the profile. But as the wavelength shortens, it becomes more sensitive to the aerofoil geometry (and by extension to the mean flow), which implies a different acoustic response compared to a flat plate at high frequencies.

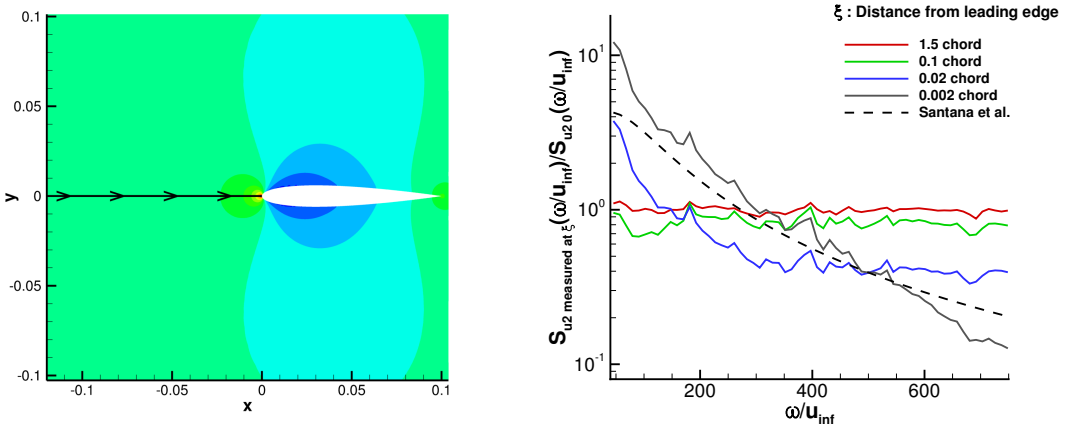


(a) (b)

Figure 6.5: (a) Contour map of the mean pressure field around the aerofoil. The black line (——) depicts the streamline which starts upstream of the aerofoil and stops at the stagnation point. (b) Distortion of turbulence upstream of the aerofoil. $S_{\mathrm{u2\ measured\ at\ }\xi}$ is the density spectrum of the transverse velocity $u_2$ at position $\xi$ along the streamline which stops at the stagnation point, and $S_{\mathrm{u2\ 0}}$ is the density spectrum of the transverse velocity $u_2$ at infinity.

### 6.1.3 Streamline to the stagnation point

The sound reduction at high frequencies between a NACA0012 aerofoil and a flat plate is partly due to the distortion of the mean flow in the vicinity of the leading edge. To better understand this phenomenon, a line of sensors is placed on a streamline which starts upstream of the profile and stops at the stagnation point of the leading edge. As the studied profile is symmetric, it corresponds to a line parallel to the $x$-axis with $y = 0$ m, as plotted on Figure 6.5a, along with the mean pressure field. In this work, other streamlines had been investigated, but the trends observed were similar than on the streamline going to the stagnation point, therefore, in this work, the turbulence distortion analysis is only presented on this central streamline.

Using measurements of the instantaneous velocity perturbations from the sensors on the considered streamline, density spectra of the transverse velocity are obtained using the Welch method. Four of these spectra, located from far upstream the aerofoil, to the closest mesh point of the leading edge tip, are plotted on Figure 6.5b where $S_{\mathrm{u2\ measured\ at\ }\xi}/S_{\mathrm{u2\ 0}}$ denotes the ratio of the distorted spectrum at position $\xi$ by the undistorted spectrum at infinity. It shows that the closer it gets to the leading edge, the larger the amplitude of small wavenumbers is with respect to the undistorted turbulence spectra, whereas the opposite effect is observed for high wavenumbers. A very similar behaviour has been predicted analytically [120, 121], as plotted in dash line on Figure 6.5b, yet it is noteworthy that the slope with the CAA results depicts discrepancies. To obtain this analytical prediction, it is assumed that the leading edge region

of a NACA0012 is a bluff body, therefore, using the generalised RDT from Hunt [122] which, using simulations around circular cylinders, showed that around bluff bodies, the slope at high wavenumbers of the energy spectrum is modified from $E(k) \propto k^{-5/3}$ to $E(k) \propto k^{-10/3}$. Using this slope at high wavenumbers, they proposed the modified von Karman spectrum [120, 121]

$$\Phi_{22}(k_x, k_y) = \frac{91}{36\pi} \frac{\overline{v'^2}}{k_e^2} \frac{\tilde{k}_x^2 + \tilde{k}_y^2}{\left[1 + \tilde{k}_x^2 + \tilde{k}_y^2\right]^{19/6}} \quad ; \quad \tilde{k}_i = \frac{k_i}{k_e} \quad ; \quad k_e = \frac{\sqrt{\pi}}{\lambda} \frac{\Gamma(5/6)}{\Gamma(1/3)} \ . \tag{6.2}$$

To better visualize the transverse velocity spectra on the streamline which goes to the stagnation point, instead of plotting density spectra at a fixed space location as a function of wavenumber, the density spectra are plotted (Figures 6.6b and 6.6a) for fixed wavenumbers, as a function of distance to the leading edge multiplied by the fixed wavenumber. Figure 6.6b is a contour map which contains all wavenumbers, and Figure 6.6a is the same graph but only plotted for three fixed wavenumbers (ranging from low to high).

From these Figures (6.5b, 6.6b and 6.6a), the following behaviour can be depicted:

- The distortion seems to be wavenumber dependent as suggested in Figure 6.6a where the ratios $S_{\text{u2 measured at } \xi}/S_{\text{u2 0}}$ show similarities with the wavenumber dependent $x$-axis.
- At a threshold distance which is wavenumber dependent, the levels of $S_{\text{u2 measured at } \xi}/S_{\text{u2 0}}$ start to decrease.
- At a much closer distance, this decay is however slowed at high wavenumbers, and inverted at low wavenumbers. This second threshold distance is also wavenumber dependent, or in other words, it is proportional to the hydrodynamic wavelength. This distance can be estimated to be about one wavelength.

## 6.2 Vorticity approach

To have a better understanding of the turbulence distortion, a different approach using vorticity is considered. The evolution of the incoming perturbations, purely vortical in 2D, are governed by the linearised vorticity equation. It can be obtained by taking the curl of the linearised Euler equation

$$\frac{\partial \boldsymbol{\omega}}{\partial t} - \nabla \times (\mathbf{u} \times \boldsymbol{\omega}) = 0 \ . \tag{6.3}$$

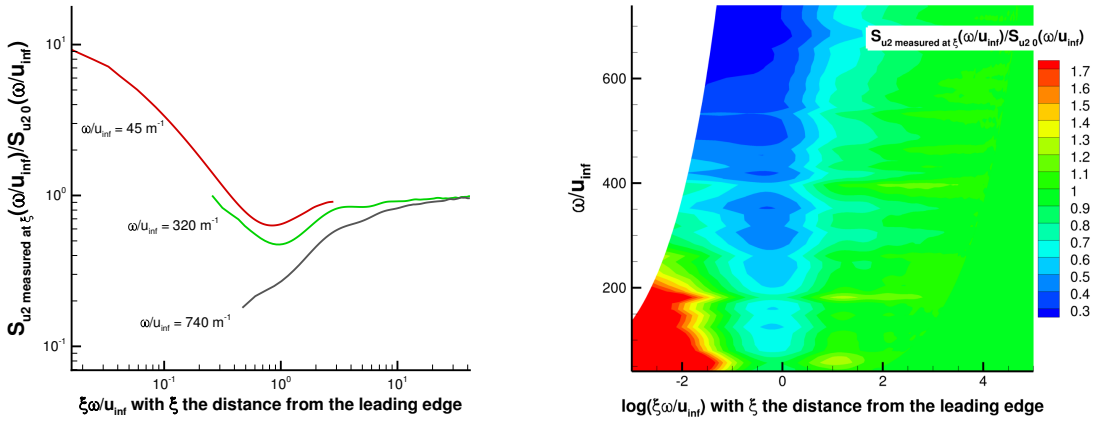


(a) (b)

Figure 6.6: Ratio of the density spectra of the transverse velocity $u_2$ measured at position $\xi$ along the streamline which stops at the stagnation point and denoted $S_{\text{u2 measured at }\xi}$, with the density spectra of the transverse velocity $u_2$ measured at infinity upstream of the aerofoil, where no distortion occurs, and denoted $S_{\text{u2 }0}$. (a) $S_{\text{u2 measured at }\xi}/S_{\text{u2 }0}$ plotted as a function of the distance to the leading edge $\xi$ multiplied by the wavenumber $\omega/u_\infty$, for 3 fixed wavenumbers: (——) $\omega/u_\infty = 45$ m$^{-1}$, (——) $\omega/u_\infty = 320$ m$^{-1}$ and (——) $\omega/u_\infty = 45$ m$^{-1}$ (b) Contour map of $S_{\text{u2 measured at }\xi}/S_{\text{u2 }0}$ plotted as a function of the distance to the leading edge $\xi$ multiplied by the wavenumber $\omega/u_\infty$ on the $x$-axis and the wavenumber $\omega/u_\infty$ on the $y$-axis.

The disturbances are considered incompressible and in 2D, hence Equation (6.3) can be reduced to

$$\frac{D\boldsymbol{\omega}}{Dt} = 0 \ . \tag{6.4}$$

which indicates that the vorticity is conserved and moves with the mean flow.

The proposed method is developed in the frequency domain. While the computation of a single frequency removes the need of a time marching procedure for the panel method detailed in Section 6.2.2, it may be computationally expensive to considered a large number of frequencies.

For single frequency gusts, the vorticity can be expressed by complex numbers such that

$$\boldsymbol{\omega}(\mathbf{x}, t) = \Re\left\{\hat{\boldsymbol{\omega}}(\mathbf{x})\mathrm{e}^{\mathrm{i}2\pi ft}\right\} \tag{6.5}$$

and in 2D turbulence, the vorticity is reduced to its normal component, $\hat{\boldsymbol{\omega}}(\mathbf{x}) = \hat{\omega}_3(\mathbf{x})\mathbf{e}_3$.

Howe [117] showed that in the presence of a solid body, incompressible velocity perturbations $\hat{\mathbf{u}}'$ can be retrieved using (given here in 2D and for complex numbers)

$$H(f)\hat{\mathbf{u}}'(\mathbf{x}) = -\iint \frac{\hat{\omega}_3(\mathbf{x})\mathbf{e}_3 \times (\mathbf{x}-\mathbf{y})}{2\pi|\mathbf{x}-\mathbf{y}|^2}\mathrm{d}y_1\mathrm{d}y_2 + \oint_C \frac{\hat{\gamma}(\mathbf{y})\mathbf{e}_3 \times (\mathbf{x}-\mathbf{y})}{2\pi|\mathbf{x}-\mathbf{y}|^2}\mathrm{d}s(\mathbf{y}). \tag{6.6}$$

where $C$ is the closed contour formed by the aerofoil and its wake vorticity, and d$s$ is the distance along that contour. The Heaviside function $H$ depends on $f$, which is defined as positive outside the aerofoil and negative inside. Finally, $\hat{\gamma}$ is the bound vorticity per unit length on the contour $C$. The bound vortices can be seen as the vorticity response of the aerofoil to respect a non-penetration condition at its boundaries.

To simplify the numerical calculation of Equation (6.6), the vorticity outside the aerofoil is represented as a sum of discrete point vortices

$$\hat{\omega}_3 = \sum_i \hat{\Gamma}_i \delta(\mathbf{y} - \mathbf{y}^{(i)}) \tag{6.7}$$

where $\hat{\Gamma}_i$ is the circulation of each vortex and $\mathbf{y}^{(i)}$ its position.

The second term of Equation (6.6) can be separated into the bound vorticity on the aerofoil surface and on the wake, denoted respectively $\hat{\gamma}^{(a)}$ and $\hat{\gamma}^{(w)}$. Moreover, the contour $C$ is discretized in panels. The aerofoil contour is discretized in $N+1$ points leading to $N$ panels. In the steady-state frequency domain, while the vorticity wake is infinitely long, requiring an infinite number of wake panel, its contribution becomes negligible after a sufficient length, hence it can be truncated in the numerical model.

As a result, Equation (6.6) is discretized in

$$\begin{aligned} H(f)\hat{\mathbf{u}}(\mathbf{x}) = &- \sum_i \frac{\hat{\Gamma}_i \mathbf{e}_3 \times (\mathbf{x} - \mathbf{y}^{(i)})}{2\pi |\mathbf{x} - \mathbf{y}^{(i)}|^2} && \text{Velocity from incoming vorticity} \\ &+ \sum_j^N \frac{\hat{\gamma}_j^{(a)} \mathbf{e}_3 \times (\mathbf{x} - \mathbf{y}^{(j)})}{2\pi |\mathbf{x} - \mathbf{y}^{(j)}|^2} d^{(j)} && \text{Induced velocity from aerofoil surface} \\ &+ \sum_l \frac{\hat{\gamma}_l^{(w)} \mathbf{e}_3 \times (\mathbf{x} - \mathbf{y}^{(l)})}{2\pi |\mathbf{x} - \mathbf{y}^{(l)}|^2} d^{(l)} && \text{Induced velocity from wake vortices.} \end{aligned} \tag{6.8}$$

where $d^{(j)}$ and $d^{(l)}$ are respectively the length of the $j$th and $l$th panel.

### 6.2.1 Methodology

The first step in this approach is to perform a mean flow calculation (independently of the unsteady calculation) and then integrate it to determine the streamlines and drift functions. The streamlines represents the path of a particle over time, hence a streamline is tangent to the velocity vector of the flow. The positions of the particles are noted $\mathbf{X}$. The concept of drift function has been described by Lighthill [123] and Goldstein [124], and represents the time needed for an particle to go between two positions on the same streamline and is noted $T(\mathbf{X})$. The first position is often a reference point located in a uniform mean flow region. Hence, in 2D, a line of constant drift, also called drift line,

starts as a straight line at the reference point, and then evolves directly depending on the local mean flow. This process can easily be implemented numerically, by integrating the velocity vector of the streamlines.

Then, the distribution of vorticity around the aerofoil is calculated. This is performed in a single step, without requiring a time marching procedure, using the streamlines and drift functions previously computed. Hence the vorticity of a harmonic gust, with an amplitude $A_g$ and a frequency $f$, can be written in 2D

$$\hat{\omega}_3(\mathbf{X}) = \nabla \times \left( A_g \exp\left[ \mathrm{i} \left( \frac{2\pi f}{u_0} T(\mathbf{X}) u_0 \right) \right] \mathbf{e}_2 \right) \mathbf{e}_3 \ . \tag{6.9}$$

However, for the first term of Equation (6.8) to converge, the vorticity $\hat{\omega}_3(\mathbf{X})$ needs to be bounded in space. This can be easily done by adding a terms which decays away from the aerofoil. Hence, Equation (6.9) becomes

$$\hat{\omega}_3(\mathbf{X}) = \nabla \times \left( A_g \exp\left[ \mathrm{i} \left( \frac{2\pi f}{u_0} T(\mathbf{X}) u_0 \right) \right] \frac{1}{1 + \mathrm{e}^{-\alpha(|\mathbf{X}-\mathbf{x}_0|-\beta)}} \mathbf{e}_2 \right) \mathbf{e}_3 \tag{6.10}$$

where $\mathbf{x}_0$ is the centre of the aerofoil, and the parameters $\alpha$ and $\beta$ control how the vorticity fades away from the aerofoil.

Using the distribution of vorticity around the aerofoil, the first term of Equation (6.8) can be calculated and serves as an input for the second and third terms of Equation (6.8). These last two terms can then be calculated, in a single step, using a vortex panel method in the frequency domain which determines the bound vortices on the aerofoil $\hat{\gamma}^{(a)}$ and on the wake $\hat{\gamma}^{(w)}$.

### 6.2.2 Vortex panel method in the frequency domain

To determine the bound vorticity $\hat{\gamma}$ on the aerofoil and the wake surfaces, a panel method in the frequency domain is derived. The aerofoil is discretized in $N+1$ points leading to $N$ panels while the wake is discretized in substantially larger number of panels. A vortex strength $\hat{\gamma}_i$ is associated at each discrete contour point. This collocation method which relies on the discrete 2D version of the Biot-Savart equation in free field, is used with polynomials to the first order, or often referred to as linear varying vortex strength panel method. This method is partly inspired from the steady linear varying panel method developed by Pozrikidis [125] but extended to harmonic perturbations in the frequency domain.

#### 6.2.2.1 Single panel in its local frame of reference

To determine the velocity induced by the aerofoil, we will first consider a single panel $i$, in its local frame of reference defined in Figure 6.7. We consider a linear varying vortex

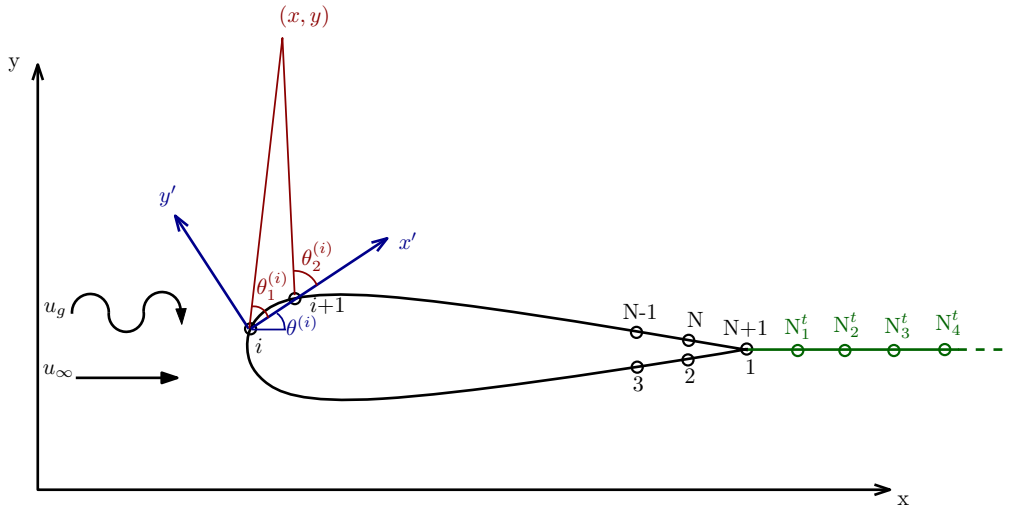


Figure 6.7: Discretization of the aerofoil in N panels, leading to N+1 points of the aerofoil surface, as well as discretization of the wake vortices in an infinite number of panels, from the trailing edge to infinity in the streamwise direction.

density, hence the vortex strength along the $i$th panel can be expressed as

$$\tilde{\gamma}^{(i)}(x') = \tilde{\gamma}_i^{(a)} + \frac{\tilde{\gamma}_{i+1}^{(a)} - \tilde{\gamma}_i^{(a)}}{d^{(i)}} x' \tag{6.11}$$

where $\tilde{\gamma}_i^{(a)}$ is the vortex strength at the $i$th point and $d^{(i)}$ is the length of the $i$th panel. It follows that the induced velocity by the $i$th panel can be expressed

$$\hat{u}_{x'_m}^{(i)}(\mathbf{x}') = a_{x'_m}^{(i,1)}(\mathbf{x}')\tilde{\gamma}_i^{(a)} + a_{x'_m}^{(i,2)}(\mathbf{x}')\tilde{\gamma}_{i+1}^{(a)} \qquad \text{with } m = 1, 2, \tag{6.12}$$

where the local influence coefficients $a$ are defined as

$$\begin{aligned} a_{x'_1}^{(i,1)}(\mathbf{x}') &= c_1\left[x'_2 c_2 + (x'_1 - d^{(i)})\Delta\theta^{(i)}\right], \quad a_{x'_2}^{(i,1)}(\mathbf{x}') = c_1\left[(x'_1 - d^{(i)})c_2 - x'_2\Delta\theta^{(i)} + d^{(i)}\right], \\ a_{x'_1}^{(i,2)}(\mathbf{x}') &= -c_1\left[x'_2 c_2 + x'\Delta\theta^{(i)}\right], \qquad a_{x'_2}^{(i,2)}(\mathbf{x}') = c_1\left[x'_1 c_2 - x'_2\Delta\theta^{(i)} + d^{(i)}\right], \end{aligned} \tag{6.13}$$

$$\text{giving } \Delta\theta^{(i)} = \arctan\frac{y'}{x' - d^{(i)}} - \arctan\frac{y'}{x'}, \quad c_1 = \frac{1}{2\pi d^{(i)}}, \quad c_2 = \ln\left(\frac{(x' - d^{(i)})^2 + y'^2}{x'^2 + y'^2}\right)^{1/2}$$

#### 6.2.2.2 Induced velocity in global coordinates

In the global frame of reference, defined in Figure 6.7, the local frame of reference of the $i$th panel is written

$$x'_1 = (x_1 - x_1^{(i)})\cos\theta^{(i)} + (x_2 - x_2^{(i)})\sin\theta^{(i)} \tag{6.14}$$

$$x'_2 = -(x_1 - x_1^{(i)})\sin\theta^{(i)} + (x_2 - x_2^{(i)})\cos\theta^{(i)} \tag{6.15}$$

where $\theta^{(i)}$ is the orientation of the $i$th panel. The induced velocity of the $i$th panel in the global frame of reference is expressed similarly as in the local frame of reference

$$\hat{u}_m^{(i)}(\mathbf{x}) = a_m^{(i,1)}(\mathbf{x})\tilde{\gamma}_i + a_m^{(i,2)}(\mathbf{x})\tilde{\gamma}_{i+1} \qquad \text{with } m = 1, 2, \tag{6.16}$$

where $a$ are global influence coefficients given by

$$\begin{aligned} a_{x_1}^{(i,q)}(\mathbf{x}) &= a_{x'}^{(i,q)}(\mathbf{x}')\cos\theta^{(i)} - a_{y'}^{(i,q)}(\mathbf{x}')\sin\theta^{(i)} \ , \\ a_{x_2}^{(i,q)}(\mathbf{x}) &= a_{x'}^{(i,q)}(\mathbf{x}')\sin\theta^{(i)} + a_{y'}^{(i,q)}(\mathbf{x}')\cos\theta^{(i)} \ , \qquad \text{with } q = 1, 2. \end{aligned} \tag{6.17}$$

The induced flow at any given point outside the aerofoil, in term of the strength of the vortex at the nodes, is obtained by superposition

$$\hat{u}_m(\mathbf{x}) = \sum_{i=1}^{N+1} b_{x_m}^{(i)}(\mathbf{x})\tilde{\gamma}_i \ , \qquad \text{with } m = 1, 2, \tag{6.18}$$

where the new coefficients $b$ are defined by

$$b_{x_m}^{(1)}(\mathbf{x}) = a_{x_m}^{(1,1)}(\mathbf{x}) \tag{6.19}$$

$$b_{x_m}^{(i)}(\mathbf{x}) = a_{x_m}^{(i-1,2)}(\mathbf{x}) + a_{x_m}^{(i,1)}(\mathbf{x}) \qquad \text{for } i = 2..N \text{ and } m = 1, 2. \tag{6.20}$$

$$b_{x_m}^{(N+1)}(\mathbf{x}) = a_{x_m}^{(N+1,2)}(\mathbf{x}) \tag{6.21}$$

#### 6.2.2.3 No-penetration condition

A no-penetration condition is applied on a collocation point located on each panel. In this work, the collocation points are chosen to be located at the middle of each panel, noted $\mathbf{x}_c^{(j)}$.

$$\mathbf{x}_c^{(j)} = \frac{1}{2}\left(\mathbf{x}^{(j)} + \mathbf{x}^{(j+1)}\right) \ , \qquad \text{where } j = 1...N \ . \tag{6.22}$$

Hence, the no-penetration condition is, for each collocation point $\mathbf{x}_c^{(j)}$, the sum of the induced velocities of all panels (given by Equation (6.18)) equals with opposite sign to the external velocity $\hat{\mathbf{u}}_g$

$$\sum_{i=1}^{N+1} A_{i,j}^{(a)}\tilde{\gamma}_i = -\hat{\mathbf{u}}_g(\mathbf{x}_c^{(j)}) \cdot \mathbf{e}_1 n_1^{(j)} - \hat{\mathbf{u}}_g(\mathbf{x}_c^{(j)}) \cdot \mathbf{e}_2 n_2^{(j)} \tag{6.23}$$

with

$$A_{i,j}^{(a)} = b_{x_1}^{(i)}(\mathbf{x}_c^{(j)})n_1(\mathbf{x}_c^{(j)}) + b_{x_2}^{(i)}(\mathbf{x}_c^{(j)})n_2(\mathbf{x}_c^{(j)}) \ , \tag{6.24}$$

where $\mathbf{n}^{(j)} = n_1^{(j)}\mathbf{e}_1 + n_2^{(j)}\mathbf{e}_2$ is the outward vector normal to the aerofoil on panel $j$.

Unlike the steady vortex panel method where the external velocity $\hat{\mathbf{u}}_g$ is constant for all collocation points $\mathbf{x}_c^{(j)}$ and is equal to the mean flow velocity at infinity, for the

unsteady panel method, $\hat{\mathbf{u}}_g$ is obtained using the first term of Equation (6.8), applied at each collocation point $\mathbf{x}_c^{(j)}$.

#### 6.2.2.4 Circulation and wake

In the current system of equations, there are $N$ equations for $N+1$ unknowns. To close the system of equations and remove this single degree of freedom, a condition on the circulation is applied.

The circulation around the aerofoil can be approximated by

$$\hat{C} = -\sum_{j=1}^{N} \hat{u}_t(\mathbf{x}_c^{(j)}) d^{(j)} = \frac{1}{2} \sum_{i=1}^{N} (\hat{\gamma}_i + \hat{\gamma}_{i+1}) d^{(i)} \ , \tag{6.25}$$

where $\hat{u}_t(\mathbf{x}_c^{(j)})$ is the tangential velocity at the collocation point $\mathbf{x}_c^{(j)}$.

For a steady vortex panel method, the Kutta condition states that there is no circulation around the trailing edge, hence no circulation between the first panel (lower side of the trailing edge) and the last panel (upper side of the trailing edge)

$$\hat{\gamma}_1 = -\hat{\gamma}_{N+1} \tag{6.26}$$

For a harmonic vortex panel method in the steady-state in the frequency domain, the wake is infinitely long and then needs to be truncated after a sufficiently long distance. As there is no time marching procedure, it is difficult to predict the location or velocity of the shed vortices, hence the shed panels are oriented along the $x$-axis, each with a panel length equal to the size of panel at the trailing edge $d^{(N)}$ and convected by the mean flow at infinity.

As the wake vortices as only convected by the mean flow in the wake, their strength $\hat{\gamma}^{(w)}$ is equal to the vortex strength at the trailing edge $\hat{\gamma}_{N+1}$, but shifted in phase such that

$$\hat{\gamma}_l^{(w)} = \hat{\gamma}_{N+1} \exp\left(-\frac{\mathrm{i}2\pi f}{u_\infty} \xi_l\right) \ , \tag{6.27}$$

where $\xi_l$ is the distance from the trailing edge to the $l$-th wake collocation point.

The geometrical influence coefficients $A_{i,j}^{(w)}$ corresponding to the influence of the wake panels on the aerofoil are derived using the same procedure as the $A_{i,j}^{(a)}$ coefficient.

To close the system of equations, the Helmholtz theorem states that the total circulation in the flow field must be kept constant, hence any changes in the circulation $\hat{C}$ around the aerofoil surface must be balanced by an equal and opposite change in the circulation in the wake.

Nevertheless, a bound vortex is expressed $\gamma = \Re\{\hat{\gamma}\mathrm{e}^{\mathrm{i}2\pi ft}\}$, thus its derivative in time can be approximated by

$$\frac{\partial \gamma}{\partial t} = \Re\left\{\frac{1-\mathrm{e}^{-\mathrm{i}2\pi f\Delta t}}{\Delta t}\hat{\gamma}\mathrm{e}^{\mathrm{i}2\pi ft}\right\} \tag{6.28}$$

where $\Delta t = d^{(N)}/u_\infty$. Hence the Helmholtz theorem becomes

$$(1-\mathrm{e}^{-\mathrm{i}2\pi f\Delta t})\frac{1}{2}\sum_{i=1}^{N}(\hat{\gamma}_i+\hat{\gamma}_{i+1})d^{(i)} = -\hat{\gamma}_{N+1}d^{(N)}\ . \tag{6.29}$$

#### 6.2.2.5 System of equations

Finding the bound vorticity $\hat{\gamma}^{(a)}$ is reduced to solving the following linear system of equations

$$\begin{pmatrix} A^{(a)}_{1,1} & A^{(a)}_{1,2} & \cdots & A^{(a)}_{1,N} & A^{(a)}_{1,N+1}+\sum_l^\infty A^{(w)}_{1,l} \\ A^{(a)}_{2,1} & A^{(a)}_{2,2} & \cdots & A^{(a)}_{2,N} & A^{(a)}_{2,N+1}+\sum_l^\infty A^{(w)}_{2,l} \\ \vdots & \vdots & \ddots & \vdots & \\ A^{(a)}_{N,1} & A^{(a)}_{N,2} & \cdots & A^{(a)}_{N,N} & A^{(a)}_{N,N+1}+\sum_l^\infty A^{(w)}_{N,l} \\ d^{(1)} & d^{(1)}+d^{(2)} & \cdots & d^{(N-1)}+d^{(N)} & d^{(N)}+d^{(N+1)}+2d^{(N+1)}/(1-\mathrm{e}^{-\mathrm{i}2\pi f\Delta t}) \end{pmatrix}\begin{pmatrix} \hat{\gamma}_1 \\ \hat{\gamma}_2 \\ \vdots \\ \hat{\gamma}_N \\ \hat{\gamma}_{N+1} \end{pmatrix}$$
$$= \begin{pmatrix} -\mathbf{u}_g(\mathbf{x}_c^{(1)})\cdot\mathbf{e}_1 n_1^{(1)} - \mathbf{u}_g(\mathbf{x}_c^{(1)})\cdot\mathbf{e}_2 n_2^{(1)} \\ -\mathbf{u}_g(\mathbf{x}_c^{(2)})\cdot\mathbf{e}_1 n_1^{(2)} - \mathbf{u}_g(\mathbf{x}_c^{(2)})\cdot\mathbf{e}_2 n_2^{(2)} \\ \vdots \\ -\mathbf{u}_g(\mathbf{x}_c^{(N)})\cdot\mathbf{e}_1 n_1^{(N)} - \mathbf{u}_g(\mathbf{x}_c^{(N)})\cdot\mathbf{e}_2 n_2^{(N)} \\ 0 \end{pmatrix} \tag{6.30}$$

## 6.3 Procedure, computational cost and numerical implementation

The proposed method is in the frequency domain, therefore it needs to be solved once per incoming gust wavenumber. The base of the method relies on Equation (6.8), which is rewritten here for convenience of the reader

$$\begin{aligned} H(f)\hat{\mathbf{u}}(\mathbf{x}) = &-\sum_i \frac{\hat{\Gamma}_i \mathbf{e}_3\times(\mathbf{x}-\mathbf{y}^{(i)})}{2\pi|\mathbf{x}-\mathbf{y}^{(i)}|^2} && \text{Velocity from incoming vorticity} \\ &+\sum_j^N \frac{\hat{\gamma}_j^{(a)}\mathbf{e}_3\times(\mathbf{x}-\mathbf{y}^{(j)})}{2\pi|\mathbf{x}-\mathbf{y}^{(j)}|^2}d^{(j)} && \text{Induced velocity from aerofoil surface} \\ &+\sum_l \frac{\hat{\gamma}_l^{(w)}\mathbf{e}_3\times(\mathbf{x}-\mathbf{y}^{(l)})}{2\pi|\mathbf{x}-\mathbf{y}^{(l)}|^2}d^{(l)} && \text{Induced velocity from wake vortices.} \end{aligned}$$

For uniform mean flows, there are no distortion of the unsteady vorticity by the mean flow, hence the solution of the first term in Equation (6.8) is known, therefore Equation (6.8) becomes

$$H(f)\hat{\mathbf{u}}(\mathbf{x}) = A_g \mathrm{e}^{\mathrm{i}2\pi f t}\mathbf{e}_2 + \sum_j^N \frac{\hat{\gamma}_j^{(a)}\mathbf{e}_3 \times (\mathbf{x}-\mathbf{y}^{(j)})}{2\pi|\mathbf{x}-\mathbf{y}^{(j)}|^2} d^{(j)} + \sum_l \frac{\hat{\gamma}_l^{(w)}\mathbf{e}_3 \times (\mathbf{x}-\mathbf{y}^{(l)})}{2\pi|\mathbf{x}-\mathbf{y}^{(l)}|^2} d^{(l)}, \quad (6.31)$$

where the only unknowns are the bound vortices $\hat{\gamma}_l^{(a)}$ and $\hat{\gamma}_l^{(w)}$, which are found by solving Equation (6.30). The problem is reduced to solving a linear system of equations, where its computational cost depends on the number of panels used to discretize the aerofoil in the vortex panel method, but even for large numbers of panels, this step remains computationally very fast.

For non-uniform mean flows, the distortion by the mean flow of the unsteady vorticity has to be taken into account. In this case, the first step is to compute the streamlines and drift lines from the mean flow solution, which allows for the computation of the point vorticity $\hat{\Gamma}$ around the aerofoil via Equation (6.7). From this vorticity field, the first term of Equation (6.8) can be solved for each position $\mathbf{x}$. However, unlike for uniform case, to compute the second and third term of Equation (6.8), the gust velocities $\mathbf{u}_g$ on the panels of the aerofoil are unknown. Therefore they need to be resolved beforehand, similarly to the first term of Equation (6.8), using the Biot-Savart, it reads

$$\hat{\mathbf{u}}_g(\mathbf{x}) = \sum_i \frac{\hat{\Gamma}_i \mathbf{e}_3 \times (\mathbf{x}-\mathbf{y}^{(i)})}{2\pi|\mathbf{x}-\mathbf{y}^{(i)}|^2} \ . \quad (6.32)$$

Finally, the bound vortices $\hat{\gamma}_l^{(a)}$ and $\hat{\gamma}_l^{(w)}$ in the second and third terms of Equation (6.8) can then be evaluated from Equation (6.30). Overall, the problem requires the first term of Equation (6.8) plus, for each panel on the aerofoil, Equation (6.32) to be computed before solving the linear system of equations given in Equation (6.30). It logically results in a largely higher computational cost than a uniform mean flow case.

In this work, the proposed method has been programmed from the ground up, in the computing language Python[1], with two external libraries: NumPy[2] for the mathematical functions on multi-dimensional matrices, and Cassiopee[3] for the read and write file operations. While Python is not a computationally fast language with respect to other languages such as C or Fortran, its high-level built-in functionalities as well as a large and comprehensive list of libraries allows for fast proof-of-concept implementations. Therefore, it is difficult to assess the computational cost against the CAA solver PIANO used in this work. Moreover, the computational cost depends on the wavenumber of the incoming vorticity field, as the discretization of the streamlines, drift lines and aerofoil

[1] Python is an interpreted computing language developed by the Python Software Foundation (www.python.org)

[2] www.numpy.org

[3] elsa.onera.fr/Cassiopee

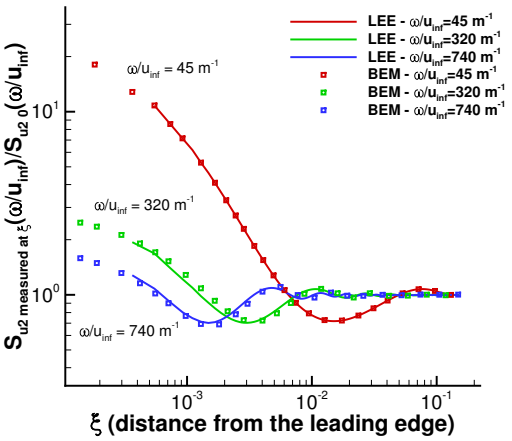


Figure 6.8: Comparison of the distortion of turbulence along the streamline which stops at the stagnation point using a uniform mean flow assumption between the LEE model and the Boundary Element Method (BEM) approach. $S_{\text{u2 measured at }\xi}$ is the density spectrum of the transverse velocity $u_2$ at position $\xi$ along the streamline which stops at the stagnation point and $S_{\text{u2 }0}$ is the density spectrum of the transverse velocity $u_2$ at infinity. Note that, for more clarity of the plot, the $x$-axis, which is the distance to the leading edge of the aerofoil, is not multiplied by the wavenumber $\omega/u_\infty$ as the curves would overlay otherwise.

panels is naturally denser as the wavenumber to solve increases. For information, the computation on a single core of the proposed method on a NACA0012-63 aerofoil using 200 panels, for a wavenumber $k_x = 320$ m$^{-1}$, takes seconds using a uniform mean flow, while taking about 15 minutes using a steady Euler mean flow solution.

## 6.4 Verification

The proposed BEM is verified on a NACA0012-63 using two different mean flows. A first unrealistic uniform mean flow, and then a steady Euler solution as the mean flow. The turbulence distortion is verified against the LEE model. Unlike the LEE model, the proposed BEM does not include the acoustic velocity generated from the interaction with the aerofoil, nevertheless, it can be neglected as acoustic velocities have a small amplitude with respects to hydrodynamic waves.

The uniform mean flow case allows to check the implementation of the vortex panel method alone. Indeed, in such mean flow conditions, the solution of the first term of Equation (6.8) is known, leading to Equation (6.31), as decribed in Section 6.3.

On the streamline which stops at the stagnation point, the distortion of turbulence at different fixed wavenumbers as a function of distance from the leading edge is plotted

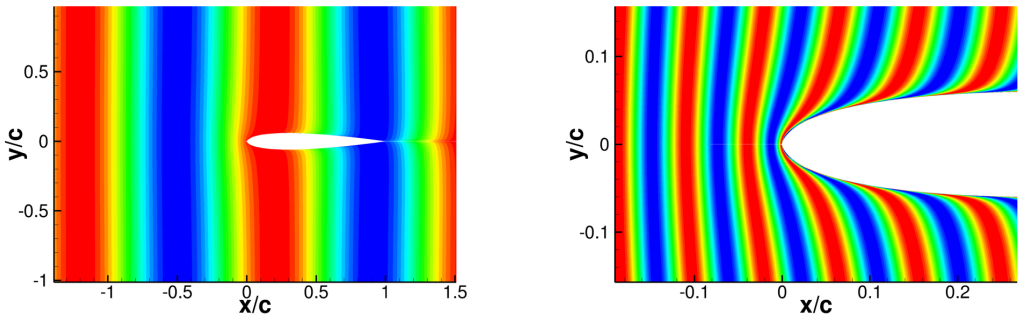


(a) $\omega/u_0 = 45$ m$^{-1}$.
Contour between $\pm 45$ s$^{-1}$.

(b) $\omega/u_0 = 740$ m$^{-1}$.
Contour between $\pm 650$ s$^{-1}$.

Figure 6.9: Vorticity at fixed wavenumber $\omega/u_\infty$ around a NACA0012 aerofoil, computed from the streamlines and drift functions integrated from the mean flow solution.

on Figure 6.8 for both the LEE model and the BEM approach. The results show a good agreement between the two methods, which verifies the implementation of the vortex panel method.

For the second case, which uses a steady Euler solution as the mean flow, the analytical solution of the first term of Equation (6.8) is unknown. The distribution of vorticity around the aerofoil is then required and is obtained using the streamline and drift lines extracted from the mean flow. The Figure 6.9 shows this distribution for two wavenumbers.

Using the vorticity around the aerofoil as an input, the vortex panel method can be performed to find the bound vortices on the aerofoil and wake surfaces, as decribed in Section 6.3. Finally, the turbulence distortion is obtained by applying Equation (6.8). On the streamline which stops at the stagnation point, the distortion of turbulence at different fixed wavenumbers as a function of distance from the leading edge is plotted on Figure 6.10 for both the LEE model and the BEM approach. The results show a good agreement between the two methods.

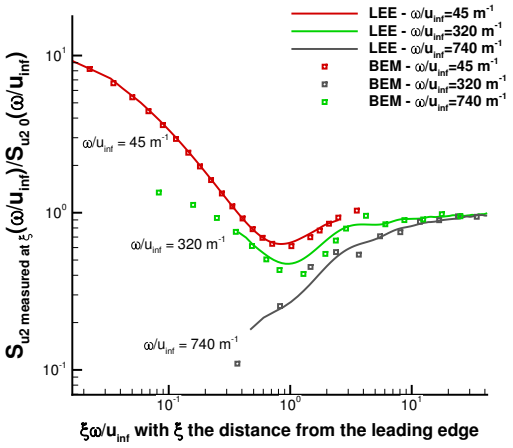


Figure 6.10: Comparison of the distortion of turbulence along the streamline which stops at the stagnation point using a steady Euler mean flow assumption between the LEE model and the BEM approach for three fixed wavenumbers. $S_{\mathrm{u2\ measured\ at\ }\xi}$ is the density spectrum of the transverse velocity $u_2$ at position $\xi$ along the streamline which stops at the stagnation point and $S_{\mathrm{u2\ 0}}$ is the density spectrum of the transverse velocity $u_2$ at infinity.

## 6.5 Conclusion

The distortion of the incoming turbulence by the mean flow close to the leading edge is believed to play an important role in the interaction noise. The results suggest that the distortion of turbulence is a wavenumber mechanism. Upstream of the aerofoil, the turbulence levels of the upwash velocity fluctuations starts to decrease as it gets closer to the leading edge. This decay is however slowed at high wavenumbers, and inverted at low wavenumbers, after a second wavenumber dependent threshold distance, much closer to the leading edge. This distance is estimated to be about one wavelength.

To better understand this distortion, a different numerical approach is derived. Similar numerical methods have already been proposed but have not been used in the context of predicting the turbulence distortion by the mean flow. The proposed boundary element method partly relies on a harmonic vortex panel method in the frequency domain which allows the computation of the distortion in a single step per wavenumber.

From the boundary element method, the distortion of the turbulence upstream of the aerofoil comes from three mechanisms, the velocity retrieved from the distorted incoming vorticity field around the geometry, the induced velocity of the bound vortices on the aerofoil and the induced velocity of the bound vortices in the wake. The bound vortices on the aerofoil surface and in the wake are the vorticity response of the aerofoil and wake to respect the non-penetration condition at the solid boundaries.

In Chapter 7, using both the LEE model and the boundary element method, this distortion is first analysed on the NACA0012 profile. Secondly, a parametric study on turbulence, mean flow and geometric factors is carried out to depict trends and physical insights.

# Chapter 7

# Analysis of turbulence distortion

In Chapter 6, using both a LEE model approach and a vorticity approach, the turbulence distortion on a streamline upstream of a NACA0012-63 aerofoil is shown to be the consequence of two mechanisms: the distortion of the incoming vorticity in the vicinity of the leading edge of the aerofoil, and the vorticity response of the aerofoil and wake to respect the non-penetration condition at the solid boundaries. This chapter aims at analysing turbulence distortion by first investigating the influence of each of these mechanisms on a NACA0012-63 aerofoil, and then by performing a parametric study on turbulence, mean flow and geometric parameters. A better knowledge of the sensitive parameters in the turbulence distortion help understand the physics involved while potentially helping the development of future analytical or numerical methods.

## 7.1 Distortion of the incoming vorticity and induced velocities

The derived boundary element method developed in Chapter 6 allows to individually assess the influence of the distortion of the incoming vorticity, the induced velocity from the aerofoil and the induced velocity from the wake. By applying the boundary element method to the NACA0012 aerofoil case described in Section 6.1.1, the influence of the wake is found negligible regardless of the mean flow, as plotted for the uniform mean flow in Figure 7.1. Indeed, with a uniform mean flow, the wake induced velocity is a few orders of magnitude below the other two components and can then be neglected. With the steady Euler mean flow, the wake induced velocity has more influence than with a uniform mean flow, especially as the wavenumber increases, however the levels are still small with respect to the full turbulence distortion. This result is not surprising as the wake vortices are located far from the leading edge, hence their influence is limited.

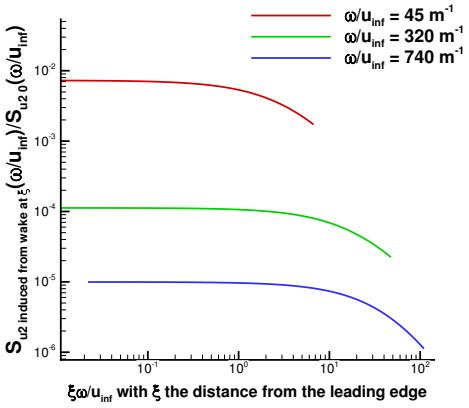


Figure 7.1: Influence of the wake vortices on the incoming turbulence upstream of the leading edge with a uniform mean flow, plotted for three fixed wavenumbers. $S_{\text{u2 induced from wake at } \xi}$ is the density spectrum of the transverse velocity $u_2$ induced by the bound vortices in the wake of the aerofoil, evaluated at position $\xi$ along the streamline which stops at the stagnation point and $S_{\text{u2 }0}$ is the density spectrum of the transverse velocity $u_2$ at infinity.

Using a uniform mean flow, the turbulence distortion upstream of the leading edge is plotted in Figure 7.2. The response between the different wavenumbers is very similar until a distance smaller than one fourth of a wavelength to the leading edge. Then, the response gets stronger as the wavenumber decreases, which is the direct consequence of the induced velocity being stronger close to the leading edge at these wavenumbers, as plotted in Figure 7.3a.

The phase difference between the incoming vorticity perturbations and the induced velocities from the bound vortices, plotted at the bottom of Figure 7.2, varies as the distance to the leading edge reduces. It causes a succession of constructive ($0 \pm 2\pi$ (rad)) and destructive ($\pi \pm 2\pi$ (rad)) waves, shown on the turbulence distortion Figure 7.2.

With a steady Euler mean flow, the distortion is different. Indeed, the incoming vorticity, which follows the streamlines and drift lines, gets distorted near the leading edge. Naturally, the distortion of all perturbations by the mean flow is identical regardless of its wavenumber, however, its effects depend on the wavelength of the perturbations. Indeed, the restricted region around the leading edge where this distortion occurs only alters a small portion of a single wavelength for low wavenumber perturbations, while multiples wavelengths are skewed for large wavenumbers, as visible in Figure 6.9. Consequently, the first term of equation (6.8) which retrieves perturbation velocities from the incoming vorticity field shows a clear amplitude attenuation as the wavenumber increases (Figure 7.3b).

Moreover, the incoming vorticity field is also used as an input for the vortex panel method via Equation (6.32). Hence, with a uniform mean flow, the amplitude of the right-hand side of the vortex panel method is $S_{\text{u2 on NACA0012 at } x/c}/S_{\text{u2 }0} = 1$ on all panels on the

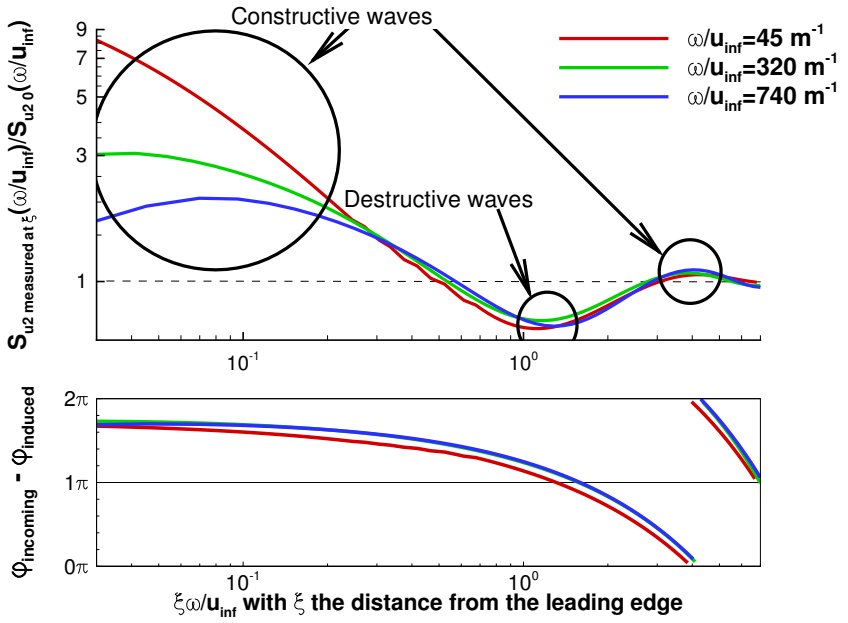


Figure 7.2: Turbulence distortion upstream the leading edge and phase difference between the incoming perturbations and induced velocities from the aerofoil, using a uniform mean flow assumption. $S_{\text{u2 measured at }\xi}$ is the density spectrum of the transverse velocity $u_2$ at position $\xi$ along the streamline which stops at the stagnation point, $S_{\text{u2 }0}$ is the density spectrum of the transverse velocity $u_2$ at infinity and $\varphi_{\text{incoming}}$ and $\varphi_{\text{induced}}$ are the phase of respectivelly the incoming velocity perturbations and the velocity induced by the bound vortices on the aerofoil surface.

aerofoil surface. $S_{\text{u2 on NACA at }x/c}$ is the density spectrum of the transverse velocity $u_2$ retrieved from the incoming vorticity on the aerofoil surface at the chordwise position $x/c$, and $S_{\text{u2 }0}$ is the density spectrum of the transverse velocity $u_2$ at infinity. But with a steady Euler mean flow, this amplitude decreases as the wavenumber increases, as shown in Figure 7.4. The direct consequence of this smaller input on the vortex panel method, which means is a less important induced velocity from the aerofoil bound vortices, as plotted on Figure 7.3a. For high wavenumbers, the right-hand-side of Equation (6.30) is close to zero, therefore the bound vortices on the aerofoil surface, and, by extension the induced velocities, are close to zero.

## 7.2 Effect of incoming turbulence

The effect of energy distribution of the incoming isentropic turbulence is studied. The considered cases follow a von Karman energy spectrum, hence it can be fully characterized by a turbulent intensity and an integral length scale. The evolution of the spectrum with the turbulent intensity is quadratic, therefore trivial to predict, as long as the turbulent intensity remains small with regards to the mean flow, otherwise non-linear effects need to be considered. On the other hand, a change of the integral length scale leads to

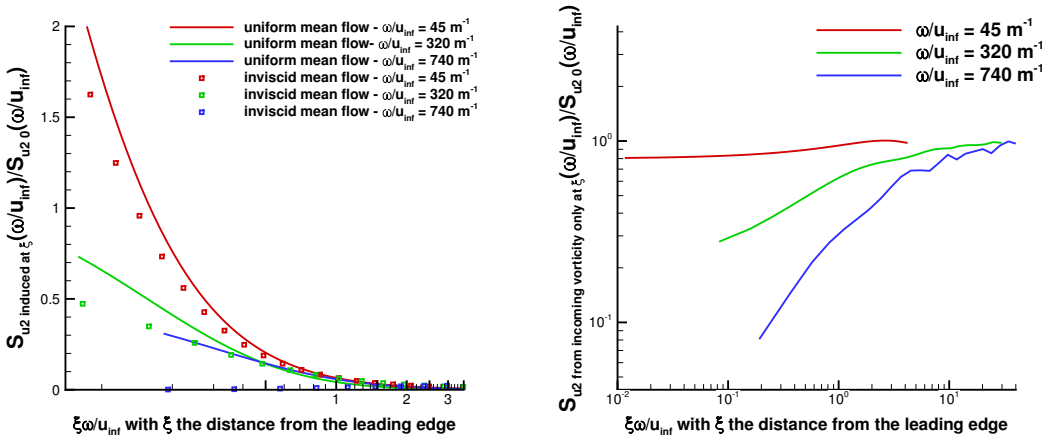


(a) (b)

Figure 7.3: (a) Influence of the bound vortices on the aerofoil surface on the incoming turbulence upstream of the leading edge with a uniform mean flow against a steady Euler mean flow assumption, plotted for three fixed wavenumbers. $S_{\text{u2 induced at }\xi}$ is the density spectrum of the transverse velocity $u_2$ induced by the bound vortices on the aerofoil surface at position $\xi$ along the streamline which stops at the stagnation point, and $S_{\text{u2 }0}$ is the density spectrum of the transverse velocity $u_2$ at infinity. (b) Effect of the distortion of the vorticity by a Euler mean flow solution, upstream of the leading edge. $S_{\text{u2 from incoming vorticity only at }\xi}$ is the density spectrum of the transverse velocity $u_2$ retrieved only from the vorticity around the aerofoil, at position $\xi$, and $S_{\text{u2 }0}$ is the density spectrum of the transverse velocity $u_2$ at infinity.

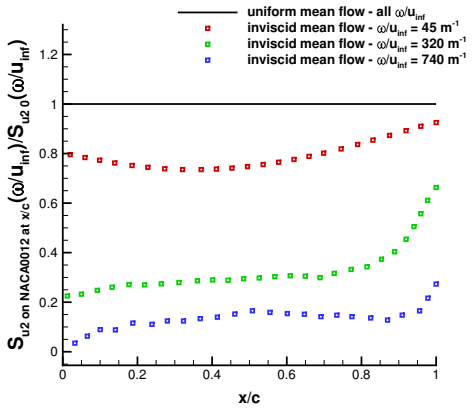


Figure 7.4: Right-hand side of the vortex panel system of equations, for the uniform mean flow against the steady Euler mean flow. The ratio $S_{\text{u2 on NACA0012 at }x/c}/S_{\text{u2 }0}$ where $S_{\text{u2 on NACA at }x/c}$ is the density spectrum of the transverse velocity $u_2$ retrieved from the incoming vorticity on the aerofoil surface at position $x/c$, and $S_{\text{u2 }0}$ is the density spectrum of the transverse velocity $u_2$ at infinity.

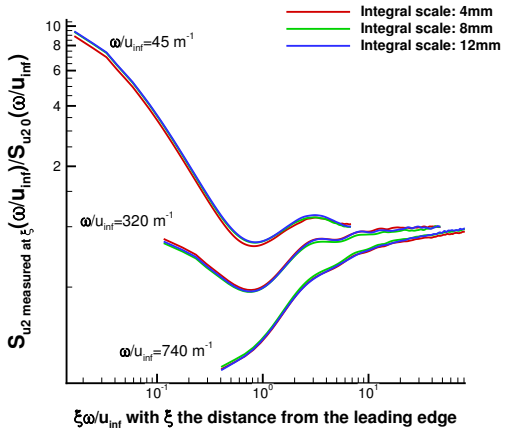


Figure 7.5: Effect of the integral length scale on turbulence distortion, plotted for three fixed wavenumbers and three integral scales. $S_{\text{u2 measured at } \xi}$ is the density spectrum of the transverse velocity $u_2$ at position $\xi$ along the streamline which stops at the stagnation point, $S_{\text{u2 }0}$ is the density spectrum of the transverse velocity $u_2$ at infinity.

a change of the distribution of turbulent energy which is more complex to predict. In this section, the impact of the integral length scale on the distortion of the turbulence is studied using three different values: 0.004m, 0.008m and 0.012m.

In Chapter 5, Section 5.2.2, by comparing SPL in the far field of an isolated 2D cambered thick aerofoil with a flat plate, using multiple turbulent integral length scales, the loading of the aerofoil seemed to be only modulated in amplitude by the incoming turbulence. A similar observation can be made regarding turbulence distortion as, for all three turbulent integral length scales, the turbulence distortion are identical, as plotted in Figure 7.5. Indeed, in the vicinity of the leading edge, the spectral density for each wavenumber has the same evolution regardless of the incoming turbulence.

## 7.3 Effect of the mean flow velocity

In this section, the effect of the mean flow velocity is investigated on a symmetric NACA0012-63, using mean flow velocities ranging from 60 to 140 m/s. A steady Euler is still used as a mean flow, as it has been found satisfactory to study interaction noise while limiting potential linear instabilities in the LEE. The same mesh has been used for all LEE simulations, therefore the time step is adjusted for each simulation, keeping a CFL close to unity.

The Sound Power Level (PWL) integrated over 360° of each simulation is plotted in Figure 7.6a. It shows the same slope when plotted as a function of $fc/u_\infty$, as previously observed [99], which suggests a wavenumber dependence. The wavenumber dependence

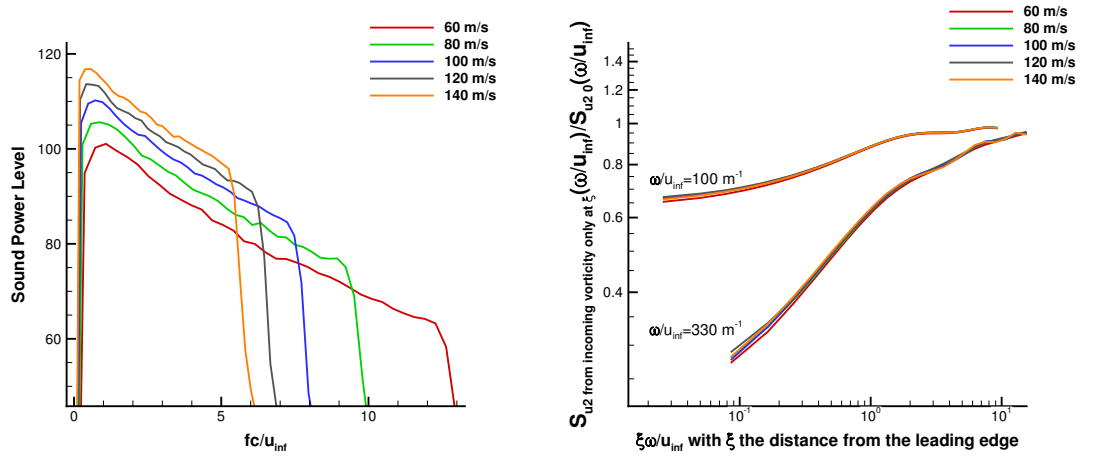


(a) (b)

Figure 7.6: Effect of the mean flow velocity on (a) Sound Power Levels integrated over 360° around the aerofoil at R=1.2 m and (b) Turbulence distortion on the streamline which stops at the stagnation point. $S_{\text{u2 from incoming vorticity only at } \xi}$ is the density spectrum of the transverse velocity $u_2$ retrieved only from the incoming vorticity around the aerofoil, at position $\xi$ and $S_{\text{u2 }0}$ is the density spectrum of the transverse velocity $u_2$ at infinity.

of turbulence distortion is confirmed to some extent in Figure 7.7 (for better readability, it only includes three mean flow velocities: 60m/s, 100m/s and 140m/s) of the evolution of $S_{\text{u2 from incoming vorticity only at } \xi}/S_{\text{u2 }0}$. $S_{\text{u2 from incoming vorticity only at } \xi}$ is the density spectrum of the transverse velocity $u_2$ retrieved only from the incoming vorticity around the aerofoil, at position $\xi$ and $S_{\text{u2 }0}$ is the density spectrum of the transverse velocity $u_2$ at infinity.

The small discrepancies in Figure 7.7 between the mean flow velocities are both a shift of the constructive and destructive oscillations closer to the leading edge and a decrease in amplitude as the velocity increases. This is probably due to compressibility effects. Indeed, up to a mean flow of 100 m/s, the differences in the distortion are very small, which corresponds to Mach numbers smaller than 0.3, where compressibility effects are negligible [126]. For larger Mach numbers, compressibility effects should not be neglected [126], as visible by the compression of the vorticity lines shown for a fixed wavenumber, between 60 m/s at the top and 140 m/s at the bottom in Figure 7.8. This effect does not modify the amplitude of the transverse velocities resulting from the distortion of the vorticity lines, in Figure 7.6b, but it seems to be responsible in the shift of the phase difference between velocities from the incoming vorticity and the induced velocity from the bound vortices on the aerofoil (bottom part in Figure 7.7). The combination of these two elements lead to the small discrepancies observed in Figure 7.7).

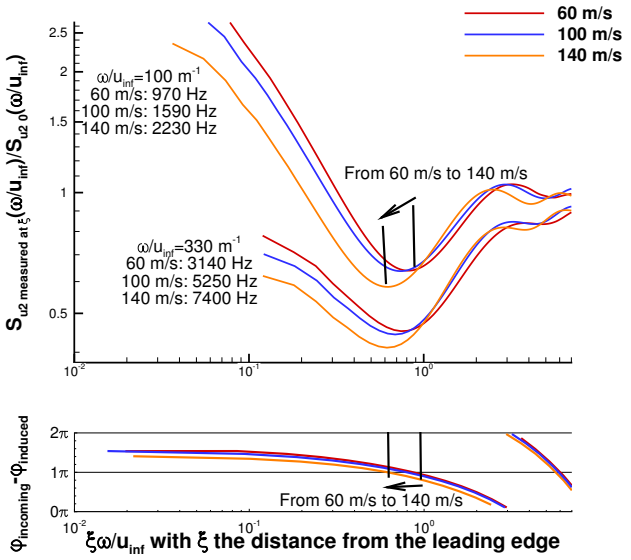


Figure 7.7: Effect of the mean flow velocity on turbulence distortion upstream of the leading edge, using a uniform mean flow assumption. $S_{\text{u2 measured at }\xi}$ is the density spectrum of the transverse velocity $u_2$ at position $\xi$ along the streamline which stops at the stagnation point, $S_{\text{u2 }0}$ is the density spectrum of the transverse velocity $u_2$ at infinity and $\varphi_{\text{incoming}}$ and $\varphi_{\text{induced}}$ are the phase of respectivelly the incoming velocity perturbations and the velocity induced by the bound vortices on the aerofoil surface.

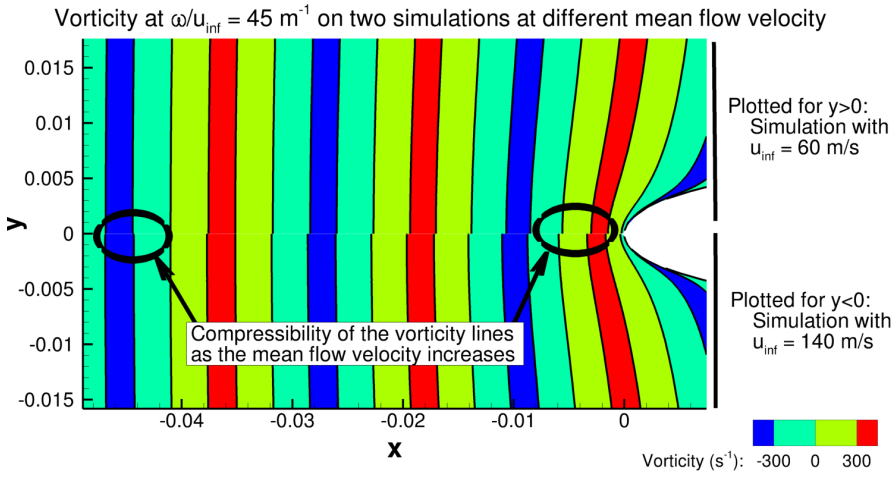


Figure 7.8: Compressibility effect on vorticity field between two mean flow velocities: 60 m/s for $y > 0$ and 140 m/s for $y \leq 0$.

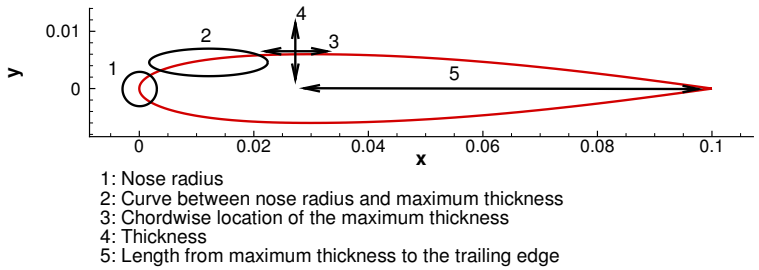


Figure 7.9: List of geometrical factors investigated.

## 7.4 Effects of geometry

To study the effect of aerofoil geometry on turbulence distortion, the geometry is progressively altered from the leading edge to the trailing edge. Firstly, the size of the nose radius is investigated, while keeping the rest of the geometry identical. Then, while keeping a constant nose radius and maximum thickness, the curve which links these two parts is studied. The maximum of thickness is then investigated by first changing its chord-wise location and then its thickness. Finally, the impact of the length from the maximum thickness to the trailing edge of the aerofoil is studied. A sketch of the different geometrical part altered is shown in Figure 7.9.

### 7.4.1 Nose radius

To study the effect of the size of the nose radius, the thickness and location of the maximum ordinate are kept constant throughout the different nose radii considered. Three nose radii have been studied, a nose radius from a NACA0012-63, which acts as a baseline and noted $\mathrm{R_{LE}}$, and then a nose radius two times smaller ($0.5\mathrm{R_{LE}}$) and two times larger ($2\mathrm{R_{LE}}$) than this baseline. To construct these profiles, the parameter $I$ of the modified 4-digit NACA notation [119] is chosen accordingly using equation (6.1). The obtained parameters of the profiles are written in Table 7.1.

| | Nose radius | equivalent index $I$ |
|---|---|---|
| $0.5\mathrm{R_{LE}}$ | $\approx 0.79e^{-3}$ m | $I \approx 4.24$ |
| $\mathrm{R_{LE}}$ | $\approx 1.59e^{-3}$ m | $I = 6$ |
| $2\mathrm{R_{LE}}$ | $\approx 3.17e^{-3}$ m | $I \approx 8.48$ |

Table 7.1: Parameters of the profiles with different nose radii

Figure 7.10a shows the SPL at 90° above the aerofoil with the different nose radii. It depicts that the blunter the nose radius is, the larger the nose reduction occurs at high-frequency, as observed experimentally [99] and numerically [62]. Regarding turbulence distortion (Figure 7.10b), a first observation shows a small difference at low wavenumbers close to the leading edge, yet, it is not visible on the radiated far field noise. This

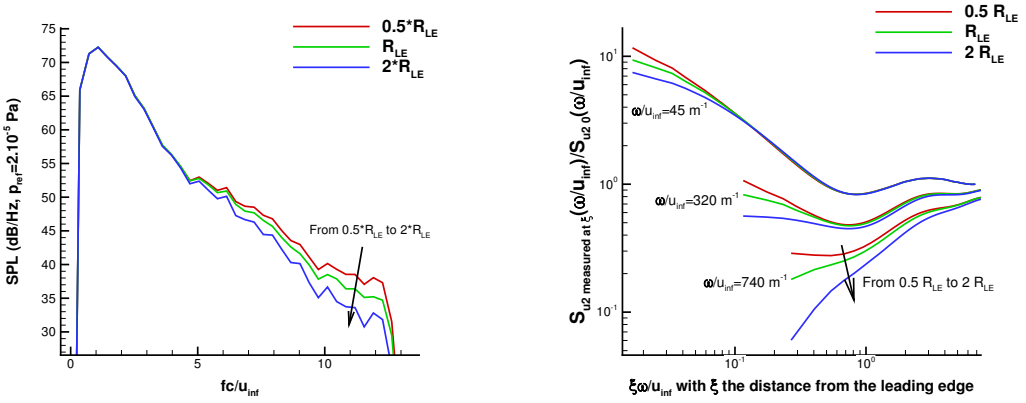


(a) (b)

Figure 7.10: Effect of the nose radius on (a) Sound pressure levels at 90°and R=1.2m above the aerofoil and (b) turbulence distortion upstream of the aerofoil. $S_{\text{u2 measured at }\xi}$ is the density spectrum of the transverse velocity $u_2$ at position $\xi$ along the streamline which stops at the stagnation point, $S_{\text{u2 }0}$ is the density spectrum of the transverse velocity $u_2$ at infinity.

indicates that the distortion of the transverse velocity on the streamline which goes to the stagnation point alone does not seem to provide sufficient information to fully predict the far field radiated noise.

The geometric changes in nose radius are restricted around the leading edge region. Thus, changes in the mean flow are also restricted in this region. A larger nose radius increases the size of the stagnation region, as plotted for the mean flow velocity in the $x$-axis for two nose radii in Figure 7.11a, and has previously been observed by Gill [61] or Kim *et al.* [114]. The stagnation region distorts the incoming vorticity wave fronts, plotted in Figure 7.11b for $\omega/u_\infty = 45$ m$^{-1}$ and in Figure 7.11c for $\omega/u_\infty = 740$ m$^{-1}$. As the stagnation region is larger as the nose radius increases, the wave fronts of the vorticity lines get closer to each others in the $x$-direction, and their inclination above and below the leading edge are more pronounced. This effects is easily visible for large wavenumbers (Figure 7.11c). Nevertheless, for small wavenumbers (Figure 7.11b), the distortion region is small with respect to the wavelength, hence it does not modify the velocity retrieved from the incoming vorticity, plotted in Figure 7.11d. On the other hand, for large wavenumbers, as wavelengths are smaller, it can not be neglected, consequently the velocity retrieved from the incoming vorticity is more attenuated with a larger nose radius (Figure 7.11c).

For small wavenumbers, as the wake contribution is negligible and the velocity retrieved from the incoming vorticity field is not altered, the differences in the distortion of turbulence upstream of the aerofoil in Figure 7.10b come from the induced velocities from the bound vortices on the aerofoil. Indeed, despite having very similar responses with a uniform mean flow, as plotted in Figure 7.12a at $\omega/u_\infty = 45$ m$^{-1}$, very close to the leading edge, the induced velocity responses depict large discrepancies. The sharper

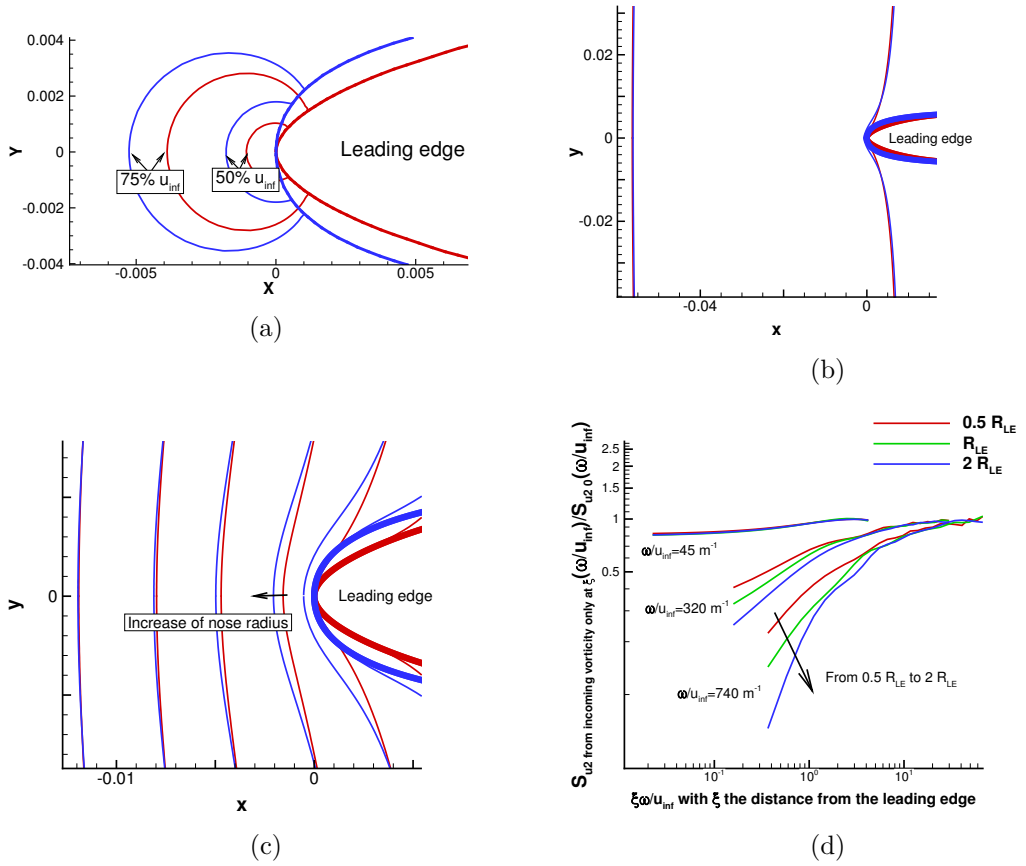


Figure 7.11: Effect of the nose radius on the mean flow, vorticity and velocity retrieved from this vorticity for $I \approx 4.24$ (——), $I = 6$ (——), and $I \approx 8.48$ (——). (a) Iso-lines of the mean flow velocity which depicts the stagnation region, plotted for $I \approx 4.24$ and 8.48. (b) and (c) are the minimal and maximal vorticity wavefronts at respectivelly $\omega/u_\infty = 45$ m$^{-1}$ and 740 m$^{-1}$. (d) is its effect on velocity perturbations retrieved from the incoming vorticity only. $S_{\text{u2 from incoming vorticity only at } \xi}$ is the density spectrum of the transverse velocity $u_2$ retrieved from the incoming vorticity only, at position $\xi$ along the streamline which stops at the stagnation point, $S_{\text{u2 0}}$ is the density spectrum of the transverse velocity $u_2$ at infinity.

nose radius imply a large rise in the induced velocity compared to blunter nose radius, shown in Figure 7.12b upstream of the aerofoil.

The discrepancies in the turbulence distortion upstream of the aerofoils plotted in Figure 7.10b are then due to changes in the shape of the induced velocity from the aerofoil at small wavenumbers, while for large wavenumbers, the attenuation of the velocity retrieved from the distorted vorticity field is dominant.

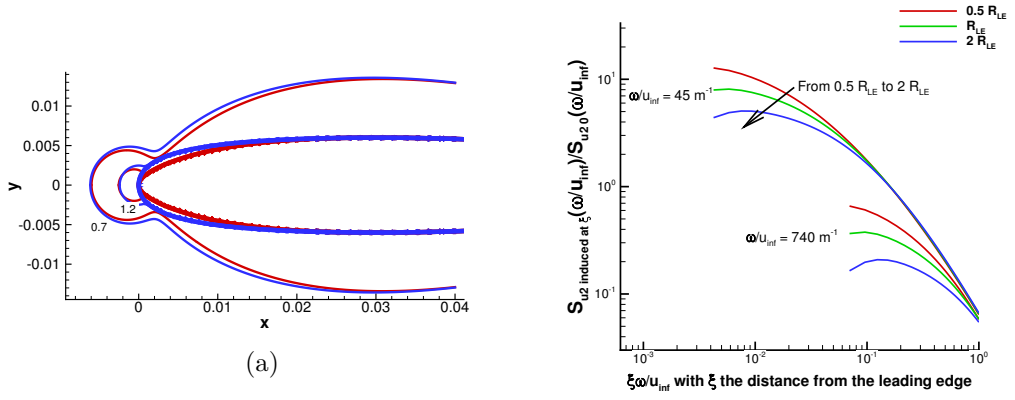


(a) (b)

Figure 7.12: Effect of nose radius on induced velocities from bound vortices on the aerofoil surface in a uniform mean flow for $I \approx 4.24$ (—), $I = 6$ (—), and $I \approx 8.48$ (—). (a) Iso-lines of $S_{\text{u2 induced}}/S_{\text{u2 0}}$ at $\omega/u_\infty = 45$ m$^{-1}$ at two values: 1.2 and 0.7. (b) Evolution of $S_{\text{u2 induced at }\xi}/S_{\text{u2 0}}$ on the streamline which stops at the stagnation point.

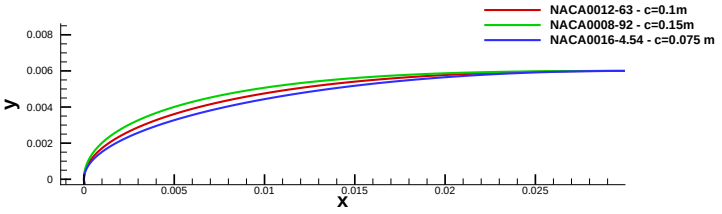


Figure 7.13: Profiles used to study the effect of the curvature forward of the maximum thickness.

### 7.4.2 Curve forward of the maximum thickness

To understand the effect of the curve between the leading edge and the maximum thickness, three profiles are studied. These profiles keep a constant nose radius, thickness and location of the maximum thickness. To construct these profiles, a NACA0012-63 with a chord of $c = 0.1$m is chosen as a baseline. Then, for the two other profiles, only the part forward of the maximum thickness is modified (the part after the maximum thickness and by extension the chord are strictly identical in all three profiles). To obtain the new curves while conserving the same physical dimensions of the nose radius, thickness and location of the maximum thickness, the first modified profile is constructed using a NACA0008-92 with a chord of c=0.15m before the maximum thickness and the second profile uses a NACA0016-$4_{1/2}$4 with a chord of c=0.075m. The resulting profiles are plotted in Figure 7.13 and their parameters are listed in Table 7.2.

Despite having the same nose radius, thickness and location of the maximum thickness, the SPL at 90° above the aerofoil, plotted in Figure 7.14a, shows a noise reduction at high frequencies when the bluntness of the profile after the nose is more important.

| | Foward the maximum thickness | | After the maximum thickness | |
|---|---|---|---|---|
| | 4-digit NACA | Chord | 4-digit NACA | Chord |
| Profile 1 | NACA0008-92 | $c = 0.15$ m | | |
| Profile 2 | NACA0012-63 | $c = 0.1$ m | | |
| Profile 3 | NACA0016-$4_{1/2}$4 | $c = 0.075$ m | NACA0012-63 | $c = 0.1$ m |

Table 7.2: Parameters of the profiles with different curve forward of the maximum thickness

Nevertheless, the far field acoustic reduction is less important than with the changes in nose radii.

A similar trend is observed on the turbulence distortion on the streamline upstream of the aerofoil, plotted in Figure 7.14b. Nevertheless, as the leading edge is being kept identical throughout the profiles and the differences in the curves being small, the mean flow and by extension the vorticity lines have a similar distortion around the nose radius, as plotted for $\omega/u_\infty = 740$ m$^{-1}$ in Figure 7.15a. The only noticeable difference are located very close to the upper and lower surfaces of the aerofoils. Therefore, at large wavenumbers, the retrieved velocities from this distorted vorticity field (Figure 7.15b) depict a smaller impact than with a change of nose radii. Low wavenumbers remain unaltered as their wavelength is large with respect to the distortion region.

Moreover, the shape of the induced velocity responses from aerofoils does not significantly vary with the curve forward of the maximum thickness, regardless of the wavenumber of the perturbations. For instance, the contour lines of the induced velocities for $\omega/u_\infty = 740$ m$^{-1}$ are plotted in Figure 7.16a. On the streamline forward of the leading edge, the induced velocities also show little effect with the variations of the curve, plotted for the three profiles at three different fixed wavenumbers in Figure 7.16b.

Therefore, the discrepancies in the turbulence distortion upstream of the aerofoils plotted in Figure 7.14b are then, regardless of the wavenumber, a combination of both the distortion of the vorticity lines and the changes in the shape of the induced velocity from the aerofoil.

### 7.4.3 Chord-wise location of the maximum thickness

The location of the maximum thickness is now studied for positions ranging from 20% (m=2) to 50% (m=5) of the chord from the leading edge. The resulting profiles are shown in Figure 7.17.

Changing the location of the maximum thickness can be partly assimilated in a change of the curve between the leading edge and the maximum thickness, as studied in Section 7.4.2, yet in this Section, the geometric changes of curves are more significant.

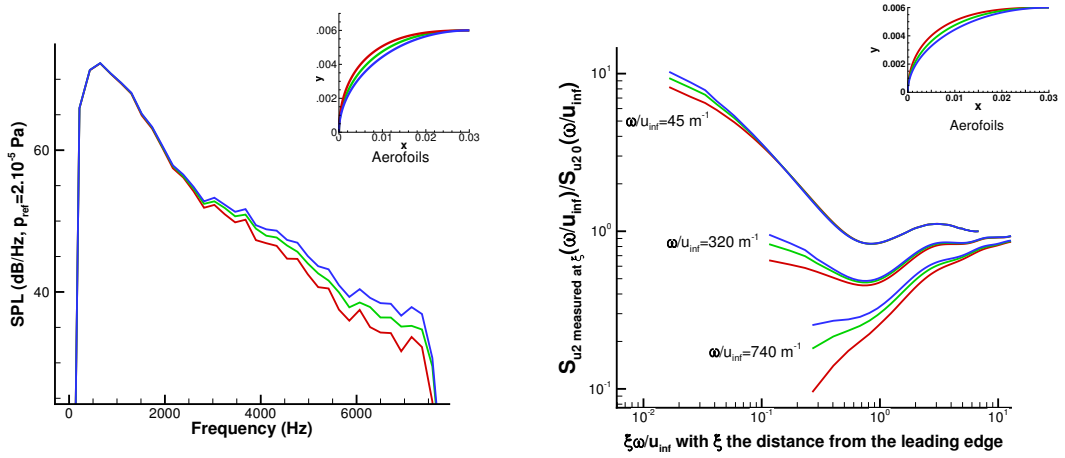


(a) (b)

Figure 7.14: Effect of the curve forward of the maximum thickness on (a) Sound pressure levels at 90°and R=1.2m above the aerofoil and (b) turbulence distortion upstream of the aerofoil. $S_{\mathrm{u2\ measured\ at}\ \xi}$ is the density spectrum of the transverse velocity $u_2$ at position $\xi$ along the streamline which stops at the stagnation point, $S_{\mathrm{u2\ 0}}$ is the density spectrum of the transverse velocity $u_2$ at infinity.

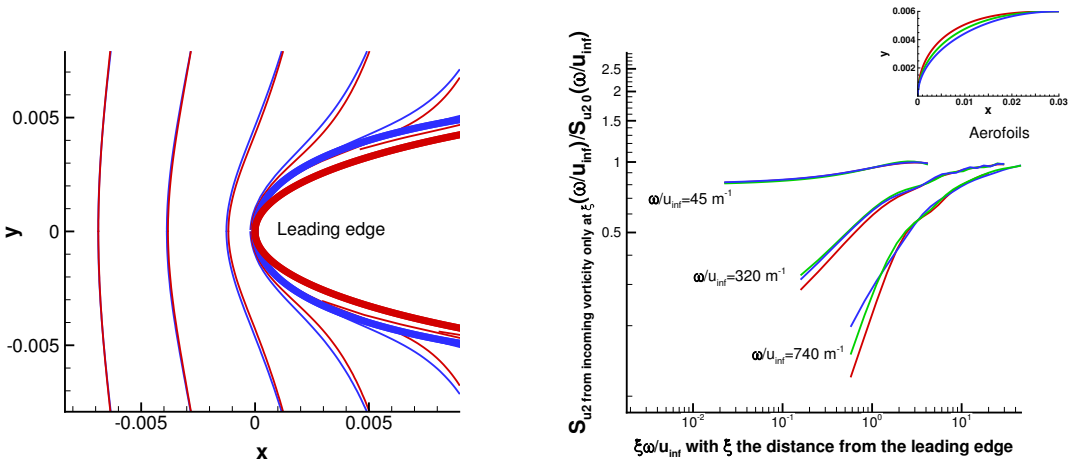


(a) (b)

Figure 7.15: Effect of the curve forward of the maximum thickness on vorticity and the associated velocity for profiles: 1 (—), 2 (—), and 3 (—). See Table 7.2 for details on profiles. (a) Minimal and maximal vorticity wavefront at $\omega/u_\infty = 740$ m$^{-1}$. (b) Velocity perturbations retrieved from the incoming vorticity only. $S_{\mathrm{u2\ from\ incoming\ vorticity\ only\ at}\ \xi}$ is the density spectrum of the transverse velocity $u_2$ retrieved from the incoming vorticity only, at position $\xi$ along the streamline which stops at the stagnation point, $S_{\mathrm{u2\ 0}}$ is the density spectrum of the transverse velocity $u_2$ at infinity.

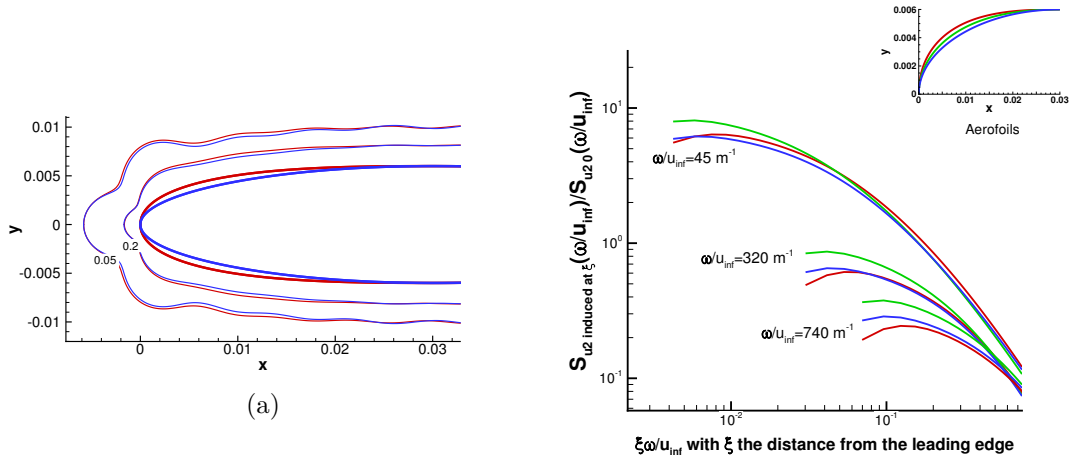


(a) (b)

Figure 7.16: Induced velocities from bound vortices on the aerofoil surface in a uniform mean flow for profiles: 1 (—), 2 (—), and 3 (—). See Table 7.2 for details on profiles. (a) Iso-lines of $S_{\text{u2 induced}}/S_{\text{u2 0}}$ at $\omega/u_\infty = 740$ m$^{-1}$ at two values: 0.05 and 0.2. (b) Evolution of $S_{\text{u2 induced at }\xi}/S_{\text{u2 0}}$ on the streamline which stops at the stagnation point.

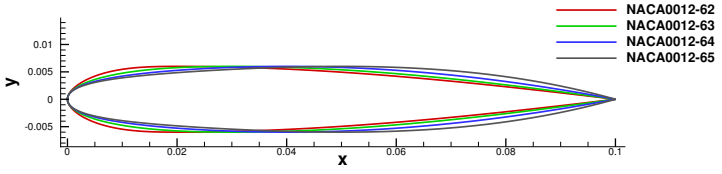


Figure 7.17: NACA0012-6$m$ with $m$ varying from 2 to 5.

Therefore, the SPL above the aerofoil (Figure 7.18a) depicts a similar trend, i.e. the blunter the aerofoil (via a closer location of the maximum thickness to the leading edge), the larger the noise reduction occurs at high-frequency. This trend has been previously observed by Gill [62]. Moreover, the differences in radiated noise are more important between $m = 2$ and $m = 3$ than between $m = 4$ and $m = 5$ as the majority of the geometric changes in this last configuration occur far from the leading edge.

While for the changes of the curve forward of the maximum thickness in Section 7.4.2 the incoming vorticity wave fronts were weakly altered, this time, the changes in curves forward of the maximum are more important, which largely modifies the mean flow in the stagnation region, and thus it alters the incoming vorticity wave fronts as plotted for $\omega/u_\infty = 740$ m$^{-1}$ in Figure 7.19a. While there is a small compression of the vorticity lines with the decrease of $m$, the main changes are located above and lower the leading edge. Consequently, the retrieved velocity from these incoming vorticity fields at large wavenumbers get more attenuated as the geometry gets blunter. On the other hand, like with previous changes in geometry, low wavenumber perturbations stay constant because their wavelength is large with respect to the distorted region.

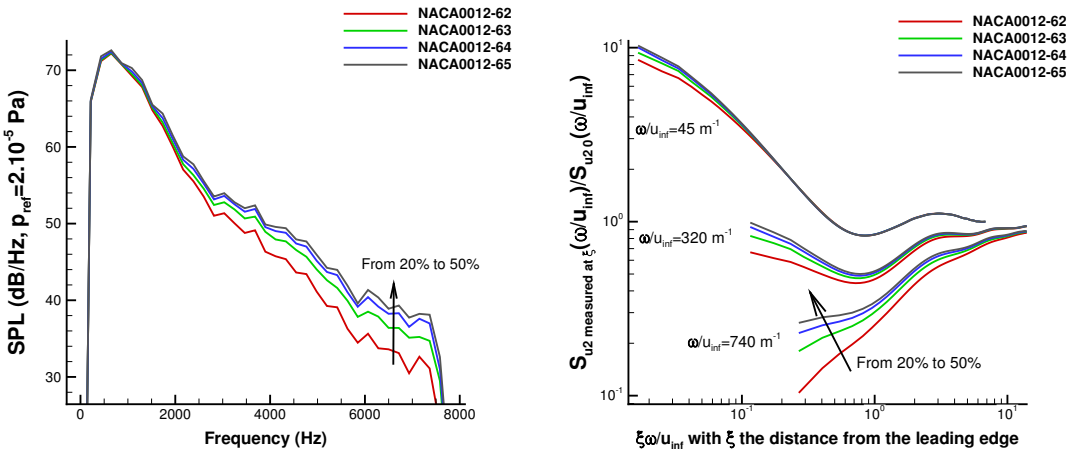


(a) (b)

Figure 7.18: Effect of the location of the maximum thickness curve forward of the maximum thickness with $m = 2$ (—), $m = 3$ (—), $m = 4$ (—) and $m = 5$ (—). (a) Sound pressure levels at 90°and R=1.2m above the aerofoil and (b) turbulence distortion upstream of the aerofoil. $S_{\text{u2 measured at } \xi}$ is the density spectrum of the transverse velocity $u_2$ at position $\xi$ along the streamline which stops at the stagnation point, $S_{\text{u2 }0}$ is the density spectrum of the transverse velocity $u_2$ at infinity.

The shifts of the location of the maximum thickness of the aerofoils largely modify the lower and upper surfaces, while excluding the nose radius area. Thus, the induced velocities are naturally very different around the aerofoils, as plotted for $\omega/u_\infty = 740$ m$^{-1}$ with a uniform mean flow in Figure 7.20a. However, despite these large physical differences, the induced velocity responses for a uniform mean flow depict a surprisingly similar behaviour for the different geometries (Figure 7.20b).

Therefore, the changes in the turbulence distortion upstream of the aerofoils plotted in Figure 7.18b are mostly due to changes in the distortion of the vorticity field around the leading edge region.

### 7.4.4 Thickness

The effect of the maximum thickness is now studied, considering three different thickness (6%, 12% to 24%), each with the same nose radius size. The NACA0012-63 serves as a baseline. To construct the two other profiles while keeping the nose radius of a NACA0012-63, the parameter $I$ of the modified 4-digit NACA notation [119] is chosen accordingly using equation (6.1). The Table 7.3 details the parameters of the profiles.

As previously observed [99, 62], the levels of SPL, plotted at 90° above the aerofoil in Figure 7.21a, depict a large noise reduction as the frequencies and the thickness increase.

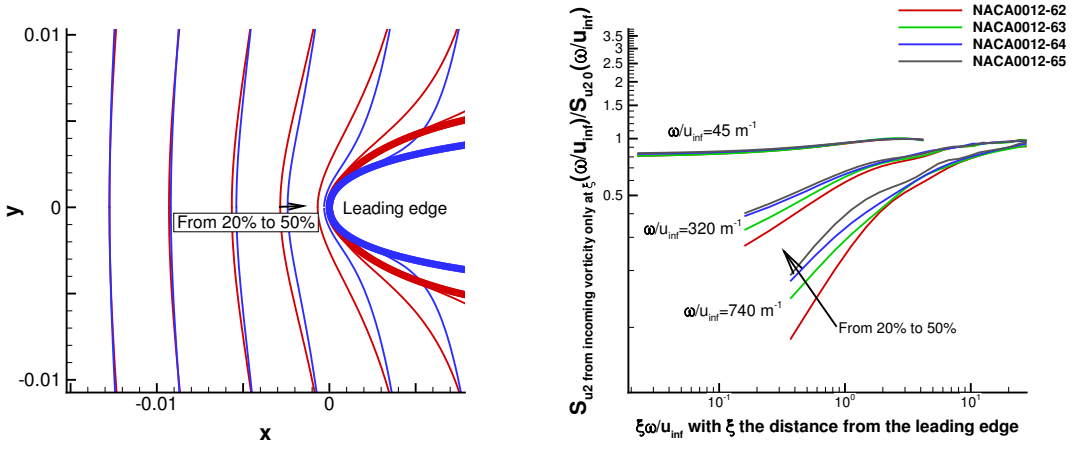


(a) (b)

Figure 7.19: Effect of the location of the maximum thickness on vorticity and the associated velocity for profiles with $m = 2$ (——), $m = 3$ (——), $m = 4$ (——) and $m = 5$ (——). (a) Minimal and maximal vorticity wavefront at $\omega/u_\infty = 740$ m$^{-1}$. (b) Velocity perturbations retrieved from the incoming vorticity only. $S_{\text{u2 from incoming vorticity only at }\xi}$ is the density spectrum of the transverse velocity $u_2$ retrieved from the incoming vorticity only, at position $\xi$ along the streamline which stops at the stagnation point, $S_{\text{u2 0}}$ is the density spectrum of the transverse velocity $u_2$ at infinity.

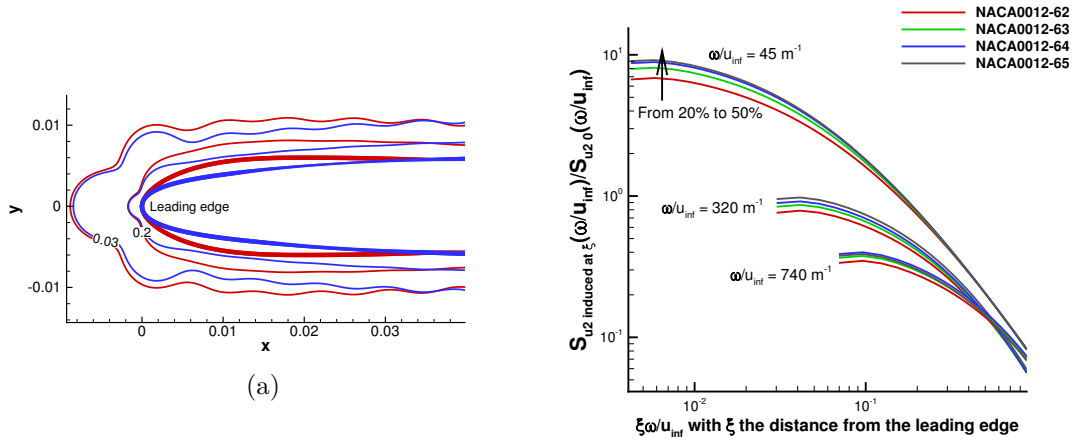


(a) (b)

Figure 7.20: Induced velocities from bound vortices on the aerofoil surface in a uniform mean flow for profiles with $m = 2$ (——), $m = 3$ (——), $m = 4$ (——) and $m = 5$ (——) (a) Iso-lines of $S_{\text{u2 induced}}/S_{\text{u2 0}}$ at two values: 0.03 and 0.2. (b) Evolution of $S_{\text{u2 induced at }\xi}/S_{\text{u2 0}}$ on the streamline which stops at the stagnation point.

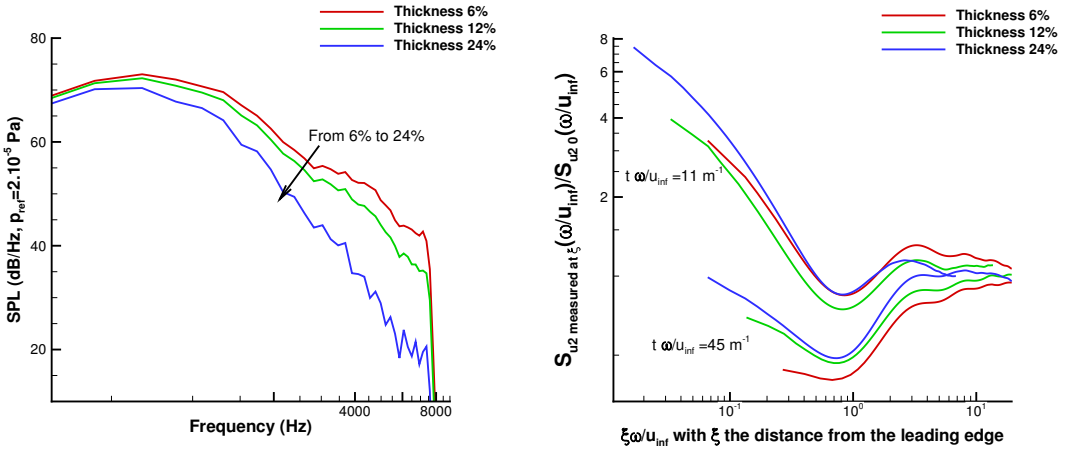


(a) (b)

Figure 7.21: Thickness effect with $t = 6\%$ (——), $t = 12\%$ (——) and $t = 24\%$ (——) on (a) Sound pressure levels at 90°and R=1.2m above the aerofoil and (b) turbulence distortion upstream of the aerofoil. $S_{\text{u2 measured at } \xi}$ is the density spectrum of the transverse velocity $u_2$ at position $\xi$ along the streamline which stops at the stagnation point, $S_{\text{u2 }0}$ is the density spectrum of the transverse velocity $u_2$ at infinity.

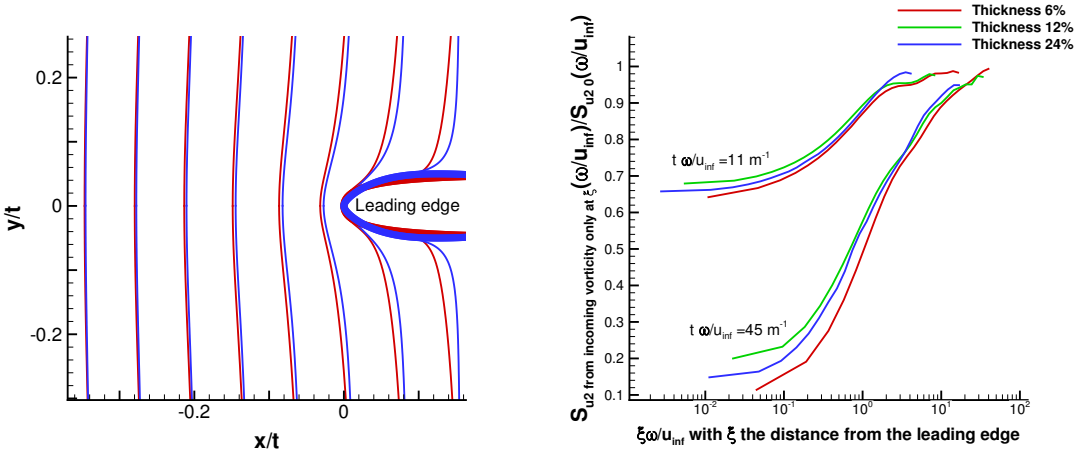


(a) (b)

Figure 7.22: Similarity with $t$ on vorticity and the associated velocity for profiles with $t = 6\%$ (——), $t = 12\%$ (——) and $t = 24\%$ (——). (a) Minimal and maximal vorticity wavefront at $\omega/u_\infty = 740$ m$^{-1}$, plotted as a function of $x/t$ and $y/t$. (b) Velocity perturbations retrieved from the incoming vorticity only, at fixed wavenumbers multiplied by the thickness parameter $t$. $S_{\text{u2 from incoming vorticity only at } \xi}$ is the density spectrum of the transverse velocity $u_2$ retrieved from the incoming vorticity only, at position $\xi$ along the streamline which stops at the stagnation point, $S_{\text{u2 }0}$ is the density spectrum of the transverse velocity $u_2$ at infinity.

| Thickness | Nose radius | equivalent index $I$ |
|---|---|---|
| 6% | $\approx 1.59e^{-3}$ m | $I = 12$ |
| 12% | $\approx 1.59e^{-3}$ m | $I = 6$ |
| 24% | $\approx 1.59e^{-3}$ m | $I = 3$ |

Table 7.3: Parameters of the profiles with different thickness

The thickness parameter $t$ seems to be an important factor regarding the turbulence distortion of the transverse velocity upstream the aerofoil. Indeed, in Figure 7.21b, instead of plotting the distortion of the three profiles at a fixed wavenumber, a partial similarity of the evolution can be obtained with the parameter $t\omega/u_\infty$, yet the curves do not collapse perfectly.

This partial similarity using the parameter $t$ mostly comes from the distortion of the incoming vorticity field. Indeed, when the vorticity lines for a fixed $t\omega/u_\infty$ are plotted with the axis $x/t$, $y/t$, the wave fronts are similar, for instance at $t\omega/u_\infty = 740$ m$^{-1}$ in Figure 7.22a. Therefore, the velocity amplitudes retrieved from the vorticity field are also very close, as plotted in Figure 7.22b.

Nevertheless, this similarity does not seem to apply to the induced velocity with a uniform mean flow (not plotted as no clear trend appears).

### 7.4.5 Length from the maximum thickness to the trailing edge

Finally, the length from the maximum thickness to the trailing edge is investigated. To construct the profiles, a NACA0012-63 with a chord $c = 0.1$m serves as a baseline. Then, after the maximum thickness, the profile is stretched in the chord-wise direction to extend the full chord of the aerofoil to $c = 0.15$m. The two studied profiles are plotted in Figure 7.23.

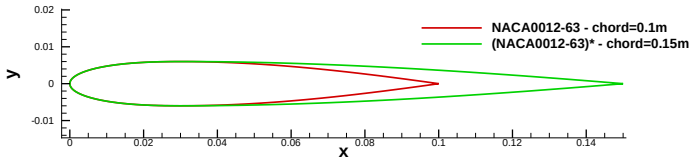


Figure 7.23: Profiles with different length from the maximum thickness to the trailing edge.

As the two considered profiles are identical from the leading edge to the maximum thickness location, the mean flow velocity in the $x$-direction is close to identical around the nose radius and noticeable discrepancies can be observed from the maximum thickness onwards, as plotted in Figure 7.24. Therefore, the stagnation region do not change in between the two profiles.

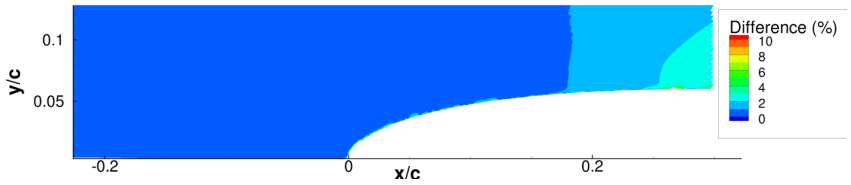


Figure 7.24: Differences in the mean flow velocity in the $x$-direction around the leading edge region between profiles with different length from the maximum thickness to the trailing edge.

The mean flow being very similar forward of the maximum thickness, the distortion of the vorticity lines only differs from the maximum thickness onwards. As a result, the wave fronts of the vorticity lines remain unchanged and therefore are not plotted. Hence, upstream of the aerofoil, the velocities retrieved from the incoming vorticity field are unchanged. Therefore, the distortion of the transverse velocity upstream of the stagnation point is also unchanged as plotted in Figure 7.25b.

The SPL, for instance at 90° above the aerofoil as plotted in Figure 7.25a, does not indicate differences other than those expected from the change in chord length in the Amiet model [60], such as a shift in the lobe location. It suggests that the turbulence distortion does not depend on the geometry after the maximum thickness of the profile. This result further suggests that the boundary layer has a negligible effect on interaction noise [5, 61].

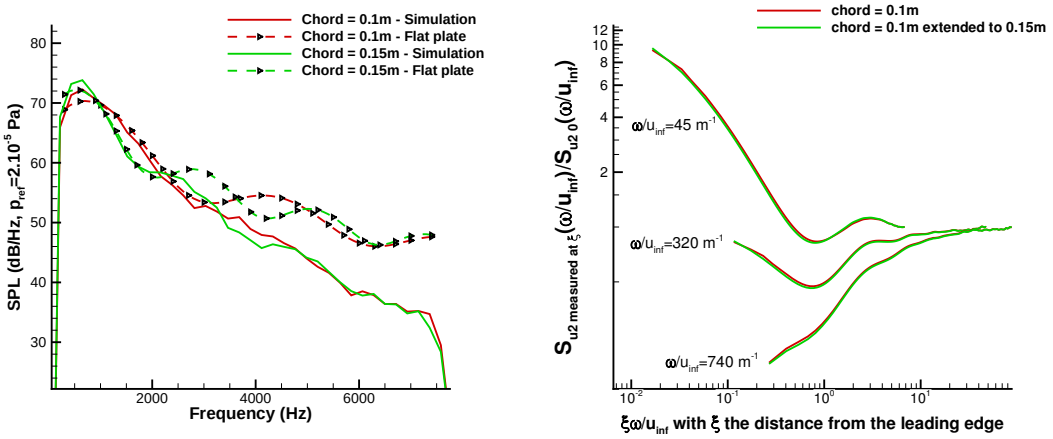


(a) (b)

Figure 7.25: Effect of the length from the maximum thickness to the trailing edge on (a) Sound pressure levels at 90°above the aerofoil at R=1.2m (b) Turbulence distortion upstream the leading edge, using a steady Euler mean flow assumption, plotted for three fixed wavenumbers $\omega/u_\infty$. $S_{\mathrm{u2\ measured\ at\ }\xi}$ is the density spectrum of the transverse velocity $u_2$ at position $\xi$ along the streamline which stops at the stagnation point, and $S_{\mathrm{u2\ 0}}$ is the density spectrum of the transverse velocity $u_2$ at infinity.

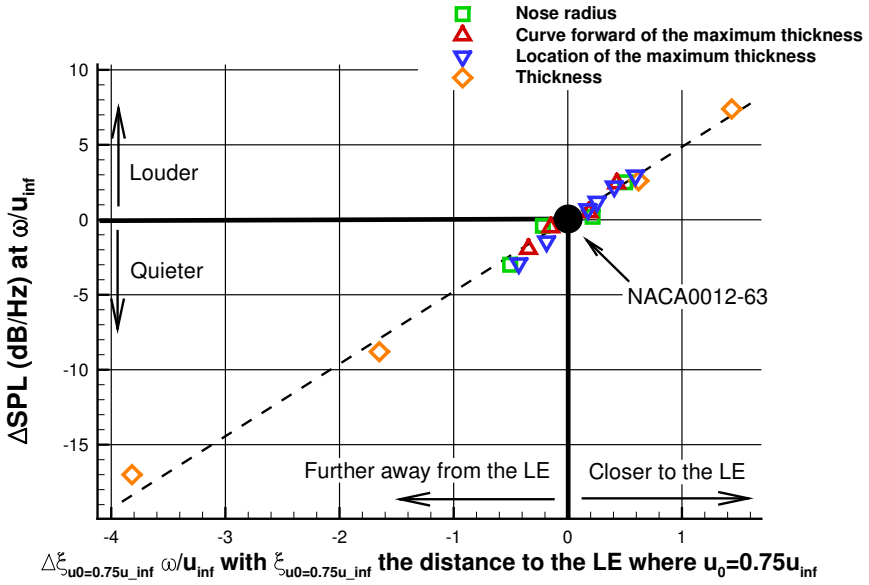


Figure 7.26: Correlation between the size of the stagnation region near the leading edge and the SPL reduction at $\omega/u_\infty = 320$ m$^{-1}$ and 740 m$^{-1}$. The $x$-axis is the difference with the NACA0012-63 case of the distance to the leading edge (where the streamwise mean flow velocity $u_{01}$ is equal to 75% of the mean flow velocity at infinity $u_\infty$), multiplied by the wavenumber $\omega/u_\infty$. The $y$-axis represents the difference with the NACA0012-63 at $u_\infty = 60$ m/s of SPL levels (dB/Hz, $p_{\text{ref}} = 2.10^{-5}$ Pa) at $\omega/u_\infty = 320$ m$^{-1}$ and 740 m$^{-1}$. In green (□) the variation of the nose radius, with each symbol from left to right: $2\text{R}_{\text{LE}}$ at $\omega/u_\infty = 740$ m$^{-1}$, $2\text{R}_{\text{LE}}$ at $\omega/u_\infty = 320$ m$^{-1}$, $0.5\text{R}_{\text{LE}}$ at $\omega/u_\infty = 320$ m$^{-1}$ and $0.5\text{R}_{\text{LE}}$ at $\omega/u_\infty = 740$ m$^{-1}$ with $\text{R}_{\text{LE}}$ the nose radius (see Table 7.1). In red (△) the variation of the curve forward of the maximum thickness, with each symbol from left to right: profile 1 at $\omega/u_\infty = 740$ m$^{-1}$, profile 1 at $\omega/u_\infty = 320$ m$^{-1}$, profile 3 at $\omega/u_\infty = 320$ m$^{-1}$ and profile 3 at $\omega/u_\infty = 740$ m$^{-1}$ 1 (see Table 7.2). In blue (▽) the variation of the chordwise location of the maximum thickness, with each symbol from left to right: $m = 2$ at $\omega/u_\infty = 740$ m$^{-1}$, $m = 2$ at $\omega/u_\infty = 320$ m$^{-1}$, $m = 4$ at $\omega/u_\infty = 320$ m$^{-1}$, $m = 5$ at $\omega/u_\infty = 320$ m$^{-1}$, $m = 5$ at $\omega/u_\infty = 320$ m$^{-1}$ and $m = 5$ at $\omega/u_\infty = 740$ m$^{-1}$ with $m$ the parameter NACA0012-6$m$. In orange (◊) the variation of the maximum thickness, with each symbol from left to right: 24% at $\omega/u_\infty = 740$ m$^{-1}$, 24% at $\omega/u_\infty = 320$ m$^{-1}$, 6% at $\omega/u_\infty = 320$ m$^{-1}$ and 6% at $\omega/u_\infty = 740$ m$^{-1}$. The dashed line (- - -) is the trend line.

### 7.4.6 Size of the stagnation region

The influence of aerofoil geometry on turbulence distortion and far field acoustics investigated in this work shows that the closer the geometry alteration is to the leading, the greater impact it will have on both the turbulence distortion and the far field acoustics. It is mainly because blunter geometries near the leading edges result in larger stagnation regions.

Physically, a larger stagnation region locally skews more the incoming vorticity field. It

results in attenuated transverse velocities retrieved from this vorticity field (via the first term of Equation 6.8). Moreover, the vorticity field is also an input in the vortex panel method via Equation 6.32, therefore the input velocities for the panel method, which can be viewed as the velocities (from the incoming vorticity) which want to get inside the solid boundaries of the aerofoil, are also attenuated. To respect the non-penetration condition, bound vortices are imposed at the surface of the aerofoil and the wake, but if the input of the panel method is smaller, the amplitude of these bound vortices is also less important. Therefore, for all the geometric changes performed in this work, the stagnation region at the leading edge seems the key factor in turbulence distortion and far field acoustics. A correlation is found between the size of the stagnation region and the far field acoustics, as plotted in Figure 7.26. In this figure, to characterize the size of the stagnation region, it has been chosen arbitrary that the stagnation region starts when the streamwise mean flow velocity goes down to 75% of the mean flow velocity at infinity. The correlation is plotted at two wavenumbers $\omega/u_\infty = 320$ m$^-$1 and 740 m$^-$1, but not $\omega/u_\infty = 45$ m$^-$1 as no noise reduction have been obtained at this wavenumber with any of the geometric changes studied in this work. In this case, a near linear trend seems to be obtained, nevertheless other investigations need to be carried out to confirm such behaviour with other geometric parameters as well as other profiles.

## 7.5 Conclusion

This Chapter aims at gaining physical insights as well as understanding the sensitivity of turbulence distortion to changes in turbulence, mean flow and geometrical parameters, to potentially help the design of future analytical or numerical models.

The distortion of the transverse velocity on a single streamline which goes from upstream of the aerofoil to the stagnation point is investigated and is found to be the sum of the velocity retrieved from the vorticity field around the aerofoil and the induced velocity from the bound vortices on the aerofoil and wake, which are created in response to the vorticity field to respect the non-penetration condition at the aerofoil surface. Due to the distance between the wake and the leading edge, the bound vortices in the wake are found to have a negligible effect on turbulence distortion upstream of the aerofoil. With a uniform mean flow assumption, the induced velocity from the bound vortices on the aerofoil is wavenumber dependent and similar regardless of the wavenumber until a distance close to the leading edge. Then, the response gets stronger as the wavenumber decreases. Moreover, most geometrical changes alter the induced aerofoil response, at all wavenumbers.

Due to the phase difference between the velocity retrieved from the vorticity field and the induced velocity, a succession of constructive and destructive waves appears as oscillations on turbulence distortion. This phase difference gets slightly shifted as the

mean flow velocity increases, likely due to compressibility effects, which causes small discrepancies on the distortion of vorticity compared with incompressible cases.

While the distortion of the vorticity field by the mean flow is not wavenumber dependent, its effects is. Indeed, the restricted region around the leading edge where this distortion occurs only alters a small portion of a single wavelength for low wavenumber perturbations, while multiples wavelengths are skewed for large wavenumbers. As a result, the amplitude of the retrieve transverse velocity perturbations at large wavenumbers are largely reduced close to the leading edge, while low wavenumber perturbations remain unchanged. Hence, changes in the geometry which modify the distortion of the vorticity field, especially close to the leading edge such as the nose radius, only alters large wavenumbers. On the other hand, none of the considered geometries modified the low wavenumber perturbations retrieved from the vorticity field. Moreover, the velocities from the incoming vorticity are also attenuated at the surface of the aerofoil, resulting in less intense bound vortices, and therefore smaller induced velocities. Thus, the size of the stagnation region is a key element in turbulence distortion as the bigger the size of the stagnation region, the more skewed the vorticity field is, hence the retrieve velocities from this vorticity and the bound vortices are smaller. Furthermore, attenuated turbulence levels mostly resulted in noise reductions in this work, which is confirmed by the correlation found between the size of the stagnation region and the far field acoustics. If such correlation can be generalized for 2D aerofoils, it could lead to improved analytical models, or allow for quick noise predictions with respect to a baseline case by only using mean flow calculations.

Finally, in some cases, there are a few small dicrepencies in turbulence distortion, yet they do not appear on the far field acoustic response, which yields to the conclusion that the distortion of the transverse velocity on the streamline which goes to the stagnation point alone does not provide sufficient information to predict far field noise. Hence, further research needs to be performed to understand the relation between turbulence distortion and radiated noise.

# Chapter 8

# Conclusion and future work

## 8.1 Stochastic methods

From a literature review on numerical methods to generate synthetic turbulence and predict interaction noise, the choice to use frozen turbulence injected in the computational domain has been made. Indeed, frozen turbulence is satisfactory to study interaction noise and is less computationally expensive in comparison to evolving turbulence as it does not require to follow the particles after their injection. This is particularly important to make this project easily expandable to more realistic configurations such as profiles in cascade in 2D or to full 3D simulations. Moreover, to synthesize turbulence, a discretized distribution of vortices is preferred over a sum of Fourier modes approach as it can become resource intensive when a large number of frequencies is required.

The perturbations are directly injected in the domain which simplifies the convection by the mean flow as it is naturally done by the governing equations. Unlike a windowing function or an inlet boundary, a new method using localized vorticity sources is proposed to inject frozen perturbations. Its main advantage is its ease of implementation in a already existing CAA solver, with no influence on its parallelization. The proposed method can be used to generate either one-component or two-component turbulence. For the two-component turbulence, it allows to independently control the turbulent spectrum in the two directions, thus it could be used to synthesize isotropic turbulent fields as well as anisotropic turbulent fields.

## 8.2 Interaction noise

The proposed method to inject turbulence is implemented in a CAA solver named PIANO. It contains the LEE model, a linear inviscid interaction model between vorticity and sound capable of supporting vortical, entropy and acoustic modes. It is applied on

an isolated NACA 65(12)10 aerofoil which is a cambered and thick aerofoil. Indeed, for such complex 2D geometries, numerical models are still required as analytical flat plate models overestimate noise predictions at high frequencies. This case, part of the Fundamental test Case 1 (FC1) of the Fan Stage Broadband Noise Benchmarking Programme, is compared with good agreement against experiments and confirms the suitability of such numerical approach for interaction noise.

To perform fast acoustic predictions, analytical methods seem ideal, nevertheless, they still fail to fully take into account the effect of the mean flow on the incoming perturbations for thick aerofoils. Indeed, the use of inviscid mean flows over uniform mean flows allowed to numerically provide accurate radiated noise, from low frequency to high frequencies. This also suggests that the boundary layer region has a weak influence on the interaction noise generation mechanisms in 2D profiles.

## 8.3 Turbulence distortion

Compared to a uniform mean flow, inviscid or viscous mean flows distort the incoming turbulence, which is believed to play an important role for high frequencies perturbations. To study turbulence distortion, in combination with the LEE model, a vorticity approach in the frequency domain is developed. It shows that the distortion of turbulence is the sum of the velocity retrieved from the vorticity field around the aerofoil and the induced velocity from the bound vortices on the aerofoil and wake, which are created in response to the vorticity field to respect the non-penetration condition at the aerofoil surface.

On the streamline upstream of the aerofoil which goes to the stagnation point, the turbulence levels depict oscillations, which are the result of a phase difference between the velocity retrieved from the vorticity field and the induced velocities from the bound vortices, which forms a succession of constructive and destructive waves.

Due to the distance between the wake and the leading edge, the bound vortices in the wake are found to have a negligible effect on turbulence distortion upstream of the aerofoil. With a uniform mean flow assumption, the induced velocity from the bound vortices on the aerofoil is wavenumber dependent and similar regardless of the wavenumber until a distance close to the leading edge. Then, the response gets stronger as the wavenumber decreases.

With realistic mean flows, the vorticity field gets distorted close to the leading edge by the mean flow, and this effect can be easily visualized using streamlines and drift lines. The larger the stagnation region at the leading edge is, the more skewed the incoming vorticity field is. It results in attenuated transverse velocities retrieved from this vorticity field as well as reduced velocity perturbations from the bound vortices. Therefore, for

all the geometric changes performed in this work, the stagnation region at the leading edge seems the key factor in turbulence distortion. Moreover, attenuated turbulence levels mostly resulted in noise reductions, which is confirmed by the correlation between the size of the stagnation region and the far field acoustics. If such correlation can be generalized for 2D aerofoils, it could allow for quick noise predictions with respect to a baseline case by only using mean flow calculations. It can also help designing new analytical models, as accounting for the full geometry is cumbersome.

However, the size of the region where this distortion occurs implies different consequences based on the wavenumber of the perturbations. At low wavenumbers, this region is small with respect to the wavelength, thus only a small portion of a single wavelength is altered. On the other hand, at large wavenumber perturbations, the distortion skews multiple wavelengths. As a result, at low wavenumbers, no change of the geometry altered the distortion of turbulence while at large wavenumbers, important discrepancies on the turbulence levels can be obtained resulting in important modification of the noise levels. To maximize the effect on the distortion of turbulence, the geometric changes need to be located as close as possible to the leading edge, as it will have more influence on the size of the stagnation region. Indeed, in this work, the geometry after the maximum thickness is found to have no effect on turbulence distortion, further suggesting that the boundary layer has a weak influence on interaction noise.

## 8.4 Future work

There are several ways in which this work could be extended by future investigations.

### Extend the 2D parametric study

Extend the 2D parametric study on turbulence distortion to more geometric and mean flow factors. Indeed, this study could be extended to the effect of camber, the effect of the angle of attack, as well as aerofoils in cascade, to study its impact on turbulence distortion and potentially help better understand the physics of more realistic OGV configurations. However, for asymmetric aerofoils, as the vortex panel method is decribed in the steady-state frequency domain (Section 6.2.2), the direction of the wake vortices could be an issue.

### Investigate the links with acoustics

Investigate the relation between turbulence distortion and far field acoustics. This could provide a fast interaction noise prediction without the need to run CAA or more complex simulations. However, as observed in Chapter 7, not every changes in the distortion

of the incoming turbulence upstream of the aerofoil imply a change in the far field radiated acoustic. Hence, it suggests that only investigating turbulence distortion on a single streamline which goes to the stagnation point is not sufficient for interaction noise predictions, therefore using multiple streamlines seems required.

Another strategy could be to directly compute the unsteady pressure on the aerofoil surface and use a Ffowcs-Williams Hawking analogy to propagate the acoustics to the far field. To determine the unsteady pressure on the surface, the unsteady Bernoulli equation can be used [115].

Finally, if the correlation between the size of the stagnation region and the noise levels can be generalized for 2D aerofoils, it could help design improved analytical models, or allow for quick noise predictions with respect to a baseline case by only performing mean flow calculations.

### 3D profiles

Extend the turbulence distortion study to 3D profiles. Indeed, some innovative leading edge serrations showed very promising interaction noise reductions [127], hence, to help understand the physics, investigate turbulence distortion in such complex geometries could provide useful insights. This requires to extend this work in 3D where vorticity streching needs to be added to the vorticity equation, and necessarily on multiple streamlines in the spanwise direction. A numerical vorticity approach used for a different purpose than turbulence distortion, was developed by Glegg *et al.* [115] to consider 3D geometries. However, the geometries were extruded in the span direction over a large distance (no serrations), hence the problem was reduced to a 2D problem.

# Appendices

# Appendix A

# Spatial distribution of the source term and its associated Fourier transform

A vortex source term $\mathbf{S}_v$ is the curl of a velocity vector potential which ensure a divergence-free flow. We assume that the velocity potential $\mathbf{\Psi}(\mathbf{x}, t)$ is a Gaussian distribution

$$\mathbf{\Psi}(\mathbf{x}, t) = Ab\sqrt{\frac{e}{\ln(4)}} \exp\left[-\ln(2)\frac{|\mathbf{x} - \mathbf{x}_c|^2}{b^2}\right] s(t)\mathbf{e}_\Psi, \tag{A.1}$$

where $b$ is the half-radius of the Gaussian, $A$ a parameter of the amplitude, $\mathbf{x}_c$ the coordinates of the centre of the Gaussian, $s(t)$ the temporal signal and $\mathbf{e}_\Psi$ the axis of rotation.

The source term is expressed as

$$\mathbf{S}_v(\mathbf{x}, t) = \nabla \times \mathbf{\Psi}(\mathbf{x}, t), \tag{A.2}$$

which gives

$$\mathbf{S}_v(\mathbf{x}, t) = A\mathbf{e}_\Psi \times (\mathbf{x} - \mathbf{x}_c)\frac{(e\ln(4))^{0.5}}{b} \exp\left[-\ln(2)\frac{|\mathbf{x} - \mathbf{x}_c|^2}{b^2}\right] s(t). \tag{A.3}$$

We can identify the spatial distribution $\mathbf{g}(\mathbf{x})$ of the source term, and is defined as $\mathbf{S}_v(\mathbf{x}, t) = \mathbf{g}(\mathbf{x})s(t)$

$$\mathbf{g}(\mathbf{x}) = A\mathbf{e}_\Psi \times (\mathbf{x} - \mathbf{x}_c)\frac{(e\ln(4))^{0.5}}{b} \exp\left[-\ln(2)\frac{|\mathbf{x} - \mathbf{x}_c|^2}{b^2}\right]. \tag{A.4}$$

We suppose the axis of rotation is the z-axis, hence $\mathbf{e}_\Psi = \begin{pmatrix} 0 \\ 0 \\ 1 \end{pmatrix}$. It follows

$$\mathbf{g}(\mathbf{x}) = \begin{pmatrix} g_1(\mathbf{x}) \\ g_2(\mathbf{x}) \\ g_3(\mathbf{x}) \end{pmatrix} = \begin{pmatrix} -y + y_c \\ x - x_c \\ 0 \end{pmatrix} A\sqrt{e}\frac{\sqrt{2\ln 2}}{b} \exp\left(-\frac{\ln 2}{b^2}|\mathbf{x} - \mathbf{x}_c|^2\right). \tag{A.5}$$

## A.1 Streamwise direction

On the streamwise direction, it writes

$$g_1(x, y) = -A\sqrt{e}\frac{\sqrt{2\ln 2}}{b}(y - y_c)\exp\left[-\frac{\ln 2}{b^2}\left((x - x_c)^2 + (y - y_c)^2\right)\right]. \tag{A.6}$$

Its forward Fourier transform on the streamwise direction gives

$$\hat{g}_1(k_x, y) = \frac{1}{2\pi}\int_{\Re} g_1(x, y)\mathrm{e}^{+\mathrm{i}k_x x}\mathrm{d}x, \tag{A.7}$$

$$\hat{g}_1(k_x, y) = -\frac{1}{2\pi}A\sqrt{e}\frac{\sqrt{2\ln 2}}{b}(y - y_c)\exp\left[-\frac{\ln 2}{b^2}(y - y_c)^2\right]\int_{\Re}\exp\left[-\frac{\ln(2)}{b^2}(x - x_c)^2\right]\mathrm{e}^{+\mathrm{i}k_x x}\mathrm{d}x. \tag{A.8}$$

Using the change of variable $\frac{X^2}{2} = \frac{\ln 2}{b^2}(x - x_c)^2$,

$$\hat{g}_1(k_x, y) = -\frac{A\sqrt{e}}{2\pi}(y - y_c)\exp\left[-\frac{\ln 2}{b^2}(y - y_c)^2\right]\exp\left(\mathrm{i}k_x x_c\right)\int_{\Re}\exp\left[-\frac{X^2}{2}\right]\exp\left[\mathrm{i}k_x\sqrt{\frac{b^2}{2\ln 2}}X\right]\mathrm{d}X, \tag{A.9}$$

However, we know that

$$\int_{\Re}\exp\left(-\frac{x^2}{2}\right)\mathrm{e}^{+\mathrm{i}ax}\mathrm{d}x = \sqrt{2\pi}\exp\left(-\frac{a^2}{2}\right), \tag{A.10}$$

which gives

$$\hat{g}_1(k_x, y) = -\frac{A\sqrt{e}}{\sqrt{2\pi}}\frac{b}{\sqrt{2\ln 2}}(y - y_c)\exp\left[-\frac{\ln 2}{b^2}(y - y_c)^2\right]\exp\left(\mathrm{i}k_x x_c\right)\exp\left[-\frac{b^2}{4\ln 2}k_x^2\right], \tag{A.11}$$

Given the decomposition $\hat{g}_1(k_x, y) = \hat{g}_{1x}(k_x)g_{1y}(y)$, with

$$\hat{g}_{1x}(k_x) = -\frac{A\sqrt{e}}{\sqrt{2\pi}}\frac{b}{\sqrt{2\ln 2}}\exp\left(\mathrm{i}k_x x_c\right)\exp\left[-\frac{b^2}{4\ln 2}k_x^2\right], \tag{A.12}$$

and

$$g_{1y}(y) = (y - y_c)\exp\left[-\frac{\ln(2)}{b^2}(y - y_c)^2\right]. \tag{A.13}$$

We can then write

$$\hat{g}_{1y}(k_y) = \frac{1}{2\pi}\int_{\Re}(y-y_c)\exp\left[-\frac{\ln(2)}{b^2}(y-y_c)^2\right]\exp\left(\mathrm{i}k_y y\right)\mathrm{d}y. \tag{A.14}$$

Using a change of variable $\frac{Y^2}{2} = \frac{\ln 2}{b^2}(y-y_c)^2$,

$$\hat{g}_{1y}(k_y) = \frac{1}{2\pi}\frac{b}{\sqrt{2\ln 2}}\exp(\mathrm{i}k_y y_c)\int_{\Re} Y\exp\left[-\frac{Y^2}{2}\right]\exp\left[\mathrm{i}k_y\sqrt{\frac{b^2}{2\ln 2}}Y\right]\mathrm{d}Y. \tag{A.15}$$

However, we know that

$$\int_{\Re} x\exp\left(-\frac{x^2}{2}\right)\mathrm{e}^{+\mathrm{i}kx}\mathrm{d}x = +\mathrm{i}2\sqrt{\pi}k\exp\left(-\frac{k^2}{2}\right), \tag{A.16}$$

hence

$$\hat{g}_{1y}(k_y) = \frac{\mathrm{i}}{\sqrt{\pi}}\left(\frac{b}{\sqrt{2\ln 2}}\right)^2 k_y\exp(\mathrm{i}k_y y_c)\exp\left[-\frac{b^2}{4\ln 2}k_y^2\right]. \tag{A.17}$$

## A.2 Transverse direction

On the transverse direction, it writes

$$g_2(x,y) = A\sqrt{e}\frac{\sqrt{2\ln 2}}{b}(x-x_c)\exp\left[-\frac{\ln 2}{b^2}\left((x-x_c)^2+(y-y_c)^2\right)\right]. \tag{A.18}$$

Its forward Fourier transform on the streamwise direction gives

$$\hat{g}_2(k_x,y) = \frac{1}{2\pi}\int_{\Re} g_2(x,y)\mathrm{e}^{+\mathrm{i}k_x x}\mathrm{d}x, \tag{A.19}$$

$$\hat{g}_2(k_x,y) = \frac{A\sqrt{e}}{2\pi}\frac{\sqrt{2\ln 2}}{b}\exp\left[-\frac{\ln 2}{b^2}(y-y_c)^2\right]\int_{\Re}(x-x_c)\exp\left[-\frac{\ln(2)}{b^2}(x-x_c)^2\right]\exp\left(\mathrm{i}k_x x\right)\mathrm{d}x. \tag{A.20}$$

This last equation can also be written as follow, using a change of variable $X = \frac{\sqrt{2\ln 2}}{b}(x-x_c)$

$$\hat{g}_2(k_x,y) = \frac{A\sqrt{e}}{2\pi}\frac{b}{\sqrt{2\ln 2}}\exp\left[-\frac{\ln(2)}{b^2}(y-y_c)^2\right]\exp(\mathrm{i}k_x x_c)$$
$$\int_{\Re} X\exp\left(-\frac{X^2}{2}\right)\exp\left[\mathrm{i}k_x\left(\frac{Xb}{\sqrt{2\ln(2)}}+x_c\right)\right]\mathrm{d}X. \tag{A.21}$$

However, we know that

$$\int_{\Re} x\exp\left(-\frac{x^2}{2}\right)\exp\left(+\mathrm{i}kx\right)\mathrm{d}x = +\mathrm{i}2\sqrt{\pi}k\exp\left(-\frac{k^2}{2}\right), \tag{A.22}$$

hence, we have

$$\hat{g}_2(k_x, y) = \mathrm{i}\frac{A\sqrt{e}}{\sqrt{\pi}}\left(\frac{b}{\sqrt{2\ln 2}}\right)^2 k_x \exp(\mathrm{i}k_x x_c)\exp\left[-\frac{\ln 2}{b^2}(y-y_c)^2\right]\exp\left[-\frac{b^2}{4\ln 2}k_x^2\right], \tag{A.23}$$

Given the decomposition $\hat{g}_2(k_x, y) = \hat{g}_{2x}(k_x)g_{2y}(y)$, with

$$\hat{g}_{2x}(k_x) = \mathrm{i}\frac{A\sqrt{e}}{\sqrt{\pi}}\left(\frac{b}{\sqrt{2\ln 2}}\right)^2 k_x \exp(\mathrm{i}k_x x_c)\exp\left[-\frac{b^2}{4\ln 2}k_x^2\right], \tag{A.24}$$

and

$$g_{2y}(y) = \exp\left[-\frac{\ln 2}{b^2}(y-y_c)^2\right]. \tag{A.25}$$

We can then write

$$\hat{g}_{2y}(k_y) = \frac{1}{2\pi}\int_{\Re}\exp\left[-\frac{\ln 2}{b^2}(y-y_c)^2\right]\exp\left(\mathrm{i}k_y y\right)\mathrm{d}y. \tag{A.26}$$

Using the change of variable $\frac{Y^2}{2} = \frac{\ln 2}{b^2}(y-y_c)^2$,

$$\hat{g}_{2y}(k_y) = \frac{1}{2\pi}\sqrt{\frac{b^2}{2\ln 2}}\exp\left(\mathrm{i}k_y y_c\right)\int_{\Re}\exp\left[-\frac{Y^2}{2}\right]\exp\left[\mathrm{i}k_y\sqrt{\frac{b^2}{2\ln 2}}Y\right]\mathrm{d}Y, \tag{A.27}$$

$$\hat{g}_{2y}(k_y) = \frac{b}{\sqrt{2\pi}\sqrt{2\ln 2}}\exp\left(\mathrm{i}k_y y_c\right)\exp\left[-\frac{b^2}{4\ln 2}k_y^2\right]. \tag{A.28}$$

## A.3 Summary

Using the spatial distribution $\mathbf{g}$ in 2D expressed as

$$\begin{pmatrix} g_1(\mathbf{x}) \\ g_2(\mathbf{x}) \end{pmatrix} = \begin{pmatrix} -y+y_c \\ x-x_c \end{pmatrix} A\sqrt{e}\frac{\sqrt{2\ln 2}}{b}\exp\left(-\frac{\ln 2}{b^2}|\mathbf{x}-\mathbf{x}_c|^2\right), \tag{A.29}$$

the forward Fourier transform on the streamwise direction of $g_2$, defined by

$$\hat{g}_2(k_x, y) = \frac{1}{2\pi}\int_{\Re} g_2(x, y)\mathrm{e}^{+\mathrm{i}k_x x}\mathrm{d}x, \tag{A.30}$$

gives

$$\hat{g}_2(k_x, y) = \mathrm{i}\frac{A\sqrt{e}}{\sqrt{\pi}}\left(\frac{b}{\sqrt{2\ln 2}}\right)^2 k_x \exp(\mathrm{i}k_x x_c)\exp\left[-\frac{\ln 2}{b^2}(y-y_c)^2\right]\exp\left[-\frac{b^2}{4\ln 2}k_x^2\right], \tag{A.31}$$

and the double spatial Fourier transform in the x- and y-direction, defined by

$$\hat{\mathbf{g}}(\mathbf{k}) = \begin{pmatrix} \hat{g_1}(\mathbf{k}) \\ \hat{g_2}(\mathbf{k}) \end{pmatrix} = \frac{1}{4\pi^2}\iint_{\Re^2}\mathbf{g}(\mathbf{x})\exp\left(\mathrm{i}\mathbf{k}.\mathbf{x}\right)\mathrm{d}\mathbf{x}, \tag{A.32}$$

gives

$$\begin{pmatrix} \hat{g_1}(\mathbf{k}) \\ \hat{g_2}(\mathbf{k}) \end{pmatrix} = \mathrm{i}\frac{A\sqrt{e}}{\pi\sqrt{2}} \left( \frac{b}{\sqrt{2\ln 2}} \right)^3 \begin{pmatrix} -k_y \\ k_x \end{pmatrix} \exp\left(\mathrm{i}\mathbf{k}.\mathbf{x}_c\right) \exp\left( -\frac{b^2}{4\ln 2} |\mathbf{k}|^2 \right). \tag{A.33}$$

# Appendix B

# Acoustic analogy and Green function

## B.1 Ffowcs-Williams & Hawkings analogy

The Ffowcs-Williams & Hawkings analogy is an exact rearrangement of the general Navier-Stokes equations with the assumption that the source region is limited within a control surface. It simplifies to a non homogeneous wave equation with equivalent sources located on the control surface that will generate the same acoustic field as if the full Navier-Stokes equations were solved. These equivalent sources are separated into monopole $Q$, dipole $F$ and quadrupole $T$ sources. The integral form of the analogy is given here [109, 110] in the frequency domain

$$\begin{aligned}\hat{p}(\mathbf{y},\omega) = &\iint_S \mathrm{i}\omega\hat{Q}_n(\mathbf{x},\omega)\hat{\mathcal{G}}(\mathbf{y}|\mathbf{x},\omega)\,\mathrm{d}S + \iint_S \hat{F}_i(\mathbf{x},\omega)\frac{\partial\hat{\mathcal{G}}(\mathbf{y},\omega|\mathbf{x})}{\partial x_i}\,\mathrm{d}S \\ &+ \iiint_V \hat{T}_{ij}(\mathbf{x},\omega)\frac{\partial^2\hat{\mathcal{G}}(\mathbf{y},\omega|\mathbf{x})}{\partial x_i\partial x_j}\,\mathrm{d}V\end{aligned} \tag{B.1}$$

with $\mathbf{y}$ the location of the observer, $\mathbf{x}$ the points on the control surface $S$ and $\hat{\mathcal{G}}(\mathbf{y}|\mathbf{x},\omega)$ the Green function in the frequency domain. $\mathbf{n}$ are the outwards unit normals associated with the control surface $S$ and

- $Q_n = [(\rho_0+\rho')(u_{0i}+u_i') - \rho_0 u_{0i}]\,n_i$ represents the monopole contribution,
- $F_i = \Big[(p_0+p')\delta_{ij} + (\rho_0+\rho')(u_i'-u_{0i})(u_{0j}+u_j') + \rho_0 u_{0i}u_{0j}\Big]\,n_j$ represents the dipole contribution,
- $T_{ij}$ is the Lighthill stress tensor, associated to the quadrupole contribution.

The sources are assumed to be contained within the control surface, hence the volumetric integral corresponding to the quadrupolar contribution is equal to zero. The source term contributions are calculated in the temporal domain, and then the Fourier transform is applied to $Q_n$ and $F_i$.

The analytical model (i.e. LEE) used is linear, and the acoustic propagation is assumed to be linear, hence we can linearise the FWH equations. Moreover, the steady components do not contribute to the farfield acoustic, hence it can be reduced to $Q_n = [\rho_0 u_i' + \rho' u_{0i}]\, n_i$ and $F_i = \left[p'\delta_{ij} + (\rho_0 u_i' - \rho' u_{0i})\, u_{0j} - \rho_0 u_{0i} u_j'\right] n_j$.

## B.2 Green function in the frequency domain (free-field and uniform mean flow)

The Green function describes the response at the position $\mathbf{y}$ of an impulse coming from position $\mathbf{x}$. They are written below in the frequency domain, for a problem in free-space with a uniform mean flow on the $x_1$-axis.

### B.2.1 2D

In two dimensions, the convected Green function can be expressed [128]

$$\hat{\mathcal{G}}^{2D}(\mathbf{y}|\mathbf{x},\omega) = \frac{\mathrm{i}}{4\beta} H_0^{(2)}\left(\frac{kS_0}{\beta^2}\right) \exp\left(\frac{\mathrm{i}kM_x}{\beta^2}(y_1 - x_1)\right) \tag{B.2}$$

where $S_0 = \sqrt{(y_1 - x_1)^2 + \beta^2 (y_2 - x_2)^2}$, $\beta^2 = 1 - M_x^2$ and $H_0^{(2)}(.)$ is the Hankel function of the second kind and $0^{th}$ order. It directly follows the derivatives in the spatial directions

$$\frac{\partial \hat{\mathcal{G}}^{2D}(\mathbf{y}|\mathbf{x},\omega)}{\partial x_1} = \frac{k}{4\beta^3} \exp\left(\frac{\mathrm{i}kM_x}{\beta^2}(y_1 - x_1)\right) \left[\mathrm{i}\frac{(y_1 - x_1)}{S_0} H_1^{(2)}\left(\frac{kS_0}{\beta^2}\right) + M_x H_0^{(2)}\left(\frac{kS_0}{\beta^2}\right)\right] \tag{B.3}$$

$$\frac{\partial \hat{\mathcal{G}}^{2D}(\mathbf{y}|\mathbf{x},\omega)}{\partial x_2} = \frac{\mathrm{i}k}{4S_0\beta}(y_2 - x_2) \exp\left(\frac{\mathrm{i}kM_x}{\beta^2}(y_1 - x_1)\right) H_1^{(2)}\left(\frac{kS_0}{\beta^2}\right) \tag{B.4}$$

### B.2.2 3D

In three dimensions, the convected Green function can be expressed [128]

$$\hat{\mathcal{G}}^{3D}(\mathbf{y}|\mathbf{x},\omega) = \frac{1}{4\pi S_0} \exp\left(-\frac{\mathrm{i}k}{\beta^2}\left(S_0 - M_x(y_1 - x_1)\right)\right) \tag{B.5}$$

where $S_0 = \sqrt{(y_1 - x_1)^2 + \beta^2[(y_2 - x_2)^2 + (y_3 - x_3)^2]}$ and $\beta^2 = 1 - M_x^2$. It directly follows the derivatives in the spatial directions

$$\frac{\partial \hat{\mathcal{G}}^{3D}(\mathbf{y}|\mathbf{x},\omega)}{\partial x_1} = \frac{1}{4\pi S_0}\left[\frac{y_1 - x_1}{S_0^2} - \mathrm{i}\frac{k}{\beta^2}\left(M - \frac{y_1 - x_1}{S_0}\right)\right]\exp\left(-\frac{\mathrm{i}k}{\beta^2}\left(S_0 - M_x(y_1 - x_1)\right)\right) \tag{B.6}$$

$$\frac{\partial \hat{\mathcal{G}}^{3D}(\mathbf{y}|\mathbf{x},\omega)}{\partial x_2} = \frac{(y_2 - x_2)}{4\pi S_0^2}\left[\frac{\beta^2}{S_0} + \mathrm{i}k\right]\exp\left(-\frac{\mathrm{i}k}{\beta^2}\left(S_0 - M_x(y_1 - x_1)\right)\right) \tag{B.7}$$

$$\frac{\partial \hat{\mathcal{G}}^{3D}(\mathbf{y}|\mathbf{x},\omega)}{\partial x_3} = \frac{(y_3 - x_3)}{4\pi S_0^2}\left[\frac{\beta^2}{S_0} + \mathrm{i}k\right]\exp\left(-\frac{\mathrm{i}k}{\beta^2}\left(S_0 - M_x(y_1 - x_1)\right)\right) \tag{B.8}$$

# References


[1] R.J. Astley, A. Agarwal, K.R. Holland, P.F. Joseph, R.H. Self, M.G. Smith, R. Sugimoto, and B.J. Tester. Predicting and reducing aircraft noise. In *14th International Congress on Sound and Vibration*, page 34, 2007.

[2] M. Gruber, P. Joseph, and T.P. Chong. On the mechanisms of serrated airfoil trailing edge noise reduction. In *17th AIAA/CEAS Aeroacoustics Conference*, number AIAA-2011-2781, 2011.

[3] M. Gruber. *Airfoil noise reduction by edge treatments*. PhD thesis, University of Southampton, ISVR, 2012.

[4] R. Amiet. Refraction of sound by a shear layer. *Journal of Sound and Vibration*, 54(4):467–482, 1978.

[5] T. Hainaut, G. Gabard, and V. Clair. Caa study of airfoil broadband interaction noise using stochastic turbulent vorticity sources. In *21st AIAA/CEAS Aeroacoustics Conference*, number AIAA-2015-2222, June 2015.

[6] T. Hainaut, G. Gabard, and V. Clair. A caa study of turbulence distortion in broadband fan interaction noise. In *22nd AIAA/CEAS Aeroacoustics Conference*, number AIAA-2016-2839, 2016.

[7] T. Hainaut, G. Gabard, and V. Clair. A numerical study of inflow turbulence distortion in the vicinity of blade leading edges. In *Acoustical Society of America*, December 2016.

[8] P. R. Gliebe and B. A. Janardan. Ultra-high bypass engine aeroacoustic study. Technical report, NASA, 2003.

[9] R. Kraichnan. Diffusion by a random velocity field. *Physics of Fluids*, 13(1):22–31, 1970.

[10] R. Ewert and W. Schrøder. Acoustic perturbation equations based on flow decomposition via source filtering. *J. Comput. Phys.*, 188:365–398, 2003.

[11] M. Dieste and G. Gabard. Broadband fan interaction noise using synthetic inhomogeneous non-stationary turbulence. In *17th AIAA/CEAS Aeroacoustics Conference*, number AIAA-2009-3267, 2011.

[12] M. Dieste and G. Gabard. Random particle methods applied to broadband fan interaction noise. *Journal of Computational Physics*, 231:8133–8151, 2012.

[13] N. Jarrin, S. Benhamadouche, D. Laurence, and R. Prosser. A synthetic-eddy method for generating inflow conditions for large-eddy simulations. *International Journal of Heat and Fluid Flow*, 27:585–593, 2006.

[14] N. Jarrin, J-C. Uribe, R. Prosser, and D. Laurence. *Advances in Hybrid RANS-LES Modelling*, volume 97, chapter Synthetic Inflow Boundary Conditions for Wall Bounded Flows, pages 77–86. Springer, 2008.

[15] N. Jarrin, R. Prosser, J-C. Uribe, S. Benhamadouche, and D. Laurence. Reconstruction of turbulent fluctuations for hybrid rans/les simulations using a synthetic-eddy method. *International Journal of Heat and Fluid Flow*, 30:435–442, 2009.

[16] T. Hainaut. Evaluation aérodynamique et aéroacoustique du code LaBS. Master's thesis, Ecole Nationale Supérieure d'Arts et Métiers (ENSAM), 2013.

[17] P. L. Bhatnagar, E. P. Gross, and M. Krook. A model for collision processes in gases. 1. small amplitude processes in charged and neutral one-component systems. *Physical Review*, 94:511–525, 1954.

[18] Lewis Fry Richardson. *Weather Prediction by Numerical Process*. Cambridge University Press, 2nd edition edition, 2007.

[19] J. Fung. *Kinetic Simulation of Turbulent Flow and Particle Motions*. PhD thesis, University of Cambridge, 1990.

[20] J.C.H. Fung, J.C.R. Hunt, N.A. Malik, and R.J. Perkins. Kinematic simulation of homogeneous turbulence by unsteady random fourier modes. *J. Fluid Mech.*, 236:281–318, 1992.

[21] R. Ewert. Broadband slat noise prediction based on CAA and stochastic sound sources from a fast Random Particle-Mesh (RPM) method. *Computers and Fluids*, 37:369–387, 2008.

[22] M. Siefert and R. Ewert. Sweeping sound generation in jets realized with a random particle-mesh method. In *15th AIAA/CEAS Aeroacoustics Conference*, number AIAA-2009-3369, 2009.

[23] M. Dieste and G. Gabard. Random-vortex-particle methods for broadband fan interaction noise. In *16th AIAA/CEAS Aeroacoustics Conference*, number AIAA-2010-3885, 2010.

[24] T. Lund, X. Wu, and D. Squires. Generation of turbulent inflow data for spatially-developing boundary layer simulations. *Journal of Computational Physics*, 140:233–258, 1998.

[25] R. Poletto, A. Revell, T. Craft, and N. Jarrin. Divergence free synthetic eddy method for embedded les inflow boundary conditions. In *Seventh International Symposium On Turbulence and Shear Flow Phenomena*, 2011.

[26] R. Poletto, T. Craft, and A. Revell. *Flow, Turbulence and Combustion*, volume 91, chapter A New Divergence Free Synthetic Eddy Method for the Reproduction of Inlet Flow Conditions for LES, pages 519–539. Springer, October 2013.

[27] A. Sescu and R. Hixon. Toward low-noise synthetic turbulent inflow conditions for aeroacoustic calculation. *International journal for numerical methods in fluids*, 73:1001–1010, 2013.

[28] C. Bailly and D. Juvé. A stochastic approach to compute subsonic noise using linearized Euler's equations. In *5th AIAA/CEAS Aeroacoustics Conference*, number AIAA-99-1872, 1999.

[29] I. Drummond and W. Munch. Turbulent stretching of line and surface elements. *Journal of Fluid Mechanics*, 215:45–59, 1990.

[30] M. Billson, L. Eriksson, and L. Davidson. Jet noise prediction using stochastic turbulence modeling. In *9th AIAA/CEAS Aeroacoustics Conference*, number AIAA-2003-3282, 2003.

[31] W. Bechara, C. Bailly, P. Lafon, and S. Candel. Stochastic approach to noise modeling for free turbulent flows. *AIAA Journal*, 32(3):455–463, 1994.

[32] M. Billson, L.E. Eriksson, L. Davidson, and P. Jordan. Modeling of synthetic anisotropic turbulence and its sound emission. In *10th AIAA/CEAS Aeroacoustics Conference*, number AIAA-2004-2858, 2004.

[33] R. Ewert, J. Dierke, M. Pott-Pollenske, C. Appel, R. Edmunds, and M. Sutcliffe. CAA-RPM prediction and validation of slat setting influence on broadband high-lift noise generation. In *16th AIAA/CEAS Aeroacoustics Conference*, number AIAA-2010-3883, 2010.

[34] E Krasnoff and R Peskin. The langevin model for turbulent diffusion. *Geophysical Fluid Dynamics*, 2:123–146, 1971.

[35] A. Lafitte. *Prédiction de l'aéroacoustique de jets subsoniques confinés à l'aide d'une méthode stochastique de génération de la turbulence.* PhD thesis, École Centrale de Lyon, 2012.

[36] A. Lafitte, E. Laurendeau, T. Le Garrec, and C. Bailly. A study based on the sweeping hypothesis to generate stochastic turbulence. In *17th AIAA/CEAS Aeroacoustics conference*, number AIAA-2011-2888, 2011.

[37] A. Lafitte, T. Le Garrec, C. Bailly, and E. Laurendeau. Prediction of subsonic jet noise relying on a sweeping based turbulence generation process. In *18th AIAA/CEAS Aeroacoustics conference*, number AIAA-2012-2149, 2012.

[38] M. Omais, B. Caruelle, S. Redonnet, E. Manoha, and P. Sagaut. Jet noise prediction using RANS CFD input. In *5th AIAA/CEAS Aeroacoustics Conference*, number AIAA-2008-2938, 2008.

[39] M. Dieste. *Random-Vortex-Particle Methods Applied to Broadband Fan Interaction Noise.* PhD thesis, University of Southampton, 2011.

[40] M. R. Maxey. The gravitational settling of aerosol particles in homogeneous turbulence and random flow fields. *Journal of Fluid Mechanics*, 174:441–465, 1987.

[41] A. Smirnov, S. Shi, and I. Celik. Random flow generation technique for large eddy simulations and particle dynamics modeling. *Journal of Fluids Engineering*, 123:359–371, 2001.

[42] Yu R. and Bai X.-S. A fully divergence-free method for generation of inhomogeneous and anisotropic turbulence with large spatial variation. *Journal of Computational Physics*, 256:234–253, 2014.

[43] M. Siefert and R. Ewert. *Progress in Turbulence III*, volume 131, chapter Anisotropic Synthetic Turbulence with Sweeping Generated by Random Particle-Mesh Method, pages 143–146. Springer, 2010.

[44] W. J. Devenport, C. Muthanna, R. Ma, and S. A. L. Glegg. Two-point descriptions of wake turbulence with application to noise prediction. *AIAA Journal*, 39(12):2302–2307, 2001.

[45] F. Gea-Aguilera, J. Gill, X. Zhang, X. Chen, and T. Nodé-Langlois. Leading edge noise predictions using anisotropic synthetic turbulence. In *22nd AIAA/CEAS Aeroacoustics Conference*, number AIAA-2016-2840, 2016.

[46] J. Scott and H. Atassi. Numerical solution of periodic vortical flows about a thin airfoil. In *24th AIAA Thermophysics Conference*, number AIAA-89-1691, 1989.

[47] J.R. Scott. Single airfoil gust response problem, category 3, problem 1. *Fourth computational aeroacoustics, workshop on benchmark problems,* NASA CP-2004-212954, pages 45–58, 2004.

[48] H. Atassi, S. Subramaniam, and J. Scott. Acoustic radiation from lifting airfoils in compressible subsonic flows. In *13th AIAA Aeroacoustic Conference*, number AIAA-90-3911, 1990.

[49] J. Scott, H. Atassi, and R. Susan-Resiga. A new domain decomposition approach for the gust response problem. In *41st AIAA Aerospace Sciences Meeting*, number AIAA-2003–0883, 2003.

[50] D. Lockard and P. Morris. A parallel implementation of a computational aeroacoustic algorith for airfoil noise. In *2nd AIAA/CEAS Aeroacoustics Conference*, number AIAA-96-1754, 1996.

[51] D. Lockard and P. Morris. Radiated noise from airfoils in realistic mean flows. *AIAA Journal*, 36(6):907–914, 1998.

[52] R. Hixon, J. Scott, S. Sawyer, and M. Nalasamy. Application of a nonlinear computational aeroacoustics code to the gust-airfoil problem. *AIAA Journal*, 44(2):323–328, 2006.

[53] V. Golubev, R. Mankbadi, and J. Scott. Numerical inviscid analysis of nonlinear airfoil response to impinging high-intensity high-frequency gust. In *10th AIAA/CEAS Aeroacoustics Conference*, number AIAA-2004-3002, 2004.

[54] V. Golubev, R. Mankbadi, M. Visbal, J. Scott, and R. Hixon. A parametric study of nonlinear gust-airfoil interaction. In *12th AIAA/CEAS Aeroacoustics Conference*, number AIAA-2006-2426, 2006.

[55] M. Karweit, P. Blanc-Benon, D. Juvé, and G. Comte-Bellot. Simulation of the propagation of an acoustic wave through a turbulent velocity field: a study of phase variance. *Journal of the Acoustical Society of America*, 89(1):52–62, 1991.

[56] R. Ewert and R. Edmunds. CAA slat noise studies applying stochastic sound sources based on solenoidal digital filters. In *11th AIAA/CEAS Aeroacoustics Conference*, number AIAA-2005-2862, 2005.

[57] R. Ewert, C. Appel, J. Dierke, and M. Herr. RANS/CAA based prediction of NACA 0012 broadband trailing edge noise and experimental validation. In *15th AIAA/CEAS Aeroacoustics Conference*, number AIAA-2009-3269, 2009.

[58] M. Bauer, J. Dierke, and R. Ewert. On the performance of airframe noise prediction on unstructured grids. In *18th AIAA/CEAS Aeroacoustics Conference*, number AIAA-2012-2148, 2012.

[59] V. Clair. *Calcul numérique de la réponse acoustique d'un aubage soumis à un sillage turbulent*. PhD thesis, Université Claude Bernard – Lyon 1, 2013.

[60] R.K. Amiet. Acoustic radiation from an airfoil in turbulent stream. *Journal of Sound and Vibration*, 41(4):407–420, 1975.

[61] J. Gill. *Broadband Noise Generation of a Contra-Rotating Open Rotor Blade*. PhD thesis, Airbus Noise Technology Centre, University of Southampton, 2015.

[62] James Gill, X. Zhang, and P. Joseph. Symmetric airfoil geometry effects on leading edge noise. *Journal of acoustical society of America*, 134(4), 2013.

[63] J. Gill, X. Zhang, P. Joseph, and T. Node-Langlois. Effects of real airfoil geometry on leading edge gust interaction noise. In *19th AIAA/CEAS Aeroacoustics Conference*, number AIAA-2013-2203, 2013.

[64] F. Gea-Aguilera, X. Zhang, X. Chen, J. R. Gill, and T. Nodé-Langlois. Synthetic turbulence methods for leading edge noise predictions. In *21st AIAA/CEAS Aeroacoustics Conference*, number AIAA-2015-2670, 2015.

[65] J. W. Kim and S. Haeri. An advanced synthetic eddy method for the computation of aerofoil–turbulence interaction noise. *Journal of Computational Physics*, 287, 2015.

[66] K. Hall and J. Verdon. Gust response analysis for cascades operating in nonuniform mean flows. *AIAA Journal*, 29(9):1463–1471, 1991.

[67] M. Nallasamy, R. Hixon, and S. Sawyer. Solution of unsteady Euler equations: Gust–cascade interaction tones. *Computer & Fluids*, 36:724–741, 2007.

[68] R. Hixon, A. Sescu, M. Nallasamy, and S. Sawyer. Prediction of noise from realistic rotor-wake/stator-row interaction using computational aeroacoustics. In *15th AIAA/CEAS Aeroacoustics Conference*, number AIAA-2009-3339, 2009.

[69] H. Atassi and I. Vinogradov. A model for fan broadband interaction noise in nonuniform flow. In *11th AIAA/CEAS Aeroacoustics Conference*, number AIAA-2005-2880, 2005.

[70] H. Atassi and I. Vinogradov. Modelling broadband fan noise and comparison with experiments. In *13th AIAA/CEAS Aeroacoustics Conference*, number AIAA-2007-3691, 2007.

[71] H. Atassi and M. Logue. Effect of turbulence structure on broadband fan noise. In *14th AIAA/CEAS Aeroacoustics Conference*, number AIAA-2008-2842, 2008.

[72] V. Golubev and H. Atassi. Unsteady swirling flows in annular cascades, part 2: aerodynamic blade response. *AIAA Journal*, 38(7):1150–1158, 2000.

[73] H. Atassi, A. Ali, O. Atassi, and I. Vinogradov. Scattering of incident disturbances by an annular cascade in a swirling flow. *Journal of Fluid Mechanics*, 499:111–138, 2004.

[74] B. Elhadidi and H. Atassi. High frequency sound radiation from an annular cascade in swirling flows. In *8th AIAA/CEAS Aeroacoustics Conference*, number AIAA-2002-2560, 2002.

[75] H. M. Atassi and M. M. Logue. Fan broadband noise in anisotropic turbulence. In *15th AIAA/CEAS Aeroacoustics Conference*, number AIAA-2009-3148, 2009.

[76] Attila M. Wohlbrandt, Sebastien Guerin, and Roland Ewert. Extension of the random particle mesh method to periodic turbulent flows for fan broadband noise prediction. In *21th AIAA/CEAS Aeroacoustics Conference*, number AIAA-2015-2383, June 2015.

[77] C. Rumsey, R. Biedron, and F. Farassat. Ducted-fan engine acoustic predicitions using a Navier-Stokes code. *Journal of Sound and Vibration*, 213(4):643–664, 1998.

[78] R. Biedron, C. Rumsey, G. Podboy, and M. Dunn. Prediction of the rotor-stator interaction acoustics of a ducted fan engine. In *39th AIAA Aerospace Sciences Meeting*, number AIAA-2001-0664, 2001.

[79] M. Olausson and L.-E. Eriksson. Rotor wake/stator broadband noise calculations using hybrid RANS/LES and chorochronic buffer zones. In *15th AIAA/CEAS Aeroacoustics Conference*, number AIAA-2009-3338, 2009.

[80] G. A. Gerolymos, G. J. Michon, and J. Neubauer. Analysis and application of chorochronic periodicity in turbomachinery rotor/stator interaction computations. *Journal of Propulsion and Power*, 18(6):1139–1152, 2002.

[81] M. Olausson, L.-E. Eriksson, and S. Baralon. Evaluation of nonlinear rotor wake/stator interaction by using time domain chorochronic solver. In *8th International Symposium on Experimental and Computational Aerothermodynamics of Internal Flows*, 2007.

[82] B. Greschner and F. Thiele. Wall modeled LES simulation of rotor-stator-cascade broadband noise. In *17th AIAA/CEAS Aeroacoustics Conference*, number AIAA-2011-2873, 2011.

[83] A. K. Travin, M. L. Shur, P. R. Spalart, and M. K. Strelets. *Improvement of Delayed Detached-Eddy Simulation for LES with Wall Modelling.* ECCOMAS CFD, 2006.

[84] P. R. Spalart, S. Deck, M. L. Shur, K. D. Squires, M.Kh. Strelets, and A. K. Travin. A new version of detached-eddy simulation, resistant to ambiguous grid densities. *Theoretical and Computational Fluid Dynamics*, 20 (3):181–195, 2006.

[85] T. Carolus, M. Schneider, and H. Reese. Axial flow fan broad-band noise and prediction. *Journal of Sound and Vibration*, 300:50–70, 2007.

[86] H. Reese, C. Kato, and T. Carolus. Large eddy simulation of acoustical sources in a low pressure axial-flow fan encoutering highly turbulent inflow. *Journal of Fluids Engineering*, 129:263–272, 2007.

[87] A. Mann, F. Pérot, M.-S. Kim, D. Casalino, and E. Fares. Advanced noise control fan direct aeroacoustics predictions using a Lattice-Boltzmann method. In *18th AIAA/CEAS Aeroacoustics Conference*, number AIAA-2012-2287, 2012.

[88] R. Loew, J. Lauer, J. McAllister, and D. Sutliff. The advanced noise control fan. In *25th AIAA Aerodynamic Measurement Technology and Ground Testing Conference*, 2006.

[89] J. McAllister, R. Loew, J. Lauer, and D. Sutliff. The advanced noise control fan baseline measurements. In *47th AIAA Aerospace Sciences Meeting including The New Horizons Forum and Aerospace Exposition*, number AIAA 2009-624, 2009.

[90] B.-T. Chu and L. Kovásznay. Non-linear interactions in a viscous heat-conducting compressible gas. *Journal of Fluid Mechanics*, 3(5):494–514, 1958.

[91] C. Tam and J. Webb. Dispersion-Relation-Preserving finite difference schemes for computational acoustics. *Journal of Computational Physics*, 107:262–281, 1993.

[92] F. Hu. On absorbing boundary conditions for linearized Euler equations by a perfectly matched layer. *Journal of Computational Physics*, 129:201–219, 1996.

[93] J. S. Shang. High-order compact-difference schemes for time-dependent maxwell equations. *Journal of Computational Physics*, 153(2):312–333, 1999.

[94] O. V. Vasilyev, T. S. Lund, and P. Moin. A general class of commutative filters for les in complex geometries. *Journal of Computational Physics*, 146(1):82–104, 1998.

[95] C. Tam, J. Webb, and Z. Dong. A study of the short wave components in computational acoustics. *Journal of Computational Acoustics*, 1(1):1–30, 1993.

[96] A. Wohlbrandt, S. Guérin, and R. Ewert. Simultaneous computation of surface and volume sources for fan broadband noise with the Random-Particle-Mesh method. In *19th AIAA/CEAS Aeroacoustics Conference*, number AIAA-2013-2119, 2013.

[97] R. Courant, K. Friedrichs, and H. Lewy. Ʊber die partiellen differenzengleichungen der mathematischen physik. *Mathematische Annalen*, 100 (1):32–74, 1928.

[98] R.D. Sandberg, L.E. Jones, and N.D. Sandham. Direct numerical simulations of noise generated by turbulent flow over airfoils. In *14th AIAA/CEAS Aeroacoustics Conference*, number AIAA-2008-2861, 2008.

[99] C. Paruchuri, J. R. Gill, N. Subramanian, P. Joseph, C. Vanderwel, X. Zhang, and B. Ganapathisubramani. Aerofoil geometry effects on turbulence interaction noise. In *21th AIAA/CEAS Aeroacoustics Conference*, number AIAA-2015-2830. American Institute of Aeronautics and Astronautics, June 2015.

[100] C. Tam. Computational aeroacoustics: Issues and methods. *AIAA Journal*, 33(10):1788–1796, 1995.

[101] G. Gabard. Noise sources for duct acoustics simulations: Broadband noise and tones. *AIAA Journal*, 52:1994–2006, 2014.

[102] J.M. Nichols, C.C. Olson, J.V. Michalowicz, and F. Bucholtz. A simple algorithm for generating spectrally colored, non-gaussian signals. *Probabilistic Engineering Mechanics*, 25:315–322, 2010.

[103] F. Elliott, D. Horntrop, and A. Majda. A fourier-wavelet monte carlo method for fractal random fields. *Journal of Computational Physics*, 132:384–408, 1997.

[104] J. Coupland. Fan stage broadband noise benchmarking programme - specification of fundamental test case 1 (fc1). http://www.oai.org/aeroacoustics/FBNWorkshop, 2014.

[105] Stephane Moreau, Manuel Henner, Gianluca Iaccarino, Meng Wang, and Michel Roger. Analysis of flow conditions in freejet experiments for studying airfoil self-noise. *AIAA Journal*, 41(10):1895–1905, 2003.

[106] H. Deniau, J.-F. Boussuge, C. Polacsek, and S. Moreau. Affordable compressible LES of airfoil-turbulence interaction in a free jet. In *17th AIAA/CEAS Aeroacoustics Conference*, number AIAA-2011-2707, 2011.

[107] F. R. Menter. Zonal two equation k-$\omega$ turbulence models for aerodynamic flows. *AIAA Journal*, (93-2906), 1993.

[108] V. Clair, C. Polacsek, T. Le Garrec, and G. Reboul. CAA methodology to simulate turbulence-airfoil noise. In *18th AIAA/CEAS Aeroacoustics Conference*, number AIAA-2012-2189, 2012.

[109] David P. Lockard. An efficient, two-dimensional implementation of the Ffowcs-Williams and Hawkings equation. *Journal of Sound and Vibration*, 229(4):897–911, 2000.

[110] David P. Lockard. A comparison of Ffowcs Williams-Hawkings solvers for airframe noise applications. In *8th AIAA/CEAS Aeroacoustics Conference*, number AIAA-2002-2580, 2002.

[111] S. Sinayoko, M. Wright, and R. Sandberg. A generalised ffowcs-williams and hawkings formulation applied to flow simulations with vortical outflow. In *22nd International Congress on Sound and Vibration (ICSV)*, 2015.

[112] L. Santana, C. Schram, and W. Desmet. Airfoil noise prediction from 2d3c piv data. In *21st AIAA/CEAS Aeroacoustics Conference*, 2015.

[113] G. K. Batchelor and I. Proudman. The effect of rapid distortion of a fluid in turbulent motion. *The Quarterly Journal of Mechanics and Applied Mathematics*, 7(1):83–103, 1954.

[114] Daehwan Kim, Gwang-Se Lee, and Cheolung Cheong. Inflow broadband noise from an isolated symmetric airfoil interacting with incident turbulence. *Journal of Fluids and Structures*, 55:428–450, May 2015.

[115] S. Glegg and W. Devenport. Turbulence modeling for rotor stator interaction noise. In *16th AIAA/CEAS Aeroacoustics Conference*, number AIAA-2010-3745, 2010.

[116] Peter D. Lysak, Dean E. Capone, and Michael L. Jonson. Prediction of high frequency gust response with airfoil thickness effects. *Journal of Fluids and Structures*, 39:258–274, May 2013.

[117] M. Howe. Unsteady lift and sound produced by an airfoil in a turbulent boundary layer. *Journal of Fluids and Structures*, 15(2):207–225, February 2001.

[118] S. Grace. Unsteady blade response : the BVI model vs. the gust model. In *7th AIAA/CEAS Aeroacoustics Conference*, number AIAA-2001-2209, 2001.

[119] Abbott I. H. and von Doenhoff A. E. *Theory of Wing Sections*. Dover, 1959.

[120] J. Christophe. *Application of Hybrid Methods to High Frequency Aeroacoustics*. PhD thesis, Von Karman Institute for Fluid Dynamics, Université Libre de Bruxelles, 2011.

[121] L. Santana, J. Christophe, C. Schram, and W. Desmet. A rapid distortion theory modified turbulence spectra for semi-analytical airfoil noise prediction. *Journal of Sound and Vibration*, 383:349–363, 2016.

[122] J. Hunt. A theory of turbulent flow round two-dimensional bluff bodies. *Journal of Fluid Mechanics*, 61(4):625–706, 1973.

[123] M.J. Lighthill. On sound generated aerodynamically II. Turbulence as a source of sound. *Royal Society of London*, A 222:1–32, 1954.

[124] M. Goldstein. Unsteady vortical and entropic distortions of potential flows round arbitrary obstacles. *Journal of Fluid Mechanics*, 89:433–468, 1978.

[125] Pozrikidis C. *Fluid Dynamics: Theory, Computation, and Numerical Simulation*. Springer, second edition edition, 2009.

[126] J. Anderson. *Fundamentals of Aerodynamics*. McGraw-Hill Education, 6th edition, 2011.

[127] C. Paruchuri, S. Subramaniam, Joseph P., and J. W. Kim. Leading edge serration geometries for significantly enhanced leading edge noise reductions. In *22nd AIAA/CEAS Aeroacoustics Conference*, number AIAA-2016-2736, 2016.

[128] C. Bogey, C. Bailly, and D. Juvé. Numerical simulation of sound generated by vortex pairing in a mixing layer. *AIAA Journal*, 38(12):2210–2218, 2000.